Single Photon Counting Lidar Techniques and Instrumentation for Geoscience Applications

by

Rory Alistair Barton-Grimley

B.S., University of California Santa Barbara, 2014

M.S., University of Colorado at Boulder, 2017

A thesis submitted to the

Faculty of the Graduate School of the

University of Colorado in partial fulfillment

of the requirements for the degree of

Doctor of Philosophy

Department of Aerospace Engineering Sciences

2019

This thesis entitled:
Single Photon Counting Lidar Techniques and Instrumentation for Geoscience Applications
written by Rory Alistair Barton-Grimley
has been approved for the Department of Aerospace Engineering Sciences

Prof. Jeffrey P. Thayer

Dr. Amin R. Nehrir

Prof. Robert Marshall

Prof. Kelvin Wagner

Prof. Scott Palo

Date

The final copy of this thesis has been examined by the signatories, and we find that both the content and the form meet acceptable presentation standards of scholarly work in the above mentioned discipline.

Barton-Grimley, Rory Alistair (Ph.D., Aerospace Engineering Sciences)

Single Photon Counting Lidar Techniques and Instrumentation for Geoscience Applications

Thesis directed by Prof. Jeffrey P. Thayer

The recent 2017 Earth Science Decadal Survey explicitly calls for a multi-functional lidar instrument that can address combined atmospheric, topographic, and bathymetric needs. A wide breadth of measurements are achievable with photon counting lidar sensors, establishing them as multi-functional in their ability to observe a variety of phenomena and properties with a single instrument. However, the desire to observe dynamic targets at high resolution often introduces stringent spatial and temporal requirements that cannot be met due to the prescribed nature of most photon counting techniques. The advent of advanced single photon counting lidar (SPL) sensors, utilizing time-correlated single photon counting techniques (TCSPC), addresses these difficulties while also displaying novel applicability to a number of diverse geophysical observations, allowing operation in a wide-range of regimes with several simultaneous scientific objectives. This thesis explores point cloud generation and the statistical implications on data retrievals utilizing the TCSPC approach, through ground based and airborne demonstrations. A dual-polarization SPL sensor was flown on the NSF/NCAR GV research aircraft, where the techniques and instrumentation developed were applied to atmospheric, topographic, and bathymetric retrievals. The results proved the viability and applicability of the TCSPC approach to multi-functional lidar sensor development. The published results show an ability to preserve backscattered intensity while generating photon detections at picosecond resolution from a variety of scatterers, atmospheric and hard target. They also show that utilization of the TCPSC approach for estimating backscattered intensity requires special attention to mitigate biases and non-linear distortions typically not seen in traditional sensors. The work culminated within this thesis describes the amalgamation of hardware development and model advancement, allowing testing and validation of SPL measurements while also demonstrating their applicability to geophysical parameter estimation.

Acknowledgements

This thesis work could not have happened without my parents encouragement, “stay the course”, and the sacrafices they both made to give my brothers and I opportunities of which I will be forever grateful for.

I have to thank Bailey Walker for her constant support, editorial skills, all of the great adventures we have been on, and being my absolutely fantastic person.

I thank my advisor Professor Thayer for seeing something in me while I was still an undergraduate and inviting me into ARSENL. You have helped me grow, serving as a great advisor and mentor. I also thank Dr. Amin Nehrir for his mentoring, you helped me understand my work and became a friend at the same time.

I have to give special thanks to Robert Stillwell and Bryce Garby who both became good friends of mine and were instrumental to the sucess of this work. Thanks to my friends in the department for providing me ample time to talk about work and nonsense. Particularly Greg Lucas, Andy Gisler, Nick Rainville, Brett Bender, Dawson Beatty, Ashwin Yerasi, Matt Tooth, and many others. Thanks to Matt and Scott at NCAR for so many helpful discussions and opportunities, and everyone at the RAF for the ARISTO campaign. It is necessary to acknowledge all those in CCAR that make the world go round, our research would grind to a halt without you.

This work was supported by the National Science Foundation under grant number #1500166 and by the NASA Earth and Space Sciences Fellowship under grant number #NNX16AO46H. However, any opinions, findings, conclusions, or recommendations expressed herein are those of the author and do not necessarily reflect the views of the NSF or NASA.

Contents

Chapter

Tables

Table

Figures

Figure

Chapter 1

Introduction

This thesis will describe the sensor development and observations, supported by the advancement of several statistical and polarimetric models, that facilitates the application of single photon counting lidar (SPL) instrumentation in high resolution atmospheric and topographic/bathymetric monitoring. The advent of advanced SPL sensors, utilizing photon time-tagging and time-correlated single photon counting (TCSPC), have novel applicability to a number of diverse geophysical observations, allowing operation in a wide-range of regimes with several simultaneous scientific objectives. The use of TCSPC in topographic/bathymetric sensing, where range and intensity is retrieved, has little to no prior specific development and deployment for geoscience. In addition, there is no heritage for these techniques in atmospheric monitoring, where sub-centimeter atmospheric point cloud generation is a novel method for understanding the atmosphere at higher resolution than typically considered. This gap in knowledge must be bridged in order to apply TCSPC seamlessly across measurement regimes and provide multi-functional capabilities that can facilitate high resolution geophysical parameter estimation.

Characteristic proof-of-concept analysis and laboratory demonstrations indicate that the technical readiness level (TRL) for SPL sensors employing TCSPC is TRL-3. The goal of this thesis is to advance SPL hardware and TCSPC techniques for geoscience to a TRL-5/6 and provide demonstration in the operational environment. Towards this effect, an advanced sensor was engineered and fielded for ground based and airborne measurements to demonstrate the fundamental application of TCSPC for geoscience applications. This work resulted in the publication

of several novel TCSPC applications and the required descriptions for system modeling. While previous studies have involved scalar descriptions of sensor components and scattering events and assumed simplistic statistical models for photon detection, this thesis focuses on a combination of the deterministic, stochastic, and polarimetric aspects of the sensor architecture, photon scattering, and detection processes. The amalgamation of hardware development and rigorous model advancement allows simultaneous testing and validation of SPL measurement aspects that drive sensor efficiency, photon detectability, and science applicability, creating a foundation for future multi-function SPL sensor development and design.

1.1 Background

Direct motivation for this work stems from three main components. The first being that photon counting lidar sensors have limited applicability due to the restrictions imposed by the prescribed acquisition and timing techniques. With these restrictions lifted, flexible high resolution photon lidar data can be generated. This allows a single sensor to address many different observations within a scalable resolution data stream, directly answering the call from the recent Earth Science Decadal Survey (ESDS) for multi-functional lidar sensors that can address combined atmospheric and topographic/bathymetric science needs. Work to achieve these goals also supports the recently launched ATLAS sensor onboard the ICESat-2 satellite, which is a demonstration of the photon counting lidar technique from space. With an emphasis on topographic retrievals there is limited on applicability to bathymetric and atmospheric science. Supplementation with advanced airborne sensors facilitates an understanding of ATLAS capabilities through measurement validation and verification. These sensor can also further introduce advancement by emphasizing the necessity of multi-functional capabilities for future sensor development.

Synergistic lidar approaches that measure a subset of observables have been demonstrated, such as the work discussed in [55], but technological challenges still exist and there is ample working space for this instrumentation. Multi-functional photon counting techniques and instrumentation, for addressing spans of spatial and temporal resolutions as shown in Fig. 1.1, have been identified to

address those needs. Separate demonstrations for the atmospheric and bathymetric regimes show promising results and instrumentation that leverages heritage from both fields can be designed to coalesce the two measurements together.

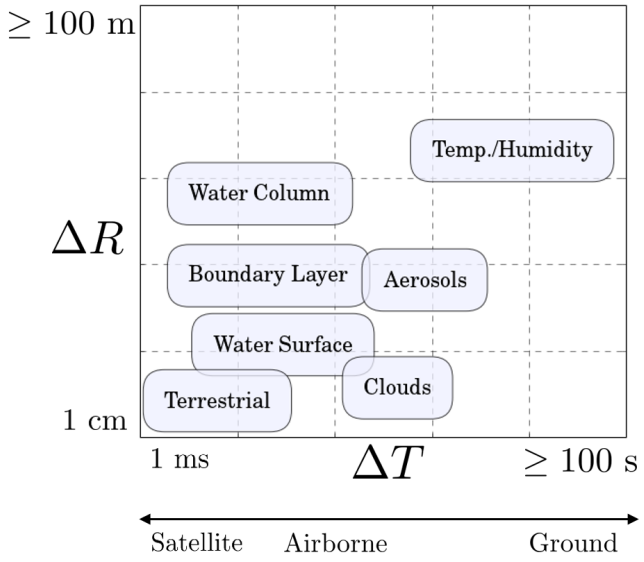

Figure 1.1: Visual representation of the approximate spatial and temporal resolutions needed to achieve the correct SNR or measurement frequency for various different geophysical measurements that photon counting lidar sensors have been applied to.

Improved, high-resolution topographic lidar mapping provides critical information for hazard assessment and mitigation, while also providing invaluable science data. Measurements of surface elevation change, sea ice freeboard, and bare surface land topography were recently identified as some of the 22 identified Targeted Observables (TO) — Table 3.5 and Appendix C. One such example is the call for an imaging laser altimeter with 10 cm vertical accuracy for the aforementioned measurements and comparable accuracy, 25 cm, to facilitate vegetation structure mapping, including 3D canopy height. Several TOs also make the explicit request for multi-functional lidar with the ability to provide high resolution data by which many geophysical parameters can be derived for a variety of applications.

The specific question of shallow water retrievals remains an open problem and has been identified in the ESDS under TO-20 and TO-21 because of its importance in addressing specific science

imperatives across the disciplines of Global Hydrological Cycles and Water Resources, Marine and Terrestrial Ecosystems and Natural Resource Management, and Climate Variability and Change. A complete list of relevant TOs is shown in Table 1.1. The ESDS candidate measurement approach for shallow water bathymetry describes the need for lidar sensors to meet the requirement of 1-5 m horizontal resolution and a vertical resolution of 10 cm. The proposed resolution and accuracy are also representative of those required for littoral zone mapping and understanding the coastal environment, which, beyond scientific purposes has immense use in defense applications. High-resolution bathymetric lidar measurements have proved challenging due to rough surface waters, varying subsurface reflectivity, water column turbidity, and an inability to differentiate water surface from near field subsurface scattering layers due to detector pulse overlap; the latter being a roadblock to attempting retrievals in the shallow regime. Work done in Mitchell et al. [92, 91] showed a measurement technique to address the shallow water bathymetry issue, but implementation has not been widespread and does not focus on retrievals of intensity and range.

Table 1.1: Summary of SPL relevant Earth Science Decadal Survey targeted observables

Targeted Observable	**Science & Applications**	**Requirements**
TO-7 Ice Elevation	Ice sheet structure & sea ice freeboard	0.1 m vert.
TO-10 Ocean Ecosystem	Biomass, spectral attenuation	2 m vert.
TO-13 Planetary Boundary Layer	Height, Temperature, Water vapor	200 m vert.
TO-20 Surface Topography	Shallow water bathymetry, topography	1-5 m horz., 0.1 m vert. acc.
TO-21 Surface Water Height	Surface structure & riverine	0.02 m vert.
TO-22 Terrestrial Ecosystem	Topographic elevation	10-15 m horizontal, 0.25 m vert.

The problem of shallow water in lidar operation also plagues open ocean measurements. Vertical resolution of the column has typically been limited to $\geq$ 1 m and correctly tying down the ocean surface for retrievals is difficult and often not done. Resolution and proper handling of surface signals is absolutely necessary in this measurement. Addressing the issues of resolving shallow water environments has cross-cutting applications, as the solutions can be equally applied between shallow and deeper water measurements. The approach of polarimetric photon counting

lidar can serve these purposes [92, 91, 4, 3] by providing backscattered surface and subsurface intensities at resolutions < 10 cm. The instrumentation and techniques developed to address the shallow water measurements also have direct translation to atmospheric monitoring [3].

The use of photon counting as a tool to generate backscattered intensity profiles has been widely utilized in lidar remote sensing of the atmosphere. Regular retrievals of aerosols and cloud microphysical properties [113, 16, 46, 116], water vapor [114, 96], Rayleigh temperature inversions [117], and many other applications have been shown. The science requirements that drive these measurements typically call for several meter vertical resolution over multiple seconds. However, recent work by Beals *et al.* [7] gives a bounding range resolution of approximately 1-10 mm as a requirement to resolve the sharpness of cloud edges without introducing ambiguities through spatial averaging. This type of measurement is necessary for constraining phase transitions within clouds and analyzing microphysical properties [7]. Current ground-based and airborne photon counting lidars are unable to operate with this resolution, nor this precision, and leaving an instrumentation void where these requirements are not fulfilled.

Several advances in photon counting instrumentation, specifically as micropulse lidars, have been made over the past two decades; some specifically in preparation for the ICESat-2 ATLAS sensor [23, 24, 43, 86]. ATLAS is a single photon counting sensor with the anticipated ability to make topographic and bathymetric measurements with horizontal resolution of 70 m — surface spot diameter of 14 m, spaced at 0.7 m along track between beams, with 100 pts integrated — and a surface vertical resolution of ~ 0.1 m, all based on pulse width estimates and an airborne validation study [79, 11]. Though the full fidelity of individual ground returns will be preserved, ~ 1 ns timing resolution, the ATLAS atmospheric product is expected to be binned on satellite at 30 m vertical resolution and 280 m horizontal [79], giving a degraded resolution for atmospheric studies and providing a single wavelength of polarization insensitive backscatter information. The acquisition scheme distinguishes between detections from the ground and the atmosphere, where each photon is processed as a discrete time-tag for surface returns and the multi-channel scaler (MCS) binning approach is applied for atmospheric returns.

The global coverage given by the ATLAS instrument will be a tremendous step forward in topographic, bathymetric, and atmospheric sensing that uses photon counting lidar technique. Though the continuation of spaceborne lidar sensing at 532 nm will provide good continuity between CALIPSO [125], CATS [128], and the next dedicated atmospheric sensor, limited science retrievals decrease the applicability of the ATLAS sensor to atmospheric science. The success of CALIPSO shows that the combination of multiple channels of backscatter measurements and dual planes of polarization for depolarization estimates provides a set of atmospheric retrievals that can now be considered the minimum spanning set of measurements for atmospheric monitoring of clouds and aerosols. In this thesis, specific advancement of SPL atmospheric sensing with these minimum capabilities will be considered.

Overall supplementation of the ATLAS sensor with instrumentation that can provide the necessary resolutions and validation in the required observable regimes represents a unique opportunity to advance novel sensor technology and engineering methods. Prior sensors have shown promising results for high resolution topographic, bathymetric, and atmospheric sensing separately, but do not yet represent a viable solution to the combined set of techniques and instrumentation needed for multi-function operation. SPL utilizing TCSPC constitutes a set of hardware and techniques suited to address the issues arising with combined measurement modalities. The work contained within this thesis will advance the TRL of SPL sensors pursuing geophysical parameter estimation and provide documentation that aides sensor description and design.

1.2 Contributions to the Understanding of Single Photon Counting Lidar

The research presented develops improved methods and instrumentation for high resolution photon time-tagging polarization lidar and the subsequent application to geophysical measurements. This is achieved by advancing an all encompassing photon time-tagging approach for SPL sensors, providing new techniques and understanding, that facilitates a lidar sensor capable of discriminating multi-resolution targeted observables for combined atmospheric and topographic/bathymetric retrievals in a measurement cycle.

The overarching hypothesis addressed within this thesis is that: **Photon counting lidar sensors utilizing time-correlated single photon counting techniques can provide multi-functional capabilities and facilitate high resolution geophysical parameter estimation.** To address this hypothesis, the following specific questions are addressed:

(1) What are the implications of utilizing the time-correlated single photon counting approach for geophysical parameter estimation from volume scattering environments?

(2) How are estimates of backscattered photon rate and target range affected by the implementation of the photon time-tagging approach?

(3) Can polarimetric lidar incorporate time-correlated single photon counting, and what are the implications to high resolution multi-functional measurements of atmosphere, ocean, and hard targets?

This thesis is organized into several main chapters and additional appendices for information specifics, each facilitating and contributing work to answer the questions posed.

The foundations of lidar theory, including polarization, scattering, and counting theory are discussed in Chapter 2. Chapter 3 introduces the detection and acquisition of single photons by a lidar sensor, including prior methods and the implications of time-correlated single photon counting in lidar. A comprehensive measurement model is developed and exercised in Chapter 4, providing bounding characteristics for sensor development and measurement strategies. Chapter 5 provides initial implementation and testing of the discussed techniques in a novel polarization sensitive SPL including: system metrics, ground testing, and data generation. Chapter 6 focuses on aircraft demonstrations of a novel SPL sensor, discussing measurement and model comparison, data acquisition in a number of operational regimes, and overall system analysis. Chapter 7 introduces a formal comparison and forward modeling of the SPL sensor, and provides new approach to verify operation in the single photon counting regime. Finally, in Chapter 8 a summary of the major results of this thesis and how they address the hypothesis and proposed research questions is given.

Chapter 2

Light Detection and Ranging

Lidar can be used to generate measurements of a remote target, range, and backscattered intensity, without relying on ancillary radiation sources to illuminate the scene under interrogation. By avoiding the use of radiant signals of opportunity and controlling the properties of the transmitted laser light — such as modulating planes of polarization, spectral and timing characteristics — the backscattered light field can be collected and used to elucidate the measurement environment with high temporal and spatial resolution. The ability to generate laser light for measurement has led to discrimination techniques, which allow for investigations of narrow frequency absorption bands [96], polarization properties of scatterers [47], high precision mapping [24], and an increasing number of new uses as advancements in associated technology makes lidar more accessible. With the ability to generate measurements over a variety of scales, ranging from terrestrial instruments with millimeter range precision and microsecond integrated time lengths to global multi-year satellite instruments, lidar is a versatile tool for contributing information to advance our knowledge of Earth's systems.

To understand the projected environmental response of lidar sensing, several mathematical formulations have been developed. SPL representations can be divided into scalar and vector with applicability to all scattering environments typically encountered in Earth science. This thesis seeks to correctly capture the complex physics present in these measurements by describing the coupling between polarization planes and overall stochastic nature of the single photon measurement.

2.1 Scalar Lidar Definitions

Fundamentals of the SPL measurement include the transmission of laser light through an attenuating medium, the collection of the light scattered at 180°, optical analysis of the light, detection of the received light, and conversion to an electrical signal that can be further analyzed in the analog or digital domains. Typical application of the lidar equation for SPL sensors assumes independent single backscattering of the laser light from a target. Formulating these ideas into a single equation [88, 122], the range dependent elastic scattering lidar equation can be used to estimate the received photon counts from a volume scattering layer for a single laser shot. This equation can be written as

$$N(\lambda, R) = \left(\frac{P_L \tau_L}{h\nu}\right) \beta(\lambda, R) \Delta R \frac{A}{R^2} O(R) T^2(\lambda, R) \eta_{rx} \eta_{tx} + N_B \ . \tag{2.1}$$

In Eq. 2.1 P_L describes the amount of laser power transmitted over a pulse length τ_L containing photons with energy $h\nu$, $\beta(\lambda, R)$ is the volumetric backscatter coefficient, ΔR is the range bin resolution and can also be given as $c\tau_{bin}/2$, $\frac{A}{R^2}$ is the solid angle term describing the amount of light collected by the telescope area taking into account the quadratic decrease in signal intensity, $O(R)$ is the geometric overlap function between the transmitter and receiver, $T^2(\lambda, R)$ is the two way transmission loss term is a derived from the Beer-Lambert law as a linear product for all intensity extinguishing volumes in the measurement path, $\eta_{rx}\eta_{tx}$ describe the relative transmit and receiver efficiencies defined up until the detector face, and N_B is the number of non-signal background counts. These terms coalesce to give the total number of counts as seen at the detector face as a function of transmit wavelength and range as $N(\lambda, R)$. This formulation assumes that the laser pulse width is less than the bin resolution, $\tau_L < \tau_{bin}$ and that the laser spot is fully contained within the FOV of the receiver. If the detector quantum efficiency is included in this, as η_{QE}, then N becomes an estimate for the number of detector generated photoelectrons that would be subjected to acquisition. In the case of scattering from discrete changes in the index of refraction at a boundary between surfaces, such as that of the air to water surface or air to hard target, the

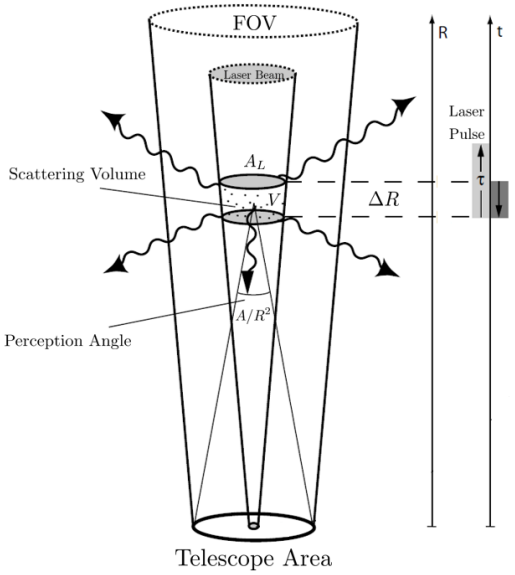

Figure 2.1: Lidar transmit and receive geometry as adapted by [122]. The scattering volume, V can be seen and is defined by the area of the laser spot, A_L and the range resolution, ΔR. The relationship between the scattering volume range and the telescope area is seen by the solid angle of A/R^2.

number of returns can be estimated as

$$N_{rx}(\lambda, R) = \left(\frac{P_L \tau_L}{h\nu}\right) \frac{\rho \cos(\theta)}{\Omega_{tgt}} \left(\frac{A_{ifov}}{A_s}\right)^2 \frac{A}{R^2} O(R) T^2(\lambda, R) \eta_{rx} \eta_{tx} + N_B \ , \tag{2.2}$$

where ρ is the target reflectivity, θ is a description of the incident angle of the laser light at the target surface, and the ratio of A_{ifov} to A_s describes the fractional area of the laser spot within the instantaneous field-of-view (FOV) of the receiver (which is typically unity). The term Ω_{tgt} provides a description of the bi-directional reflection distribution function (BRDF) to capture the scattering cross-section of the target. Under Lambertian scattering, the BRDF reduces to the commonly used value of π sr^{-1}, as is the case for many scattering targets in topographic/bathymetric ranging problems. However, when considering the discrete index change at the water surface, the specular reflection should be considered and Fresnel equations used [9]. For more complex scattering cross-sections where multiple types of surfaces are contained within the laser spot, a combination of diffuse and specular components is derived in [115] and elaborated on in Chapter 4. In this formulation the

bin width, ΔR, has now been omitted as the scattering layer is assumed to be a delta function and the driving resolution for which the the surface bin is estimated involves the convolved temporal response function of the surface and sensor.

All components in Eqs. 2.1 and 2.2 are given as scalar quantities for a single element detector, or some i_{th} detector element, and are scalable to some n_e elements or discrete receiver channels. It is often the case that scalar representations of the lidar equation are misused to describe individual planes of polarization by taking the vectorized nature of light and collapsing it to separate one dimensional equations to describe the output from each receiver channel. An example of this erroneous use of the lidar equation is the assumption two receiver channels can measure the number of counts in two crossed planes of polarization as $N_{rx}^{\parallel}$ and $N_{rx}^{\perp}$ with no coupling terms. These values are considered decoupled, but this is idealized and can rarely be correctly assumed. Coupling between polarization channels and other polarization sensitive attributes are usually present and unable to be captured by this representation of the lidar equation.

Because of a lapse in complete definition it is necessary to fully describe the measurement environment and instrumentation in a way that conserves the full polarization description and inherent vector nature of the measurement.

2.2 Vectorized Lidar Theory

Throughout this thesis research a SPL utilizing multiple planes of received polarization was deployed and used for analysis. It is thus necessary to provide a full polarization description of the sensor, generating a complete understanding of the scatterer-sensor interaction. The Stokes Vector Lidar Equation (SVLE) [49] provides a theoretical basis for performing a full polarization analysis of a direct detection lidar sensor. In this formulation the transmitted and received light is described using Stokes vectors with a defined degree of polarization (DOP). The scattering processes and polarization effects along the instrument's transmit and receive optical paths are then described using the Mueller matrix convention. The use of the Stokes and Mueller formalism is advantageous due to its ability to describe fully, partially, and un-polarized light, all of which can be naturally

occurring polarization states encountered while operating an SPL and incorrectly aggregated when distilling the lidar equation into scalar components.

Using these conventions, the full description of the vectorized lidar equation, up to the polarizers in the receiver, is given as [49]

$$\vec{S}_{rx} = \mathbf{M}_{rx}\left[\left(G(R)\frac{A}{R^2}\Delta R\right)\mathbf{T}(k_s,R)\mathbf{F}(\lambda,k_i,k_s,R)\mathbf{T}(k_i,R)\mathbf{M}_{tx}\vec{S}_{tx}+\vec{S}_B\right]. \tag{2.3}$$

In the SVLE, the term $\vec{S}_{rx}$ is the Stoke's vector for the received light and $\vec{S}_{tx}$ is the Stoke's vector for the transmitted laser light, $\mathbf{M}_{tx}$ is the polarization state generator Mueller matrix, used to code the laser light with a desired plane of polarization, $\mathbf{T}(k_i,R)$ is the linear product of all transmission Mueller matrices for the transmitted wavevector k_i, $\mathbf{F}(\lambda,k_i,k_s,R)$ is the scattering phase matrix for a particular target or scattering medium at some range R for the incident and scattered wavevectors, $\mathbf{T}(k_s,R)$ is the linear product of all transmission Mueller matrices for the scattered wavevector, and the background light detected by the receiver is given by the Stoke's vector $\vec{S}_B$. The linear product of the Mueller matrices for each optical component in the receiver is given as $\mathbf{M}_{rx}$. The scalar components contain the geometry information for the measurement, where $G(R)$ now describes the geometric overlap function and the remaining terms carry over from the scalar definition.

The general Stokes vector, used for $\vec{S}_{rx}$ and $\vec{S}_{tx}$, is defined as $\vec{S}=[S_0,S_1,S_2,S_3]^T$, where S_0 is the total intensity, S_1 is the intensity in the linear vertical/horizontal planes, S_2 is the intensity in the linear $\pm45^\circ$ planes, and S_3 is the intensity in the right/left hand circular planes. Written in terms of the linear rotation angle of the polarization state, ψ, the ellipticity angle of the polarization state, χ, DOP, p, the vector has the form [36]

$$S = S_0\begin{bmatrix}1\\ p\cos(2\psi)\cos(2\chi)\\ p\sin(2\psi)\cos(2\chi)\\ p\sin(2\chi)\end{bmatrix}, \tag{2.4}$$

where the DOP is used to describe the amount of light that is polarized and is given as

$$p = \frac{\sqrt{S_1^2 + S_2^2 + S_3^2}}{S_0} \ . \tag{2.5}$$

.

Equations 2.4 and 2.5 can be used to project any Stokes vector on to the Poincaré Sphere for visual representation, as shown in Fig. 2.2. The angle ψ is used to rotate the vector about the equator of the sphere, χ projects the vector against the S_3 axis, while the DOP describes the overall length of the vector. Advantages are quickly gained by describing the entire measurement

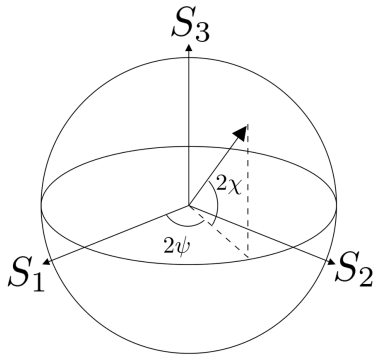

Figure 2.2: Poincar Sphere showing the linear rotation angle ψ, ellipticity angle χ, and the DOP p for a given Stokes vector $\vec{S}$. The angles 2ψ and 2χ give the location of the vector on the sphere and the DOP defines the vectors length.

with a full polarization description. Instrument effects, down to individual optics, and measurement effects, discrete scattering and absorption events, can be full described with the basis of Mueller matrices. A number of methods exist to quantify and understand the modification of the transmit and received light fields, but a simple to employ method is in the context of Polar Decomposition (PD) of Mueller matrices [71]. This method provides a convenient tool in which a Mueller matrix can be decomposed into into three fundamental contributing elements as

$$\mathbf{M} = \mathbf{M}_{\mathrm{D}}\mathbf{M}_{\mathrm{R}}\mathbf{M}_{\Delta} \ , \tag{2.6}$$

representing diattenuation, retardance, and depolarization respectively — a comprehensive explanation of PD can be found in [71, 45, 36]. With this description scattering matrices representing the

measurement medium, with the scattering matrix $\mathbf{F}$, can also be decomposed into their respective contributing terms, allowing for full polarization analysis throughout the entire measurement. Further assessment of $\mathbf{F}$ in Eq. 2.3 will be discussed within Chapter 4 in the context of a comprehensive SVLE model for atmospheric, topographic, and bathymetric scattering.

In SPL sensors the raw data is typically the number of photon events that occur per the i_{th} detector element, or channel, over the inter-pulse period (IPP) of the laser, with each received photon having an associated detection time and range. This is true for polarization sensitive SPL sensors as well, implying that the Stokes vectors must be projected onto the axes of the Poincaré Sphere to generate the received number of photon counts.

Determining the number of photon counts per polarization channel is done by applying the output projection matrix, $\mathbf{O}$, to the received Stokes vector as

$$\vec{N}_{rx} = \mathbf{O}\mathbf{M}_{rx}\left[\left(G(R)\frac{A}{R^2}\Delta R\right)\mathbf{T}(k_s,R)\mathbf{F}(\lambda,k_i,k_s,R)\mathbf{T}(k_i,R)\mathbf{M}_{tx}\vec{S}_{tx}+\vec{S}_B\right] , \tag{2.7}$$

where the number of counts in the i_{th} element, or polarization channel, is given by $N_{1\cdots n}$ for n elements, or channels, is given by the vector

$$\vec{N}_{rx} = \begin{bmatrix} N_1 \\ \vdots \\ N_n \end{bmatrix} . \tag{2.8}$$

The generalized form of the output matrix is given as

$$\mathbf{O} = \begin{bmatrix} \eta_1 & 0 & 0 & 0 & 0 & 0 & 0 & 0 & \\ 0 & 0 & 0 & 0 & \eta_n & 0 & 0 & 0 & \cdots \\ & & & & \vdots & & & & \end{bmatrix} \begin{bmatrix} \mathbf{P}_1 \\ \vdots \\ \mathbf{P}_n \end{bmatrix} , \tag{2.9}$$

where each of the channel efficiencies and the necessary receiver polarization analyzer Mueller matrices, $\mathbf{P}_i$, are included. These perform the projections onto the respective polarization planes and allow extraction of photon counts from the received vector.

It is useful to consider a specific example of Eq. 2.7. If a SPL sensor with receiver channels that discriminate signal between linear horizontal and linear vertical polarization is employed to

perform measurements of atmospheric or hard target depolarization, similar to the demonstration sensor that will be discussed in Chapter 5, equations that represent the number of received counts per single detector element in the co-polarized or cross-polarized planes can be given as

$$N_{rx}^{\parallel} = \begin{bmatrix} \eta_{\parallel} & 1 & 0 & 0 \end{bmatrix} \begin{bmatrix} 1 & 1 & 0 & 0 \\ 1 & 1 & 0 & 0 \\ 0 & 0 & 0 & 0 \\ 0 & 0 & 0 & 0 \end{bmatrix} \begin{bmatrix} S_{rx}^0 \\ S_{rx}^1 \\ S_{rx}^2 \\ S_{rx}^3 \end{bmatrix} \tag{2.10}$$

$$N_{rx}^{\perp} = \begin{bmatrix} \eta_{\perp} & 1 & 0 & 0 \end{bmatrix} \begin{bmatrix} 1 & -1 & 0 & 0 \\ -1 & 1 & 0 & 0 \\ 0 & 0 & 0 & 0 \\ 0 & 0 & 0 & 0 \end{bmatrix} \begin{bmatrix} S_{rx}^0 \\ S_{rx}^1 \\ S_{rx}^2 \\ S_{rx}^3 \end{bmatrix}, \tag{2.11}$$

where the received Stokes vector $\vec{S}rx = [S_{rx}^0, S_{rx}^1, S_{rx}^2, S_{rx}^3]^T$ is given by solving the SVLE in Eq. 2.3. Both of these simplistic examples utilize ideal linear polarizers [36], and serve as only an example of the distillation from number of elements or channels to a single output. In this example the transmitted laser light is defined as linear horizontal with the associated receiver channel being the parallel, or "co-polarized," channel, and the perpendicular, or "cross-polarized," channel receiving only linear vertical polarization. These planes are referenced to the transmitter's polarization frame with the receiver's polarized rotated to align the S and P axes, with example transmitted and received vectors shown in Fig. 2.3 projected onto the Poincaré sphere. This nomenclature sets up the polarization planes to be discussed throughout this thesis, where differences between co-polarized and cross-polarized light is investigated in theory and measurement. The discussion of the SVLE and the employment of Stokes vectors to describe the transmitted and received light has relied on a derivation of the Stokes parameters that begins at the classical formation of electromagnetic radiation. For a elliptically polarized plane wave, the light field is described by its complex amplitudes and orthogonal unit vectors. Derivations in [36, 9] provide a description by which the plane wave can be described on the polarization ellipse and thus directly compute the Stokes pa-

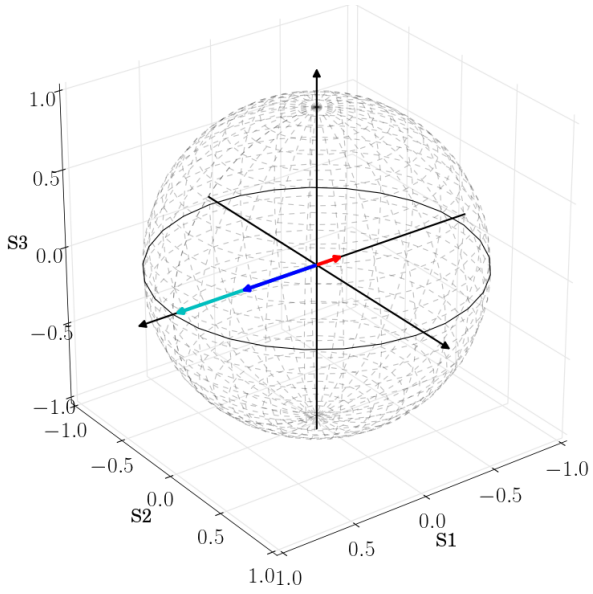

Figure 2.3: Simulated transmitted and received Stokes vectors. The normalized transmitted laser pulse with linearly horizontal polarization, $\vec{S}_{tx} = [1, -1, 0, 0]^T$, is shown in cyan. In blue is the received Stokes vector from a polarization preserving water surface, where the vector measured in the co-polarized receiver channel is $\vec{S}_{rx}^{\parallel} = [0.05462, -0.0546, 0, 0]^T$. In red is the received Stokes vector from a completely depolarizing scatterer below the water surface, measured in the cross plane of polarization as $\vec{S}_{rx}^{\perp} = [0.00201, 0.00201, 0, 0]^T$. Both received vectors are scaled by a constant to allow visualization.

rameters from the classical description. In these derivations the Stokes parameters give a time averaged representation of the polarized light field, or in the case of photons, describe the ensemble average over many photons received from an impinging stream of photons at some rate, typically described by photon counts per second. The question can be asked whether or not the SVLE is appropriate in the limit of single photon detection — it is recognized that there is some temporal width to the single photon detector output and timing electronics — and what applicability it has for polarization sensitive SPL.

The question of applicability can be addressed by deriving the Stokes parameters from the quantum description of elliptically polarized light. The linear combination of two classically defined

Jones vectors, considering two orthogonal definitions of basis states, is given as

$$\mathbf{\Psi} = c_1\psi_{\mathbf{1}} + c_2\psi_{\mathbf{2}} \ , \tag{2.12}$$

where in the classical description $|c_1|^2$ and $|c_2|^2$ give the intensities of the field in directions $\psi_{\mathbf{1}}$ and $\psi_{\mathbf{2}}$, and the linear combination of the two, $|c_1|^2 + |c_2|^2$ is the estimate of total intensity of the measured light field.

In the quantum description, Eq. 2.12 can be recast such that the field is represented by general state ket as

$$|\Psi\rangle = c_1 \, |\psi_1\rangle + c_2 \, |\psi_2\rangle \ , \tag{2.13}$$

where $|c_1|^2$ and $|c_2|^2$ now give the probabilities for a single photon to be in the respective polarization states $|\psi_1\rangle$ and $|\psi_2\rangle$ with a characteristic spin of one. This representation is valid for pure ensembles of photons where all members are characterized by the same ket with spin pointing in some definite direction, $|\psi_1\rangle$ or $|\psi_2\rangle$, mixed ensembles containing fractional populations of spin directions, or a completely random ensemble. In the classical language these combinations represent a completely polarized field, partially polarized, and un-polarized. Like the classical description shown above, the light's total intensity is arrived at by taking the inner product of the state Psi with its conjugate, $\langle\Psi| \, \Psi\rangle = c_1^*\langle\psi_1| \, \psi_1\rangle + c_2^*\langle\psi_2| \, \psi_2\rangle = |c_1|^2 + |c_2|^2$. It should be noted that the states $|\psi_1\rangle$ and $|\psi_2\rangle$ can in of themselves be decomposed into the fundamental polarization states and should be treated as linear combinations thereof and the total state $|\Psi\rangle$ is then a description of the total ensemble of $N \geq 1$ photons.

In classical definitions, the coherency matrix can be introduced to capture the range of polarizations that a field can possess, but in addition it captures the stochastic nature of the polarization field components [38]. The quantum analogy of the coherency matrix is given by the density matrix. From Eq. 2.13 the density matrix and corresponding to the density operator can be defined as [108, 36]

$$\rho_{ij} = \sum_{i,j=1}^{2} c_i c_j^* = \begin{bmatrix} c_1 c_1^* & c_1 c_2^* \\ c_2 c_1^* & c_2 c_2^* \end{bmatrix} \ . \tag{2.14}$$

From the density matrix it can be seen that the trace provides the intensity terms and the off-diagonals give relative phase information. From these components, the Stokes parameters can be defined analogously to the classical versions as

$$\vec{S} = \begin{bmatrix} S_0 \\ S_1 \\ S_2 \\ S_3 \end{bmatrix} = \begin{bmatrix} c_1 c_1^* + c_2 c_2^* \\ c_1 c_1^* - c_2 c_2^* \\ c_1 c_2^* + c_2 c_1^* \\ i(c_1 c_2^* - c_2 c_1^*) \end{bmatrix}. \tag{2.15}$$

As seen in [36], the values given in Eq. 2.15 are equivalent to those derived from the polarization ellipse and allow a single photon, or ensemble, to be described in respect to the Poincaré sphere formalism. The values contained within the density matrix shown in Eq. 2.14 are real physical quantities of the measured state and can be linked to incident photon energy by some basic assumptions, such as the use of the harmonic oscillator as a quantization method for the field, which is shown in the next section.

It appears then that it is appropriate to apply the formulation of the SVLE in the limit of single photon detection, but it is also pertinent to recognize that due to the statistical nature of estimating the polarization state of a single photon an ensemble of measurements should be made to reduce uncertainty in state estimation.

2.3 Single Photon Statistical Definitions

In all representations of the lidar equation, scalar or otherwise, there are inherent statistical properties in several of the individual components. The outcome of the lidar equation is dependent on several stochastic processes that are generally, and incorrectly, treated in a deterministic fashion. Because of this, the actual utility of these equations, and the models that result, only serve to baseline our understanding of the detection and estimation abilities of a sensor if we ignore the random processes at work. Continuing with the the quantum description of a SPL sensor, it is possible to derive the statistics that govern the distribution of photon states and detectability of each single photon event through quantization.

A single photon can be defined as an elementary excitation of a single mode of the quantized electromagnetic field [2]. For some single mode k, a single photon of frequency ν_k will have an energy of $h\nu_k$, where h is Planck's constant. Using the definitions of [26], an operational description of a single photon state can be generated such that a detector sensing single photon events measures exactly one photon for each incident state. This then implies that for each single photon state detection, the mean of the detection statistics is one, the variance is zero, and each photon has a distinct associated state. Detection then indicates the binary decision in which a detection gives unity and the non-detection gives zero.

Working through the quantization process, shown here in an abbreviated manner, the link between a photon state and inherent stochastic nature of SPL sensor operation comes freely. Quantization of the electromagnetic field can be done by employing the solutions to a 1-dimensional harmonic oscillator. It is the case that the derived Hamiltonian is mathematically equivalent to a sum of uncoupled harmonic oscillators, each with some frequency ν. This implies that the Hamiltonian can be solved for each mode, generating the series of possible discrete energies that the field contains equally spaced with photon energy values $h\nu$.

Beginning with the given definitions of the creation and annihilation operators, or raising and lowering respectively, as [108]

$$\mathbf{a} = \sqrt{\frac{m\omega}{2\hbar}\left(\hat{x} + \frac{i}{m\omega}\hat{p}\right)}, \tag{2.16}$$

$$\mathbf{a}^\dagger = \sqrt{\frac{m\omega}{2\hbar}\left(\hat{x} - \frac{i}{m\omega}\hat{p}\right)}, \tag{2.17}$$

with the commutation rules for the two frequencies, ν and ν' defined as [108]

$$\begin{aligned} [\mathbf{a}_\nu, \mathbf{a}^\dagger_{\nu'}] = \mathbf{a}_\nu \mathbf{a}^\dagger_{\nu'} - \mathbf{a}^\dagger_\nu \mathbf{a}_{\nu'} = \delta_{\nu\nu'}, \\ [\mathbf{a}_\nu, \mathbf{a}_{\nu'}] = [\mathbf{a}^\dagger_\nu, \mathbf{a}^\dagger_{\nu'}] = 0. \end{aligned} \tag{2.18}$$

The Hamiltonian operator of the radiation field for a single quantized mode is [2]

$$\hat{\mathbf{H}} = h\nu(\mathbf{a}^\dagger\mathbf{a} + 1/2) = h\nu(\mathbf{n} + 1/2), \tag{2.19}$$

where the number operator has now been introduced as $\mathbf{n} = \mathbf{a}^\dagger\mathbf{a}$. The eigenstates defining the quantized field are the Fock states, or number states, with the following being true

$$\mathbf{n}\,|n\rangle = n\,|n\rangle\,, \tag{2.20}$$

such that

$$\hat{\mathbf{H}}\,|n\rangle = h\nu(n+1/2)\,|n\rangle\,. \tag{2.21}$$

From Eqs. 2.19 and 2.20, it can be seen that the a single eigenstate of the number operator, $\mathbf{n}$, has the eigenvalue $h\nu(n+1/2)$. Considerations of the difference between the total number operator shown here and the space number operator in [77] reveals a difference between integration over all space and the localized volume, including the detector face, respectively. Recognizing that both operators commute with each other and there are methods for converting between the two, only the total number operator is considered.

To describe the closest approximation of the field generated by laser light, the phase capturing coherent state $|\alpha\rangle$ can be defined as [108]

$$|\alpha\rangle = \sum_{n=0}^{\infty} |n\rangle\,\langle n|\,\alpha\rangle, \tag{2.22}$$

$$|\alpha\rangle = \sum_{n=0}^{\infty} \frac{\alpha^n}{\sqrt{n!}} \mathrm{e}^{\frac{-|\alpha|^2}{2}}\,|n\rangle\,. \tag{2.23}$$

Though the coherent states are not stationary states of the harmonic oscillator, as they can be evolved through the time evolution operator, this definition provides the most appropriate state that take on the classical limit [108]. The argument for this is made in [2] by showing that the expectation value of the photon number operator is equal to the classical value expected.

When a SPL generates measurements of single photons, the sensor is making an instantaneous measurement of the photon number, and by considering the coherent state a single measurement will yield a spread of possible photon numbers after many measurements. This quality introduces a clear stochastic dependency to the photon detection description and it raises the question of how to compute the expectation that a single measurement of the photon number state will yield n

photons in the state $|\alpha\rangle$. Computation of this probability is done by taking the expectation of the coherent state as

$$P = |\langle n|\ \alpha\rangle|^2, \tag{2.24}$$

which for the coherent state defined by Eq. 2.23 gives

$$P = |\langle n|\ n\rangle|^2 \left| \sum_{n=0}^{\infty} \frac{\alpha^n}{\sqrt{n!}} \mathrm{e}^{\frac{-|\alpha|^2}{2}} \right|^2. \tag{2.25}$$

The solution to this gives a Poissonian distribution of

$$P = \frac{|\alpha|^{2n}}{\sqrt{n!}} \mathrm{e}^{-|\alpha|^2}, \tag{2.26}$$

for all $n = 0, 1, 2...$ possible photons, as well as a mean distribution value and standard deviation of $|\alpha|^2$.

Equation 2.26 describes the quantum intensity fluctuations of the incident laser light and inherently links the commonly referenced "shot-noise" to the quantum nature of the photon. These random fluctuations result from a non-constant arrival time of photons at a detector, as shown in Fig. 2.4. The uncertainty in each measurement of a photon, $1/\sqrt{n}$, is the most easily observable consequence of the quantization of the light field and is often the primary source of measurement uncertainty in SPL sensors.

Through the quantum definition of a single photon, several interactions can be considered. The photo-detection process proves to be the crux of SPL operation as the sensor's detection of a weak backscattered photon rate is actually a direct measurement of the incident eigenstate's photon number. The photo-detection process describes an interaction of the photon with the detector used. It is the case that for multiple photons counted over some time interval, the average photon flux is equivalent to the classical incident intensity with an added efficiency term for the photo-detection process (detector quantum efficiency, QE). This implies that the number of detected photons is $N_{detected} = \eta_{QE} N_{incident}$ with uncertainty $1/\sqrt{N_{detected}}$. A simple redefining of the variables in Eq. 2.26 gives the more general form of the discrete Poisson probability density function (PDF) [101]

$$P(k; \Delta t) = \frac{(N\Delta t)^k}{k!} e^{-N\Delta t}, \tag{2.27}$$

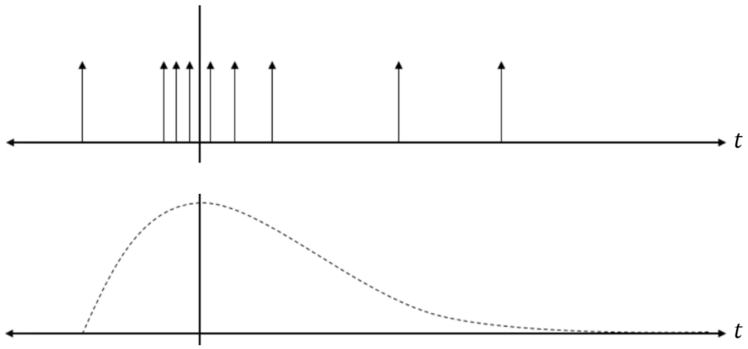

Figure 2.4: The top shows the non-constant arrival of single photons in time and the bottom is the resulting signal envelope, adapted from [38]. The lower curve is reminiscent of the envelope representing the photon rate function that will be discussed further in later chapters.

which describes the number of detections, k, over some finite time interval, Δt, for some impinging mean photon rate of N. If the electrical signal is considered, then Eq. 2.27 describes the probability of photoelectron generation and must include the conversion efficiencies for each channel or element under consideration.

From Eq. 2.27, the signal-to-noise ratio can be defined as

$$SNR = \frac{N}{\sqrt{N+\xi}}, \tag{2.28}$$

where the term ξ has been introduced to describe noise rates over some measurement period. SNR is often a useful metric for understanding the performance limitations of a photon counting sensor. The inverse of SNR provides a metric for the relative counting error expected in a noisy measurement environment. A sensor's SNR decreases as a function of increasing background, shown in Fig. 2.5, and for SPL sensors it is typical for SNR$\leq$ 1 due to the equivalency of a single noise and signal count. Analysis shows that in the regime of low mean photon rates the Poisson SNR is sensitive to increased noise rates and emphasizes the importance of proper noise management in an SPL. However, it should be noted that the concept of SNR applies to a aggregation of photons and the single photon event has no representation in SNR besides unity. Considering that a realistic SPL sensor will, at a minimum, be subjected to detector noise, it is necessary to consider what impact

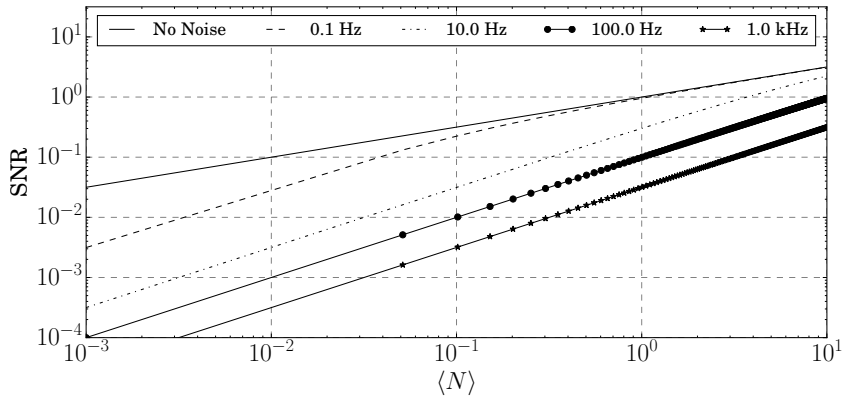

Figure 2.5: The resulting SNR curves for a single shot, single detection threshold, while varying the mean received photon counts and the input noise rate, calculated from Eq. 2.29.

the addition of a noise term will have on Eq. 2.27. The noise photons detected by the receiver subsystem are uncorrelated and arrive randomly throughout the measurement period Δt, whereas signal photons backscattered from a target will arrive correlated in time and range. Each of these detections can be treated as mutually exclusive Poisson random processes as they are independent from each other. The sum of two Poisson random processes can be shown to still be Poissonian [100], so the complete PDF for the addition of noise to the signal can be written as

$$P(k; n_s; \Delta t) = n_s^k \frac{((N+\xi)\Delta t)^k}{k!} e^{-n_s(N+\xi)\Delta t}, \tag{2.29}$$

where N again represents the average number of signal photons in the measurement time, and ξ represents the average noise photons in that time. The term n_s represents the number of laser shots that are included in probability estimation. In the case of SNR calculations with multiple pulses, Eq. 2.28 can be used with the added multiplicative factor of $\sqrt{n_s}$. The impact of multiple pulse integration on SNR can be seen in Fig. 2.6, where increased signal and fixed background rates facilitates an increased SNR. Using the Poisson description in Eq. 2.29, the probability of returns from a target as a function of mean photon rate can be generated as [23]

$$P_D = 1 - e^{-N} \sum_{k=0}^{n_t - 1} \frac{N^k}{k!}, \tag{2.30}$$

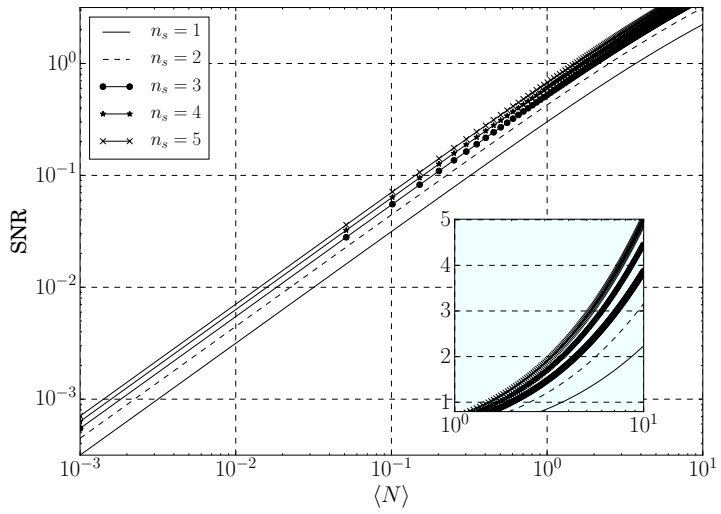

Figure 2.6: The resulting SNR curves for Eq. 2.29 while varying the mean received photon counts and integrating over some integer number of shots. A constant noise source of 100 Hz was assumed and the detection threshold was set to $k = 1$. The figure inset shows the zoomed portion of the curves on a linear SNR scale, to separate each at maximum SNR.

where it has been assumed that single shot statistics are being assumed, $n_s = 1$. From this, an analysis of noise can be determined by applying the probability of detection to the unwanted signal photons, ξ, giving the probability of false alarm as

$$P_{FA} = 1 - e^{-\xi} \sum_{k=0}^{n_t - 1} \frac{\xi^k}{k!}. \tag{2.31}$$

Figure 2.7 gives the single shot detection probability, Eq. 2.30, for a varying input mean photon rate and different threshold settings. From a purely statistical perspective, Fig. 2.7 implies that when the mean target photon rate is low, the highest detection efficiency for single photons can be achieved when the threshold is set at $n_t = 1$. This is due to the fact that single photon detections in the LSNR regime will be ignored for higher threshold settings. For sensors operating in a high SNR regime, such as those that employ analog detection schemes, larger thresholds are necessary to ensure that digitizers are not plagued by constant solar background signal, but the accompanying downside is a complete insensitivity to photon rates of $\langle N \rangle \leq 10^1$. This therefore

implies that for the LSNR there can be an efficient use of photons from every laser firing, even where the mean photon rate is less than one, but thresholds must be set low to maximize detection.

The SPL operational thresholds shown in Fig. 2.7 elude to the fact that, due to the method of detection, for a single detected photon it is impossible to estimate whether it is the result of backscattered target signal or unwanted signal from solar background and detector noise. When examining the statistics of a photon detection, the threshold of $n_t = 1$ will prevent triggering on electronic noise only. This implies that a single detection from backscattered target signal or unwanted signal will trigger the acquisition counter equally, as the photodetector's single electron responses (SER) is equivalent for both detections. Inherently, this makes the raw data collected with a SPL noisier than that of other lidar sensors, with the photons from scattered sunlight during daytime operation as the dominant noise source for SPL sensors. However, due to the lack of correlation in time, detection of photons from the solar background serves to be easily differentiable from correlated target signal.

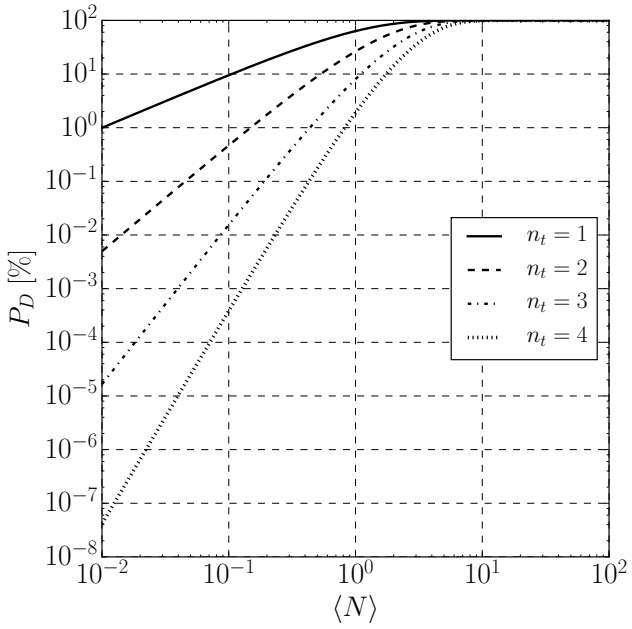

Figure 2.7: The resulting detection percentage for an input mean photon rate and various increasing detection thresholds, n_t. For low photon rates $n_t = 1$ indicates that single photon detection will provide the highest detection efficiency.

Chapter 3

Photon Detection and Acquisition

The methods employed in direct detection lidar sensors to acquire backscattered signal can be broken up into three main types: analog detection, geiger-mode (GM), and photon counting. All three methods have distinctly different implications on the operational SNR for the measurement, detection probabilities, and whether the measured signal is an indication of the backscattered photon rate. Although GM and photon counting lidar sensors fall under the regime of SPL operation, both typically operate with single photon detection sensitivity but have hardware constraints that are not consistent with each other. Separation between acquisition regimes referenced to the probability of single photon detection probability is depicted in Fig. 3.1.

Sensors employing analog detection, or full waveform recording, rely on a large flux of received photons, typically on the order of 500-1000, to produce a continuous detector current. The signal is digitized and produces a measurement linearly proportional to the incident photon rate. Typically, these sensors operate with a lower PRF and higher pulse energy, allowing high backscattered photon rates per a given transmit pulse and detectability of the entire waveform. It should be noted that some commercial sensors are available for topographic/bathymetric surveying and can provide high PRFs and digitized waveforms for every laser firing. However, these provide no atmospheric sensing capabilities. The build up of the signal waveform in both the analog detection, left panel, and photon counting, right panel, regimes is shown in Fig. 3.2. The waveform is generated per laser pulse in the analog case and over many laser pulses in the photon counting case, indicating that sampling times between the two acquisition schemes are typically on very different scales.

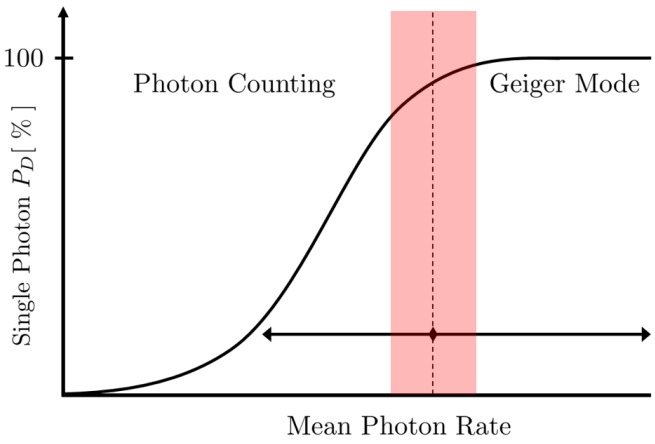

Figure 3.1: A depiction of acquisition regime change from linear photon counting to non-linear GM, with the red area documenting the ambiguity of the cross-over.

GM lidar sensors typically incorporate Geiger-Mode Avalanche Photodiodes (GmAPD) detectors, though GM-like operation can be achieved with any single photon sensitive detector. These sensors operate with a single photon sensitivity, but do not rely solely on single photons for detection, instead relying on many concurrent photons to increase target detection statistics per laser pulse. A result of GM detection schemes is an inability to provide a linear proportionality between the incident photon rate and the registered detections in the data stream. This is because the employed binary detection techniques will give equivalent results for a detector pulse generated by a single photon or many photons. The sensor is no longer counting individual photons from the target, but is instead determining whether a detection has occurred, regardless of the number of backscattered photons, and then assigning a timing measurement to the detector's output pulse. This inherently removes the intensity retrieval aspect of the sensor. There is no longer a valid assumption that the signals built up in memory represent single photons and can be histogrammed into a signal waveform representative of the photon rate.

An implication of binary operation is the assumption that the recovery time of properly biased GmAPD is on time scales equal to the separation time between laser firings, such that per laser shot there will be at most one detection. GM sensors have been limited to the topographic mapping

application as the utility of the high resolution detection measurement is limited without intensity information and restricted to detection with no estimation. Some benefits of this technique for high precision range estimates will be discussed in a later section.

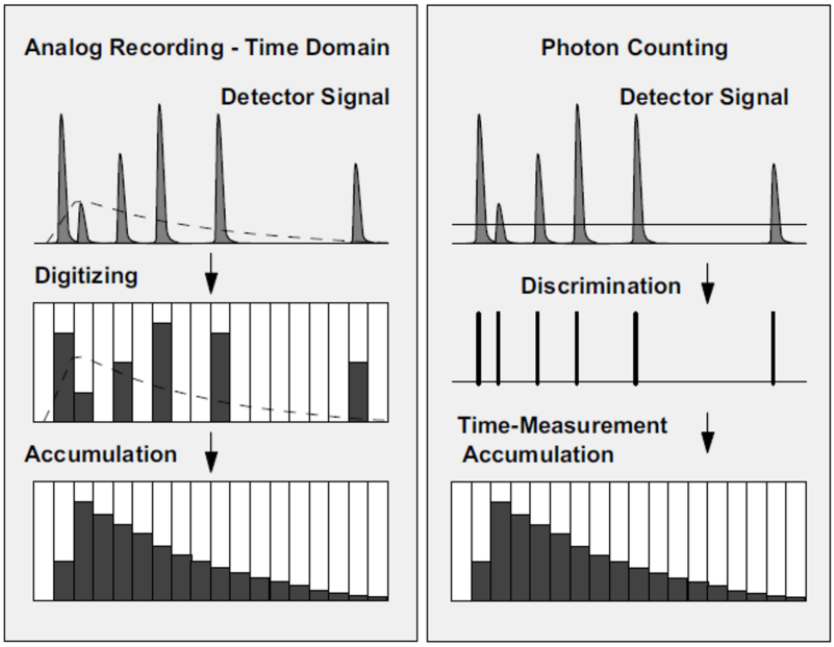

Figure 3.2: Diagram from [8], showing the digitization and discrimination process by which signal wave forms are generated via analog recording and photon counting. The analog waveform is acquired per laser firing and the photon counting waveform is acquired over many laser firings.

Modern photon counting lidar sensors also rely on high PRF, low pulse energy lasers, but, contrary to GM sensors, operate in a regime where multiple photons can be detected across the system's unambiguous range per transmitted laser pulse. In addition, these systems operate with a detuned probability of detection, less than 100%, such that every registered count is actually a single photon and the registered counts in the data stream are linearly proportional to the incident photon rate. This is a necessary condition that must be leveraged to ensure that the system is indeed counting single photons and that the issue of photon pile up at the detector, and subsequent non-linear intensity response, is avoided. As detections are built up over subsequent laser firings, a distribution of counts manifests. This creates a signal waveform that can be generated from discrete detections, as shown in the right panel of Fig. 3.2. These systems operate in a low signal

to noise ratio (LSNR) regime, where the collection of noise and signal photons is equivalent and the statistics of the uncorrelated noise to the correlated backscatter is leveraged in post detection analysis. Photon counting lidar sensors have been used for a variety of atmospheric and topographic/bathymetric applications where intensity is necessary, providing an opportunity to unify measurements for multi-functional utility.

Fundamental to photon counting and GM lidar sensors, whether used for intensity retrievals or hard target ranging, is the process by which the receiver subsystem logs the number of asynchronous detections over a measurement cycle. Due to the fact that each operational mode of these systems is asynchronously counting detections in time, Poisson statistics applies and can be utilized to describe the detection probabilities for each system. Though all three of the discussed acquisition methods are appropriate for different applications, the utility of the LSNR approach in photon counting provides high resolution range and count rate information, detection and estimation. For this reason, the LSNR approach will be discussed throughout the remainder of this thesis.

3.1 Photon Counting in Lidar Sensors

Photon counting has been widely used in lidar remote sensing as a tool to remotely derive properties of the atmosphere and hard targets from backscattered intensity profiles. This LSNR approach has been successful with applications spanning many atmospheric retrievals, including: quantitative measurements of clouds and aerosols [16, 85, 46], water vapor mixing ratios [97, 114], upper atmospheric temperature [117], and others. In hard target applications the LSNR approach has been employed for high precision topographic and bathymetric mapping [86, 24] and depolarization estimates [42, 91], among others. A breadth of measurements are achievable with photon counting lidar systems, establishing them as multi-functional due to their ability to observe a variety of phenomena and properties by a single system. However, the desire to observe highly dynamic targets at high resolutions often introduces stringent spatial and temporal requirements, which cannot be met due to the prescribed nature of most photon counting acquisition systems. The measurement dynamics can result from the nature of the target or the implemented observa-

tional method, such as aircraft or satellite based instruments. Consequently, a dynamic observing capability is needed to match the variety and variability of targets while also accounting for the inherently lower probability of detection associated with photon counting experiments.

Common photon counting lidar sensors rely on acquisition and detection processing schemes that bin received photons into discrete, pre-allocated time intervals over a defined range. Multi-channel scaler (MCS) averagers are an example of such a data acquisition system and are the photon counting equivalent of a transient recorder [8]. These units build up a histogram of detections in defined memory locations (range bins) over a time period (integration time), typically over many laser firings, before reading out a detection profile. The MCS approach, albeit very successful, is limited in its description of geophysical observations by the range and time confines imposed by the prescribed binning procedure. This limits the flexibility of investigation and establishes *a priori* what spatial and temporal scales a particular scatterer must abide by in order to be observable. In addition, typical range bin resolutions do not allow for fine feature extraction and the ability to generate single shot profiles over the sensor's full unambiguous range at higher bin resolutions results in an arduous data overhead. For example, the previously mentioned resolution of ∼1-10 mm [7] is required to resolve the sharpness of cloud edges and phase boundaries, both of which are features lost to spatial ambiguity in typical MCS implementations. An example of a photon counting sensor with MCS acquisition generating an atmospheric profile is shown in Fig. 3.3. In addition to atmospheric measurements, there are equally high resolution requirements are put on determining water surface topographic features from several kilometer stand off distances, which the MCS approach is unable to meet.

Performing a simple, but telling, analysis of the MCS system data rates, it becomes clear that this approach does not make sense for small bin widths over extended ranges. Assuming a laser PRF of 15 kHz, the unambiguous range of acquisition of the system is ∼10 km. Creating a profile over the unambiguous range at 10 cm resolution provides 10^5 measurement bins. Each bin designation and number of detections per bin is nominally represented by 32 bits. For a single shot, this gives 4×10^5 bytes/shot. Over the PRF of the laser system, the system is then writing

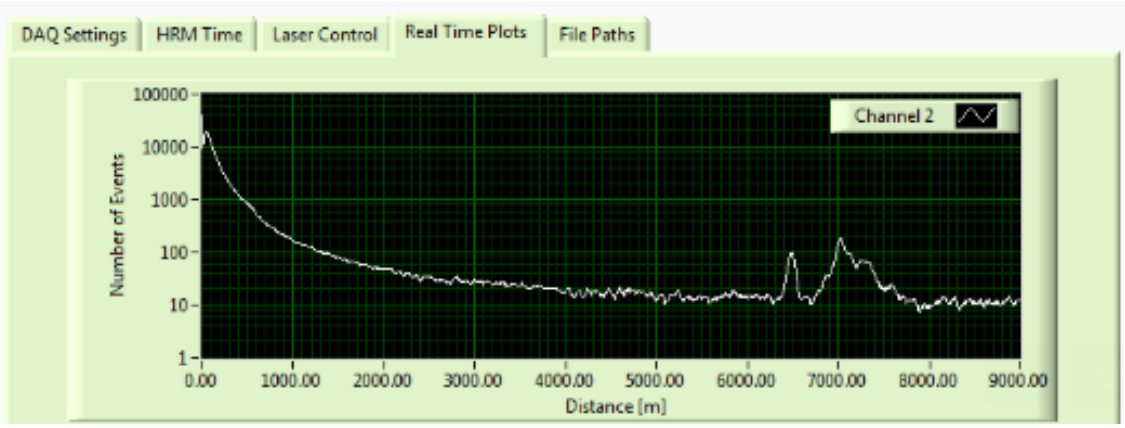

Figure 3.3: An example of an atmospheric profile generated by an SPL mated with an MCS acquisition system. The accumulation of photon detections occurred over 30 seconds and with 5 meter bin widths and a 0.1 second latency to write out the profile and begin acquisition again. Several distinct cloud features can be see between 6-8 km. The low number of detections over this integration time, shown on the vertical axis, demonstrates the inherently low probability of detection for an SPL.

out 60 GBytes/second. This then scales linearly per added channel. A typical USB 3.0 transfer rate has a theoretical maximum of 650 MBytes/second, so this acquisition is no longer feasible. It becomes more troubling when considering that for a photon counting lidar, the probability of detecting a backscattered or noise photon per pulse is normally 1%. This implies that, for the MCS approach, most bins in each profile have a null measurement and the written profile is now predominantly characterized by non-detections. When the typical picosecond (millimeter in range) bin width associated with a modern TCSPC unit the data rates inflate to clearly nonsensical values.

Because of the MCS acquisition sub-meter resolved single shot acquisition of the atmosphere or hard targets from several km stand off distances the approach becomes computationally taxing and in some cases impossible. The number of range bins necessary increases to a point at which memory allocation no longer feasible. Another downside is that once the bin width has been set in memory, the ability to adjust binning parameters on the fly during collection is lost. So, for a multi-functional lidar sensor targeting observables of differing resolution needs, the limit must be set by the smallest bin width. If the observables occur on distinctly different ranges there must be

additional acquisition units to satisfy all measurements. A brute force accommodation of all measurements becomes expensive and unsustainable. The TCSPC technique, which allows time-tagging of individual photons at picosecond resolution, offers the ability to approach these requirements with the agility needed to manage the varying signals present in a lidar profile containing multiple different types of scattering scenarios.

3.1.1 Time-Correlated Single Photon Counting

Advancements in technology associated with single photon detectors and timing electronics have facilitated emerging fields that utilize the quantum nature of light [26]. The technique of precisely time-tagging single photon detections for photon rate measurements has been implemented with large success in fluorescence lifetime experiments for over three decades [98, 8, 62]. The technological advances associated with TCSPC experiments have yielded a class of time-tagging acquisition hardware that reliably measures and processes individual photon detections with picosecond precision (millimeter scale in range) and nanosecond dead-times [121]. Implementing a combination of stable crystal oscillators, constant fraction discriminators (CFD), and time-to-digital converters (TDC), modern TCSPC instrumentation can simultaneously measure MHz count rates across multiple channels and retain laser synchronization information for post-processing time differencing.

The TCSPC approach removes the need for pre-allocating memory and time costly hardware computations prior to assigning a bin. The events from all input channels are recorded independently, giving a 32 bit number that describes the channel number and the time of the event with respect to the overall measurement starting with picosecond resolution. Detections from each TDC channel are hooked through a First In First Out (FIFO) buffer into a sorting algorithm that can handle upwards of 100's of MHz count rates shared across all input channels and a second FIFO buffer then streams the sorted time-tags to file. The typical method of using a laser firing as a trigger to start "listening" for detections is abandoned. Instead, each trigger pulse is treated as a separate detection and the "raw" data is a collection of uncorrelated channels and timing values.

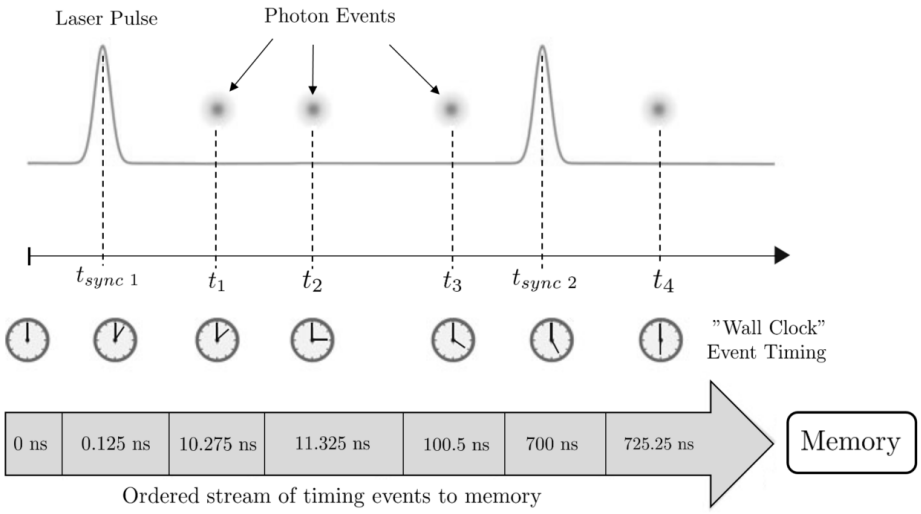

Figure 3.4: A modified diagram from [62] shows the general photon time-tagging measurement. Laser firings and photon events are referenced in time to the start of the experiment by a free running clock. Each value is given a channel number and timing reference and is then streamed to memory in the order they were detected.

A visual representation of the timing process is shown in Fig. 3.4. An implementation of TCSPC acquisition for a SPL sensor can be seen in Fig. 3.5, where the raw signals going to the CFD/TDC are shown along with the external 250 kHz clock that tracks coarse measurement cycles and synchronizes channels (the picosecond precise subdivided micro clock or macro clock are not shown). The laser sync signal and subsequent arrival of single photon events can be seen in cyan, magenta, and green. In this implementation, all channels are treated independently and have distinct time-tags in the written data file, implying that precise knowledge of every laser firing is kept through out the experiment in addition to each photon event.

When performing the same data rate analysis as done with MCS, it becomes clear that the time-tagging approach is viable with most data transfer methods. If the assumption is that there are 1 % detections over the 10 km range, then 1000 detection ranges will be reported per laser firing. Over a full second of accumulations, with a 15 kHz PRF, this translates to 60 MBytes/second per channel. Given that most time-tagging acquisition boards transfer data over PCIe x8 with a theo-

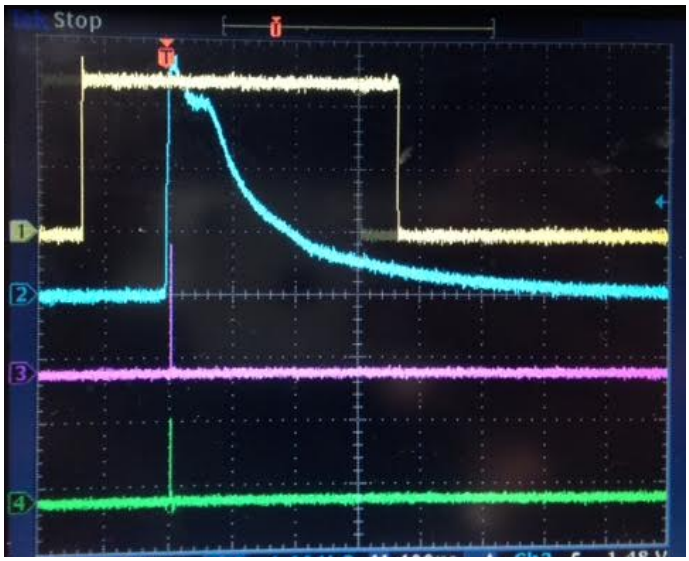

Figure 3.5: A screen shot showing the implementation of the time-tagging technique with a SensL TDC. The single external clock period (4μs) can be seen in the yellow trace, the sync pin diode to indicate a laser firing is seen in cyan, and two detector channels can be seen in magenta and green.

retical maximum of 4 GBytes/second, five independent channels can stream all photon detections to file at full resolution of the TDC without overloading the data stream transfer budget. This approach proves to be significantly more agile than the MCS approach as it transfers on positive detections, while keeping the timing of the unambiguous range of the sensor. A benefit of this technique is a scalable post processing resolution. Dynamic resolution adjustment from the base TDC resolution can be done across the measurement range to allow multiple varying observables. With lower data rates per detector and dynamic binning options, implementation of advanced detector approaches, including multi-element arrays, are achievable without ballooning data processing.

Three-dimensional imaging of hard targets by lidar successfully implementing TCSPC acquisition has yielded dense sub-centimeter point cloud generation [80, 84, 51] and simultaneous estimation of backscattered intensity. Early implementations were limited to near field measurements [80], due to the short unambiguous range of the high PRF lasers used, but advanced transmitters have led to far field point cloud generation of "hard" targets [14, 68, 51]. As a product of targeted

experiments, many of these implementations relied on a temporally gated detection scheme, with *a priori* information on the standoff distance of the scatterer. This implementation limits the ability to build a detection profile across the full measurement range typically desired in atmospheric sensing, and confines the probability of a detection to a specific range gate.

The robust literature pertaining to the TCSPC approach also provides a foundation of knowledge from which a multi-functional lidar adapting these techniques can draw. The following sections seek to address issues of statistical detection and acquisition dead-time prevalent when utilizing TCSPC and draws conclusions on future sensor design characteristics.

3.1.2 TCSPC Timing Precision

To minimize a sensor's combined measurement precision, it is necessary to understand the limitations imposed by photon event timing. The overall timing precision and feasible resolution of a SPL employing photon time-tagging is not dictated solely by the quoted timing resolution of the device, but also by a number of instrument effects convolved together. These include the laser pulse width and detector timing jitter, both of which are dominant in the definition of the instrument response function (IRF). In order to facilitate high precision measurements, the use of a CFD is necessary to remove the statistical effects of detector pulse height distributions. This is of main concern with photomultiplier tubes (PMT) where pulse height distributions cause timing uncertainties that convolve with the time transient spread (TTS) of the dynode chain, increasing the overall uncertainty of the measurement by hundreds of picoseconds [8]. Figure 3.6 shows the several different modeled PMT pulse heights and the output from a differentiating CFD for each. If a simple threshold was used, timing walk due to the height distributions would be present. The use of a CFD ensures that the time-tag applied to each output's zero crossing remains impervious to this effect and the residuals can be considered negligible when considering timing errors.

When operating a SPL sensor, the convolved width of the timing signature then dictates the achievable timing resolution of the system for a single detection, implying that, for the least uncertainty on a single detection, the IRF should be reduced until the desired standard deviation

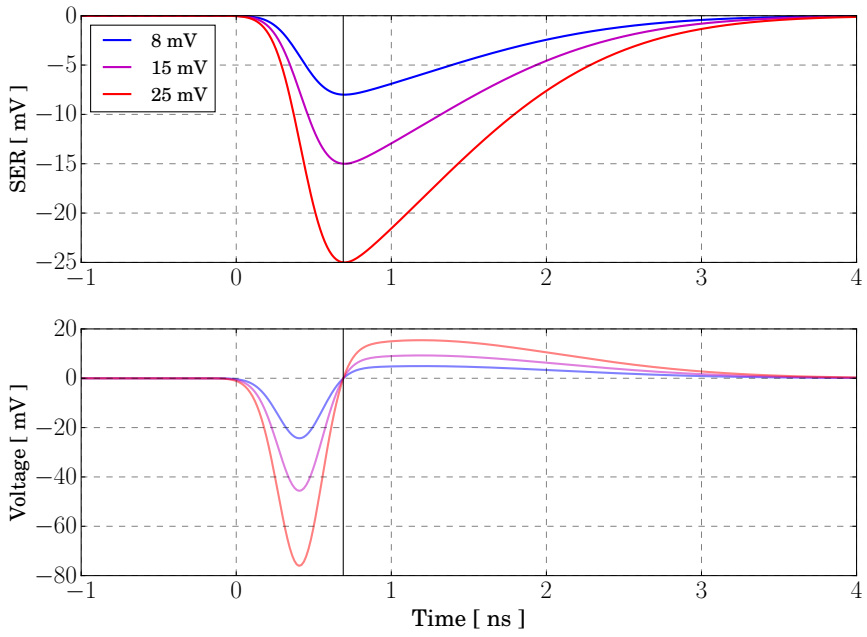

Figure 3.6: Simulated operation of a differentiating CFD. The top panel shows PMT pulses of varying amplitude. The bottom panel shows the output of a CFD circuit, where the zero crossing tracks the input PMT pulse peak. For the different PMT pulses, the zero crossing occurs in the same location, removing the statistical introduction of range jitter that occurs when a simple threshold is used for pulse discrimination. This circuit does not remove TTS uncertainty.

per detection has been reached. In theory, this is possible, but in practice this is difficult due to the availability of rugged and deployable detectors with picosecond timing jitter and < 500 ps pulse width lasers. Of course, the combination of many detections over some accumulation period allows the location of a target to be known more precisely, but for fast moving platforms this introduces target smearing by allowing the combination of detections from different scenes to put emphasis on a need low uncertainties for each photon detection.

For the SPL sensors discussed, the IRF envelope is comprised of the following

$$h_{IRF}(t) = h_L(t) * h_D(t) * h_{CFD}(t) * h_{TDC}(t), \tag{3.1}$$

where $h_L(t)$ is the temporal profile of the transmitted laser pulse, $h_D(t)$ is the temporal profile of the detectors time-transient spread, $h_{CFD}(t)$ is the timing response of the CFD, and $h_{TDC}(t)$ is the

timing response of the TDC. If it can be assumed that each component of the IRF is of Gaussian shape, then the total variance of the IRF is the sum of the components, given as

$$\sigma_{IRF}^2 = \sigma_L^2 + \sigma_D^2 + \sigma_{CFD}^2 + \sigma_{TDC}^2, \tag{3.2}$$

with the FWHM of the IRF given as $FWHM_{IRF} = 2\sqrt{2\ln 2}\sigma_{IRF}$.

In the case of making repeated measurements from a target, the histogram of photon detections builds a received signal shape with a temporal response, which is a convolution of the IRF and the target, given as $h_{rx}(t) = h_{IRF}(t) * h_{tgt}(t)$. For a specular target with minimal roughness relative to the laser wavelength, recovery of the IRF is possible and the width of the histogram should be equal to the width of the IRF.

The detector's impact on the timing stability and the contribution to the IRF is variable across detectors and incident photon rates. There is a strong dependence of the IRF on the focused spot size on the detector face, so much so that under high photon rates a difference in illumination across the detector face can result in a varying TTS, which directly alters the IRF. However, in the limit where the TTS is not the driving source of IRF uncertainty, say with a broader laser pulse width, the introduced uncertainty is dwarfed in the total convolution and is not a necessary consideration. For example, the Hamamatsu H7422-40 series of PMTs can exhibit an 8 ps shift in its TTS peak in photon rates on the order of several MHz [8]. With only an 8 ps deviation out of a total convolved width of > 500 ps, when counting single photons, this effect can safely be ignored in the sensors discussed throughout this thesis work.

There are circumstances where a high photon rate can induce changes to the IRF, which must be considered. In the case where the probability of a photon event is much less than one, i.e. operating in photon counting mode, the method of estimating the IRF is as stated in Eq. 3.1. When the probability of detection is low enough such that multiple laser firings result in a null detection from the delta target, the convolution is not constrained to any one portion of the laser pulse, allowing detections across the entire temporal profile of the pulse as the leading edge detection probability is not unity. However, under high photon rates, biased detections will change

the IRF as a function of the impinging photon rate. With a constantly varying number of photons incident on the detector, the IRF will change accordingly and with a non-linear magnitude. This challenge must be understood to correctly estimate what a system's uncertainty in each photon event is and to allow propagation of errors that are accurate for the sensor's measurement.

3.2 Bias and Uncertainty From a Changing IRF

SPL sensors employing highly precise time-tagging electronics rely on an operational probability of detection (P_d) that is much less than one, typically achieved by reducing the transmitted pulse energy until the desired P_d is reached. In some instances, a higher photon collection efficiency is needed and the operational P_d is closer to unity, as is the case with the ATLAS sensor onboard the ICESat-2 satellite, which has a targeted $P_d \geq 0.6$ over ice, depending on the beam analyzed [79]. However, SPLs operating with a high P_d risk the possibility of concurrent target photons per laser shot, leading to biasing and distortion of the accumulated photon histogram. Both effects result in retrieved data that is not linearly related to the backscattered photon rate, which poses issues for geophysical parameter estimates.

As background signal and target photons are treated equally by the acquisition electronics, the sensor's discriminator must be set to pass the detector's single electron response (SER) and block electronic noise from generating false alarms. Due to the presence of a non-zero detector and TDC dead-time, the acquisition system becomes limited to, at most, one detection from a target per laser firing, assuming that the temporal width of the laser pulse dominates the IRF and is shorter than the combined dead-time of the detector and TDC, $\tau_{rx} < \tau_d$. Typical lidar altimeters operate with a FWHM laser pulse width of < 1 ns. Different permutations of these parameters exist in SPL sensors, as is shown in [24], often with < 5 ns dead-times. Specifically for the ATLAS sensor, operation employs a longer pulse width of 1.5 ns FWHM and a 3.2 ns dead-time [79].

If the SPL sensor is transitioned out of photon counting mode and approaches $P_d \to 1$, which is possible for acquisition outside of optimized measurement altitudes or due to a target increased backscattered photon rate, the leading edge of the transmitted laser pulse begins to dominate

the contribution to detected photons. This is due to the fact that the P_d is correlated with the backscattered photon rate and. as the rate increases, one or more photons can be at the detector face. eventually leading to multiple photons incident during the same IRF timing interval. The first incident photon is detected, while the remaining fall within the resulting dead-time. In addition, the realistic photon detector is not photon-number resolving, but capable of only distinguishing between $N_{rx} = 0$ or $N_{rx} \geq 1$. Raw. unprocessed SPL ranging data plagued with this effect is shown in Fig. 3.7, where the entire distribution has been biased forward, the density of points has increased, and the spread in time has narrowed.

Yang *et al.* [126] developed a Monte-Carlo (MC) model for partially analyzing first photon bias (FPB) and found that range biases are introduced with a marginal increase in photon rate. However, this study did not elucidate the impact of this phenomenon on the temporal shape change and overall timing uncertainty introduced to the integrated histogram of photons by FPB. Mitchell *et al.* [92] show data representative of the histogram distortion that this thesis demonstrates is to be expected when operating with high laser pulse energies, as well as the resulting concurrently received target photons per laser firing. However, this effect was not quantified and the described sensor was unable to estimate backscattered signal strength due to operation outside of single photon counting mode.

It is typical to infer the incident photon rate from the retrieved count rate over some integration time, assuming a linear proportionality between the two. Accumulated photon histograms over this integration time are often assumed to have Gaussian distributed properties, simplifying science retrievals where histogram properties are used as estimators for geophysical parameters, such as surface roughness [69], sea surface bias [95], or indirect estimates of wind-speed [118]. Due to FPB, the Gaussian distribution assumption can fail when $P_d \to 1$ with greater than unity target photons, $N_{rx} > 1$. The implications of a non-linear change in count rates and thus photon histograms as a result of FPB must be understood to perform accurate geophysical estimation with SPL data and describe the error associated with each detection.

To further investigate the effect of FPB on SPL, this thesis models the stochastic Poisson

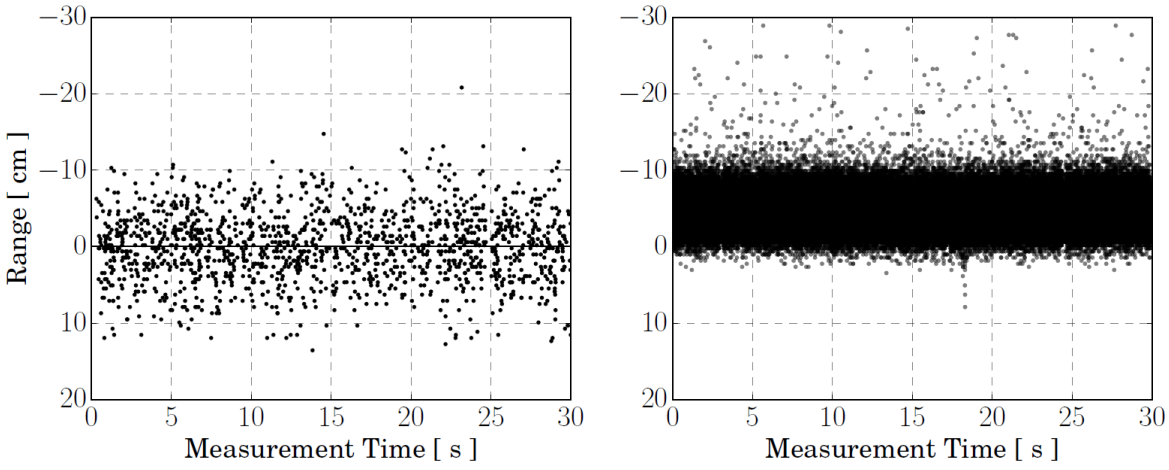

Figure 3.7: Ranging bias seen in the co-polarized channel of the POLAR SPL sensor (discussed in Chapter 5) during pre-flight calibration routines. The left panel shows photon events accumulated with $P_D \ll 1$, exhibiting no FPB. The right panel shows a $P_D = 1$ as generated by introducing a gain block ($\sim$ 10X) to the PMT's SER prior to the TDC time-tagging device. The mean range bias was calculated at -4.85 cm in the sensor direction with a clearly decreased distribution width and a heightened number of detections on the leading edge and lack after the main cluster.

process of detecting photons from a delta target (flat surface), given an assumed Gaussian IRF for a modeled single element sensor, using the MC method. A case can be made for assuming a delta target, as it provides a best case scenario for FPB effects, which are further exaggerated with temporal pulse spreading due to surface roughness or slope. The stochastic generation of photon detections is limited by the introduction of a dead-time, allowing for only the first arriving photon from a target to be recorded.

Considering the prior definitions, the received envelope of photons is a temporal convolution of the IRF and the SRF

$$h_{rx}(t) = h_{IRF}(t) * h(t)_{SRF}, \tag{3.3}$$

where $h_{SRF}(t) = \delta_{tgt}(t)$ for a discrete delta target. The resulting waveform takes the Gaussian form of

$$G_{rx}(t) = \frac{N_{rx}}{\sqrt{2\pi\sigma_{IRF}^2}} \exp\left(\frac{-t^2}{2\sigma_{IRF}^2}\right), \tag{3.4}$$

where the target location is equal to the mean of the distribution and centered at a referenced

elevation of zero. Integration over the received pulse duration gives the total number of received target photons as N_{rx}

$$\int_{-\infty}^{\infty} G_{rx}(\tau)d\tau = N_{rx}. \tag{3.5}$$

A Poissonian detection scheme was assumed with single photon event, $k = 1$, mimicking an SPL threshold set to pass the detector's SER and a total number of received target photons of N_{rx}. An ideal clear atmosphere, with no multiple scattering, is assumed and the SRF is maintained as an ideal single scattering layer. The sensor timing is set to match that of Barton-Grimley *et al.* [5], the discussed sensor in Chapter 5, with a FWHM IRF of 550 ps and a TDC resolution of 27 ps. The acquisition dead-time is assumed to be greater than τ_{rx}, $\tau_d > 1$ ns.

The left panel of Fig. 3.8 shows the distributed surface point cloud for stochastic single photon detections over 10^3 laser firings with at most one photon per laser firing, $N_{rx} \leq 1$. The right panel shows that the photon histogram fits the attributed Gaussian shape of the IRF, G_{rx}, with no distortions from the fit using Eq. 3.4, the dashed line.

Now allowing two photon events per laser firing, $N_{rx} \leq 2$, and again simulating 10^3 laser firings, the accumulated photon histogram deviates immediate from the expected IRF, shown in Fig. 3.9. Similar to results in [126], the photon histogram shifts in range, producing a forward bias that is related to the photon rate. Additional non-Gaussian responses can be seen in Fig. 3.9, including a forward skewing (towards the sensor) of the histogram's leading edge was well as a decreased distribution variance, indicated by the decreased spread about the mean.

The histogram asymmetry shown in Fig. 3.9 results from the acquisition system's heightened probability of registering a photon from the leading edge of the laser pulse, which subsequently decreases the probability of a photon from the trailing edge. This implies that the P_d at every time bin of the photon histogram is reliant on the probability that the acquisition system had not registered an event in the prior bins in accordance with the dead-time length assumptions.

Prior publications give a continuous integral form to explain the resulting histogram asymmetry from this probability [92, 45], but do little to expand the function and determine exactly

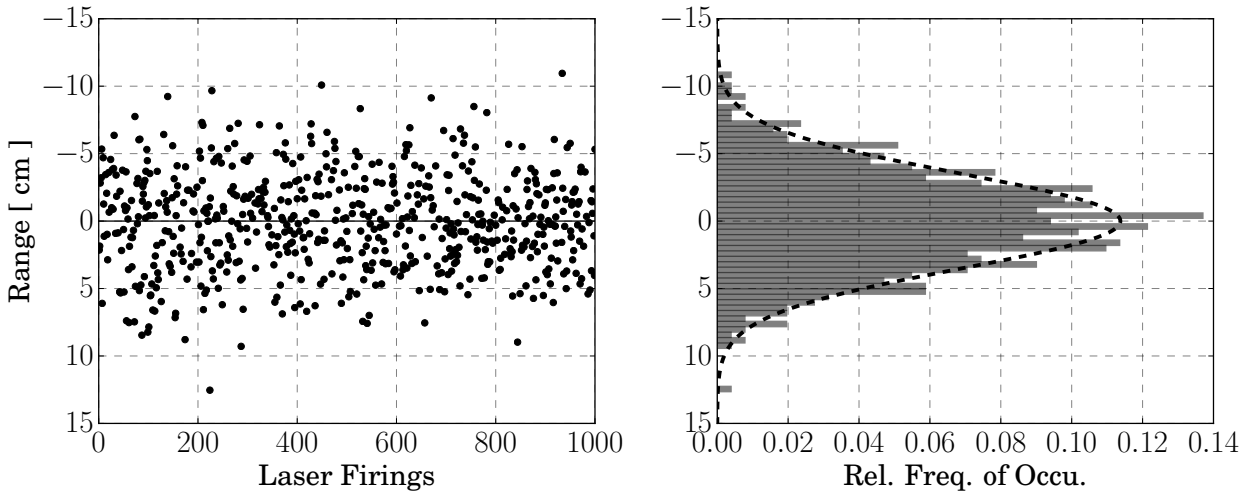

Figure 3.8: Simulated returns for a FWHM IRF of 550 ps, allowing $N_{rx} \leq 1$ per shot over 10^3 laser firings. The right panel shows the accumulated photon histogram in 27 ps bins, with the dashed envelope of the Gaussian fit using Eq. 3.4.

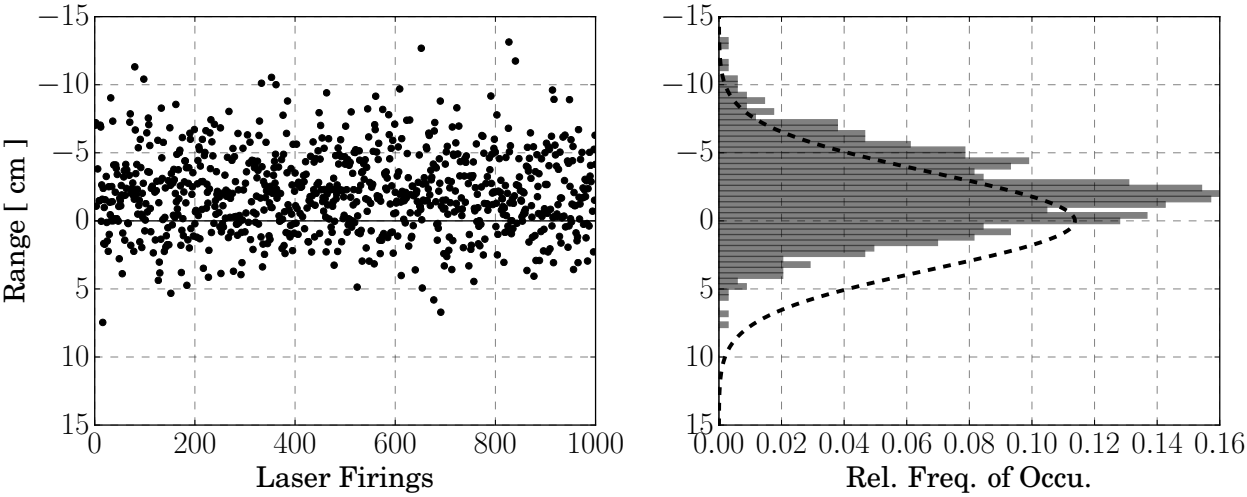

Figure 3.9: Simulated results for the same MC scheme as in Fig. 3.8, but with $N_{rx} \leq 2$ per laser firing. The dashed line shows the expected waveform of shape G_{rx}.

what terms are responsible for FPB. A modified form of this probability, where the integral has been correctly placed, is

$$P_d(t) = (1 - \int_0^t P_d(\tau)d\tau)P(t). \tag{3.6}$$

This implementation assumes Poissonian statistics, where the probability of k photons in a timing bin bounded by t_1 and t_2 is [38]

$$P\left(k; t_1, t_2\right) = \frac{\lambda^k(t_1, t_2)}{k!} \exp\left(-\lambda(t_1, t_2)\right), \tag{3.7}$$

where $\lambda(t_1, t_2)$ is the average photon rate per TDC time bin, evaluated as

$$\lambda(t_1, t_2) = \int_{t_1}^{t_2} G_{rx}(\tau)d\tau. \tag{3.8}$$

To apply these mathematics to a real sensor discretization of Eq. 3.6 is necessary. The derivation is used to facilitate an understanding of the histogram distortions, where the P_d for some λ_j counts in the j^{th} bin, initialized by the Poisson distribution, is

$$P_d(k; j) = \left(1 - \prod_{i=1}^{j-1} P(k \geq 1; i)\right) P(k; j). \tag{3.9}$$

Here the equality $P(k \geq 1; i) = 1 - P(k = 0; i)$ can be used, giving

$$P_d(k; j) = \left(\prod_{i=1}^{j-1} P(k = 0; i)\right) P(k; j), \tag{3.10}$$

which, upon substituting in Eq. 3.7, equates to

$$P_d(k; j) = \left(\prod_{i=1}^{j-1} \exp\left(-\lambda_i\right)\right) \left(\frac{\lambda_j^k}{k!} \exp(-\lambda_j)\right). \tag{3.11}$$

The fundamental relation of $\prod_{i=1}^{j-1} \exp\left(-\lambda_i\right) = \exp\left(-\sum_{i=1}^{j-1} \lambda_i\right)$ is then used to remove the product and reduce computational complexity. Re-arranging gives the final discretized form of

$$P_d(k; j) = \frac{\lambda_j^k}{k!} \exp\left(-\left[\lambda_j + \sum_{i=1}^{j-1} \lambda_i\right]\right). \tag{3.12}$$

The result is approximately Eq. 3.7 with an addition to the exponential. The summation term in Eq. 3.12 serves to introduce FPB when photon rates are high, and detection in the

j^{th} timing bin is governed by the prior $j-1$ bins. When photon rates are low, the FPB term has negligible contributions and the detection probability collapses to the standard Poisson distribution, Eq. 3.7. Examples of further experimental data, which can be predicted by the statistics in Eq. 3.12, are shown in [92]. In this example a photon counting sensor was operated in a regime of high backscattered photon rates creating histogram asymmetry. The resulting data is non-linear in count rate and has a histogram variance narrower than the expected IRF.

By treating each photon event as an independent, random variable with $N_{rx} < 1$, the Poissonian counting process is valid and typically converges to Gaussian statistics at large counts. While commonly implemented for a sensor operating with $P_d < 1$, invocation of the central limit theorem to predict a distribution mean and variance can result in incorrect distribution estimates when photon rates are high. Because of this, the photons experiencing FPB may fail the assumption of Gaussian convergence and instead obey lognormal statistics of the form [38]

$$P_{\ln}(\chi) = \frac{1}{\chi\sqrt{2\pi\sigma_\chi^2}} \exp\left(\frac{-(\ln(\chi)-\mu_\chi)^2}{2\sigma_\chi^2}\right), \tag{3.13}$$

where χ is a logarithmically distributed random variable indicative of the photon rate incident on the detector.

Figure 3.10 shows an accumulated photon histogram for an MC run with $N_{rx} \leq 10$ photons per laser firing. The histogram is fit using Eq. 3.13, providing estimated mean and variance for the binned data that differ from the expected Gaussian values.

The distorted histogram shown in Fig. 3.10 has unique implications for retrievals that rely on Gaussian statistics for parameter estimations. Due to the condition of $\tau_{rx} < \tau_d$, the non-zero dead-time prevents detection of subsequent photons after the first incident photon has been registered. Non-paralyzable dead-time corrections, as shown in [25], provides a scaling factor to adjust the estimated count rate for missed photons if $P_D \neq 1$, but only addresses dead-time due to detector pulse pile-up, not the addition of TDC dead-time, and cannot predict the results in Fig. 3.11.

Under these conditions, the estimated backscattered count rate is also marred by FPB. When $N_{rx} \gg 1$, the number of registered photons will maximize at one per laser firing. This leads signal

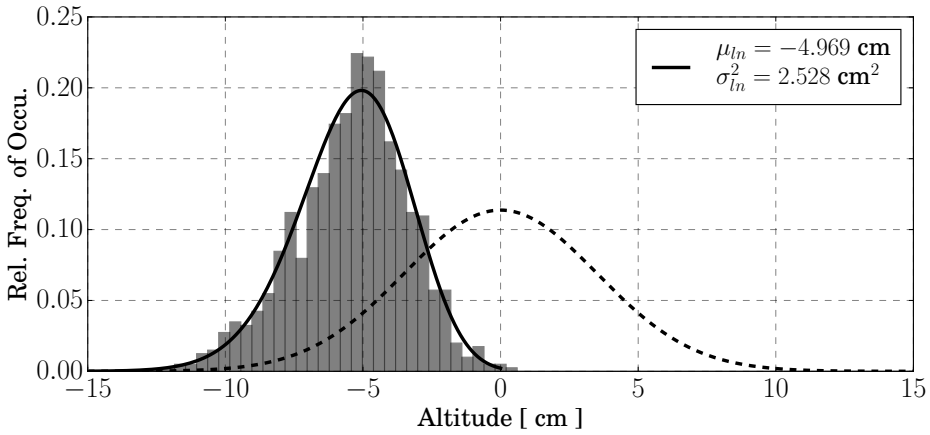

Figure 3.10: The resulting MC data for $N_{rx} \leq 10$ and a histogram fit using the lognormal statistics described by Eq. 3.13, shown by the solid line. The retrieved lognormal mean and variance are shown with a distribution peak occurring at -4.969 cm. The dashed line shows the expected SPL Gaussian distribution.

strength estimates from the photon histogram to be equal to the number of laser firings used to build it. The registered photons in the histogram reaches a steady-state value equal to the laser's PRF, and as N_{rx} increases, there is no equivalent relative increase in the registered count rate. This can be seen in Fig. 3.11, where for an increasing mean photon rate, $\langle N_{rx} \rangle$, the number of registered photons has been normalized by the PRF to give a percent detected, showing that the registered counts rapidly reach the steady-state value of the laser's PRF. The result is an estimated count rate that is no longer a true estimate of the incident photon rate. This has distinctly negative implications on estimates made from the photon histograms generated by SPL sensors in all applications, altimetry, and atmospheric sensing, if relative power retrievals are required for geophysical parameter estimation.

Using the lognormal statistics from Eq. 3.13 to generate an estimate for the distribution's mean and variance while increasing N_{rx}, the distribution's rate of change can be examined. Figure 3.12 shows that even small deviations out of single photon counting result in a rapidly changing histogram. As demonstrated in Fig. 3.12, the distribution range bias monotonically increases with

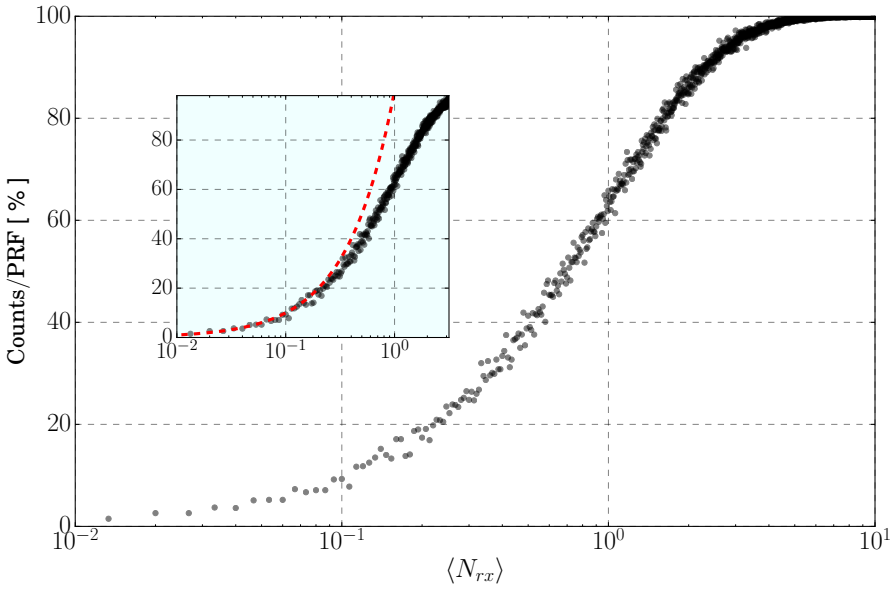

Figure 3.11: The estimated percent of photons detected per mean return photons, $\langle N_{rx} \rangle$. As $N_{rx} \gg 1$ the detection system reaches a 100 % probability of generating a single registered photon per laser firing, achieving the steady-state count rate once the laser's PRF has been reached. The inset shows the deviation of $\langle N_{rx} \rangle$ away from a linear one-to-one line.

increasing N_{rx}, while the distribution variance decreases. Once the steady-state count rate has been reached, the number of detections contributing to the estimate will remain constant with increasing N_{rx}. This implies that for a given decrease in variance the histogram requires fewer bins to be used for the same number of detections. This has the effect of an apparent relative increase in signal strength when tracking the distribution mean, but integration across the histogram yields the same number of detections because the estimated count rate does not match the incident photon rate. Figure 3.13 provides a graphical representation of the relationship between the maximized single photon detection probability and minimized IRF variance.

Figure 3.12 indicates that strict observance should be paid to retaining an SPL sensor in a mode of single photon counting, as rapid histogram changes prove difficult or impossible to calibrate. For SPL sensors that employ PMTs, such as the ATLAS sensor [79], the sensors discussed in [92, 5], and the throughout this thesis, this is especially true. Most PMTs act as binary detectors, and

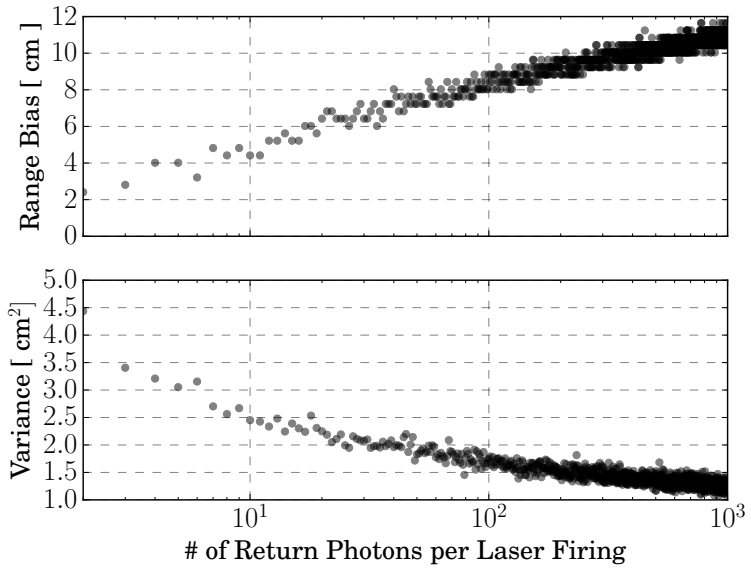

Figure 3.12: Estimated lognormal mean (absolute range bias) and variance for a varying N_{rx} per laser firing. Both parameters experience rapid change for the first few incident photons, with each reaching a point, $N_{rx} \geq 100$, where change is small compared to the overall value. These values indicate that just a small deviation in incident photon rates away from single photons creates drastic changes in the distributions.

with the addition of a TDC timing device, differentiating between no photons and one or more photons, making it impossible to distinguish between the SER and the response to concurrent incident photons. There is no direct measurement of N_{rx} unless each detector waveform is recorded and analyzed independently, which is not performed by SPL sensors. There are instances where sensors have been quoted as providing an "intensity" measurement where distinctions between the SER and additional responses are generated by recording detector pulse widths [24]. This, however, is limited to when the sensor is in a mode of $N_{rx} > 1$ and, thus, when single photon detections occur there is still no estimate of photon rates.

For sensors that do not wish to estimate photon count rate and have a singular measurement requirement of high precision ranging, FPB can have positive implications. In this case, the effects displayed in Fig. 3.12 can be minimized by reducing the rate of change of the distribution. This is achieved by operating with $P_d = 1$ and maintaining a high photon rate, $N_{rx} \gg 1$. When N_{rx} is

high, fluctuations in the photon rate will result in a relatively small range bias change compared to the instrument precision, allowing calibration of this offset. Additionally, the decreased variance facilitates a decreased standard error of the mean and a decreased ranging uncertainty on every photon event. This operational mode is similar to that of GM lidar altimeters, which are unable to linearly resolve backscattered count rate.

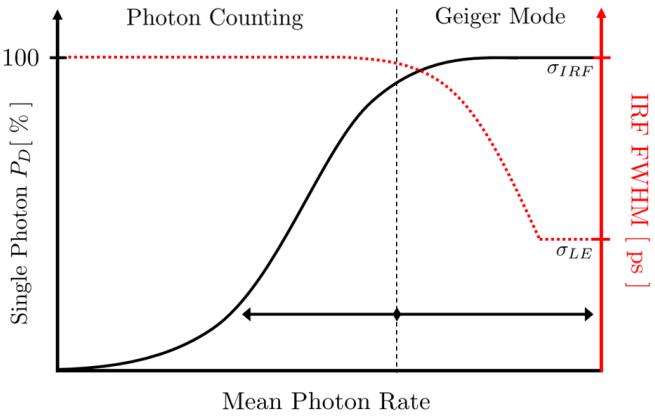

Figure 3.13: A depiction of acquisition regime change from linear photon counting to non-linear GM, with the steady state variance reached, σ_{LE}, constrained to the leading edge of the laser pulse.

Acknowledgment should be given to further analysis that considers scattering with a non-delta target over rough terrain or sloped surfaces, such as a wavy water surface or a subsurface scattering layer. The implications of added ranging uncertainty from measurements that introduce geophysical variance are examined in the next section.

3.2.1 Added Geophysical Variance

The SRF can be modeled according to the work discussed in [32], where representations for the mean square contribution to the received pulse are given. It is useful to consider this variant of surface modeling, as it provides a method for extracting surface information by fitting the equations to a distribution of surface heights collected by an SPL. This gives direct links to geophysical parameter estimation with no other adjustments, assuming that the sensor is operating in photon counting mode.

For a hard target, the timing variance introduced due to surface roughness is given as

$$\sigma_{tgt}^2 = \frac{4\sigma_\xi^2}{c^2\cos^2(\alpha)} + \frac{4R^2}{c^2\cos^2(\alpha)}\left(\tan^4(\theta_T) + \tan^2(\theta_T)\tan^2(\alpha)\right), \tag{3.14}$$

where α is the off-nadir pointing angle of the transmitted beam, R is the sensor's altitude above the surface, σ_ξ is the RMS surface roughness, and θ_T is the half-width divergence angle of the transmitted laser pulse. This expression is derived directly from the surface profile statistics within the laser footprint and accounts for nonlinear terms introduced by the roughness and off-nadir pointing.

In the case of a wavy ocean surface, it is expected that the return signal envelope will be broadened. Significant wave height (SWH) can be used as the driving factor for which surface roughness is calculated. SWH is defined as the average of the crest to trough heights, of $1/3^{\text{rd}}$ of the waves, and is related to the RMS wave height as SWH $= 4\sigma_\eta$. Furthermore, the RMS wave height magnitude is driven by the average wind speed as $\sigma_\eta = 0.016W^2$. The units of W are [m/s] and the overall units of σ_η are [m]. This creates a tangible relationship between surface wind speed and retrieved signal variance.

The temporal spreading of the pulse width due to wave ocean surfaces is then given as [118]

$$\sigma_{tgt}^2 = \frac{4\sigma_\eta^2}{c^2\cos^2(\alpha)}\left[1 - \lambda^2\left(1 - \frac{2\tan^2(\alpha)}{\langle S^2\rangle}\right)^2\right] + \frac{4R^2}{c^2\cos^2(\alpha)}\left(\tan^4(\theta_T) + \tan^2(\theta_T)\tan^2(\alpha)\right), \tag{3.15}$$

where λ^2 is a measure of the surface skewness which captures the weak nonlinear interactions between the wave components that result in a non symmetric surface structure, $\langle S^2\rangle$ is a dimensionless value that gives information about mean squared surface slope as derived from wind speed. It should be noted that this expression does not take into account the effects of capillary waves. The remaining parameters carry over from the hard target roughness definition.

As Eqs. 3.14 and 3.15 represent a variance of the timing response due to the surface morphology, they can be convolved with the IRF to give complete shape of the received signal waveform. To implement both of these equations, a pointing angle of approximately nadir was assumed, $< 1°$, and a measurement altitude of 175 m was used. The transmitter's divergence was assumed to

have a full width value of 2 mrad, giving a surface spot diameter of 0.35 m. The ocean surface was assumed to have a skewness factor of 0.02 and a mean squared surface slope of 0.03. Timing responses for an increasing surface roughness or wave height were generated and convolving with the sensor's timing signatures. These were then used as the input to the MC model and the results analyzed for surface effects on ranging bias.

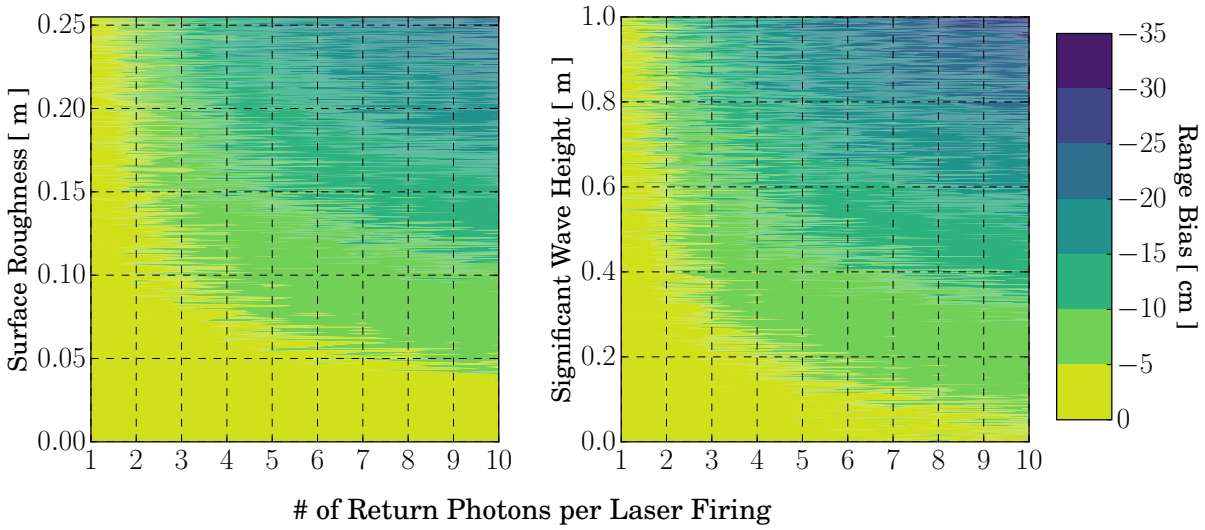

Figure 3.14: These contours show the resulting MC estimated range bias for $N_{rx} = 1 \rightarrow 10$ and varying surface roughness, left panel, and significant wave height, right panel. Both panels show that increased concurrent photons and surface morphology create bands of range bias.

The left panel of Fig. 3.14 shows the total response for multiple received concurrent from a hard target with varying surface roughness. Distinct regions of consistent range bias can be seen for different combinations of temporal stretching or number of concurrent photons per shot. The effect of a wavy water surface is shown in the right panel of Fig. 3.14, where Eq. 3.15 is utilized through the SWH to generate estimated range bias. The impact of SWH and N_{rx} reveal a banding structure similar to that of a rough hard target scatterer, but with less distinct boundaries between divisions of bias. Figure 3.14 shows that the timing variance introduced by small wave heights is on the several centimeter scale for small deviations of N_{rx}, implying that the sensor's footprint likely covers multiple cycles of surface structure and provides some immunity to height variations.

This figure displays the complexity of the backscattering problem, where if a sensor is deviated out of single photon counting, the ability to infer a unique solution for the surface roughness by performing a deconvolution of the received pulse is impossible.

Figure 3.15 shows the MC estimated range biases for $N_{rx} \leq 2$ and $N_{rx} \leq 2$ while varying the hard target roughness and SWH, e.g. extracting two columns from each panel in Fig. 3.14. All instances shown here demonstrate that, as the surface morphology increases in magnitude, so does the distribution of biases. This is due the fact that the MC model is capturing the variability in the detection process and as the surface variance introduces a broader received temporal pulse the probability for firing anywhere across that pulse is equally increased. As N_{rx} increases, the resulting distribution that is sampled for detection becomes smaller, as previously shown, so the spread in results for an increasing surface roughness becomes less distributed.

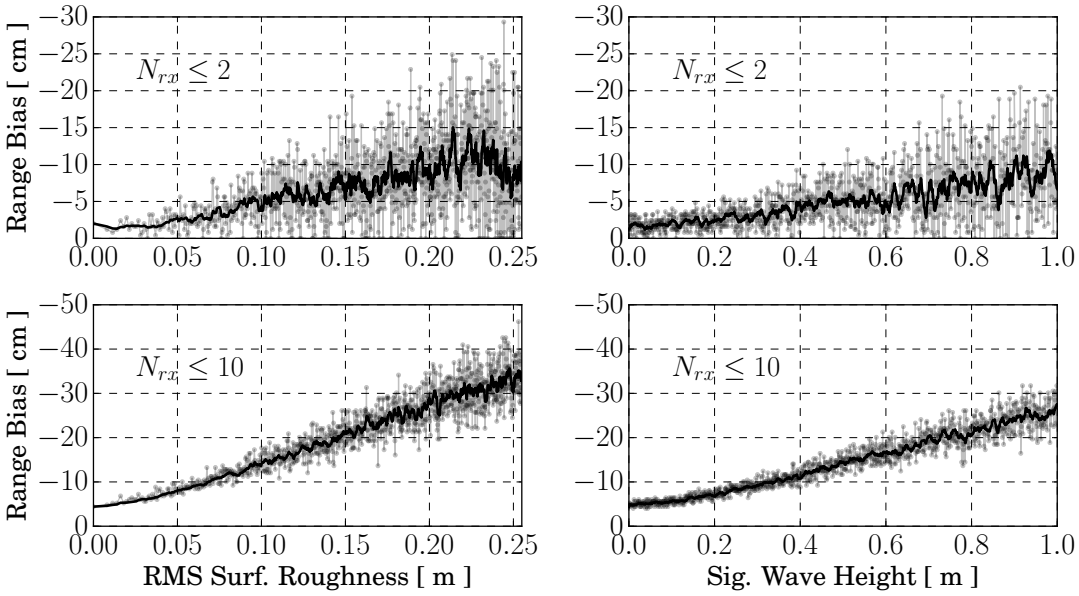

Figure 3.15: Range biases for $N_{rx} \leq 2$ and $N_{rx} \leq 10$ extracted from Fig. 3.14. The distribution of points from the MC runs can be seen along with an 11 point smoothed trend line.

Introduction of a geophysical timing response to the received waveform shows that there is a possibility to retrieve surface parameters from the accumulation of target photons. If many of

the instrument parameters are known well (laser divergence, IRF etc...) an estimate of the SWH or hard target roughness can be generated by analyzing the resulting histogram over multiple laser firings, assuming that $N_{rx} \leq 1$. It is necessary for the sensor to be operating in photon counting mode as the added width, despite likely being longer than the dead-time, can still introduce biases.

Figure 3.15 elucidates the difficulty of maintaining a sensor in single photon counting mode and what effects could be seen when a sensor is deviated out of this mode in the presence of non-delta target scatterers. It becomes readily apparent that these distortions represent a challenge. In the case where two channels are implemented to generate a measurement of separation between ocean surface and a subsurface scattering layer, the biases and distortions per channel can be drastically different due to a difference in backscattered photon rates. If either channel is deviated out of photon counting mode, or both simultaneously, comparison of photon histograms to generate a measurement of respective photon rate from each target will require special attention, as each is plagued by the aforementioned issues with non-equal contributions.

This work suggests that SPL sensors can reduce the effects of FPB by reducing dead-time, allowing fast acquisition recovery for arrival of subsequent photons. This coincides with the conclusions of [5], where short dead-times are also shown as advantageous for SPL sensors. For longer dead-times, degrading the IRF timing by increasing the laser pulse width so that $\tau_{rx} > \tau_d$, allows acquisition recovery within the IRF timing window, but reduces range resolution. Reducing the transmitted pulse energy also serves to decrease P_d, providing further FPB mitigation, but decreasing collection efficiency.

This section introduced the combined ranging bias, non-linear count rate, and distribution distortions resulting from the presence of FPB. It provided results from a MC model, first assuming a delta scatterer with no added target timing uncertainty to the received signal waveform, then introduces non-delta target timing responses, and provides a statistical explanation for the resulting lognormal distributed photon histogram. This work has implications on geophysical parameter estimations that require analysis of photon histograms and estimated count rates. Impacts can be seen in all photon counting altimeters, including the ATLAS instrument, and all lidar sensors

employing the time-tagging data acquisition approach.

The results shown in Figs. 3.10, 3.12, and others, indicate that correcting solely for the introduced range bias addresses the non-linear effects to distribution mean, but not variance. Figure 3.12 shows that the number of incident photons directly links to a change in range bias and distribution parameters. The combined results indicate that further analysis must be performed on accumulated photon histograms to properly estimate photon count rates and geophysical parameters.

3.3 Atmospheric Sensing in the Presence of Dead-Time

SPL sensors employing photon time-tagging to detect singular backscattered photons from the atmosphere is novel to this thesis and the resulting publications. Employment of these techniques is a tremendous step forward in range resolution, allowing an abundance of new atmospheric features to be probed, but it is not without its challenges. Figure 3.16 gives a clear example of the possible implications of using the time-tagging technique for the sensing of extended volume scattering targets and how dead-time can play a role in the photon detection efficiency. The dead-time distortions introduced by collections in high count rates regimes can be seen explicitly in the first 500 m of each profile. From the right panel of Fig. 3.16, it can be seen that non-physical distortions in the depolarization ratio are occurring, where for a typical elastic lidar sensor the exponential decay of Rayleigh scatterers will result in a relatively constant depolarization estimate if the scattering is due to clear air — with $\delta = 0.00365$ [13, 49]. In this case dead-time distortions are present in both receiver channels, and must be understood in order to utilize data with differing magnitudes of the effect are used for retrievals.

The temporal characteristics of distributed atmospheric scatters can be described as a volume ensemble of point targets that can be well approximated as discrete, randomly distributed delta functions. As the transmitted laser pulse propagates through the atmospheric medium, the discrete targets provide backscattering signal that seems effectively continuous at the range scales that photon events are binned. This requires the sensor to recover rapidly in order to acquire all the events that are backscattered during the acquisition period. SPL recovery is dictated by the overall

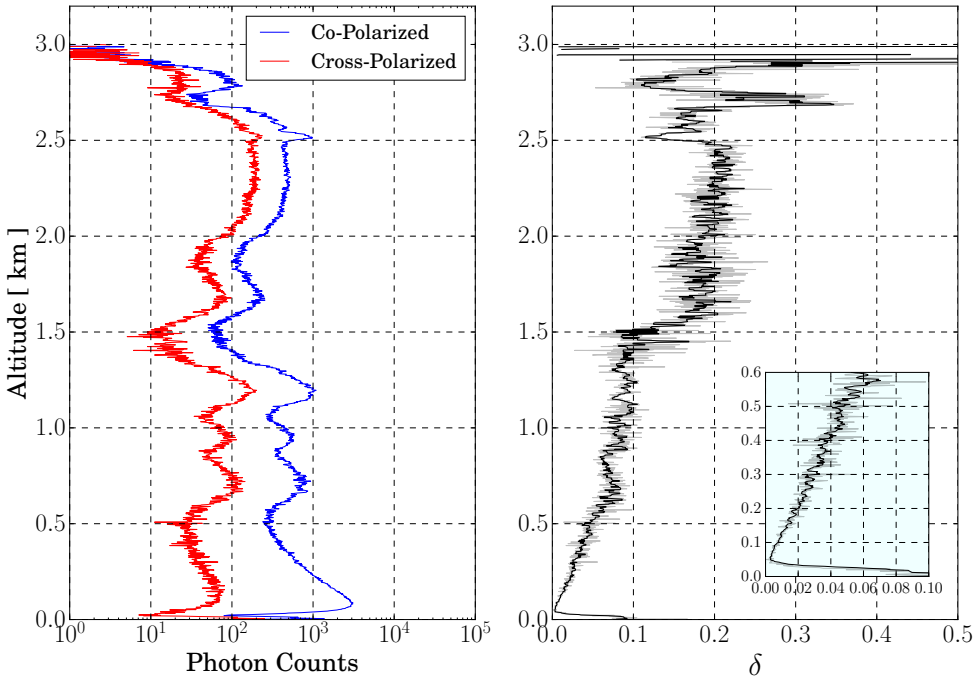

Figure 3.16: Example of co-polarized and cross-polarized profiles in a highly dynamic environment and the subsequent retrieved depolarization ratio. The two polarization profiles were generated from 10 seconds of received counts binned to 2 meters over the 10.49 km unambiguous range. The figure inset shows the instrument induced decreased depolarization ratio, where the first 500 meters show significant deviations from the expected values.

system dead-time, setting the range extent at which a sensor is "dead" after the first detection, directly linking dead-time to photon detectability. SPL dead-time is typically a linear combination of the detector and TDC contributions. For SPLs employing PMTs the dominating dead-time is due to the TDC, as the separation between pulses is typically only a few nanoseconds whereas TDC dead-times can range from two to tens of nanoseconds. It should be noted that for GmAPD use, the detector's dead-time typically dominates due to the quenching circuit's finite operation time. Dead-time analysis for hard target sensing using GmAPD detectors has been readily discussed in [33, 59, 70], providing complementary methods to the work discussed here, but focus on photon detection and not rate estimation.

Photon detectability at any specific time is impacted by the presence of a non-zero system dead-time, backscattered signal strength, and noise. For a photon counting lidar system, the arrival of backscattered signal and noise from the atmospheric volume can be modeled as a Poisson random variable [38, 100]. For a Poisson process, the probability of k events in the timing bin bounded by t_1 and t_2 is given by Eq. 3.7. For the case of atmospheric sensing, the mean value of the distribution is given as

$$\lambda(t_1, t_2) = \int_{t_1}^{t_2} [S_{RX}(t') + \xi(t')]dt', \tag{3.16}$$

where the total signal at any measurement time is composed of a backscattered signal count rate, $S_{RX}(t)$, and a noise contribution, $\xi(t) = N_{SB}(t) + n_{dark}(t)$, from solar background and detector dark counts respectively. Both $S_{RX}(t)$ and $\xi(t)$ represent photon rate functions with units of counts/second evaluated over the bin width. From Eq. 3.7, the probability of no photon events occurring between t_1 and t_2 is given by

$$P(k = 0; t_1, t_2) = \exp(-\lambda(t_1, t_2)). \tag{3.17}$$

Therefore the probability that there is at least one or more photon events in the time bin is

$$P(k \geq 1; t_1, t_2) = 1 - \exp(-\lambda(t_1, t_2)). \tag{3.18}$$

In the presence of dead-time, τ_d, and for some fixed time bin width, $\tau_b = t_2 - t_1$, the integer number of time bins within a dead-time period is $N_D = \lceil \tau_d/\tau_b \rceil$. Considering a single laser pulse, the system will register a detection in the j_{th} bin if the N_D bins before the j_{th} bin have not registered a detection. The probability that the acquisition registers a photon event in the j_{th} bin, in continuous form, is then

$$P(k \geq 1; j) = \exp\left(-\int_{(j-N_D)\tau_b}^{(j-1)\tau_b} \lambda(t')dt'\right)\left[1 - \exp\left(-\int_{(j-1)\tau_b}^{j\tau_b} \lambda(t')dt'\right)\right]. \tag{3.19}$$

The process of modeling discrete photon events is greatly simplified by considering the discrete nature of photon events. Discretization of Eq. 3.19, where $P(k \geq 1; j)$ is shortened to P_j, gives

$$P_j = \left[\prod_{i=j-N_D}^{j-1} P(k = 0; i)\right] P(k \geq 1; j), \tag{3.20}$$

which, expanded with Eqs. 3.7 and 3.16, gives

$$P_j = \exp\left(-\sum_{i=j-N_D}^{j-1} \lambda_i\right)[1-\exp(-\lambda_j)]. \tag{3.21}$$

It is assumed that the number of events per bin is generated by independent Poisson processes. The rate function can now be expressed as the backscattered signal strength in the j_{th} bin and a constant noise term, assuming that the solar background and detector dark counts are constant over the laser's IPP for single shot analysis, $\xi(t) \to \xi$, giving

$$P_j = \exp\left(-\sum_{i=j-N_D}^{j-1} (S_i+\xi)\right)[1-\exp(-S_j-\xi)]. \tag{3.22}$$

To facilitate the overall understanding of the dead-time contributions, the summation can be broken into its components as

$$P_j = \exp\left(-\sum_{i=j-N_D}^{j-1} \xi\right)\exp\left(-\sum_{i=j-N_D}^{j-1} S_i\right)[1-\exp(-S_j-\xi)]. \tag{3.23}$$

Recognizing that the sum is over a constant noise rate, generating multiplicative factor for the number of bins that could be subjected to noise detections, $(j-1)-(j-N_D)+1 = N_D$, it can be expanded as

$$P_j = \exp\left(-\xi N_D\right)\exp\left(-\sum_{i=j-N_D}^{j-1} S_i\right)[1-\exp(-S_j-\xi)]. \tag{3.24}$$

The first two terms in Eq. 3.24 introduce a combined expression for what will now be referred to as the dead-time weighting function. For a given signal count rate, noise count rate, system dead-time, and bin width, the dead-time weighting function is

$$W_j(S,\xi,N_D) = \begin{cases} 1 & N_D = 0 \\ \exp(-\xi N_D)\exp\left(-\sum_{i=j-N_D}^{j-1} S_i\right) & N_D > 0. \end{cases} \tag{3.25}$$

Separate terms describe the impact of noise and signal on the weighting function. The piece-wise defined function correctly captures the system response when dead-time is not present, showing that the statistics converge to the standard probability of detection as seen by an waveform recording sensor. As the system dead-time goes to zero, the summation yields the bounds $i = j >$

$j-1$, which gives the empty set, in turn maximizing W_j at unity and removing dead-time effects from the estimated signal.

Combining Eqs. 3.24 and 3.25 yields the probability of detection in the j_{th} bin as

$$P_j = W_j(S, \xi, N_D)[1 - \exp(-S_j - \xi)], \tag{3.26}$$

where the probability of one or more positive detections in the j_{th} bin is scaled by the value of W_j. When the number of photon events per laser firing is small, Taylor expansion of the square bracketed terms in Eq. 3.26 is expressed as

$$[1 - \exp(-S_j - \xi)] = 1 - \left(1 - (S_j + \xi) + \frac{(S_j + \xi)^2}{2!} + \cdots\right) \approx (S_j + \xi), \tag{3.27}$$

giving an approximation of P_j as

$$P_j \approx W_j(S, \xi, N_D)(S_j + \xi). \tag{3.28}$$

Equation 3.28 now shows a direct relationship between the detection probability and the signal count rate.

Figure 3.17 shows the results of Eq. 3.26, with contributions by W_j and S_{RX}. Modeling of the single-shot backscattered signal was performed utilizing the SVLE formulation introduced in Chapter 2. The sensor's transmitter and receiver parameters are listed in Table 3.1, which includes the actual parameters for the SPL sensor discussed in Chapter 5. The signal count rates were generated for assuming the sensor was zenith pointed with a 4 mm range resolution (27 ps timing resolution) and a bounding altitude equal to the instrument's unambiguous range of ~ 10.49 km. A 100 kHz Poisson noise source is assumed, re-sampled to the IPP of the laser at 4 mm bins. The case of randomly oriented particles and single scattering was assumed using the scattering matrix described in [21, 89] and combined with a clear air depolarization value of $\delta = 0.00365$. The NRLMSISE-00 atmospheric model [105] was used to generate height-dependent atmospheric density values, allowing for estimates of the volume backscatter coefficient and path extinction by molecular scattering. The simulation results were scaled by an optical efficiency factor in order to

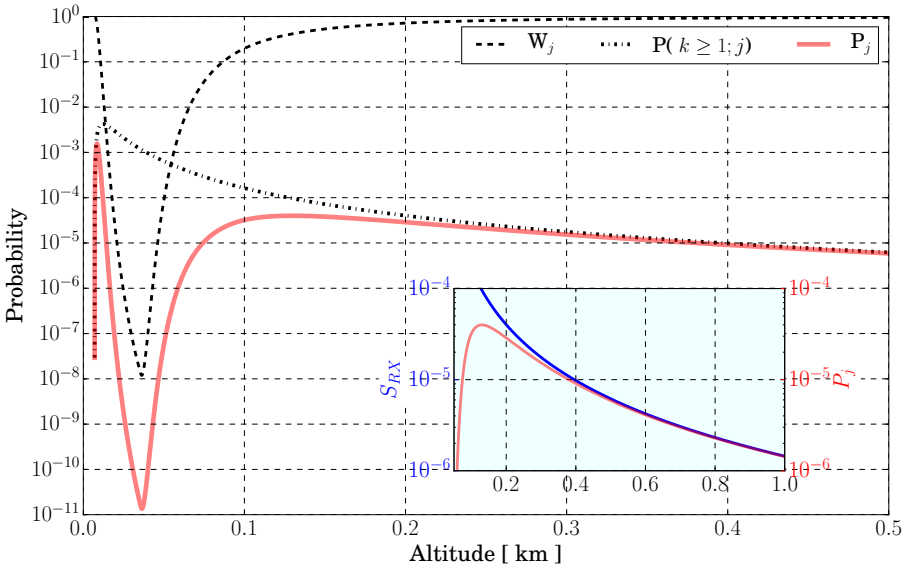

Figure 3.17: Simulated curves for the individual terms of Eq. 3.26. The dashed line shows the weighting function W_j - the null detection probability within N_D bins prior to the j_{th} bin, the dot dashed line shows the probability of one or more detections in the j_{th} bin, $P(k \geq 1, j)$, and the red line shows the combined probability P_j. The figure inset shows the effects of dead-time distortion by comparing the shape of P_j, red line, and S_{RX}, blue line.

match the actual values measured by the demonstration instrument to generate realistic single-shot probabilities.

Figure 3.17 demonstrates the interplay between backscattered signal strength, the $k = 0$ probability in the prior N_D bins, and the $k \geq 1$ probability in the j_{th} bin. High signal strengths in the lower atmosphere result in W_j being less than one, as there is a high probability of detecting a photon within prior N_D bins. As the backscattered intensity falls off with altitude, W_j increases to unity and the $k \geq 1$ probability for the j_{th} bin dominates P_j. The two curves are of opposite tendency, resulting in a peaking of the combined probability curve. The dead-time weighting function continues to contribute to the overall detection probability past this peak until it reaches unity. This behavior is similar, but distinct, from the description often attributed to the geometric overlap function of a monostatic lidar system.

The inset of Fig. 3.17 shows an overlay of the simulated signal, S_{RX}, and combined proba-

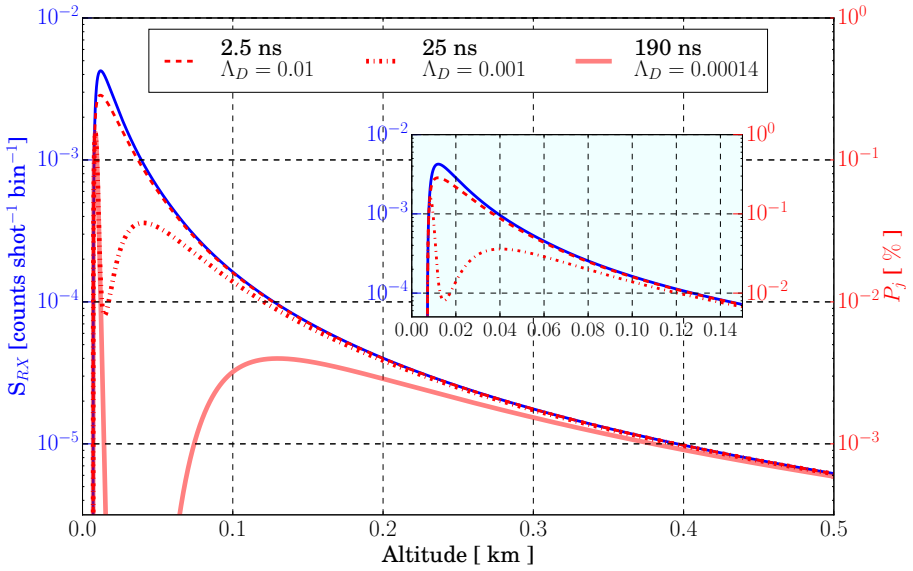

Figure 3.18: P_j curves simulated with Eq. 3.26 and varying the system dead-time with a fixed timing resolution of 27 ps. The signal term, S_{RX}, is shown in blue. The resulting P_j curves computed with different system dead-times of: 2.5 ns (dashed), 25 ns (dot-dashed), and 190 ns (solid), shown in red. The inset zooms in to the 2.5 and 25 ns curves at low altitude.

bility, P_j. The curves indicate that with a non-zero system dead-time, the shape of P_j will deviate from the incident signal count rate if $W_j < 1$, leading to intensity distortions. At lower altitudes, where count rates are high, the integrated intensity profiles are non-linear with backscattered signal. With the given relationship between the impinging photon rate and the acquired signal, signals outside of the linear regime can be recovered through non-linear fitting [102, 56]. The magnitude and extent of the intensity distortion directly depends on W_j.

Figure 3.18 shows Eq. 3.26 evaluated at 4 mm range resolution with different system dead-time values. As τ_d approaches zero, detectability of count rates increases, leading to a linear detectability across a larger altitude range, i.e. expanding the linear signal dynamic range of the sensor. Computing the percent deviation between the signal waveform and the combined probability shows that when assuming a large system dead-time (190 ns) the shape of P_j nears linearity to S_{RX} (within 1% error) at 1.0 km, whereas a shorter system dead-time of 2.5 ns (commercially available

from a number of vendors) nears linearity at 125 m. This improves linear signal dynamic range, and thus detectable backscattered photon rates, by nearly two orders of magnitude.

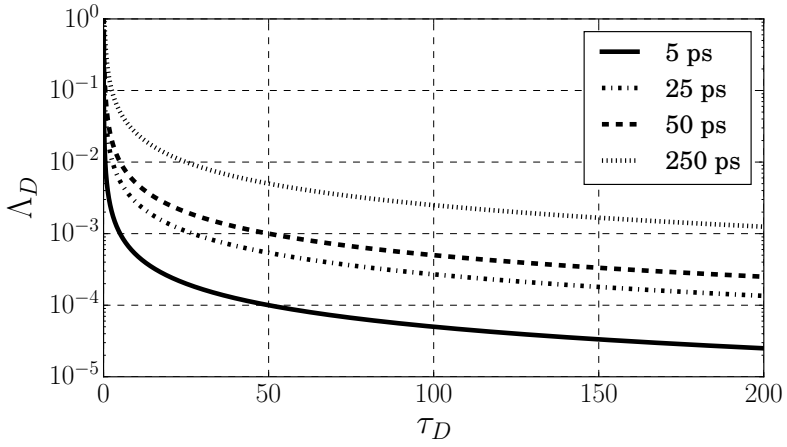

Figure 3.19: Calculated dead-time metric for a varying dead-time, in nanoseconds. Various bin resolutions are used to show what combination is advantageous for different acquisition configurations.

A figure of merit for signal dynamic range coverage can be defined as $\Lambda_D = 1/N_D = \tau_b/\tau_d$, which is the ratio of timing resolution to system dead-time. For a fixed bin width, Λ_D increases as system dead-time is decreased, thus maximizing W_j at a lower measurement altitude and effectively improving the linear signal dynamic range. A short system dead-time with high timing resolution is the most desirable, but not always achievable with current TCSPC acquisition units. Often, a short system dead-time is accompanied by poorer timing resolution. This simple relation can facilitate assessing trade-offs between covering a large signal dynamic range with reduced range resolution or achieving high range resolution, but over a smaller signal dynamic range. With an appropriate value of Λ_D, as shown in Fig. 3.19, a given set of instrument parameters can be tuned to generate accurately modeled signal strengths that account for P_j. This provides realistic detectability estimates and defines signal dynamic range limits that adequately suit the measurement requirements.

3.3.1 Atmospheric Photon Time-Tagging Observations

Photon time-tagging hardware has been incorporated into an MCS based SPL sensor to demonstrate the applicability of this technique for advancing atmospheric lidar applications. System parameters of the demonstration sensor are summarized in Table 3.1 with the FWHM of the IRF measured at 550 ps, or 8.25 cm in range. The laser's temporal width dominates the IRF for this PMT/CFD/TDC setup, causing the TDC resolution to be smaller than the IRF/target response function. Therefore, interpretation of the target at the TDC's millimeter range resolution cannot be realized unless the IRF is deconvolved from the signal waveform, or it is accepted that there is an uncertainty to each singular photo event that is equivalent to the IRF.

Initial tests were performed using independent CFD/TDCs for each start/stop channel, with 190 ns dead-time per channel. A master clock synchronized the channels and the TCSPC module was configured with 27 ps timing resolution, 4 mm, continuously streaming all channels to the host computer. Photon detections from each receiver channel were correlated to the correct laser firing assuming all detections come from the first unambiguous range (a reasonable assumption for low average power systems profiling the troposphere with no high clouds, such as cirrus, during testing). Long term drift of the master clock is unimportant, as only relative timing between laser firing and photon event are needed. The resulting data produce a real-time point cloud of photon TOF values for every photon event, with co-registered experiment detection time at 27 ps resolution.

Figure 3.20 illustrates an integrated signal profile generated by the lidar described in Table 3.1 and implementing photon time-tagging acquisition. These data represent backscattered signals received in the co-polarized channel by the zenith-directed configuration from atmospheric molecular and particulate scattering. Total counts are displayed against altitude over a ten second period with 4 mm acquisition range bins spatially integrated to 12 mm (Panel A) and 1 m (Panel B). The data profiles in panels A and B indicate decreasing volume scattering with altitude due to the exponential decrease in the density of molecular scattering and the inverse squared range dependence of volume scattering. The summing of counts over a larger bin width (by a factor of

Table 3.1: Summary of demonstration lidar system parameters

Environmental Parameter	**Value**
Wavelength	532 nm
Laser Repetition Rate	14.3 kHz
Laser Pulse-Width	< 500 ps
Laser Output Energy	2.45 μJ
Transmitter Divergence	2 mrad
Transmitter Polarization	$> 99\%$ Linear Vertical
Telescope Diameter	90 mm
Receiver Field of View	2 mrad
Receiver Filter Bandwidth	300 pm FWHM
Receiver Detectors	40% QE, 280 ps TTS
Data Acquisition Dead-Time	190 ns
Minimum Acquisition Range Resolution	4 mm
Instrument Response Function	550 ps
System Dead-Time Metric (Λ_D)	0.00014

100) in Panel B improves the estimate of mean counts within a bin by the square root of the total counts within that bin while sacrificing range resolution.

There remain challenges with photon time-tagging acquisition that were discussed in the previous section - notably the effects of non-registered photon events due to system dead-time as a function of count rate. Panel C of Fig. 3.20 illustrates the simulated P_j curve using the system parameters given in Table 3.1, a geometric overlap function, and simulated count rates determined from panels A and B. Panel C describes many of the features observed in the measurements. At low altitudes the ideal counts are high, but the observed counts are low due to the probability of having a detection prior to the observing bin - W_j being much less than one. Full geometric overlap occurs relatively quickly, at 30 m, leaving deviations of observed counts to ideal counts above this altitude due solely to system dead-time effects. The simulated near ground spiked feature is evidence of this fact and it is also observed in the data, where geometric overlap and system dead-time simultaneously influence the probability curve. This feature marks the location where the decreasing backscatter signal and the fraction of transmitter/receiver geometric overlap produces signal behavior that is low and only weakly influenced by W_j. This condition is eliminated quickly as the geometric overlap increases the signal count rate and, consequently, a rapidly decreasing W_j

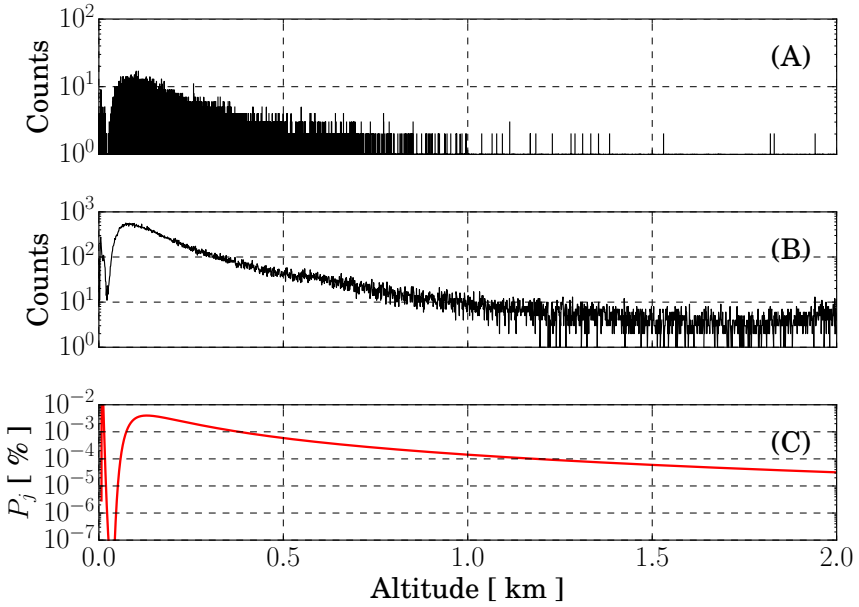

Figure 3.20: Intensity profiles integrated from 10 s of raw atmospheric point cloud data at 12 mm (panel A) and 1 m (panel B) range resolution. Panel C shows the computed P_j from Fig. 3.17 using the instrument parameters in Table 1.

reduces the probability of detection. According to the simulation, the weighting factor approaches unity before 1 km altitude. Thus, for altitudes below 1 km the signal intensity is distorted by the system dead-time. Per Fig. 3.18, reducing the system dead-time and degrading timing resolution are means to reduce distortion, resulting in a greater linear signal dynamic range and constraining systematic effects to lower altitudes.

The power of post-acquisition binning of photon events can be seen in Fig. 3.21, where five different spatial integration schemes were chosen. The several cloud features shown between 2.7-3.2 km vary in their small scale structures, which are sharp at smaller bin resolutions but smoothed at larger bin resolutions. Figure 3.21 shows the necessity for allowing sharp features to be defined by the scale needed to accurately depict their variability instead of a scale that is defined by the hardware limitations imposed prior to the measurement was generated.

Figure 3.22 illustrates the agility of the system where signals from different scatterers can be

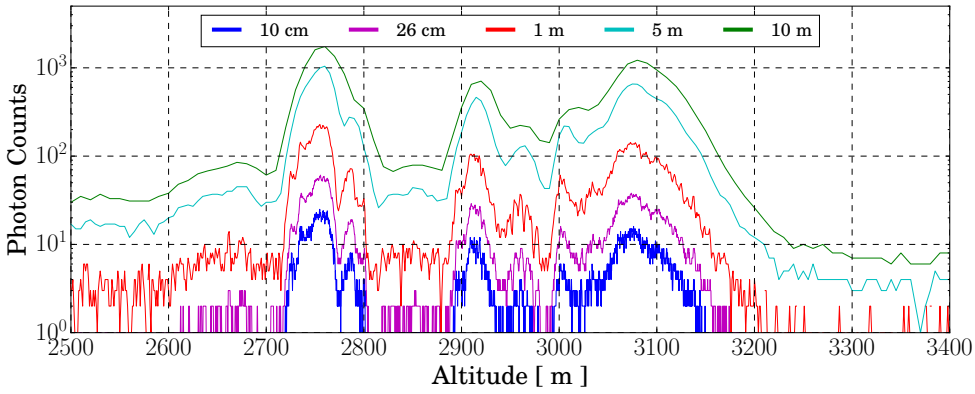

Figure 3.21: Different post processed profiles for the same 10 second set of time-tags. The profiles are not background subtracted and have a smoothing function of three bins to reduce noise variations. Most notable is the loss of fine scale structure for the 5 and 10 m bin resolutions

handled separately in post processing to achieve the temporal/spatial resolutions and parameter accuracy required for that particular investigation. Molecular scattering can be coarse and slow in evolution, while cloud dynamics can be fine and rapid. Both aspects can be studied by independently using a variety of post processing methods. Figure 3.22 shows the results for a simple SNR based dynamic binning process, where a feature threshold of SNR ≥ 3 for signals beyond 1 km, was used to select bin widths. The resulting integrated profile gives 2 m bins from 1-2.7 km, where individual diffuse aerosol scattering layers can be seen at 2, 2.3, and 2.6 km. From 2.7-3.3 km, the profile structure increases bin resolution to 26 cm, capturing the sharp cloud returns. Performing dynamic signal evaluations in post processing relies on the capability to record data at the highest resolution possible, every photon event per laser firing at the full TDC timing resolution. The demonstrated method provides equivalent raw data to a typical MCS acquisition, but at 14.3 kHz and 4 mm resolution. This type of collection, per laser firing, may not be feasible for lidars utilizing MCS acquisition. Every bin within the laser's unambiguous range would be a memory location, and data recorded (zero or non-zero) over a large range ($\sim$ 10.49 km) at high resolution (4 mm) would require unfeasible memory capacity and data transfer rates.

With a more complete understanding of the photon time-tagging approach, the augmented

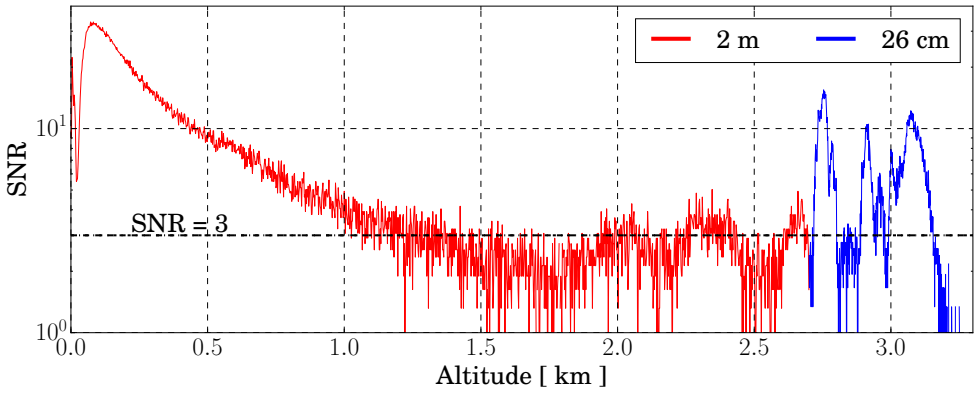

Figure 3.22: Dynamically integrated intensity profile using a SNR≥3 feature filter, the labeled dot-dashed line, over 10 s of photon events. The aerosol features present from 1.5-2.7 km are extracted using a 2 m bin width, and the sharp cloud features from 2.7-3.3 km are extracted using a 26 cm bin width. Background signal, ξ, was computed as a geometric mean between 4-5 km.

lidar was directed vertically to acquire atmospheric backscattered signals over several hours. The profiles shown in Fig. 3.20 were integrated from the post-processing of singular photon time-tags. Figure 3.23 illustrates the backscattered signals over time and altitude without any post processing. These data are atmospheric point clouds where every photon was assigned a time-tag with 27 ps resolution. The increased density of photons (darker shade of gray) indicates higher count rates due to greater scattering efficiency - either an increase in cross section of the scatterers, a greater concentration of the same scatterers, or both.

The point clouds show the ability of the detection scheme to acquire photon events at high temporal and spatial resolutions and to capture the measurement scene dynamics. In the atmospheric point cloud, features and transitions are seen as clusters of dense returns. The backscattered signal demonstrates variability consistent with molecular, aerosol, and cloud particle scattering. The low-altitude, high-density signal is largely due to molecular scattering at close range. The band of high-density points between 2 and 3.3 km demonstrate strong and frequent photons from the base and interior of clouds. The cutoff of signal above the cloud is due to extinction of the laser energy. Diffuse scatterers with significant variability are also observed in Figs. 3.23 and 3.24,

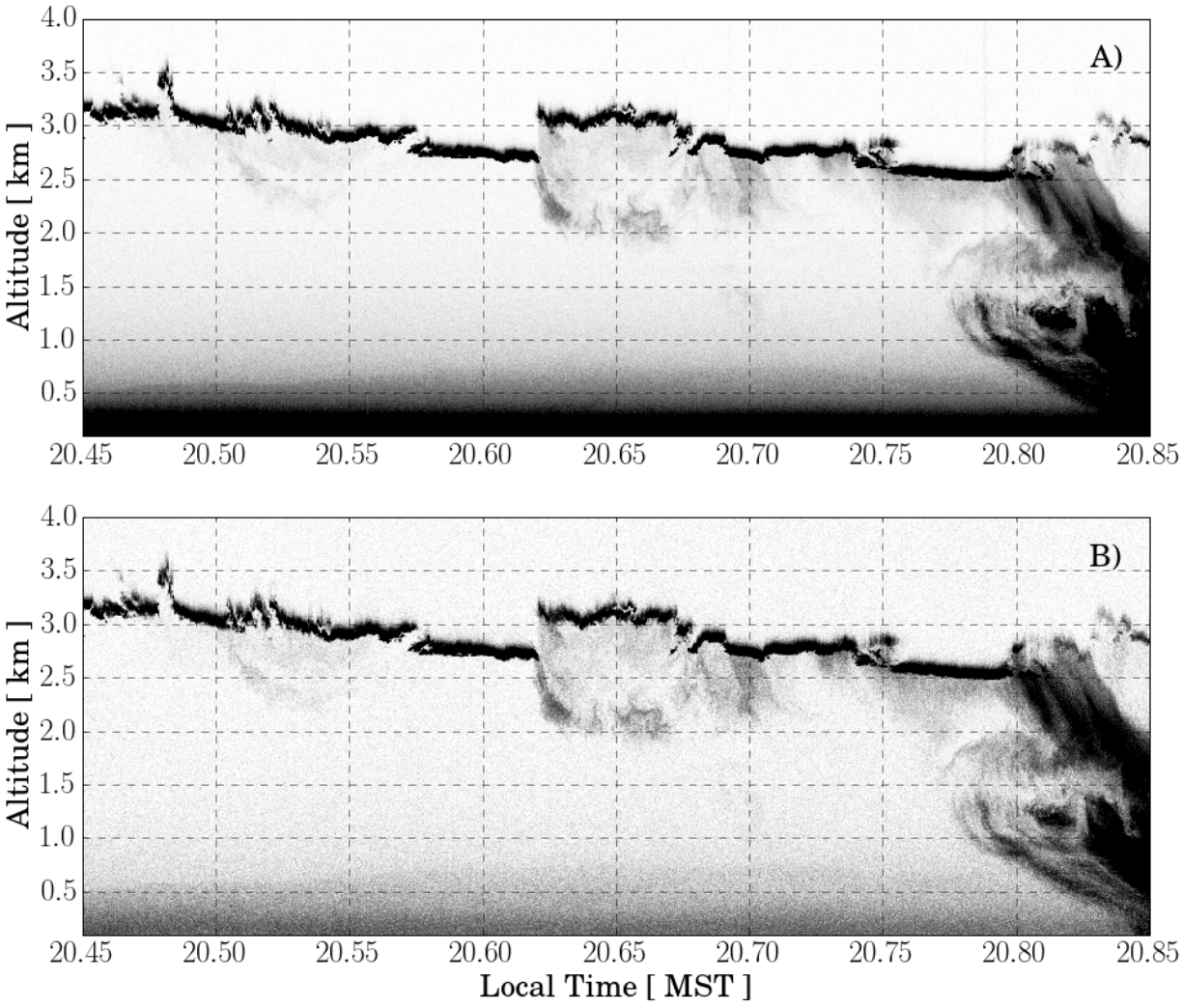

Figure 3.23: Time-correlated portion of the collected atmospheric point cloud for the co-polarized, panel A), and cross-polarized, B), receiver channels. Each photon was correlated to the associated laser firing at the full 27 ps resolution of the TDC and plotted as computed range versus collection time. The atmospheric density gradient and dense locations of returns indicative of highly reflective cloud structures and rainfall are evident. In both polarizations, a boundary layer enhancement can be seen starting at 500 m at 20.45 MST and reaching 750 m from 20.65 MST and on-wards, this is likely due to diurnal variations expected in the boundary layer of a mildly polluted city environment.

possibly representing evaporating rain (virga) or actual rainfall at the end of observations. Figure 3.25 shows a subset of Fig. 3.24, where the cloud base and other tenuous features are seen at high resolution.

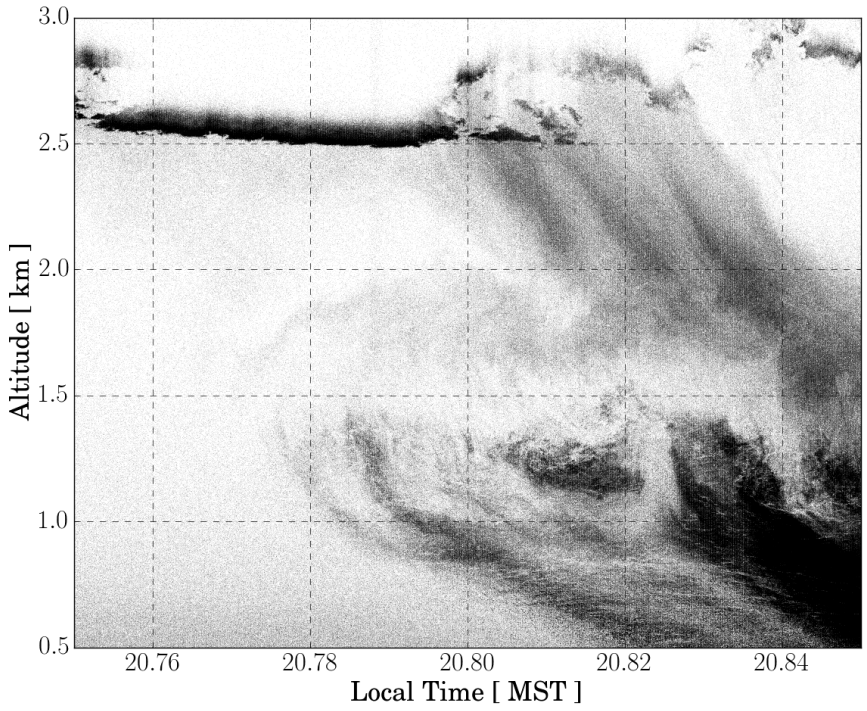

Figure 3.24: Subset of Fig. 3.23 panel A), showing zoomed in features in the co-polarized channel that represent dense structure among the Poisson distributed noise field. The data also shows what could be virga and the beginning of rainfall.

Figure 3.24 shows the ability to detect density changes in diffuse and sharp atmospheric features among the randomly Poisson-distributed noise field. A single co-polarized plane was used for analysis. In the case of systems employing a cross-polarization receiver channel for depolarization estimates, the crossed polarization planes will experience different time evolving count rates, typically with co-polarized producing higher count rates than cross-polarized [116]. This results in a channel dependent W_j and P_j. However, time-tagging systems handle both regimes, as system dead-times (including detector) exist within each channel independently, not across channels, allowing cross-correlations between channels within the system dead-time [121]. Challenges arise

when analyzing the signals together, often in the form of a ratio to determine scatterer-induced signal depolarization. Systematic effects can significantly impact signal depolarization [1, 49, 29] and such effects require careful evaluation of signal behavior. Here, the signals can be evaluated in the context of the W_j and the prior statistical analysis.

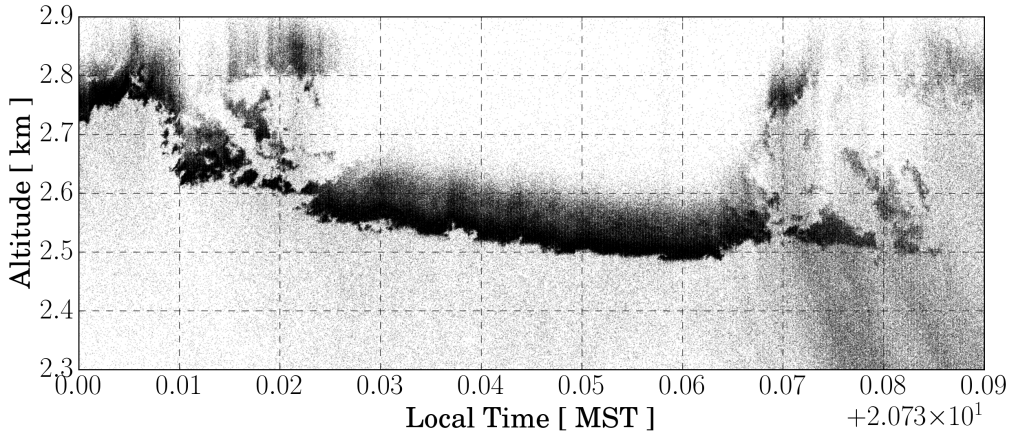

Figure 3.25: Subset of Fig. 3.24, showing zoomed in features in the co-polarized channel. The data also shows the small scale features present at the base of clouds.

Scientific retrievals typically rely on inversions of integrated backscatter, requiring further processing of the atmospheric point cloud. Standard techniques employ histogram generation at bin sizes greater or equal to the TDC resolution, typically driven by the desired SNR. Binning is performed over a selectable number of laser firings, allowing single-shot profile generation to any multiple of the instrument's IPP. This method allows a dynamic approach to generating time series of photon detections, where the number of laser firings integrated and the desired timing resolution can be approached in a manner that best suits the science retrievals pursued. Performing an optimum search for the time and range integration scheme is then driven by the the ability to resolve features, providing agility in the final product. Thus, photon time-tagging provides more flexibility over traditional MCS. Limitations on resolution are driven by the Nyquist criterion, where the oversampling of the signal waveform is bounded by the temporal structure of the IRF.

To demonstrate the applicability of the atmospheric point cloud for intensity based retrievals,

the data window in Fig. 3.23 was binned to 10 m vertical spatial and 10 s temporal resolutions using the methods discussed. The resolution choice was driven by the need for high SNR, 20 or above was chosen, to ensure that retrieval algorithms converged. The individual profiles were background subtracted and passed through a speckle filter to reduce the noise field. The normalized backscatter ratio was calculated using the Klett inversion technique [66]. A combination of the specific implemented methods can be seen in [116], and were employed here with the help of Dr. Stillwell. The backscatter ratio is defined as [117]

$$R = \frac{\beta_{tot}}{\beta_{mol}} = \frac{\beta_{aer} + \beta_{mol}}{\beta_{mol}}, \tag{3.29}$$

where β_{aer} is the contribution to the total backscattering coefficient due to aerosols, and β_{mol} is the contribution due to molecular scattering. When the detected backscattered signal is solely due to the presence of molecular scatterers, Eq. 3.29 minimizes to one. Any contributions due to aerosols or other scatterers increase the ratio to a number greater than unity.

The results for the retrieved normalized backscatter ratio are shown in Figs. 3.26 and 3.27. It should be noted that cloud tops showing a low backscatter ratio are not physical, but rather an artifact of the Klett inversion used to calculate backscatter ratio and imperfect tuning of the estimation process. Emphasis was not put on tuning, but on the overall ability to perform the estimates.

Several of the macroscopic structures present in Figs. 3.23 and 3.24 (note that the time scales are not equal between the two figures) were captured in the binning and retrieval processes, shown in Fig. 3.26. An extracted vertical profile of the backscatter ratio is shown in Fig. 3.27, demonstrating that high variability is still present even at decreased resolutions.

Depolarization, $d(R)$, was calculated according to [116] by inverting the the SVLE with an assumed scattering matrix $F(R)$. The most general form of the depolarization expression, assuming that the outgoing polarization is not fully linear and there is some ellipticity (often possible due to no perfectly coated steering mirrors or transmit window), is given as [45]

$$d(R) = \frac{4N_{\perp}(R)}{(N_{\perp}(R) + N_{\parallel}(R))(3 - \cos(4\chi))}. \tag{3.30}$$

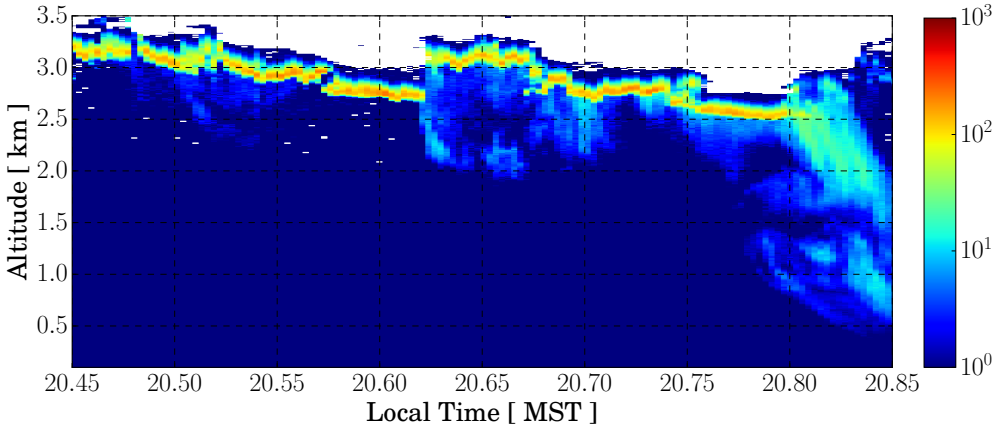

Figure 3.26: Retrieved normalized backscatter ratio, computed according to [66, 116], from the atmospheric point cloud shown in Fig. 3.23. White areas above 3 km are locations where the integrated signal fell below the SNR threshold for the retrieval algorithm.

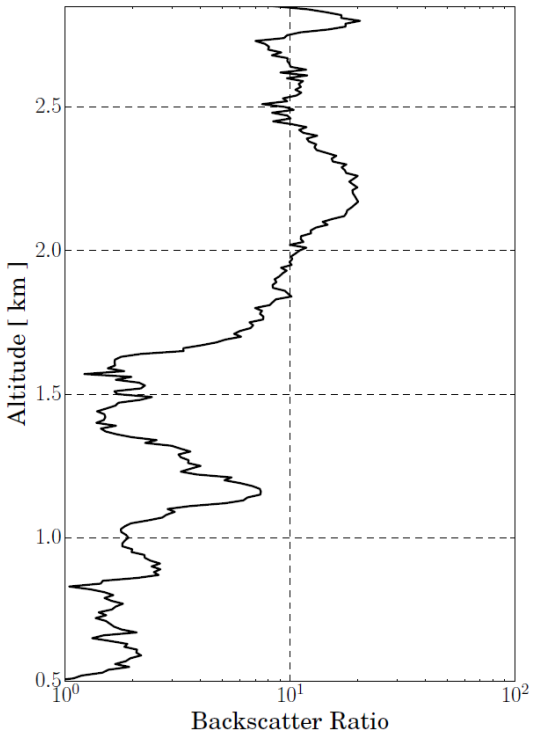

Figure 3.27: A single profile of the retrieved normalized backscatter ratio take at 20.81 MST from Fig. 3.26. The profile is generated over 10 s with 10 m bins to provide the correct SNR retrievals, but structure is still present.

Assuming that there is no retardance, $\chi = 0$, or diattenuation introduced in the scattering process or in the transmit/receive optical paths, the depolarization can be reduced to [34]

$$d(R) = \frac{2N_{\perp}(R)}{N_{\perp}(R) + N_{\parallel}(R)}. \tag{3.31}$$

The depolarization estimate can then be converted to the legacy depolarization parameter using

$$\delta(R) = \frac{d(R)}{2 - d(R)}. \tag{3.32}$$

Because of the dual receiver channel approach, calibration was necessary to set the relative gain differences between the two channels. This includes accounting for differing path efficiencies, and in the case of the sensor discussed here, accounting for the respective gain of each PMT. Calibration for the receiver channels was done according to the [1], modified to include a rotating half wave plate (HWP) installed at the output of the transmitter, and performed with data collected from a hard scattering target. The sensor generated measurements of backscattered signal from a cinder block target at a 5 meter stand off distance, and the transmit power was brought down several orders of magnitude with neutral density filters to maintain linearity in the received signals. Backscattered light was collected at 2 degree increments of the HWP for 10 seconds each. The time-tags were filtered for noise outside of the expected target range, histogrammed with 1 cm bins, and Gaussian fit to integrate the total target counts under the curve for a power estimate.

A measured depolarization value was computed from the integrated counts shown in Fig. 3.28. The points on the curve, along with the half wave plate orientation, allowed a non-linear least squares regression. From this the gain ratio between the receiver channels and the angular offset between the transmitter and receiver polarizations was extracted. This was performed with

$$m_j(R) = G\left\{\frac{\delta(R) + \tan^2[2(\theta + \phi_j)]}{1 + \delta(R)\tan^2[2(\theta + \phi_j)]}\right\}, \tag{3.33}$$

where $m_j(R)$ is the measured depolarization value from the integrated histograms, and ϕ_j is the orientation of the HWP. The scaling equation, inverted from Eq. 3.33, is then

$$\delta = \frac{m_j/G - \tan^2(2\theta)}{1 - m_j/G\tan^2(2\theta)}. \tag{3.34}$$

A non-linear Levenberg-Marquardt fitting routine was used to fit Eq. 3.33 to the measured data, shown as the solid line in Fig. 3.28. In this routine, the measured depolarization ratio and the HWP orientation are the known parameters and the rest are estimated.

The fitted parameters extracted from the curve shown in 3.28 provide the terms for correcting the measured depolarization with Eq. 3.34, and are:

$$\begin{gathered} \text{Gain Ratio} = 1.885 \\ \text{Polarization Offset Angle} = 1.9^\circ \\ \text{Retrieved } \delta = 33.7\% \end{gathered} \tag{3.35}$$

The retrieved depolarization profiles were corrected with the calibration terms and the full time series is shown in Fig. 3.29. The clear air retrievals is within the limitations of the receiver system, namely at a few percent, and several features match the expected values, such as the high depolarization due to multiple scattering within the cloud structures.

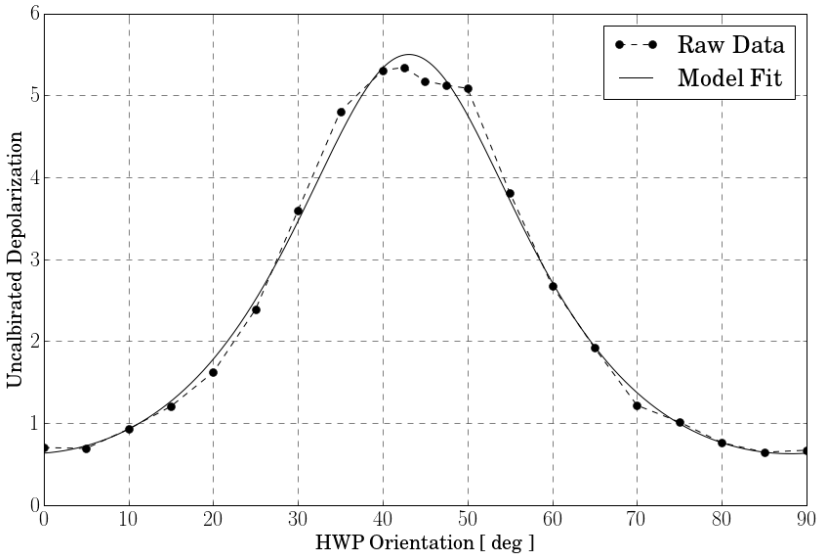

Figure 3.28: The measured and fitted depolarization ratios as a function of the HWP rotation angle. The estimated gain ratio, offset angle, and the retrieved depolarization ratio of the target are $G = 1.885$, $\theta = 1.9^\circ$, and $\delta = 33.7\%$.

Figure 3.30 shows the distribution of retrieved and corrected depolarization values for the area bounded between 20.45-20.75 MST and 0-2 km. This is a distinct peak around $\delta = 8\%$,

indicating that there are scatterers with a low magnitude of backscatter but which have a small amount of depolarization that can be attributed to them. These scatterers are not visible in Fig. 3.26 due to the speckle and SNR filtering process, but are clearly present in Fig. 3.23, where a heightened backscattering layer is seen in the first 1 km of the time series and in several pockets of heightened backscattering around 1.5 km.

In a desire to achieve the correct SNR needed for the inversion techniques, spatial and temporal ambiguities are introduced to the final output produced. In fact, many of the finer structures shown in Figs. 3.23 and 3.24 are no longer present in Figs. 3.26 and 3.29. These traditional processing techniques serve to significantly decrease the resolution of the photon time-tagging technique, opening opportunities for algorithm development and applications that exploit the full utility of the technique. The demonstrated sensor did not operate with an SNR properly matched to the desired retrievals, but future iterations would allow higher collection efficiencies, which in turn allow higher SNR at finer resolutions.

Multiple techniques have been developed to estimate clustered target densities, not emphasizing simultaneous intensity retrievals, among Poisson noise fields [52]. Methods to extract features from noise in photon limited data, utilizing traditional histogram approaches for binning structure, have been successful with the optimal estimation approach [78, 46]. However, the high resolution atmospheric point cloud opens the possibility for applying vetted image processing techniques that can maximize the usefulness of the temporal and spatial resolutions. Photon limited non-parametric Poisson intensity and density estimations have been shown in [124], and [44] show promising results in reconstructing scenes using Poisson likelihood estimators. Leveraging the known Poissonian nature of photon counting lidar and the time-tagging technique, these methods provide alternative approaches, with enhanced flexibility, to working with atmospheric point clouds. Initial investigation of these methods has been performed and shown to be viable for the photon time-tagging techniques in this work.

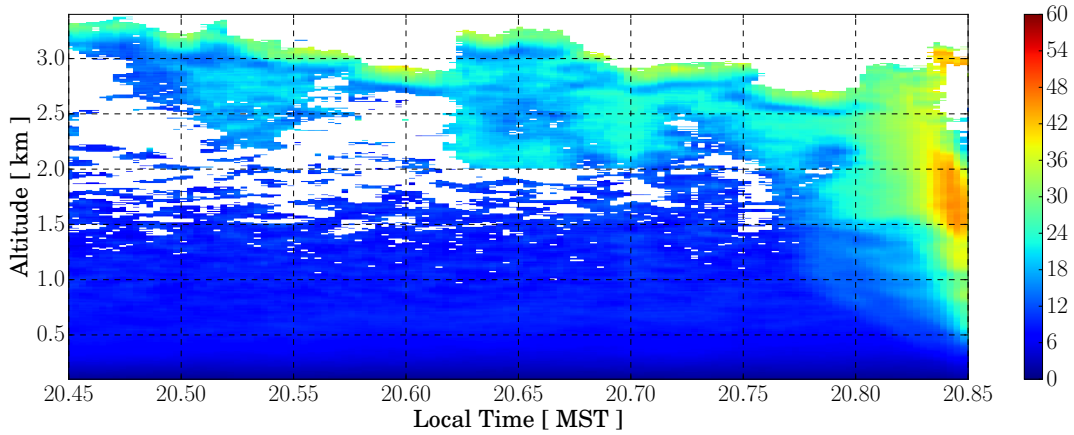

Figure 3.29: The corrected depolarization time series for the time-tags shown in Fig. 3.23, integrated spatially and temporally to 10 m and 10 s, respectively.

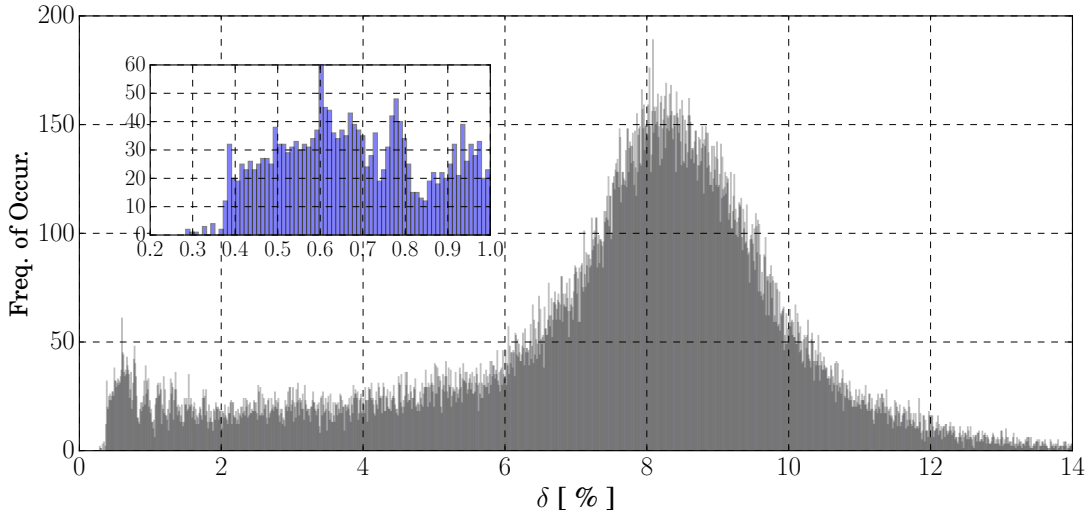

Figure 3.30: The computed distribution of retrieved and corrected depolarization values in Fig. 3.29 filtered between 20.45-20.75 and 0-2 km.

3.4 Relevance to Posed Thesis Questions

Implementation of the photon time-tagging technique provides an efficient method to acquire photon events, with the advantages of generating detections per laser firing at picosecond timing resolution throughout the atmospheric column. The resulting data are an atmospheric point cloud in time and range, capable of revealing fine-scale features and enabling dynamic integration. This capability can prove favorable for measurement scenarios with limited time on target due to relative platform motion, such as aircraft and spacecraft observations. Low data rate demands, because of the sparse nature of single-shot photon counting data, are also conducive to situations where high bandwidth telemetry is not possible. Furthermore, nadir viewing airborne and spaceborne lidar systems often capture both atmosphere as well as land and ocean backscattered returns [125, 55]. Acquisition system flexibility would allow for such diverse scattering scenarios to be fully captured and post-processed for multi-functional retrievals requiring dynamic resolutions.

Several attributes of a photon time-tagging lidar for atmospheric applications that differ from typical atmospheric lidar systems were presented. Acquisition dead-time is an important parameter that can affect signal behavior in high count rate domains - such as those that occur at low-altitude or in backscattered cloud signals. A ratio of acquisition timing resolution to dead-time was shown as a reasonable metric for optimizing a system's linear signal dynamic range. The discussed technique significantly reduces the IRF, which is largely driven by the laser pulse-width and the detector's timing jitter. The detected signal waveform is then a convolution between the IRF and the uniform spread of the atmospheric scatterers over the pulse width. Thus, backscattered signals recorded with picosecond timing cannot be considered independent until integration to the IRF width has been reached — approximately 550 ps for the sensor discussed here. In this situation, a decrease in timing resolution can be afforded if the system dead-time is also reduced.

The reduction of system dead-time also reduces FPB effects. For hard target sensing the impact of FPB can be significant. For SPL sensors that are targeting atmospheric measurements, prominent peaks in the histograms are likely generated by photon events backscattered by sharp

features, such as cloud edges. It is also likely that the reduction of system dead-time does not explicitly solve the FPB challenge until the temporal profile of the target exceeds that of τ_d. However, the challenge can be overlooked if the width of the histogram bins are larger than the expected FPB range bias. This ensures that the shifting of counts to earlier times is fully contained within a single bin and not cross bin edges.

This chapter served to introduce some of the challenges that are present when implementing the photon time-tagging technique in a multi-functional measurement, where dead-time can be seen to impact different parts of the measurement profile in different manners. The work in this chapter served to answer the posed thesis questions in the following ways:

(1) What are the implications of utilizing the time-correlated single photon counting approach for geophysical parameter estimation from volume scattering environments?

- The results shown in Section 3.3.1 showed novel applications of an SPL sensor utilizing TCSPC for atmospheric monitoring. This resulted in the concept of the atmospheric point cloud, which provides an alternative method by which high resolution atmospheric data can acquired, viewed, and analyzed. Utilizing TCSPC and time-tagging every photon event in a semi-porous medium emphasizes a sensor's recovery time and its ability to detect subsequent returns from the extended medium. Dead-time was shown to govern detectability, linearity, and dynamic range for atmospheric measurements. A stochastic dead-time model was generated and validated, showing that the atmospheric profile's response to dead-time can be understood and removed to perform scientific retrievals. These results were published by Barton-Grimley et. al. in "High resolution photon time-tagging lidar for atmospheric point cloud generation" [5], providing the first documented application of TCSPC to the atmosphere.

(2) How are estimates of backscattered photon rate and target range affected by the implementation of the photon time-tagging approach?

- The data, analysis, and MC results presented in Section 3.2 document the effects that result from deviating an SPL sensor out of single photon counting. The analysis indicated that FPB introduces non-linearity to the retrieved data, altering estimates of backscattered photon rate and range. The FPB term in Eq. 3.12 serves to bring the count rate to a steady-state value, where a detection is made per laser firing and the total count rate is equal to the laser's PRF, and the target's range becomes biased such that estimates are no longer made over the full IRF but are instead constrained to the leading edge of the laser pulse. Implementation of TCSPC and time-tagging each received photon directly causes these effects, therefore dead-time introduce conditions to the measurement that must be considered. These results were published by Barton-Grimley *et al.* in "Nonlinear target count rate estimation in single-photon lidar due to first photon bias" [6], providing documentation of FPB and resulting effects..

(3) Can polarimetric lidar incorporate time-correlated single photon counting, and what are the implications to high resolution multi-functional measurements of atmosphere, ocean, and hard targets?

- Section 3.3.1 showed the applicability of SPL sensors utilizing TCSPC to generate data for atmospheric science. Cross-polarized receiver channels were employed to acquire atmospheric depolarization, which was subsequently calibrated and used for estimating differing depolarization regions. The co-polarized channel was utilized to calculate the backscatter ratio, an estimate of aerosol to molecular backscattering. These were published by Barton-Grimley *et al.* in "High resolution photon time-tagging lidar for atmospheric point cloud generation" [5]. Dead-time was shown contaminate receiver channels differently and induce retrieval distortions. With dead-time effects correctly modeled they can be either removed or avoided, implying that a polarimetric SPL employing TCSPC targeting topographic/bathymetric mapping can be applied with success for high resolution atmospheric science.

Chapter 4

Multi-Functional SPL Sensor Modeling

The primary goal of this chapter is to define the polarization and scattering equations, specific timing prescription, and other necessary information needed to accurately predict a polarization sensitive SPL sensor's system metrics, environmental response, and overall performance. The resulting combined measurement model provides the framework in which different permutations of sensor components can be evaluated for atmospheric, water surface, and hard target sensing performance in a single measurement profile as generated from a nadir viewing sensor. To correctly predict sensor performance a combination of deterministic and stochastic methods are combined that capture varying processes along the measurement path and the resulting impacts of operating on an airborne platform are also included. Fundamentals of the SPL measurement include the transmission of laser light through an attenuating medium, the collection of the backscattered photons from some scattering medium, optical analysis for polarization determination of the received light, detection and amplification, and conversion to an electrical signal that can be further analyzed in the analog or digital domains. Sampling of this electronic signal into discrete detected event times over many laser firings is then performed and provides a basis for statistical analysis.

4.1 Resolution Implications of Multi-Functional Operation

Some preliminary understanding of the SPL response to different measurement regimes is needed prior to a full discussion of the driving equations for a full multi-functional SPL model. The measurement resolution of an SPL sensor differs from traditional lidar sensors because of the time-

tagging procedures employed. A typical photon counting lidar sensor's resolution is comparable to the laser pulse width, such that detected photons can be assigned to distinct bins with the predominant source of uncertainty coming from the counting statistics. Picosecond sub-sampling of the received signal results in photons that are assigned resolutions less than the laser pulse width. The prior chapter showed that with higher resolution comes added uncertainty beyond shot noise, as many of the sensor's components exhibit uncertainties on scale with the TDC's resolution. It is necessary to document these resolution uncertainties.

An understanding of SPL resolutions, and how they can change within a single measurement, can come from a discussion of Fermat's theory of least time and its coupling with single photon measurements. The SPL measurement inherently is a least time measurement, where the arrival of target scattered photons is defined by the envelope width σ_{rx} and the photon that traversed the least time path will trigger the TDC. Multi-functional measurements require that this theory be considered and applied where necessary within the measurement column. Interactions of the sensor at the atmosphere-water boundary are a direct example of this.

Fermat's theory of least time can be directly applied to these retrieved photon time-tags. In the case of time-tags generated by water column scatter, or subsurface ground, this is occurs in two ways. First is the standard index of refraction correction which adjusts the range estimate for the associated time-tag, performed as a multiplicative factor this reduces the distance estimate according to the medium's index. The second, more subtle, application is to adjust the estimated time-tag's resolution when originating from a non-air index. Converting this to range is simple using $\Delta R = c\tau_b/2n$, where for air $n = 1$ and for water $n = n_w$. Considering an in air resolution of 4 mm the in water resolution (assuming ocean water with $n_w = 1.338$) is approximately 3.02 mm. The result is that bathymetric point clouds, or other mediums besides water that have a > 1 index, have increased resolution and decreased uncertainty compared to those in air. For multi-functional operation, this has unique implications. Considering time-tags originating from the atmosphere and water subsurface, the physics indicates that the sensor will have varying resolution throughout that column and careful consideration should be paid to retrievals in different regimes.

4.2 SVLE for Multi-Functional SPL Sensors

A specific formulation of the SVLE will be presented in this chapter to provide a single equation, derived from first principles, that captures the various components of the SPL sensor's measurement and can be evaluated for a "total column" measurement, including atmospheric, water surface, water column, and ground contributions.

The general form for the SVLE that is used throughout the measurement model is

$$\vec{N}_{rx} = \mathbf{OM}_{rx}\left[\kappa(R)\prod_{j}^{N}\mathbf{T}_j(k_s,R)\mathbf{F}(\lambda,k_i,k_s,R)\prod_{j}^{N}\mathbf{T}_j(k_i,R)\mathbf{M}_{tx}\vec{S}_{tx}+\vec{S}_B\right], \tag{4.1}$$

where many of the definitions have carried over from those shown in Chapter 2, and with added terms to compensate for the different measurement regimes that are typically seen in a multi-functional SPL sensor. This includes defining a matrix product operation in which N terms are combined to evaluate the total contribution to scattering or extinction. The term $\kappa(R)$ is defined to contain all relevant scalars to the particular scattering environment under consideration and also captures additional physics of the processes, such as energy loss to water column scattering, geometric factors, and transmission losses.

Previously, Polar Decomposition was introduced as a method by which Mueller matrices can be broken down into three basic components, specifically diattenuation, retardance, and depolarization [71]. For the remainder of this thesis, the contributions of diattenuation and retardance are considered a result of non-ideal instrument effects and the simplification is made that scatterers will not introduce diattenuation or ellipticity to the received Stokes vector. By making this assumption the addition of non-perfect polarizing elements in the optical path (such as a retarding aircraft window or a non-ideal HWP) can be considered, and their relative impacts to the received signals evaluated [48].

Furthermore, in this thesis the formal polarization descriptions are motivated primarily by the scientific applicability of a depolarization estimate and the realization that sensor design for depolarization estimates requires a dual channel approach with orthogonal polarization planes. Estimates of depolarization facilitate an SPL in providing classifications of atmospheric scatterers,

such as aerosol typing in [99], and the potential for hard target morphology by typing scattering surfaces, such as man-made object typing in [22]. Although these retrievals rely on a calibrated absolute depolarization estimate, in the void of a well calibrated sensor, a tremendous amount can be done with relative depolarization changes, such as discriminating between a polarization preserving water surface and subsequent depolarizing media. This is an indication of the utility of polarization insensitive SPL sensors, and will not be investigated further in this thesis.

A general Mueller matrix form to capture the partially depolarizing backscattering processes that SPL sensors observe is necessary. Whether the SPL is recording photon events from atmospheric, ground, or water scatterers, there is a high likelihood that there will be a partial depolarizing effect upon scattering. The most general form for a pure depolarizer with zero diattenuation or retardance is the diagonal Mueller matrix [71]

$$\mathbf{M}_{\Delta,g}(a,b,c) = \begin{bmatrix} 1 & 0 & 0 & 0 \\ 0 & a & 0 & 0 \\ 0 & 0 & b & 0 \\ 0 & 0 & 0 & c \end{bmatrix}, \quad |a|,|b|,|c| \leq 1, \tag{4.2}$$

where $1-|a|$, $1-|b|$, are $1-|c|$ are the depolarizing capability of the polarizer along the principal eigenvectors. This formulation also ignores any polarizance contributions, in which unpolarized light can be made polarized by the scatterer or by passage through an optic. Like most general formulations, this representation provides decent explanation but is limited in the applicability to measurements. Typically, scatterers can be viewed in two macroscopic ways, either ensembles that exhibit random orientation or preferentially orientation, such as oriented ice crystals in clouds [116]. For transmitted, linearly polarized light that is scattered by an ensemble of randomly oriented scatterers, chosen due to the likelihood of random orientation of particles in water, clouds, aerosols, and surface particulates, the partially depolarizing Mueller matrix that describes this process can

be defined as [89, 34]

$$\mathbf{M}_{\Delta}(d) = \begin{bmatrix} 1 & 0 & 0 & 0 \\ 0 & 1-d & 0 & 0 \\ 0 & 0 & d-1 & 0 \\ 0 & 0 & 0 & 2d-1 \end{bmatrix}, \tag{4.3}$$

where d is a measure of the propensity of the scatterer to depolarize the incident laser light. This can be seen when the linear horizontal/vertical response is set to be fully depolarizing and the $[2,2]$ matrix element gives a value of zero. Using this formulation for the depolarizing element of the scattering interaction a general expression for the backscattering coefficient $\mathbf{F}$ can be given as [28, 34, 49]

$$\begin{aligned} \mathbf{F}_{\pi}(\lambda, R) &= \beta(\lambda, R, \pi)\mathbf{M}_D\mathbf{M}_R\mathbf{M}_{\Delta}(d) \\ &= \beta(\lambda, R, \pi)\mathbf{I}\mathbf{M}_{\Delta}(d), \end{aligned} \tag{4.4}$$

where $\mathbf{M}_D\mathbf{M}_R$ have been replaced by the identity matrix $\mathbf{I}$ to show that introduction of diattenuation or retardance by the scatterer will be ignored (for the remainder of this thesis the identity matrix will also no longer be shown and assumed present). In this formulation, the $[1,1]$ matrix element is equal to the volumetric backscattering coefficient β, which describes the intensity of the backscatter. When considering the reflection from a water surface or scatter from a hard target, the β term in Eq. 4.4 is removed and the applicable scalar Fresnel term or reflection matrix is substituted.

With a general form for the backscattering matrix each scattering environment can be examined for how this term can be applied across the full measurement column. The remaining sections will introduce the necessary mathematics to evaluate the Eq. 4.1 by solving the matrix transmission products and introducing unique forms for $\mathbf{F}_{\pi}(\lambda, R)$ and $\kappa(R)$.

4.2.1 Atmospheric Equations

For single photon detections from the atmospheric column, it is necessary to consider the Rayleigh backscattering processes that contribute to the mean photon rate at the sensor. It should

be noted that with the SPL sensor discussed throughout this thesis, the atmospheric measurements will be constrained to observations of or in the troposphere. Specifically, in the case of measurements generated in the lower troposphere it is reasonable to define the volumetric backscatter and extinction coefficients as a linear combination of contributions from molecular and aerosol scattering, given as

$$\beta_{atm}(\lambda, R, \pi) = \beta_{mol}(\lambda, R, \pi) + \beta_{aer}(\lambda, R, \pi), \tag{4.5}$$

$$\alpha_{atm}(\lambda, R) = \alpha_{mol}(\lambda, R) + \alpha_{aer}(\lambda, R). \tag{4.6}$$

The molecular contributions to the backscattering coefficient as a function of the total volumetric scattering coefficient can be given as [13]

$$\beta_{mol}(\lambda, R, \pi) = \frac{\beta_T(R)}{4\pi} P(\theta = \pi), \tag{4.7}$$

where the scattering phase function is given as

$$P(\theta) = \frac{3}{4(1+2\gamma)} \left[(1+3\gamma) + (1-\gamma)\cos^2(\theta) \right], \tag{4.8}$$

which is a function of the clear air depolarization relationship parameter $\gamma = \delta_{mol}/(2-\delta_{mol})$. In this formulation, the total scattering coefficient can be generated as a function of the scattering phase function and as any angle θ and clear air depolarization parameter. Bucholtz *et al.* [13] give values for γ and δ_{mol} for different wavelengths of light allowing the scattering phase function to be estimated from near truth values. The inherent molecular Rayleigh depolarization arises from the anisotropy of the polarizability tensor. Throughout this analysis it is assumed that narrow band spectral filtering is employed in such a way that the contributions are due to the Cabannes line and not from rotational Raman lines.

It is the case that for the lower troposphere molecular and aerosol scattering dominate and absorption is low. Given that aerosols are highly forward scattering, it is reasonable to approximate the atmospheric backscatter coefficient as solely due to molecular scattering, $\beta_{atm} = \beta_{mol}$, and the extinction coefficient due to both molecular and aerosol contributions, $\alpha_{atm} = \alpha_{mol} + \alpha_{aer}$. For this

scenario, the backscatter coefficient can be given as a function of atmospheric height dependent temperature and pressure as [30]

$$\beta_{atm}(\lambda, R, \pi) = 2.938 \times 10^{-32} \frac{P(R)}{T(R)} \frac{1}{\lambda^{4.0117}}, \tag{4.9}$$

with the units of $[m^{-1}sr^{-1}]$. The wavelength dependency does not have the standard fourth power, indicating that in the conversion from number density to pressure and temperature a wavelength correction factor has been applied. This equation requires the input of a height dependent parameters, allowing further use of atmospheric models, such as the NRLMSISE-00 empirical model used in Chapter 3, to give geo-referenced estimates of pressure, temperature, and density from the ground through the troposphere at specific values of latitude and longitude.

The molecular portion of the extinction coefficient can be defined through the total volumetric scattering coefficient used in Eqs. 4.7 and 4.9

$$\alpha_{\lambda,mol} = \beta_T(R) = \frac{\beta_{mol}(R, \pi)4\pi}{P(\theta = \pi)}. \tag{4.10}$$

To generate the aerosol contribution to the along path extinction, the definitions in Measures [88] provide a compact and simple relation that is dependent on the visibility range and the incident laser light wavelength. This then gives the total extinction coefficient as

$$\alpha_{atm}(\lambda, R) = 1.5859 \times 10^{-33} \frac{P(R)}{T(R)} \frac{1}{\lambda^{4.0117}} + \frac{3.91 \times 10^{-3}}{R_v} \left\{ \frac{550}{\lambda} \right\}^{0.585 R_v^{1/3}}, \tag{4.11}$$

with units of [m^{-1}]. R_v is the daylight visibility range, which has typical values of 5 km for light haze and 10 km for very clear aerosol conditions. In Eq. 4.11, the scattering phase function has been solved at $\theta = \pi$ with an assumed clear air depolarization.

When the signal being considered originates from the atmospheric column between the the airborne SPL sensor, the transmission loss at any range R can be attributed solely to extinction caused by in column scattering and absorption, which is an integrated quantity resulting from the solution to the Lambert-Beer law. This gives a compact form for the transmission matrices in Eq. 4.1, where $N = 1$, that describes a one-way path loss as

$$\prod_j \mathbf{T}_j(k_{i,s}, R) = \mathbf{T}_{atm}(\lambda, R) = e^{-\int_0^R \alpha_{atm}(\lambda, R')dR'} \mathbf{I}, \tag{4.12}$$

where $\alpha_{atm}(\lambda, R)$ is computed with Eq. 4.11 and the column is integrated to the range bin in question. An assumption of single scattering is made such that the use of an identity matrix in the transmission definition implies that the extinction is polarization independent, and that all polarization altering processes are contained within the physics of backscattering interaction with the scatterer.

The Mueller matrix describing the atmospheric backscatter is comprised of a depolarizer, Eq. 4.3, and the molecular backscattering coefficient, Eq. 4.9. The complete form is given as

$$\mathbf{F}_{atm}(\pi, R) = \beta_{atm}(R, \pi)\mathbf{M}_{\Delta}, \tag{4.13}$$

which is a function of range, depolarization, wavelength, temperature, and pressure. Equation 4.13 exhibits the expected decay with atmospheric density and the clear air polarization dependence.

The applicable scalar factors are consistent with the definitions introduced in Chapter 2 as

$$\kappa_{atm}(R) = G(R)\frac{A}{R^2}\Delta R. \tag{4.14}$$

The equations in this section define a simplistic version of the atmospheric medium, where no aerosols, haze, or other additional scatterers contribute to the calculated backscattered signal. The resulting model is not therefore appropriate for estimating a SPL's cloud and aerosol detectability.

4.2.2 Water Surface Equations

The received Stokes vector from a water surface combines the prior atmospheric effects and reflection components that are generated as a result of the index of refraction change at the air-water interface, $n_{air}/n_w \neq 1$. This is an inherent use of Fermat's theory of least time through the implementation of Snell's law at the interface. In this case, the surface scattering at the interface can be interpreted as a combination of two effects: 1) the polarization dependent response as governed by Fresnel's equations, and 2) a partially depolarizing ensemble of scatterers on the surface that cause energy to be distributed into additional polarization planes. These equations can take into account the inherent depolarization due to the anisotropy of water molecules, which allows d to be

a linear combination of the inherent depolarization due to the molecules and the added depolarizing effect of added surface clutter.

The transmission integral applied to the water surface is estimated by the atmospheric extinction up to the water surface, as no other transmission losses have yet to occur, given as

$$\prod_j \mathbf{T}_j(k_{i,s}, R_{surf}) = e^{-\int_0^{R_{surf}} \alpha_{atm}(\lambda, R')dR'}\mathbf{I}, \tag{4.15}$$

which is equivalent to Eq. 4.11 but integrated from the platform over the entire atmospheric column.

The complexity of the water surface interaction is contained within the Mueller matrix $\mathbf{F}_{surf}$, which captures the polarization dependencies in the reflection process. This scattering matrix is given as

$$\mathbf{F}_{surf} = \mathbf{M}_{\Delta}(d)\mathbf{R}(\theta_i, n_w), \tag{4.16}$$

where $\mathbf{M}_{\Delta}$ is used for the presence of non-spherical, randomly oriented scatterers for simplicity. Equation 4.2 could be used with the appropriate values of a, b, c, but a direct link between the inherent anisotropy of the water molecules and its depolarizing effect can be captured by d and was found to be appropriate for this computation. The Mueller matrix, $\mathbf{R}(\theta_i, n_w)$, contains the Fresnel dependent reflection coefficients, given as [64, 63]

$$\mathbf{R}(\theta_i, n_w) = \begin{bmatrix} \alpha+\eta & \alpha-\eta & 0 & 0 \\ \alpha-\eta & \alpha+\eta & 0 & 0 \\ 0 & 0 & \gamma_{Re} & -\gamma_{Im} \\ 0 & 0 & \gamma_{Im} & \gamma_{Re} \end{bmatrix}, \tag{4.17}$$

where for $\theta_i < \theta_{crit} \approx 48°$, and the following equations are used to compute the coefficients $\alpha(\theta_i, \theta_t), \eta(\theta_i, \theta_t), \gamma(\theta_i, \theta_t)$ as

$$\alpha = 0.5\left[\frac{\tan(\theta_i - \theta_t)}{\tan(\theta_i + \theta_t)}\right]^2, \tag{4.18}$$

$$\eta = 0.5\left[\frac{\sin(\theta_i - \theta_t)}{\sin(\theta_i + \theta_t)}\right]^2, \tag{4.19}$$

$$\gamma_{Re} = -\frac{\tan(\theta_i - \theta_t)\sin(\theta_i - \theta_t)}{\tan(\theta_i + \theta_t)\sin(\theta_i + \theta_t)}, \tag{4.20}$$

$$\gamma_{Im} = 0. \tag{4.21}$$

When $\theta_i > \theta_{crit}$, $\gamma_{Im} \neq 0$ and complex form of γ must be used [63], but as the SPL sensor discussed throughout this thesis is approximately nadir pointing and the incident angle with the ocean surface, considering the aircraft's angle of attack, can be assumed to be less than the critical angle so as to reduce the complicated surface interaction and introduction of imaginaries. Here θ_t is solved for through Snell's law. The angular response to the F_{11}, F_{12}, F_{33} terms are shown as a function of the incidence angle in Fig. 4.1. The F_{11} and F_{12} terms shown in Fig. 4.1 are the standard Fresnel equations for water surface interaction.

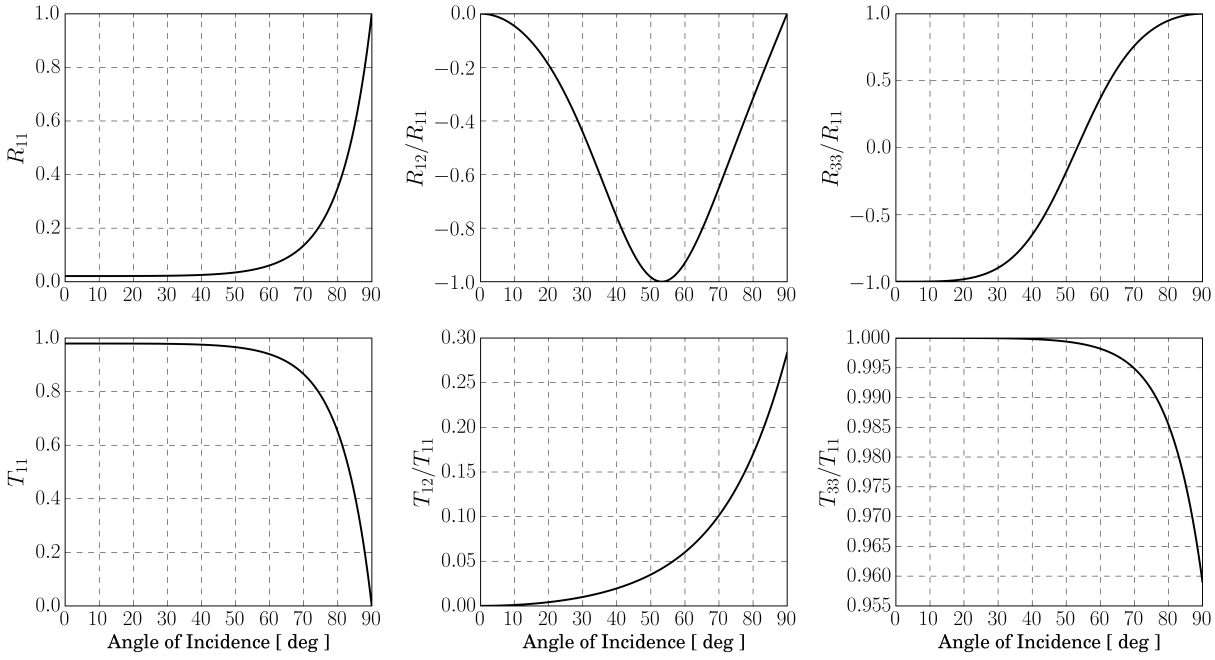

Figure 4.1: Mueller matrix elements of the reflected and transmitted light fields assuming a transition from air to water with a refractive index of $n = 1.338$. All values are normalized by the R_{11} or T_{11} components respectively.

The applicable scalar factors are consistent with the atmospheric definition given by Eq. 4.14, with no modifications and solved at the water surface bins, R_{surf}.

Sensing in the littoral zone introduces a heightened probability of the surface water structure having sea foam, due to breaking waves, or whitecaps present. The fractional coverage of whitecaps

is different in the littoral zone compared to open ocean, because of differing processes of formation. Whitecaps in a coastal environment are attributed to breaking waves, whereas the open ocean whitecaps are driven solely by wind. The presence of sea foam or whitecaps serves to decrease the specular reflection due to its Lambertian nature and can thus be viewed as a decrease in the backscattered surface photon rate, while also inflicting depolarization. Because of this, it is appropriate to view the non-presence of sea foam or whitecaps as a best case scenario. Expressions for the impact of these phenomena on surface reflectivity can be seen in [61]. Due to the complex nature of this phenomena, and its subsequent effect on the surface reflectivity, it is not considered within the basis of this modeling. Further analysis could be done to include these effects and their subsequent polarization attributes.

4.2.3 Water Column Equations

Signal from the water column requires special attention due to the combined number of transmission losses that severely decreases the backscattered photon rate. Typical lidar sensors that probe water columns to measure the inherent optical properties (IOPs) operate with high pulse energies and temporal averaging of returns in order to achieve the required high SNR [19, 55, 18]. Although the inherently LSNR approach of SPL sensors results in less photons events from the column, requiring long integration times to recover IOPs, water column returns are still frequently seen. Triggering of the acquisition unit from these sporadic column returns also decreases the probability of detection of any subsequent bottom surface (this is also applicable to the techniques discussed in [92] and [91], as the water column can typically be viewed as partially depolarizing) and understanding is considered vital for subsurface bathymetry. Therefore, water column modeling is important to SPL sensors estimating bathymetric quantities for two reasons: 1) the inversion of signals to retrieve column IOPs, and 2) understanding the detectability of subsurface scattering layers or targets.

It is typical for IOP values vary with depth and change in a non-linear manner, making the exact simulation of such parameters difficult. It is appropriate in many cases to assume a constant

value for the absorption coefficient, a_λ, the scattering coefficient, b_λ, and thus for the total column extinction, which is the linear sum of the two $c_\lambda = a_\lambda + b_\lambda$ [60], over shallow depth ranges. With the typical pulse energies transmitted by SPL sensors, <10 μJ, it is assumed that the pulse will fully extinguish prior to reaching water depths greater than 5 m. The assumption of a zero rate of change over the column is also applied to the volume scattering function (VSF). The VSF is utilized by evaluating the phase function at $\theta = \pi$ to estimate the backscatter efficiency and thus the total received photon counts due to the particulate scattering in the column. Values for different ocean water scenarios are given in Table 4.1, taken from the in situ measured values in [93]. Fresh water bodies, such as lakes and riverine environments, have IOPs that have been readily documented [106], but will not be examined here. In the case of glacial melt ponds and run off from supraglacial lakes, it is assumed that the water present is clear, pure water with no suspended particulates in the column [112], such that any backscattered photons collected from the column are due to the scattering from the water molecules themselves and provide a relatively simple simulation.

Table 4.1: VSF, column extinction, and forward scattering for $\lambda = 514$ nm [93]

Scattering Scenario	$\beta_{\mathbf{col}}(\lambda, \pi)$ $[m^{-1}sr^{-1}]$	$\mathbf{c}_\lambda$ $[m^{-1}]$	$\mathbf{b}^{\mathbf{f}}_\lambda$ $[m^{-1}]$
Clear Ocean	5.019×10^{-4}	0.151	0.0301
Coastal Ocean	1.03×10^{-3}	0.398	0.3697
Turbid Harbor	5.686×10^{-3}	2.19	1.8461

The complete product of the transmission terms in Eq. 4.1 must be considered with respect to the incident and scattered wave vectors, as the interaction with the air-water interface in the forward and backward direction differ. In the forward direction, the transmitted Stokes vector experiences transmission loss from the atmosphere through the water interface and in the water column prior to scattering off of a hydrosol or water molecule. The complete product of the incident wave vector k_i is

$$\prod_j \mathbf{T}_j(k_i, R) = \mathbf{T}_{col}(R_w)\mathbf{T}_{a\to w}(\theta_i, n_w)\mathbf{T}_{atm}(R_{air}). \tag{4.22}$$

For the backscattered wave vector k_s, the order is reversed and given as

$$\prod_j \mathbf{T}_j(k_s, R) = \mathbf{T}_{atm}(R_{air})\mathbf{T}_{w\to a}(\theta_i, n_w)\mathbf{T}_{col}(R_w). \tag{4.23}$$

The one-way extinction through the water column with extinction parameter c_λ is given according to the Lambert-Beer law as

$$\mathbf{T}_{col}(R_w) = e^{-\int_{R_{surf}}^{R_w} c_\lambda(R')dR'}\mathbf{I}, \tag{4.24}$$

where the integral is performed from the surface bin, R_{surf}, to the in water scattering bin, R_w. The extinction coefficient is wavelength dependent, but here values for $\lambda = 514$ nm are used and are deemed relatively close to the SPL's frequency doubled Nd:YAG operating wavelength of 532 nm.

The Mueller matrix used to described the polarization response upon transmission from the air to water interface is given as [63]

$$\mathbf{T}_{a\to w}(\theta_i, n_w) = \zeta \begin{bmatrix} \alpha' + \eta' & \alpha' - \eta' & 0 & 0 \\ \alpha' - \eta' & \alpha' + \eta' & 0 & 0 \\ 0 & 0 & \gamma'_{Re} & 0 \\ 0 & 0 & 0 & \gamma'_{Re} \end{bmatrix}, \tag{4.25}$$

where, for $\theta_i < \theta_{crit}$ the components $\alpha'(\theta_i, \theta_t)$, $\eta'(\theta_i, \theta_t)$, and $\gamma'(\theta_i, \theta_t)$ are calculated as

$$\alpha' = 0.5\left[\frac{2\sin(\theta_i)\cos(\theta_t)}{\sin(\theta_i + \theta_t)\cos(\theta_i - \theta_t)}\right]^2, \tag{4.26}$$

$$\eta' = 0.5\left[\frac{2\sin(\theta_i)\cos(\theta_t)}{\sin(\theta_i + \theta_t)}\right]^2, \tag{4.27}$$

$$\gamma'_{Re} = \frac{4\sin^2(\theta_t)\cos^2(\theta_i)}{\sin^2(\theta_i + \theta_t)\cos(\theta_i - \theta_t)}, \tag{4.28}$$

$$\zeta = n_w\frac{\cos(\theta_t)}{cos(\theta_i)}. \tag{4.29}$$

Transmission at the air-water interface must be accounted for twice in order to properly scale the returned photon counts. Conservation of energy, according to [132], takes place in the ζ term and varies according to n_w/n_{air} for the air-water transition and n_{air}/n_w at the water-air

transition. Otherwise, the Mueller matrix applied to k_s is implemented in the exact same manner as k_i, assuming that the backscattered light takes the same path back through the surface into the atmosphere as the incident light. This is typically an appropriate assumption, given that the IPP of the SPL is normally <100 μs and the surface state is unchanging for such time scales, though this assumption fails when considering spaceborne platforms. The individual components for transmission from air to water can been seen in the lower panels of Fig. 4.1.

Scattering interactions in the water column are assumed to be solely due to the presence of hydrosols, and scattering due to temperature induced index of refraction changes are not considered. With this assumption, the Mueller matrix that describes the scattering of the incident light and subsequent polarization response at some range R_w in the column is given by

$$\mathbf{F}_{col} = \beta_{col}(\lambda, R_w, \pi)\mathbf{M}_{\Delta}(d), \tag{4.30}$$

where the VSF takes on the form $\beta_{col}(\lambda, R_w, \pi)$ with units of [m^{-1} sr^{-1}], given here as a measured constant as opposed to a functional form. $\mathbf{M}_{\Delta}(d)$ gives the ability to allow the water column to exhibit depolarizing properties — again the depolarization matrix used for atmospheric scattering is appropriate as for turbid water it can be assumed that the suspended particulates have a random orientation and are non-spherical. Example values for β_{col} are given in Table 4.1.

The scalar constants applied to the water column now include an added term to account for the loss of light that has been scattered out of the FOV of the receiver, $\Gamma(R_w)$, given as

$$\kappa_{col}(R) = \Gamma(R_w)G(R)\frac{A}{R^2}\Delta R. \tag{4.31}$$

The spreading factor $\Gamma(R_w)$ is described in an effort to capture the physics of "Guenther's Trumpet" [39], which describes the spreading of the transmit light's divergence and the receiver's FOV, due to the presence of strong forward scatterers in the water column. This equation makes the assumption that the photons will undergo multiple forward scattering events, but only a single backscatter. In the scenario of FOV with a value of $\geq$ 10 mrad, an integrated expression (from the water surface to the bin under evaluation) for the in column loss caused by multiple scattering can

be calculated as a scalar efficiency term [67, 17]

$$\Gamma(R_w) = \frac{m^2\Psi^2 e^{-2b_f R_w}}{2} \int_0^\infty \left[x + \sqrt{1+x^2}\right]^{\frac{2b_f R_w}{x}} \exp\left[\frac{-m^2x^2}{4}\left(\frac{r_s^2 + r_t^2}{R_w^2} + \Theta^2 + \Psi^2\right)\right] x dx, \tag{4.32}$$

where

$$\Theta = \tfrac{DIV}{2}\gamma; \quad \Psi = \tfrac{FOV}{2}\gamma; \quad \gamma = \tfrac{R_p}{R_w} + \tfrac{1}{n_w} \ . \tag{4.33}$$

In this definition R_p refers to the platform altitude, R_w is the depth within the water column below the water surface, r_s is the radius of the laser spot on the water surface (not accounting for slope effects), r_t is the radius of the telescope, b_f is the forward scattering coefficient, and m is related to the average cosine of the scattering angle. Values for m depend on the conditions of the water, but examples can be gathered from [67, 17]. The forward scattering coefficient in Table 4.1 is calculated using the measured values for the VSF($\theta = 0.1°$) and the particle phase function at the forward direction as given in [93] (Table 3.10). Though these values are given at the scattering angle 0.1°, the approximation to complete forward scattering at 0° is tolerable within the larger simulation.

Equation 4.32 is most applicable to the measurement of deeper bodies of water, where depths of > 10 m are reached, but for completeness the physics has been instilled into the model. The assumption that the SPL derived bathymetric measurements are from shallow waters implies that the $\Gamma(R_w)$, could be at a minimum 90% depending on water conditions. For an SPL operating with a very narrow FOV, such as the IFOV of a single detector element, and observing shallow waters the effects of $\Gamma(R_w)$, can be ignored in the modeling process and still achieve accurate estimates of bottom surface photon rates.

4.2.4 Subsurface Ground Scattering Equations

The received Stokes vector from the subsurface ground scatter is typically depolarized, with some amount of energy in the orthogonal plane to the transmit polarization. For most subsurface scatterers it is typical to expect the return signal to be completely depolarized as the roughness is

typically on the order of the wavelength, especially for sand, as seen for sensing in the surf zone. An exception to this assumption is in the presence of subsurface ice, which is in itself polarization preserving, but contributes small amounts of depolarization due to volume scattering within the ice itself. For a completely depolarized signal it is therefore expected that both the co-polarized and cross-polarized signal will exhibit detections from the subsurface ground. Examination of the return signal will show that it is truncated due to the losses in path integrated over the whole atmosphere and water column. In total, the backscattered ground signal experiences losses due to the water column, transmission from water to atmosphere, and subsequent extinction through the atmosphere back to the sensor.

Similar to the description in the prior section, the complete product for the incident wave vector k_i is

$$\prod_j \mathbf{T}_j(k_i, R) = \mathbf{T}_{col}(R_{gnd})\mathbf{T}_{a\to w}(\theta_i, n_w)\mathbf{T}_{atm}(R_{air}), \tag{4.34}$$

and for the backscattered wave vector k_s, the order is reversed, given as

$$\prod_j \mathbf{T}_j(k_s, R) = \mathbf{T}_{atm}(R_{air})\mathbf{T}_{w\to a}(\theta_i, n_w)\mathbf{T}_{col}(R_{gnd}). \tag{4.35}$$

These two equations are equivalent to those describing the water column, but integrated from $R_{surf} \to R_{gnd}$ over the full column.

The Mueller matrix use to capture the ground scattering is given by a scalar reflectivity term multiplied by the Mueller matrix for a general depolarizer, given by Eq. 4.2. The most general depolarizing matrix for the hard target used because of available literature that quotes values for the diagonal terms, such that depolarizing parameters of the scatterer — a, b, and c — can be varied to fit the target. The total scattering matrix is then given by

$$\mathbf{F}_{gnd} = \frac{\rho_{gnd}\cos(\theta_i^w)}{\pi}\mathbf{M}_{\Delta,g}(d), \tag{4.36}$$

where the target's reflectivity is modulated by the pointing angle, θ_i^w — where the added "w" indicates that it has been corrected for refraction through the water surface, and it is assumed that the BRDF is equal to π for Lambertian scattering.

With the assumption that the hard target scatter is completely diffuse the reflectivity becomes a relatively simple computation of Fresnel coefficients. In addition, the full Mueller matrix for measured scatterers, such as concrete or sand, as given in [22] and discussed in [65], can provide a more accurate polarization description. In the case of examining scattering a subsurface ice scatterer, more elaborate reflectivity must be considered. The ice is semi-specular with low reflectivity at the water-ice boundary due to similar indices of refraction. Detections from porous ice typically arrive with a time delay resulting from multiple scattering within the ice column [111] when considering an SPL operating at visible wavelengths.

The scalar components in κ are equivalent to Eq. 4.31, where the $\Gamma(R)$ term still applies, and should be integrated from the water surface over the entire water column, stopping at the first ground bin, to provide the accurate loss of signal photons.

4.2.5 Background Signal Contributions

In each instance of the SVLE calculation, a background contribution is described by $\vec{S}_B$. This vector contains the number of counts contributed to the overall signal as generated by solar background and detector dark counts. After the background counts have been re-sampled, they are converted to vector form and added to the bin being computed. The total background contribution is considered constant over the single laser firing, which is reasonable for a detector with a low dark count rate (the PMTs employed in the SPL sensor discussed in this thesis work have a dark count rate of <300 Hz) and under the assumption that the atmosphere is static over the IPP of the laser (roughly μs time scales).

It is necessary to parameterize the detector dark count rate, $\xi_d(t)$, in order to correctly capture the number of added counts per unambiguous range of the counting system. The dark count photon rate is given in units of [counts/s], the PRF is in units of [1/s], ΔR is in units of [m/bin], and the unambiguous range is in units of [m]. n_{dark} can be computed with the resulting units of [counts/shot/bin], accurately describing the correct contribution of dark counts when the TDC bin width and laser PRF/IPP is considered.

Solar background contribution is described by a noise model for nadir viewing altimeters that was introduced in [23, 24]. This model describes the expected noise counts per bin due to diffuse surface and isotropic atmospheric scattered solar radiation as

$$n_b = \frac{N_\lambda \beta_\lambda A_r \Omega_r}{h\nu} \left[\Omega_{tgt} T_0^{1+\sec\theta_s} + \frac{1 - T_0^{1+\sec\theta_s}}{4\pi(1+\sec\theta_s)} \right], \tag{4.37}$$

where N_λ is the wavelength-dependent exoatmospheric solar spectral illuminance, β_λ is the receiver's spectral bandpass, A_r is the collection area of the receiver's telescope, Ω_r is the receiver's FOV in steradians, θ_s is the solar zenith angle, and T_0 is the one-way atmospheric transmission. The two bracketed terms describe the ground, assuming a flat scattering surface, and atmospheric contributions, respectively.

The transmission factors in Eq. 4.37 are calculated as

$$T_0^{1+\sec\theta_s} = \exp\left[-(1+\sec(\theta_s)) \int_{R_{alt}}^{\infty} \alpha_{atm}(R')dR' \right], \tag{4.38}$$

with the solar zenith angle defined over the range of 0° indicating zenith and 90° indicating the horizon. The integration is performed using the previously calculated molecular portion of the atmospheric extinction coefficient, Eq. 4.10, from R_{alt}, which is the measurement altitude of the sensor, to the top of the atmosphere $R \approx \infty$. In an effort to speed up computation the integral's upper bound is capped when it reaches the stratosphere at 60 km. The NRLMSIS-00 model introduces negligible changes in transmission when including higher altitude terms, and by decreasing the number of bins, the overall computation time was reduced by an order of magnitude.

As solar background is the dominant source of noise in SPL sensors. A more complete definition of the reflection coefficient has been included to capture the reality of surface scattering by including a mixture of diffuse and specular scatterers. Steinvall *et al.* [115] gives a validated model for a BRDF of this type as

$$\Omega_{tgt} = \frac{A}{\cos^6(\alpha)} \exp\left[-\tan^2(\alpha)/s^2 \right] + B\cos^m(\alpha), \tag{4.39}$$

where the specular and diffuse contributions are given by the first and second terms, respectively. The term s is a measure of the incident surface slope, θ is the angle of incidence and reflection, m is

a roughness indicator, and the ratio A/B is an indication of the specular to diffuse behavior. The use of this definition for the BRDF allows a noise model that can accurately describe the complex nature of non-uniform surface scattering types within a single laser spot, including the specular noise returns from water surfaces.

The Stokes vector describing the total contribution of noise counts per bin can now be given as

$$\vec{S}_B = n_b \tau_b \begin{bmatrix} 1 \\ p\cos(2\psi)\cos(2\chi) \\ p\sin(2\psi)\cos(2\chi) \\ p\sin(2\chi) \end{bmatrix} + \frac{n_{dark}}{\eta_i} \begin{bmatrix} 1 \\ 0 \\ 0 \\ 0 \end{bmatrix}, \tag{4.40}$$

where n_b is given by Eq. 4.37, τ_b is the TDC timing resolution, and η_i is the efficiency per receiver channel. Since the contribution of detector dark counts is not polarization dependent n_{dark} is multiplied by a Stokes vector containing only the S_0 term. The inclusion of n_{dark} into the $\vec{S}_B$ is for completeness and that the physics of the SVLE describe the polarization and intensity in the optical path, which dark counts are not subjected to. Removal of the effects of the multiplicative channel efficiencies in the projection matrix $\mathbf{O}$ is done with a normalization factor of η_i^{-1} for the i^{th} polarization channel.

The polarization definition in Eq. 4.40 allows for the solar background counts to be varied in polarization orientation to simulate that of the naturally occurring polarized signal during day time conditions. Furthermore, this allows the correct rotation matrices to be applied for aligning the scatterer's polarization orientation to that of the receiver's polarizing beam splitter (PBS), when needed. With Eqs. 4.40 and 4.37 it is now possible to link the noise rate directly to the instrument parameters. By examining the receiver's spectral band pass and timing resolution, the direct impact of detuning SPL sensor parameters on each polarization channel can be calculated. This facilitates a deeper understanding of of tolerances for particular optics, such as the tilt-tuning of the receiver's etalon and how target detectability in turn degrades.

4.3 Signal Waveform Generation

For a given set of system, atmospheric, ocean, and other miscellaneous parameters, the entire column measurement is generated as a deterministic signal waveform, similar to that of an analog recorder, but at magnitudes of single photons per bin. By using the specific SVLE necessary per bin, the correct estimate for the received photon rate, or power, over the entire measurement column is computed for a single laser firing. Various compensating factors for indices of refraction can then be applied per bin, correctly computing the resolution per measurement regime.

The entire signal waveform is parsed into a binning structure with a single bin width defined by the TDC resolution and spans from the aircraft's altitude to the ground and any subsequent scattering layers (if a water body is assumed present). In the example of a 300 m measurement altitude above ground level (AGL) and with a TDC resolution of 4 mm, there is a total of 75,000 bins in which the deterministic waveform is valued. Equating the resolution of the waveform to that of the sampling TDC is crucial for avoiding inadvertent weighting of the probabilistic sampling function that determines if a detection has been made.

The temporal characteristics of the signal waveform are a combination of the SPL's IRF and the target's non-instantaneous reflection caused by surface roughness or temporal stretching due to a non-zero surface slope. The timing uncertainty added due to a surface roughness or ocean surface, as discussed in Chapter 3, are utilized such that the total width of the received signal is $\sigma_{rx}^2 = \sigma_{IRF}^2 + \sigma_{tgt}^2$, where the IRF is first computed by convolving the input timing response of the sensor's receiver chain with the input width of the transmitted laser pulse. In the case of the atmosphere, the timing resolution is set to the IRF and the target is assumed to be a delta scatterer, $\sigma_{tgt} = \delta(t)$, so that there is no added uncertainty from the scattering process. This is a reasonable approximation for atmospheric scatterers when there are no clouds present. Yang *et al.* [126] discuss topographic ranging delays as a result of multiple forward scattering through clouds during atmospheric propagation, showing that the contributions are small but can be accounted for through MC modeling. In the case of surface scatter (e.g. ocean or hard target) each point has a

specific valued of σ_{tgt}. This allows for variable surface roughness across the measurement grid and for the angle of incidence of the laser light to be modulated, simulating the variability of boresight alignment and sensor pointing.

Descriptions of the mean timing delay of the return pulse's centroid differ with surface type, generating different magnitudes of delay that are distinct from the uncertainty added to the width of the IRF. For ocean sensing, mean surface slope, roughness, and skewness contribute to overall delayed timing of the return surface pulse. Tsai *et al.* [118] give the expression as

$$\left\langle \tau_{delay}^{surf} \right\rangle = \frac{2R}{c\cos(\alpha)} + \frac{2R}{c\cos(\alpha)}\tan^2(\theta_T) + \frac{2}{c\cos(\alpha)}\sigma_\xi \lambda_3 \left(1 - \frac{2\tan^2(\alpha)}{S^2}\right), \tag{4.41}$$

where as defined in Chapter 3, S^2 is the wind driven mean-squared surface slope, λ_3 is the surface skewness, α is the off-nadir pointing angle, and σ_ξ is the surface roughness. The delay is expressed as a mean over multiple measurement cycles and the defined surface terms are ensemble averages. To consider a single laser firing, it is necessary to assume that surface features are Gaussian over long measurements and then to use $\left\langle \tau_{delay}^{surf} \right\rangle$ as the center of this Gaussian with a standard deviation equivalent to σ_ξ. A random number generator then allows a draw from this distribution to generate a value for the single shot delay, shown in Fig. 4.2.

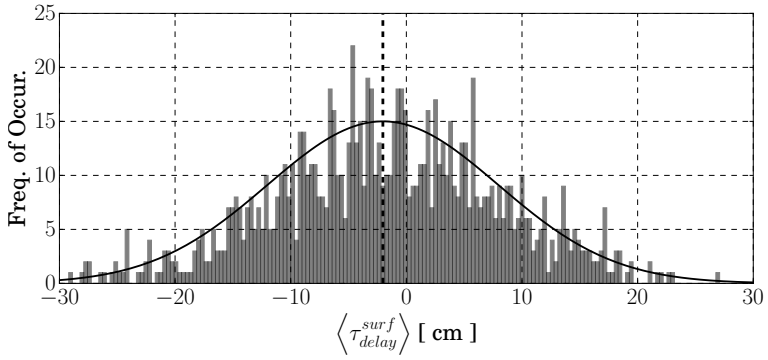

Figure 4.2: Random draws of surface delays for 1000 laser firings, for an aircraft altitude of $R = 300$ m, $\sigma_\xi = 0.1$, $\lambda_3 = 0.2$ and $S^2 = 0.03$. Equation 4.41 estimates a mean delay of -2.03 cm. Orientation is such that the ocean surface is at zero and negative is into the water column.

The description for hard target roughness serves to be a simpler implementation because it

is reliant only on the sensor's off-nadir pointing and the laser's divergence, given by [32] as

$$\left\langle \tau_{delay}^{gnd} \right\rangle = \frac{2R}{c\cos(\alpha)} \left(1 + \tan^2(\theta_T)\right). \tag{4.42}$$

From this the hard target delay can be computed for a per shot basis with no modification.

The overall process of taking the discrete counts and generating a signal waveform can be thought of as an application of a transfer function where the geophysical environment is viewed as the "system". The input signal is convolved with the timing information for each scattering event in the atmosphere, water surface and column, and subsurface ground. The output signal has the correct timing and magnitude responses. Photons incident on the receiver's detector faces result from the envelope of this return waveform, causing the output photon counts in the data stream to be discrete sampled realizations of this waveform.

4.3.1 Discrete Photon Time-Tag Generation

To generate a point cloud of photon events from the deterministic waveform, the binomial distribution can be invoked to replicate the uncertainty of the detector's photoelectron generation process [33, 127]. The binomial distribution can be reduced to describe Bernoulli trials for which the probabilities of binary outcomes can be computed, providing a good fit for calculating sampling statistics. The PMTs discussed throughout this thesis have a quantum efficiency of 40%, which can also be thought of as the probability, p_{QE}, that the incident photon generates a photoelectron that then enters the dynode chain. Using these definitions, the envelope can be randomly sampled to provide the realistic output of an SPL, namely event time-tags.

The most general form of the binomial distribution is give as [101]

$$P = \sum_{j=k}^{n} \begin{pmatrix} n \\ k \end{pmatrix} p^k (1-p)^{n-k} \text{ , where } \begin{pmatrix} n \\ k \end{pmatrix} = \frac{n!}{k!(n-k)!}, \tag{4.43}$$

where the latter is the binomial coefficient for k detections in n trials. Re-indexing the summation

gives a more usable probability of one or more events detected, $k \geq 1$, as

$$P = 1 - \sum_{j=0}^{k-1} \left(\begin{array}{c} n \\ k \end{array} \right) p^k (1-p)^{n-k}. \tag{4.44}$$

For $k = 1$, this reduces to the cumulative binomial distribution for one or more successes in n Bernoulli trials: $P(k \geq 1, n) = 1 - (1-p)^n$.

Assuming that there are some N_{rx} statistically independent event times in the bounded timing bin between t_1 and t_2, the general description for which the probability of $k \geq 1$ events registered with an input photon rate and detector efficiency becomes

$$P(k \geq 1, p_{QE}, N_{rx}) = 1 - (1 - p_{QE})^{N_{rx}(t_1,t_2)}. \tag{4.45}$$

With a known system dead-time and an indexed experiment start ($t_0 = 0$), this method gives realistic photon detections throughout the entire measurement column for any specified number of laser firings. Implementation of the system dead-time is done as a binary toggle after each detection so that when a photon event is registered, the subsequent timing bins spanned by τ_d are attributed with zero events. This is propagated over the signal waveform for some n_{shots} laser shots, with each shot requiring discrete iteration over the waveform. The output from this sampling process is an ordered stream of event time-tags representing the range of the detected photon, at the TDC timing resolution, and the associated detection time in the IPP range gate ($\sim 70\mu$s). The correct interpretation of the number of detected events is that each discrete event is of itself a Poissonian random process that has been subjected to a binary filtering process. From this, the simulated point cloud can be compared to measured data and simulated performance metrics can be analyzed.

4.4 Airborne SPL Model Flow

The model inputs include the SPL sensor specifications and the environmental parameters, shown in Tables 4.2 and 4.3. A flow diagram depicting how the model's inputs and outputs are handled are shown in Fig. 4.3, color coded such that yellow shows model inputs, blue shows deterministic calculations, green shows stochastic calculations, and orange for the total output.

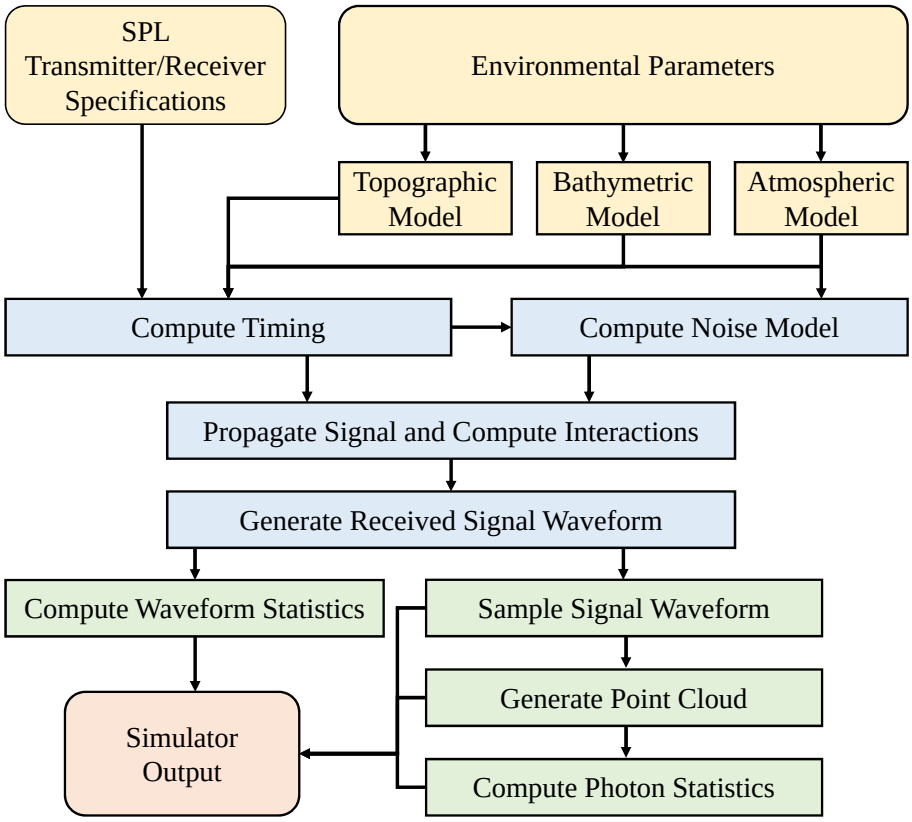

Figure 4.3: The SPL model inputs are shown in yellow, taking in sensor specifications and environmental parameters, including the topographic, bathymetric, and atmospheric models. The bulk of the computation is shown in blue, which includes computation of the timing information and uncertainty, the noise model, signal propagation and solving of the SVLE per range bin, and combination into the deterministic waveform. The stochastic calculations are shown in green, which include: the sampled signal waveform and associated statistics, the time-tagged photon point cloud and associated statistics, integrated profiles from the time-tagged photons, and other associated metrics. The total model's outputs are shown in orange. The model's inputs and outputs are shown distinctly as beveled boxes.

Table 4.2: Summary of the model's input SPL specifications

System Parameter	**Value**
Pointing Angle	0.01°
Wavelength	532.18 nm
Laser Repetition Rate	14.3 kHz
Laser Pulse-Width	450 ps
Laser Output Energy	2.45 μJ
Transmitter Divergence	2 mrad
Transmitter Polarization	$[1,-1,0,0]^T$
Transmitter Polarization Offset	0°
Telescope Diameter	90 mm
Receiver Field of View	10 mrad
Receiver Filter Bandwidth	300 pm FWHM
Range Bin Width	27 ps
Integrated Range Bin	4 mm
Number of Pulses Sampled	500
Detector QE	40% QE
Overall Receiver Efficiency	Variable
Overall Transmitter Efficiency	Variable
Overall System Dead Time	Variable

Table 4.3: Summary of the model's input environmental specifications

Environmental Parameter	**Value**
Platform Altitude	Variable
Atmospheric Visibility	10 km, Clear
Atmospheric Backscatter	Rayleigh
Atmospheric Extinction	Rayleigh & Mie
Clear Air Depolarization	$\delta = 0.00365$
Solar Zenith Angle θ_s	45°
Water Type	Coastal Ocean
Water Refractive Index	1.338
Water Depth	3 & 5 m considered
Water Surface Depolarization	1%
Water Column Depolarization	10%
Ground Reflectivity	$20\%/\pi$
Ground Depolarization	99%
Ground Roughness	0.01 m^2

4.5 Airborne SPL Modeling Results

The airborne time-tagging lidar simulator (ATLIS) was run in several scenarios in an effort to understand a proposed sensor's response to the airborne environment in a daytime ocean environment. Specifically, the settings input to ATLIS are those of the sensor discussed in Chapter 5. ATLIS can be utilized to estimate uncertainties and relative errors from the signal strengths and point clouds, facilitating development or turning of sensor parameters. A prominent use for a simulated SPL sensor is to predict the different probabilities of detection as well as where the sensor will be in photon counting mode. This helps answer the questions related to sensor linearity and operational regimes that degrade sensor performance.

4.5.1 Signal Waveforms

The single shot signal waveforms for the co-polarized and cross-polarized channels over > 300 m of range are seen in Figs. 4.4 and 4.5. Of particular note is that, for a single laser firing, the return signal strength is very low in both channels, with the noise floor occurring close to 10^{-4} counts per bin, as expected for SPL's low pulse energies. In the first 30 m, the co-polarized atmospheric molecular scatter can be seen after the sensor has come into full geometric overlap and is due to the clear air depolarization.

Figure 4.5 shows a window of the water returns for each polarization channel. In the higher intensity co-polarized channel, the water surface, column, and bottom scatterers can all be seen. This is expected as the surface and column are predominantly polarization preserving, as attributed, whereas the bottom signal is depolarized. The cross-polarized channel has no signal strength until the bottom scattering surface is reached, in which $\sim$50% of the scattered light goes into the $[1, 1, 0, 0]^T$ polarization plane. The timing signatures of the water surface and the bottom scattering layer can also be seen in Figs. 4.5 and 4.6, where the water surface is broad and indicative of the surface wave structure. The bottom can be seen as narrower because of the finite roughness of the ground and zero added slope from operation at approximately nadir.

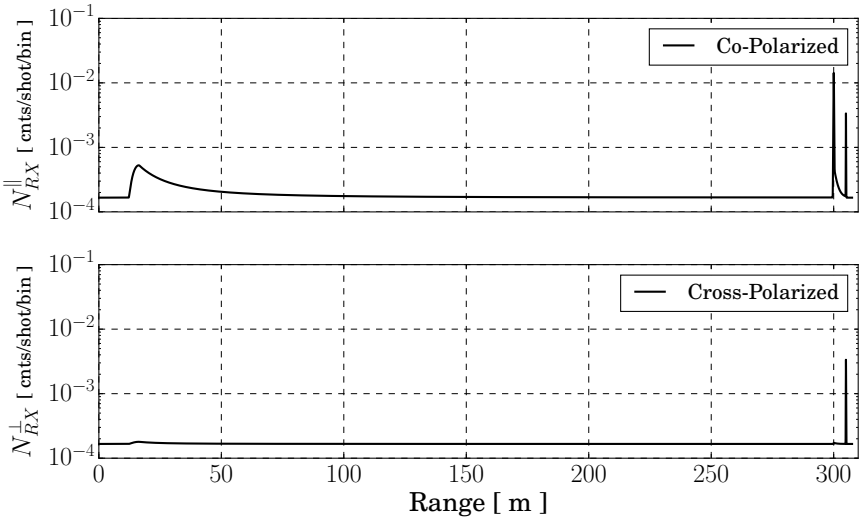

Figure 4.4: The computed signal waveforms for the model inputs given in Tables 4.2 and 4.3 with water body IOPs from Tab. 4.1. The co-polarized channel has significant signal from the clear air atmospheric returns and water surface, both clearly above the noise floor. Signal strengths in the cross-polarized channel can be seen in the noise until the subsurface scatterer is reached.

These signatures are evident in the computed probability profiles as well, where the peak detection probability occurs at the respective surface and ground bins. There is also heightened P_D for signal from the leading or trailing edge of the stretched waveform. This accounts for the photon distribution in histograms accumulated from rough targets, replicating the expected broadening.

The probability curves in Fig. 4.6 provide insight into the ability of the SPL sensor to recover from strong specular surface returns. The received signal waveform, $N^{\parallel}_{RX}$, is shown in blue and the subsequent probabilities of detection with different system dead-times are shown in red. The clear conclusion is that from 2.5 $\rightarrow$ 190 ns P_D decreases a full order of magnitude for the post surface recovered value. However, regardless of the increased P_D associated with a lower dead-time, there is still a recovery period in which the system is being subjected to $W_j < 1$, in accordance with the mathematics in Chapter 3. For 2.5 ns, this recovery occurs in under 20 cm, allowing the system to be free for column detections. In the 25 ns example, the system is in a state of $W_j < 1$ for several

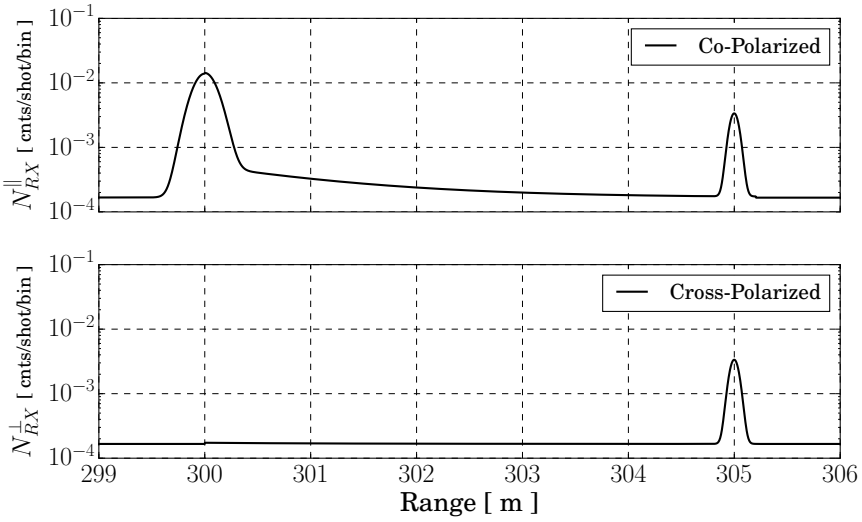

Figure 4.5: Zoom in to the surface and bottom returns for the signal waveforms shown in Fig. 4.4. The polarization preserving surface return can be seen distinctly in the co-polarized channel and not present in the cross-polarized channel. However, the fully depolarizing bottom return distinctly shows the cross-polarized channel. Water column returns are predominantly seen only in the co-polarized channel due to relative single strengths between the two polarization planes.

meters reducing column returns, but recovers before the ground signal.

The 190 ns dead-time proves interesting due to the longer recovery times after strong signals. The surface signal remains comparable to the other dead-time examples, but is in recovery through the ground return, where it is expected that the system could recover at some point in the column from $W_j \ll 1$. The comparable values of P_D at the surface can be explained by the fact that prior to the surface detection $W_j = 1$, so that when the peak surface signal is reached the 190 ns still has high $W_j \approx 1$. Though the indication that the longer dead-time is likely suitable for surface detections is enticing, the overall lower P_D restricts the dynamic range of the sensor and it is only able to capture the strong surface return. This doesn't follow with the assumed process of maximizing P_D across the full range to facilitate multiple measurement regimes. From this analysis, it can be concluded that, for detections of subsequent scattering layers in a single channel, shorter dead-times enable a higher P_D across the full profile.

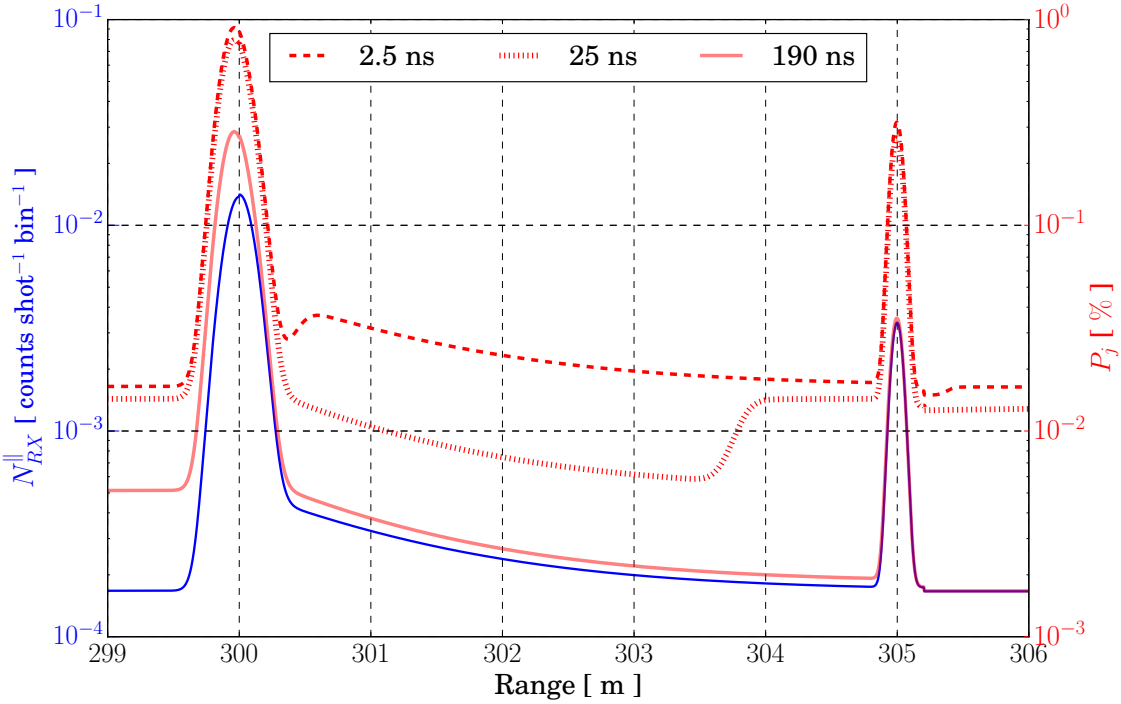

Figure 4.6: P_j calculated for the co-polarized receiver channel, looking at a coastal ocean surface with a 5 m deep water column, while varying the system dead-time. The 2.5 ns dead-time exhibits the highest P_D in every range bin, and has a post water surface recovery of < 10 cm. The 25 ns dead-time has a comparable P_D for each scattering surface but the post water surface recovery occurs several meters into the water column, implying that volume scattering detections would be low. The 190 ns dead-time exhibits a decreased surface P_D (less than an order difference) but the column returns are over an order below the peaked surface return, implying that there will be predominantly only surface returns in the 190 ns channel and small numbers of column returns.

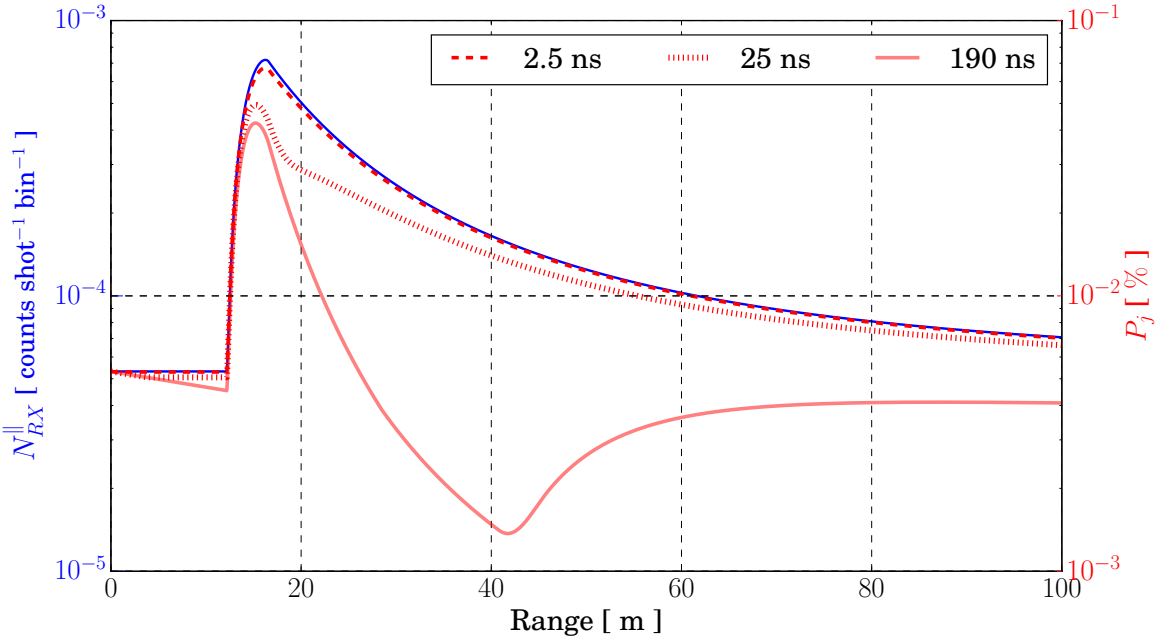

Figure 4.7: P_j calculated for the co-polarized receiver channel, showing the recovery after overlap and the introduction of atmospheric returns. The 2.5 ns dead-time shows the closest match to the input $N_{RX}^{\parallel}$, with the P_D maximized throughout the profile and minimal dead-time effects right after full geometric overlap. The 25 ns dead-time clear deviation from the input waveform, where the strong signal at full geometric overlap causes the recovery to extend out to 100 m. The 190 ns dead-time shows the largest deviation, with a clear response from the high signal at full geometric overlap, bringing the subsequent P_D down almost two orders of magnitude. Recovery of the 190 ns dead-time does not occur until after > 250 m.

4.5.2 Modeled Point Clouds

Figure 4.8 shows the point clouds for each polarization channel sampled over 500 laser firings at 27 ps and with a full dead-time of 190 ns in each channel. The associated integrated histograms at an equivalent bin width over the full acquisition time are shown on the right. Surface returns in the co-polarized channel are clearly shown in both the point cloud and the histogram, whereas the cross-polarized channel shows small numbers of counts from the bottom surface, as expected due to the depolarization and system dead-time. An interesting take away from looking at the point clouds is that neither the atmosphere nor the water column are discernible from noise. It is likely that due to the low micro-joule pulse energies examined, the signals from these regimes require longer integration times to achieve the required SNR to rise above the floor of the solar background. This indicates that an SPL sensor operating on these time scales would expect to see sporadic signal from the column, either as noise, unwanted solar signal or actual returns, but not a substantial signal to extract IOPs from. This could be remedied by increasing the PRF of the sensor so that time between shots is shorter and thus the total integration time over more laser shots is shorter.

A slight decrease in counts can be seen between the $50 \rightarrow 100$ m ranges in Fig. 4.8. This is expected due to the longer recovery required after the peak atmospheric signal occurs and the implementation of a 190 ns dead-time. This is explicitly seen in Fig. 4.7, where, for the longer dead-time, the system reaches a point where the P_D becomes lower than the solar background noise floor, so there is a zone of decreased counts introduced. This also indicates that the use of a longer dead-time is likely not suited to cloud or aerosol studies, where signals can be large in small pockets of range and fast recovery is required. According to Fig. 4.7, this effect would be seen mildly with a medium length dead-time, but not present with short dead-times.

It is useful to consider the results shown in Fig. 4.8 from simulations run with multiple permutations of environmental parameters. By calculating performance metrics, such as relative error and distribution properties, the SPL sensor's performance can be analyzed. In Table 4.4 surface and

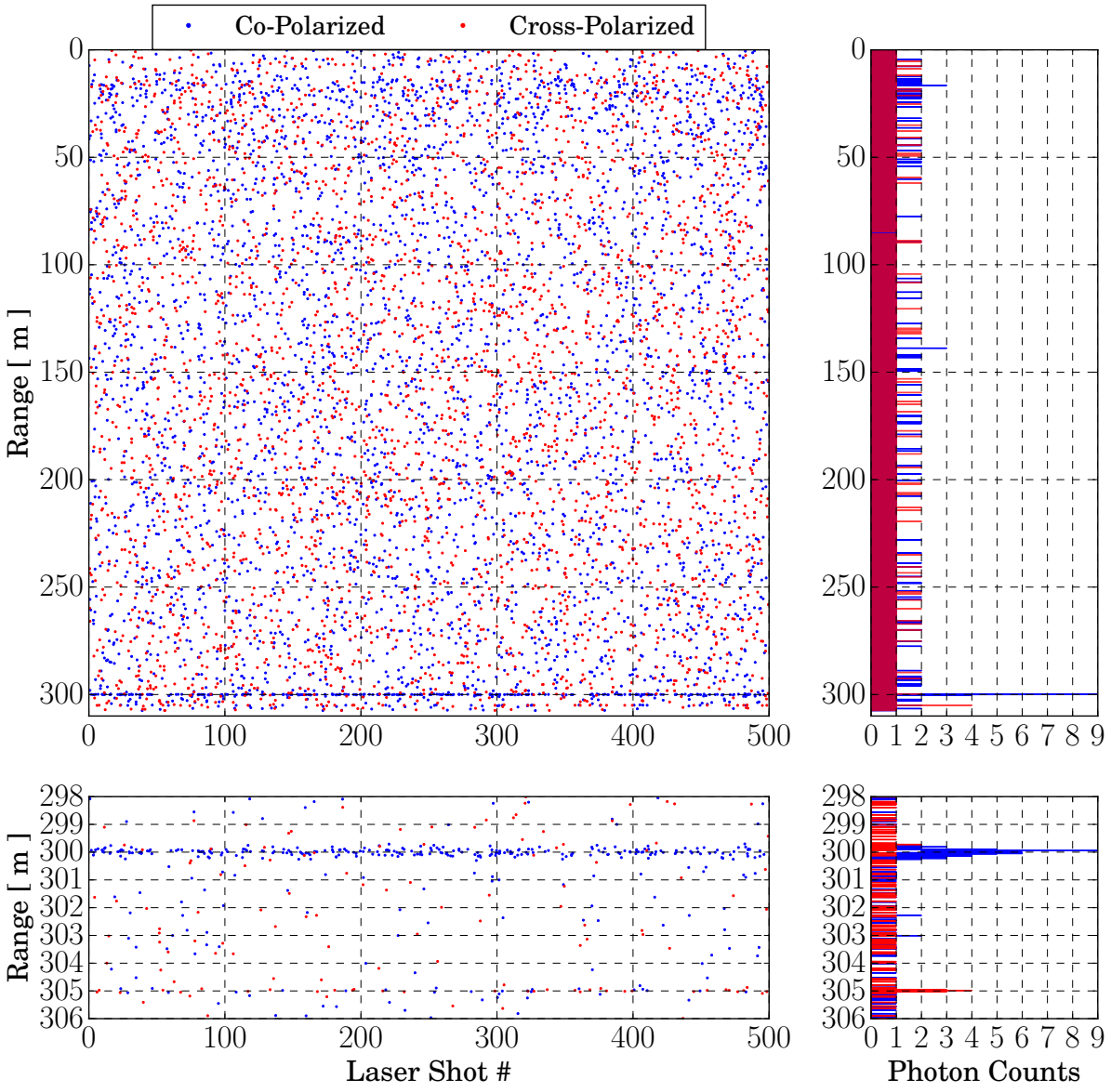

Figure 4.8: Simulated point clouds for the co-polarized and cross-polarized receiver polarization planes. The point clouds are computed by sampling the deterministic signal waveforms shown in Fig. 4.4. The upper left panel shows the full range of measurements, with the associated 4 mm integrated point cloud on the upper right. The lower panels show a zoom in to the water surface and 5 m depth returns in the co and cross-polarized channels. This configuration shows depth performance, but the limited number of laser firings considered does not provide the density of returns from the clear air atmospheric scatterers. However, the medium solar background environment provides enough returns that the long sensor dead-time of 190 ns reduces the density of returns from the surfaces at 300 and 305 m.

bottom detection performance is analyzed for different dead-times and noise environments. Though it is not expected that a demonstration sensor will be flown in a shallow ocean water environment, surface target detection metrics are still useful for future deployments and target statistics can be extrapolated to column scattering layers.

Analysis was conducted in a high solar background environment, where the results could facilitate an understanding of operation in high solar elevation environments. When subjected to a high noise environment, the sensor is expected to see a noise count every ~ 0.5 meters, with detector dark counts considered as well. In contrast, for operation in the low noise environment the sensor will see a noise count every ~ 7 meters. For acquisition over 300 m, each measurement will give roughly 600 and 42 noise counts per laser firing, respectively. This may seem high when considering that P_D for signal photons is likely low, but the general impact of noise counts is of concern when the arrival rate comes within an order of magnitude of the dead-time, causing an overload of the acquisition unit.

Per laser shot, the number of detected signal photons is calculated by widowing the surface and bottom signals using the the expected distribution widths, summing the number of detected photons across those bins, and dividing by the number of laser firings. This gives a detection rate for each target, and is easily derivable from both the simulated and actual point clouds. Employment of this method does introduce variability in the estimate due to the location of the bounding ranges for integration, but with bounds chosen suitably wide, the difference between subsequent analysis would be predominantly due to noise, which can be removed. For low probabilities of detection it is then implied that there will be a clear variance among subsequent analyses due to a significant noise variance.

The results of varying noise conditions are shown in Table 4.4. Retrievals performed on the simulated data show that differences between the high and low solar background levels have little indication on the detectability of water surfaces when the signal detection rate is already high, with the values for all dead-times and both noise environments $> 50\%$. For the bottom signal, it appears that the low noise environment allows a slight increase in the number of detected

Table 4.4: Percent detected photons per 500 laser firings from the sampled point cloud. The surface return was calculated from co-polarized signal and the bottom return was calculated from the cross-polarized signal. The system-dead time was varied and the noise environment was switched from low to high to analyze differences in detection rates.

	Low Noise Level		**High Noise Level**	
Dead-Time (τ_d)	**Surface**	**Bottom**	**Surface**	**Bottom**
2.5 ns	87.5 %	7.6 %	90.88 %	7.6 %
25 ns	89.6 %	6.0 %	85.8 %	6.6 %
190 ns	87.8 %	5.0 %	89.8 %	6.4 %

Table 4.5: The calculated standard deviation, error of the mean, and Poisson error from the accumulated time-tags over 500 laser firings with a *low* noise contribution, input deterministic values of $\sigma_{surf} = 10.91$ cm and $\sigma_{gnd} = 4.44$ cm.

	Surface			**Bottom**		
Dead-Time (τ_d)	σ (cm)	$\sigma/\sqrt{N}$ (mm)	$\sqrt{N}/N$	σ (cm)	$\sigma/\sqrt{N}$ (mm)	$\sqrt{N}/N$
2.5 ns	10.68	5.11	4.79%	4.30	6.98	16.22%
25 ns	10.55	4.98	4.72%	3.25	5.93	18.26%
190 ns	10.81	5.16	4.77%	4.27	8.55	20.00%

Table 4.6: The calculated standard deviation, error of the mean, and Poisson error from the accumulated time-tags over 500 laser firings with a *high* noise contribution, input deterministic values of $\sigma_{surf} = 10.91$ cm and $\sigma_{gnd} = 4.44$ cm.

	Surface			**Bottom**		
Dead-Time (τ_d)	σ (cm)	$\sigma/\sqrt{N}$ (mm)	$\sqrt{N}/N$	σ (cm)	$\sigma/\sqrt{N}$ (mm)	$\sqrt{N}/N$
2.5 ns	11.38	5.57	4.89%	4.74	8.24	17.40%
25 ns	11.12	5.37	4.82%	6.07	10.56	17.41%
190 ns	10.96	5.18	4.72%	4.92	9.47	19.25%

photons, but due to the water column providing signal prior to ground bins and the ability for that signal to subsequently blank the bottom surface, signal detection rates do not change significantly with different noise environments. However, in the case of overwhelming background counts, the subsurface detection rate goes to zero due to an in ability to generate enough correlated signal counts to stand out from the noise field.

Using the same set of data, distribution parameters can be computed and compared to the known timing uncertainty that was introduced into the model. In Tables 4.5 and 4.6 the surface and bottom distributions were compiled at the 4 mm bin resolution and then the Gaussian standard deviation, error of the mean, and Poisson uncertainty were calculated for both noise environments. In both cases, as expected, the retrieved surface signal has less uncertainty than the retrieved bottom. This is due to the relative number of points used to build the distribution and is directly related to the probability of detection. With the bottom's low probability of detection, the subsequent uncertainty of each range estimate is higher.

When comparing between noise environments, the error due to shot noise does not drastically increase with the high noise environment, seeing a few percent increase. This is likely due to the increased noise detections that fall into the signal analysis window and cannot be differentiated from signal photons. However, by considering the error of the mean estimate, it can be seen that the distribution built for the bottom in the high noise environment has higher error. This indicates a broadening in the return signal envelope's range values in the higher noise environment compared to that of the lower noise environment.

Tables 4.4, 4.5, and 4.6 indicate that, for surface detection in either noise environment, there is not a drastic loss in counts due to an increased dead-time, and that either a short or a long dead-time will provide sufficient surface detectability. This is partly due to the fact that the surface signal is much larger than the noise or atmospheric signal, causing some of the dead-time induced dynamic range loss to be made up for by the increased photon rate. This is compatible with the probability analysis shown for surface detections in Fig. 4.6, further indicating that a longer dead-time provides ample ability to detect water surface photons.

It becomes pertinent to have a shorter dead-time for either subsurface ground or column detections. The fast recovery time after the high strength specular surface is needed to subsequently detect the following scattering layers with high probabilities of detection. By decreasing the dead-time, the uncertainty of the bottom measurement also decreases. This allows estimates of photon rate and range to be made with less error. With these conclusions, it should be expected that employing a long dead-time to generate column or subsurface ground measurements, while in photon counting mode, will provide at best sporadic signals and will require large numbers of shots to be integrated for signals to rise above noise.

The subsurface ground's reflectivity was changed from $\rho = 0.1 - 0.5$ to facilitate an understanding of how detection rates change with different surface types composed of pure Lambertian scatterers. The noise was maintained at high and the longest dead-time was considered. As the ground reflectivity increases, all subsequent metrics become more precise due to the slightly increased number of signal photons. The Gaussian standard deviation of the retrieved distribution approximately reaches the expected timing uncertainty introduced by the roughness. However, due to the still low probability of detection at $\rho = 0.5$ of 8.6%, the uncertainty of the measurement is still high. The calculated Poisson error reaches a plateau, where larger numbers of counts will be necessary for decreased error. These results indicate that though the measurements can be made in variable reflectivity, the uncertainty at each will be high until the backscattered photon rate can be increased. Increasing laser pulse energies will bias returns from other regimes when the dead-time is still long, further indicating that, for increased subsurface detectability, a short dead-time should be employed for subsurface detection. An understanding of why the high noise environment did not drastically degrade the sensor's performance metrics can be understood by in partial by an explanation given in [91]. When the noise environment is high, the probability of the counter to trigger off of a noise photon increases. This turns the subsequent dead-time window into a random process that is distributed Poissonianly throughout the profile, so the introduction of noise can really be thought of as a blocking window that shifts whatever part of the signal waveform's envelope is being sampled. The implication is that there will be some laser shots in which there is

Table 4.7: Depth sounding performance metrics calculated for the cross-polarized receiver channel considering a 190 ns dead-time and a 3 m deep water column in a coastal ocean environment. The P_D and photon distribution parameters are shown along with the Poisson error. The resulting increased reflectivity gives high backscattered photon rates and better statistics.

	High Noise $\tau_D = 190$ **ns**			
Reflectivity (ρ)	**% Detected**	σ (cm)	$\sigma/\sqrt{N}$ (mm)	$\sqrt{N}/N$
0.1	1.8	10.29	34.30	33.33%
0.2	4.0	7.87	17.60	22.36%
0.3	5.4	7.79	15.0	19.25%
0.4	8.2	6.21	9.71	15.62%
0.5	8.6	5.76	8.79	15.25%

probability for a strong signal to fall into a noise induced dead-time window. By blanking out the large signal, the system is not in a recovery mode and therefore allows the subsequent detection of weaker signals. Thus background can sometimes be seen to increase the probability of detection of the weak scatterers that would otherwise be expected to fall into the dead-time following strong signals.

From these model runs, it appears that implementation of specific pulse energies, repetition rates, and flight altitudes will result in poor cross-polarized performance due to the lack of signal strengths. With the low surface depolarization and losses to the column, it is expected that a significant number of the acquired data in a real sensor will be noise. Coupling this with the 190 ns dead-time employed in the demonstration SPL sensor in Chapter 5, it is anticipated that aircraft retrievals requiring the cross-polarized receiver channel will prove cumbersome. Contrasting with the co-polarized receiver channel, the demonstrated SPL sensor will see atmospheric molecular signal and surface returns readily despite the use of a longer dead-time. The results in Chapter 5 confirm and elaborate these conclusions. Through comparison between the measurements present and the ATLIS model results, a guide to decision making with respect to system architecture in future systems will be possible.

4.6 Extension to Arrayed Detectors

Analysis in the prior chapters and sections was done with the assumption that light would pass through the receiver chain and be focused onto a detector with a single cathode and a single output anode (in the case of PMTs). With the advent of relatively inexpensive detector arrays (SiPMs) and the widespread availability of SPAD arrays and micro-channel plate (MCP) PMTs, it is advantageous to consider their use in a multi-functional SPL sensor. Several iterations of multi-element detectors have been analyzed and utilized in TCSPC applications [8], but, as discussed by Becker *et al.*, the signal diversity in traditional TCSPC measurements is such that a single TDC can be shared by all elements due to an assumption < 0.1 photons per laser firing and minimal noise. This is not the case in a fielded SPL sensor. The presence of asynchronous solar background and varying levels of backscattered photon rates within a given IPP nullify this assumption, and an array with all elements linked to a single output would suffer the same tall poles as a single element detector. This section will introduce the arrayed detection approach to the ATLIS simulator and perform initial analysis on the resulting modeled data.

The introduction of arrayed detectors facilitates a reduction in FPB [23] by allowing the temporal profile of the received signal to be sampled independently across the array. As will be shown here, discriminating the signal across an array also partially addresses the issues of dynamic range and signal linearity resulting from TDC dead-time. It is necessary to understand how multi-element detector arrays could be utilized in an SPL sensor in order to decrease biases and non-linear traits, while potentially increasing the atmospheric and surface collection rates.

From Fig. 4.9 it becomes clear that if a Gaussian beam is focused onto the array such that all of the energy falls onto the array face, there will be some subset of array elements that will not be triggered, and only a fraction of some n_e elements will register signal photons at any given time. This indicates that there is a point of diminishing returns for increased sensor complexity when a large format array is considered in this manner. There are solutions where the beam can be de-focused onto the array so a Gaussian beam has at least 2σ of the energy distribution falls across

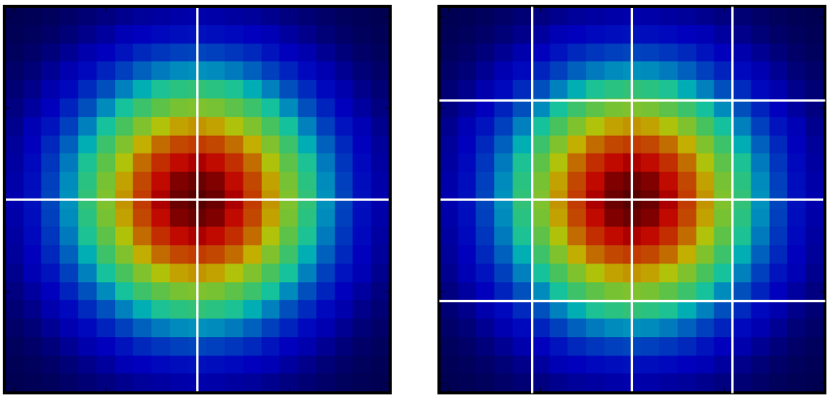

Figure 4.9: Example of a received Gaussian energy distribution subdivided by 4 and 16 elements.

the entire array, but for a square array (which is common in SPAD and PMT arrays) there will still be a subset of elements that do not fire from signal. The inclusion of back end electronics for the unused elements drastically increases the sensor's accompanying electronics with no associated measurement advantage.

To gain a better understanding of what the ideal number of array elements are per SPL receiver channel, it is advantageous to define the probability of detection per element and the total array. In this analysis, it is assumed that each detector element has an anode connected to its own discrete TDC with a particular dead-time associated with it. It is further assumed that they are ideal elements with no cross-talk. In this case, the total probability of the detector array with n_e elements is given by the sum of individual probabilities for each n_{ij} detector element, representing the i_{th}/j_{th} row/column location. The total probability of detection, for one or more detections, from all elements in the q_{th} timing bin bounded by t_1 and t_2 for N counts incident over the entire array is adopted and modified from the prior chapter, given as

$$P_d(k \geq 1; q) = \sum_i \sum_j \left\{ \exp\left(-\frac{\xi N_D}{n_e}\right) \exp\left(-\sum_{q'=q-N_D}^{q-1} S_{q'}^{ij}\right) \left[1 - \exp\left(-S_q^{ij} - \frac{\xi}{n_e}\right)\right] \right\}, \quad (4.46)$$

where the summations over the i, j detector elements are geometric sums across the array and the sum over q represents the advance in time. The number of signal photons to fall upon each detector

element is given by the following relation

$$S_q^{ij} = \Delta^{ij} N_q, \tag{4.47}$$

where Δ^{ij} takes into account the single element pitch to overall array ratio and the fill-factor. It also holds the specific information about how the beam profile is imaged onto the detector array so that proportionate weights can be given to elements expecting signal or not. The sum over all i, j rows and columns will give the total signal, $\sum_i \sum_j S_q^{ij} = N_q$, as would be incident onto a single element detector, validating the definition.

Immediately it is apparent from Eq. 4.46 that regardless of what the signal incident per element is, i.e. if $\Delta^{ij} < 1$, the incident solar background will be reduced by a factor of n_e. Examining the case of a 16 element array, this gives an order of magnitude reduction in noise. This has the further effect of reducing the probability of detection for the unwanted signal and thus reducing the overall number of noise detections per acquisition period over the entire array, allowing the elements to be outside of the noise induced dead-time window and available for higher detection rates. This is an immense gain and could facilitate relaxation of stringent optical design parameters, such as the required inclusion of an etalon or other < 100 pm filter for spectral blocking.

A simplified analysis can be done to understand the best case scenario for array implementation. In the case of uniform illumination over the entire detector face, the efficiency weights for each element are $\Delta^{ij} = 1/n_e$ and the probability of detection across the entire array reduces to the simplified form

$$P_d(k \geq 1; q) = \exp\left(-\frac{\xi N_D}{n_e}\right) \exp\left(-\frac{1}{n_e} \sum_{q'=q-N_D}^{q-1} N_{q'}\right) \left[1 - \exp\left(-\frac{N_q + \xi}{n_e}\right)\right], \tag{4.48}$$

which can be further reduced to give

$$P_d(k \geq 1; q) = \left\{ \exp\left(-\xi N_D\right) \exp\left(-\sum_{q'=q-N_D}^{q-1} N_{q'}\right) \right\}^{1/n_e} \left[1 - \exp\left(-\frac{N_q + \xi}{n_e}\right)\right]. \tag{4.49}$$

It can now be recognized that the terms contained within the braces are just the dead-time weighting function derived in Chapter 3. With this, the final form of the equation with the dead-

time weighting function, shown as W_q here, is

$$P_d(k \geq 1; q) = \{W_q\}^{1/n_e} \left[1 - \exp\left(-\frac{N_q + \xi}{n_e}\right)\right]. \tag{4.50}$$

Though this is derived for the case of uniform illumination, it is clear now where the advantage of the detector array comes in, specifically for the dead-time weighting function, as in this case it is raised to the power of $1/n_e$. This serves to bring the weighting factor closer to 1 for all measurements, ideal for maximizing dynamic range and signal linearity. For example, in Fig. 4.7 the weighting function for the 190 ns dead-time reaches a minimum value of 0.1241 at 41 m into the atmosphere. If this signal was considered in the case of an array of $n_e = 4$ the weighting factor would be increased to 0.5935, or, in the case of $n_e = 16$, the factor is increased to 0.8778. The increase in the weighting function is significant and on the order of the results from the 2.5 ns dead-time, implying that an array can be paired with a TDC that has relaxed dead-time requirements while maintaining a high dynamic range and signal linearity. When uniform illumination is not present, there will still be an increase in the weighting function, but it will vary per element and will be proportional to Δ^{ij}. Expressions for the calculation of Δ^{ij} that consider the distribution of energy due to a Gaussian beam profile are given in [23, 73].

The case of uniform illumination across the array can easily be examined for any N counts in any receiver channel using the prior mathematics and ATLIS model framework. Implementation of the individual element weights and sampling each element independently yields an output photon event time-tag stream for all elements. Figure 4.10 shows the cumulative density of points for $n_e = 4$ array elements in the co-polarized channel assuming a 190 ns dead-time per element. The density of points at the ocean surface can easily be seen in the overall point cloud, as well as in the atmospheric returns. Figure 4.11 shows a zoom-in to the ocean surface and the resulting histogram generated by integrating all detections across the array at 4 mm binning resolution. The distribution of points generated by the histogram closely matches that of the prior single element detector despite the signal strength per element being decreased by $1/n_e$. This is due to the increased dynamic range and linear sensitivity from the increased weighting function. In addition

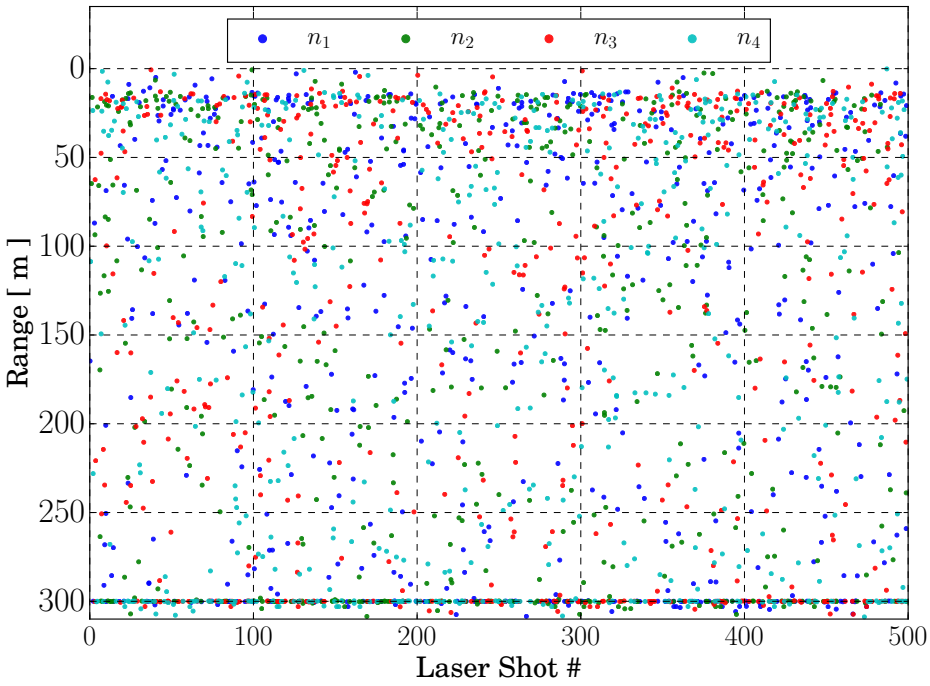

Figure 4.10: Scatter plot of all detections generated for 4 independent detector elements, each with 190 ns dead-time for the co-polarized channel. Atmospheric, solar background, and surface counts can be seen generated from each element.

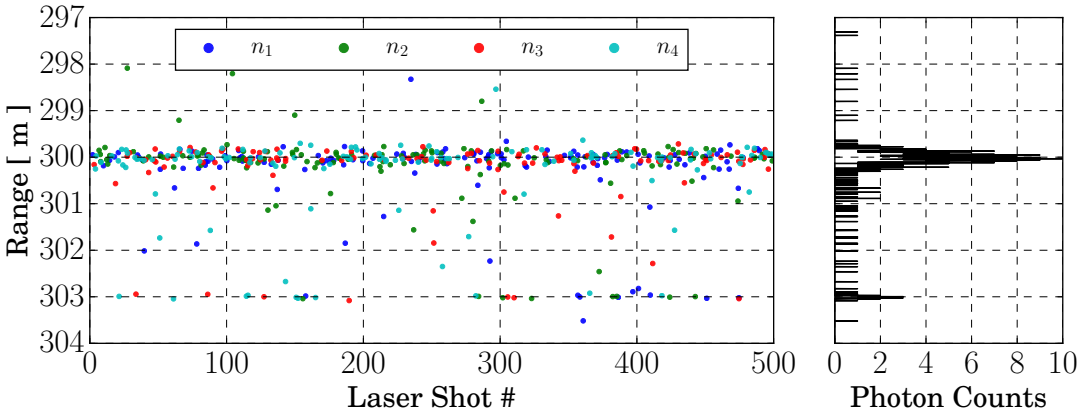

Figure 4.11: Surface windowed portion of Fig. 4.10. The histogram for all detector elements in point cloud is shown to the right at a 4 mm binning resolution. Specular water surface and diffuse bottom can be seen in each elements' returns.

to the surface signal, recovery is such that sporadic column returns and the bottom surface can also be seen.

The total accumulated point clouds for both polarization channels and $n_e = 16$ detector elements are shown in Fig. 4.12. The returns from all elements within each receiver channel have been collapsed into a single time-tag stream, as each detection is sampled and attributed a detection time from a common timer for all elements. The cumulative time-tags for all elements per channel were integrated into a histogram with 4 mm bins, as shown on the right of the figure. Despite the decreased signal strength in each element, the combined signal across the full measurement range remains comparable to the single element case. In comparison to Fig. 4.8, the total integrated noise counts have decreased by a factor of ~ 16 as expected. In the lower right histogram, zoomed in to the surface, it appears that the distribution of signals has filled out the expected timing width compared to the single element case, implying that there are more detections made across the full temporal profile of the received signal, which would in turn facilitate FPB reduction. This simple simulation indicates that, for a given array size and expected decrease in signal per element, integrated SNR of the SPL can be increased by the combination of decreased noise and sensor parameter tuning.

Comparing the number of detections per element in the two different n_e cases provides a better understanding of which elements are contributing signal during the accumulation over some subset of laser firings. It also elucidates the randomness of detection across the array. Figure 4.13 shows the array for $n_e = 4$ and $n_e = 16$ elements and number of detections made over 100 laser shots per element. In the $n_e = 4$,case each element is seeing roughly 20% detection rates over the accumulation period for a total detection rate of 91% across the whole array. In the $n_e = 16$ case, each element sees roughly 8% detection rates over the period, but > 100 detections across the entire array, implying that some elements are seeing multiple detections per laser shot. This effectively ensures that there is one or more detection per laser shot while each element remains linear at low probabilities of detection.

In Fig. 4.14 the number of detections made over 500 laser shots is examined to see if there

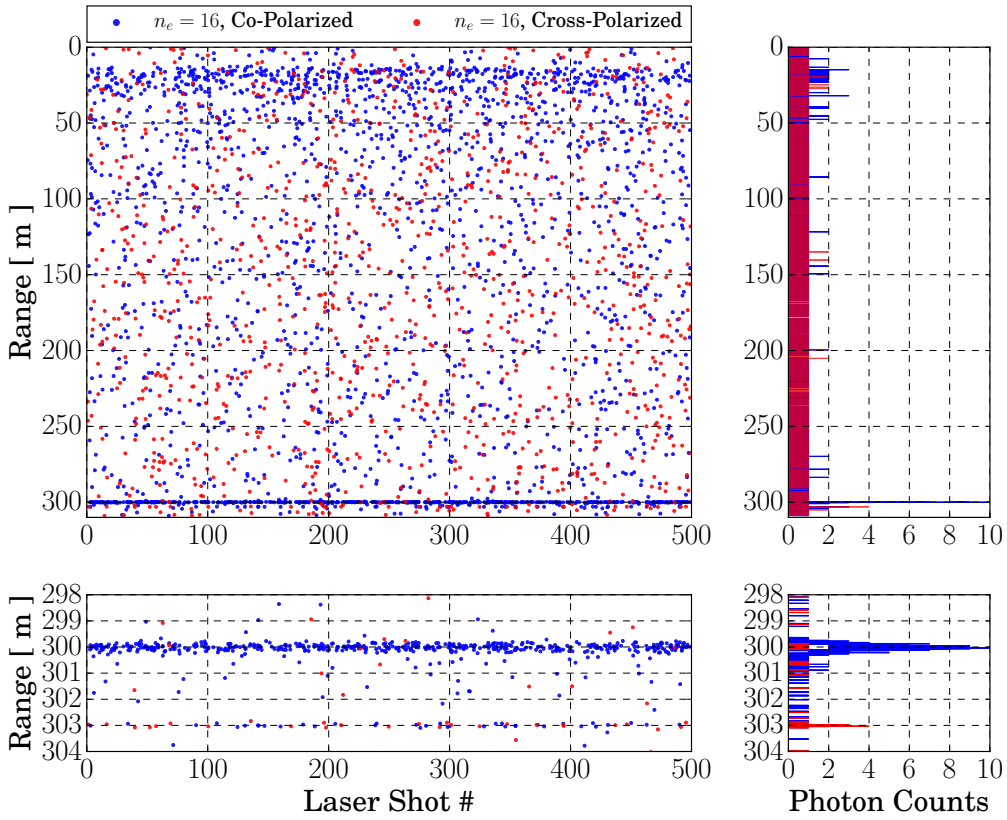

Figure 4.12: The point clouds and integrated profiles, with 4 mm bins, for photon detections made across a $n_e = 16$ element detector array in each polarization channel. Uniform illumination was assumed for the element efficiencies, and each element had its own 190 ns dead-time. The simulation was run assuming a high noise environment and bottom scattering plane 3 m below the water surface with $\rho = 0.5$. The remaining sensor and environmental parameters are shown in Tables 4.2 and 4.3. The decreased counts between 50-100 m as seen in Fig. 4.8 are no longer seen due to the overall increase in the dead-time weighting function.

is any significant difference per element. Regardless of the different value of n_e the total number of detections made per 500 laser shots is approximately 90-93% for both arrays. However, like the 100 laser shot case, the $n_e = 4$ array maintains a detection rate of 20-25%, which is still significantly higher than typically preferred for single photon counting. The $n_e = 16$ array maintains the preferred detection rates at 3-8% per element, while overall having a high detection rate across the entire array when summed to a combined rate estimate.

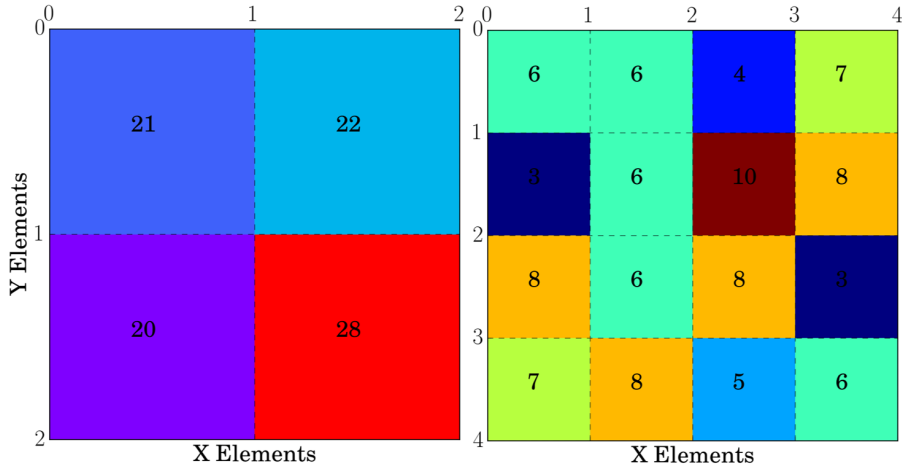

Figure 4.13: Example of the co-polarized backscattered surface signal over 100 laser shots subdivided over 4 and 16 element detectors, assuming uniform illumination across the array. In the left panel, the $n_e = 4$ detector generates detections from the backscatter per laser shot at approximately 20-30% per element. In the right panel, the $n_e = 16$ detector maintains the probability of 4-10% per element.

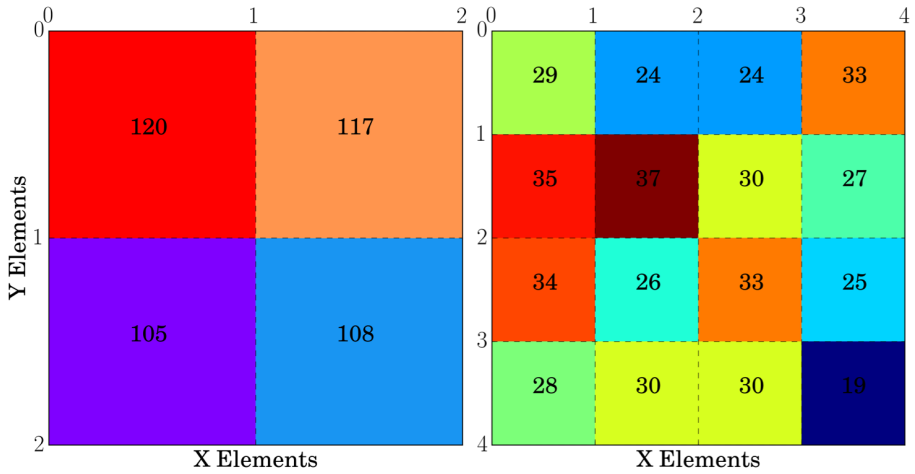

Figure 4.14: Increasing the accumulation window to 500 laser shots, while still assuming uniform illumination. The $n_e = 4$ detector generates detections from the backscatter per laser shot at approximately 20-25% per element. In the right panel, the $n_e = 16$ detector maintains the probability of 3-8% per element.

Figures 4.13 and 4.14 demonstrate the advantage for employing arrays with much larger numbers of elements. This research shows that, for at least a moderate number of array elements under uniform illumination, detections rates for the entire array stay higher than the single element detector while the individual elements maintain lower detection rates and remain in linear photon counting mode. In the case of the $n_e = 4$ compared to the $n_e = 16$ cases, these effects scale with the total number of elements, including extension to $n_e > 16$ arrays. This is highly advantageous for a number of bright scattering planes, such as cloud tops, water surfaces, and ice.

4.6.1 Target Induced Power Fluctuations

It is necessary to briefly discuss the impact of speckle on the received signal, which in the single element detector could be safely ignored as the detector averages the impinging wavefront. When considering a specular scatterer the received signal can be shown to obey the aforementioned Poissonian statistics [100]. However, for partially or fully developed speckle due to an optically rough scatterer, there is a departure from Poissonian statistics and the target-induced power fluctuations can be described by a Gamma distribution [37]. Goodman [37, 38] gives an expression to capture the stochastic properties of the resulting joint cumulative distribution as

$$P_D = \int_0^\infty P(k|w)p(w)dw, \tag{4.51}$$

in which $P(k|w)$ is the Poissonian conditional probability of k detections with w incident power and $p(w)$ is the Gamma distributed marginal probability. Here w is the optical power of the backscattered signal that has some distributed speckle across the wavefront, given in joules/second, and can be converted to the incident number of counts through $N = \eta_{QE}\frac{w}{h\nu}$. Using this notation and the relative distributions, the integral then becomes

$$P_D = \int_0^\infty \left(\frac{N^k}{k!}\exp(-N)\right)\left(\frac{a^M w^{M-1}}{\Gamma(M)}\exp\left(-aw\right)\right)dw. \tag{4.52}$$

The solution to this integral is discussed thoroughly in [37], and versions are also given in

[100, 33]. Integrating over the power gives the probability of detection as

$$P_D = \frac{\Gamma(k+M)}{k!\Gamma(M)} \left[1 + \frac{M}{N}\right]^{-k} \left[1 + \frac{N}{M}\right]^{-M}, \tag{4.53}$$

where it can be seen that the joint cumulative distribution is actually the negative binomial distribution in the absence of noise. The term $\Gamma(M)$ is the well known Gamma function with value $(M-1)!$. For a highly diverse signal such that $M/N \gg 1$, i.e. Poisson shot noise dominates, this equation truncates back to the standard Poisson probability. To show this, each term can be approximated by a series expansion, or as in the case of the Gamma function ratio, can be approximated by an asymptotic form [100] to give $M^k/k!$. Looking at each of the second and third terms individually, it is seen that the second term can be replaced through equivalence with

$$\left[1 + \frac{N}{M}\right]^{-M} = \exp\left\{-M \ln\left(1 + \frac{N}{M}\right)\right\}. \tag{4.54}$$

Recognizing that the natural logarithm can also be Taylor expanded

$$\ln\left(1 + \frac{N}{M}\right) \approx \frac{N}{M} - \frac{1}{2}\left(\frac{N}{M}\right)^2 + \cdots, \tag{4.55}$$

and gives

$$\exp\left\{-M\left[\frac{N}{M} - \frac{1}{2}\left(\frac{N}{M}\right)^2 + \cdots\right]\right\} = \exp\{-N\}, \tag{4.56}$$

since $(N/M)^2 \approx 0$ and all higher order terms go to zero as well.

When $M \gg N$, $M + N \approx M$ is also true that

$$\left[\frac{N}{M+N}\right]^k \approx \left[\frac{N}{M}\right]^k. \tag{4.57}$$

Substitution of each approximated component back into Eq. 4.53 gives the Poisson distribution, showing convergence when speckle is eliminated.

It is clear that utilizing detector arrays in an SPL's receiver chain has advantages, namely for increased collection rates, reduction of the non-linear effects, and reduction of the solar background detection rates. From Figs. 4.11 and 4.12, it appears that utilizing multi-element detectors allows a scatterer's surface distribution to be approximated with reduced shots, implying that the time over

target can be reduced. Further more, spatial ambiguities introduced by a moving platform would be decreased. This is an advantage, especially for sensors on airborne or spaceborne platforms that require sub-millisecond collections. For these reasons, a linear PMT array was utilized in the ICESat-2 ATLAS sensor, facilitating FPB mitigation and increasing collection rates. An SPL sensor equipped with these detectors has many advantages over the single element detector and arrayed technology should be considered a primary design criteria in future sensor designs.

Inclusion, however, comes with increased system complexity. To take full advantage of the arrayed technology, each element should be paired with its own picosecond precise timing system. This is impractical when considering commercial TCSPC products, where three inputs require PCIe slots and cost >$10k. This implies that custom FPGA/TDC electronics are needed, which is a non-trivial endeavor. Proper handling of data to avoid high data rates would also be necessary. Suitable GmAPD arrays exist, but operation in the near-IR restricts science applicability.

4.7 Relevance to Posed Thesis Questions

The development of an encompassing simulator in which the generation of photon time-tags, through robust statistical techniques, from a deterministic signal waveform, where all polarization and environmental components are considered, directly addresses several of the posed thesis questions. The relevant finds can be summarized as:

(1) What are the implications of utilizing the time-correlated single photon counting approach for geophysical parameter estimation from volume scattering environments?

- The ATLIS simulator showed the expectation of different SPL configurations and measurement regimes by demonstrating models of the signal waveform and photon point clouds. Figures 4.6 and 4.7 give the relative differences for volume scattering layers, atmosphere and water column, for different input dead-times. The resulting point clouds are shown in Fig. 4.8, giving a full indication of what detection rates are expected in an operational environment. It was shown through several model runs that robust water column and

subsurface layer detection with a long dead-time is improbable. Instead, sporadic low rate returns are likely. These findings can be translatable to the atmospheric regime as well. Low photon rates introduce a hindrance to the multi-functionality of a SPL when acquisition electronics' parameters are not tuned for the measurements. The introduction of arrayed detectors was shown as a possible method for partially mitigating these problems and increasing detection rates.

(2) How are estimates of backscattered photon rate and target range affected by the implementation of the photon time-tagging approach?

- Maintaining operation in linear photon counting mode and preventing biases from transitioning into GM are of the upmost importance for an SPL pursuing detection and estimation. Results from ATLIS indicated that there are locations where photon rates are decreased due to a sensor's response to the measurement environment, implying that geophysical retrievals can be biased through improper data representation of the environment. Analysis of detector arrays showed that a sensor can mitigate these effects solely by replacing a single element detector with an array, reducing the impact of the dead-time weighting function and non-linearities.

(3) Can polarimetric lidar incorporate time-correlated single photon counting, and what are the implications to high resolution multi-functional measurements of atmosphere, ocean, and hard targets?

- The work in this chapter laid out the full formulation for modeling a polarized SPL sensor and the response to photon returns from the atmosphere, ocean, and subsurface scattering layers. With the formulation of the SVLE contained herein, the ability for SPLs to employ TCSPC and make measurements of multiple different regimes has been shown. Emphasis on sensor parameters, such as dead-time, is necessary depending on what geophysical parameters being sought.

Chapter 5

A Polarization Sensitive SPL for Geoscience Research

The remainder of the thesis work to be discussed describes the efforts to develop, experimentally demonstrate, and provide measurement validation of many of the topics and concepts presented in prior chapters. This body of work has been divided into three distinct chapters pertaining to each portion so as to emphasize the undertakings and conclusions of each.

This chapter specifically describes the iterative development of a polarimetric SPL sensor using a majority of components procured for a prior sensor developed within the CU Active Remote Sensing Lab (originally slated for laboratory demonstration of high resolution GM technique to shallow water depths - see [90]). Many of the transmitter and receiver optical components were reconfigured to allow the addition of new components that would facilitate airborne operation. The added optical components and overall reconfiguration advanced the sensor from a laboratory testing unit to a flight-ready unit. Effort was made to keep the sensor in a compact configuration while simultaneously fitting all components into a light-tight housing that was previously built. This included the isolation of the transmit and received optical paths to prevent acquisition triggering from stray light. It was necessary to maintain ample space to allow for a series of filters and folding mirrors to steer the received light to the detectors. An iteration of this sensor was used for the atmospheric point cloud generation shown in Chapter 3 and the final version was used for generating engineering data from a series of flights discussed in Chapters 6 & 7.

5.1 Airborne Detection of Noise-Like Signals

In the past single objective implementations of SPL-like measurements have examined topographic or bathymetric surfaces. By limiting instrument scope to a single targeted observable the presence of other scatterers in the measurement column is often relegated to a noise flag and filtered out of the final data product, such as the presence of clear air or aerosol scattering. Regardless of measurement objective, it is the case that this signal is inherently not noise, but is characterized as such due to the methods by which SPL employ for photon detection and time-tag generation.

A perfect example of this school of thought is with the ICESat-2 airborne prototype, MABEL [86]. In [69], data from the MABEL sensor was used to examine Arctic sea ice cover, where the first 5 km of signal above the surface was incorrectly labeled as noise and used to characterize observed background signal rates. Due to the concentration of atmospheric scatterers in this range window the observed background signal rats are skewed by heightened count rates, giving an incorrect estimate of solar background contributions to the point cloud.

The approach employed throughout this thesis establishes a different school of thought on how to determine what is characterized as noise. The view is taken that information content exists in the areas typically considered as noise, such as the atmospheric column, and can prove valuable to a plethora of scientific objectives or sensor performance analysis. Through retention of this data a high resolution SPL could enhance our understanding of the atmospheric-ocean boundary, or provide a known stratification of scatterers that could assist in understanding sensor linearity.

It is necessary to establish a difference between what is typically considered noise and what could instead be considered unwanted signal. In the sea ice example, the atmospheric detections were not noise but actually unwanted signal. These sporadic signals originate not from the surface, but rather from other geophysical scattering processes. Over time, the integration of these signals exhibit spatial correlation due to atmospheric structure, namely the density gradient or aerosols. The same is true for detections originating from a water column when the water surface is the primary target of investigation.

In lidar remote sensing the term noise has previously been defined as a detection generated by the processing of internal electronic fluctuations of the receiver components, including detector dark counts or CFD/TDC errors. However, detections originating from solar background also lead to false detections. The total sum of these two sources should be considered the sole contributors of noise. Estimates of these values must be performed over ranges where backscattered laser light is not present. For a nadir viewing airborne SPL these ranges are below the apparent ground return, or, in the case of water sensing, where column signals are expected to be extinguished. This directly distinguishes the wanted and unwanted signals. By this definition it would therefore be erroneous to estimate noise where atmospheric signal is present. In the case of [69] a true estimate of noise would be performed on detections made beyond the ice surface and before the unambiguous range value of the sensor, where it would be expected that only solar background and electronic noise would be present. The atmospheric returns would then be considered unwanted signal.

The multi-functional SPL has several measurement modalities, all of which require the detection of noise-like signals. Arguments have been made for implementing a special case of the Bayes criterion, specifically the Neyman-Pearson criterion [100]. This approach emphasizes minimization of false-alarm probabilities, detection of unwanted signal, while maximizing the probability of wanted signal photons. Although this seems like a viable approach, in practice there are caveats and the application is not one-to-one with SPL sensors. The challenge of this approach arises due to the asynchronous binary detection of solar background and its similarity to a diffuse stratified medium (atmosphere, ocean column). By removing asynchronous solar background there will be removal of wanted signal. This approach is not advantageous, nor applicable to SPL sensors pursuing multi-functional operation. Implementation inevitably leads to errors in which wanted signals are present, but not detected.

SPLs targeting multi-functional operation instead must rely on the spatial and temporal correlations of the desired received signal and decrease contributions from unwanted signals through hardware alterations. This corresponds to a minimization of the detected solar background rate, while maximizing the detection rate of signal photons that originate from different areas of the

measurement column. The difference between rate and photon detection probability is subtle, but has the effect of mitigating errors and, in practice, has a different method of implementation. By allowing the detection of atmospheric signals, the detection of solar background and other errant noise signals is inevitable and will occur during daytime operation. Accepting this, truncating solar background detections is done partially through spectral and spatial filtering of the return signals. The remainder of differentiation is performed statistically in post-processing, allowing the Poissonian nature of the signals to be fully exploited.

The SPL sensor discussed throughout this chapter operates at a wavelength of 532 nm due to its proximity to the transmission peak through water, high Rayleigh backscatter cross-sections, and readily available laser subsystems. However, the choice in wavelength results in heightened susceptibility to the peak of the solar spectrum. Solar background rates can vary from several Hz, when operating at night, to $>$ 10 MHz in day time operation, depending on the local surface reflectivity. These values also change as a function of polarization, implying that different receiver channels will be exposed to different rates. For example, the modeling work in preparation for the ICESat-2 satellite estimated that, for unpolarized single photon counting at 532 nm in the Arctic regions, background rates upwards of 15 MHz could be expected [79]. In high background environments signal detections can decrease due to the presence of a detector or TDC dead-time. The discussions in prior chapters have shown how dead-time can influence signal count rates, dynamic range, and introduce non-linear effects. Since the ability to detect wanted signal from a particular observation regime relies on the sensor being out of dead-time and able to process time-tags, proper handling of unwanted signals is vital for increased sensor performance and is explored in the design section this chapter.

5.2 The Polarization Lidar for Aquatic Research (POLAR) Sensor Design

The Polarization Lidar for Aquatic Research (POLAR) SPL was assembled in an effort to meet several sensing requirements and advance the technology from TRL-3 to TRL-5/6. Measurements made in either a relevant or operational environment put significant demands on the

prototype sensor's design. To exit TRL-5 within the work of this thesis, airborne demonstration was necessary, including: 1) continuous operation in day-time and night-time environments to test the response to varying levels of unwanted scattered light, 2) provide detections of water surface, column, and subsurface layer detection in < 5 m of water depth, and 3) provide high resolution topographic mapping in both planes of receiver polarization.

5.2.1 System Overview

A passively Q-switched, frequency-doubled Nd:YAG microchip laser with a central wavelength of 532 nm, a PRF of 14.3 kHz, 35 mW of average power, and an FWHM pulse-width of < 700 ps was used as the transmitter source. The implemented PRF gave the system a range ambiguity of 70 μs, $\sim$ 10.49 km, which is sufficient for lower tropospheric detections from the ground pointing zenith during calibration and all altitudes from aircraft with proper measurable SNR considering the 2.45 μJ pulse energy. The physical laser head measures approximately 2x1x1", providing a compact solution to pulse generation, and is manually controlled through an external controller, or through an RS232 connection.

The beam is passed through a 5X Galilean beam expander to set the outgoing divergence at 2 mrad, and then a rotating zero-order HWP and a Glan-Thompson polarizer to ensure that the transmitted light has no excess loss in average power and a high degree of linear polarization. The beam is steered through rotating AR coated wedge pairs for far field alignment and to force transmitter/receiver overlap at a desired distance. A back reflection from the steering system is directed to a pin diode, which provides the laser firing signal to the counting system.

The transmit and receive channels are arranged biaxially and separated spatially so that full geometric overlap is achieved after 30 m when the wedges are in proper alignment. The backscattered photons are collected with a commercial 90 mm aperture F13.9 Maksutov-Cassegrain telescope and spatially filtered by an adjustable field stop at the telescope focus prior to collimation with an F/2 lens. The backscattered signals are then passed through a Glan-Taylor polarizer to split the S and P planes of polarization. Each channel is steered through laser line mirrors to

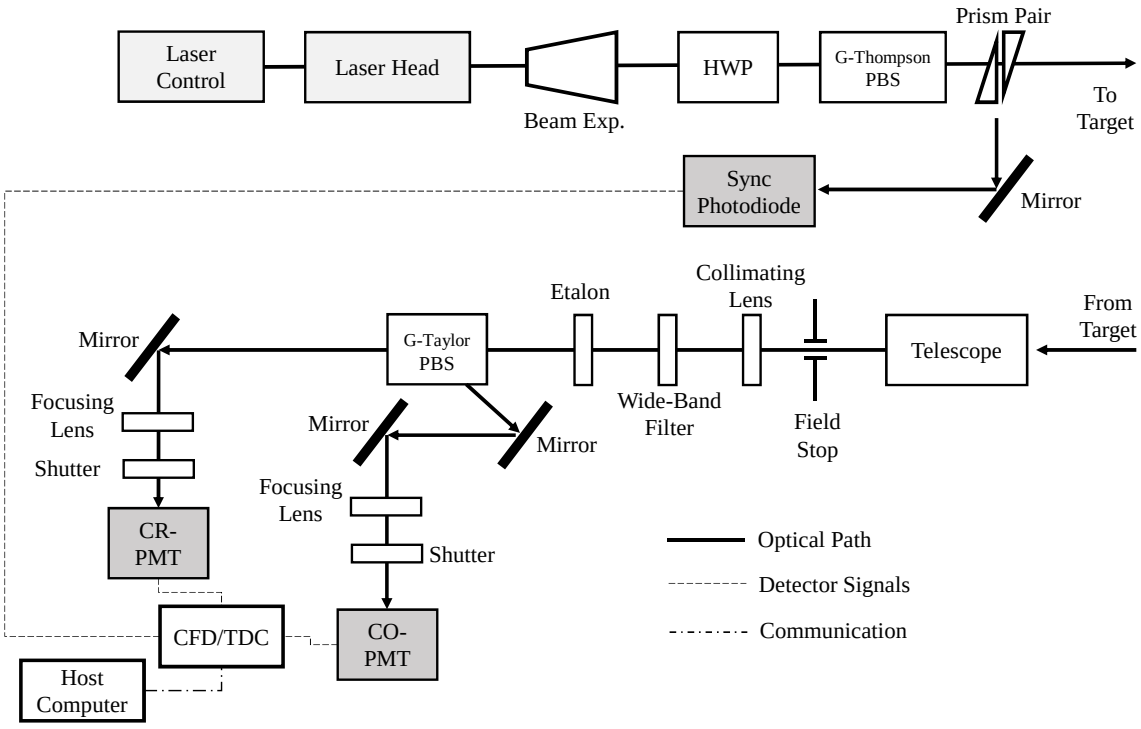

Figure 5.1: A block diagram of the POLAR SPL sensor. Here HWP stands for half-wave plate, G-Thompson PBS for the Glan-Thompson polarizing beam splitter, G-Taylor PBS for the Glan-Taylor polarizing beam splitter, CO-PMT for the co-polarized PMT, and CR-PMT for the cross-polarized PMT.

be focused onto separate Hamamatsu H7422PA-40 PMTs. The detectors have an average dark count rate of < 300 Hz, the TTS was measured to be ~ 280 ps, matching previously published values [8], and an FWHM SER output pulse width of ~ 3 ns at an average height of ~ 15 mV. Though these detectors were purchased for a different type of photon detection demonstration, the H7422PA-40 PMT is an excellent single element detector for TCSPC experiments due to the relatively low TTS value, high gain ($\sim 10^6$ at 800 mV), and overall stable operation. A Glan-Taylor polarizer in the receiver was placed in the receiver path to maintain the highest polarization purity in the co-polarized, or the S polarized reflection. There are benefits of adding additional clean up polarizers for the cross-polarized channel. Strong co-polarized specular reflections originating from the water surface sometimes surpass the rejection ratio of the polarizer and contribute erroneous cross-polarization detections. It was assumed that these effects would be infrequent with the pulse energies transmitted and any further decimation to the weak cross-polarized channel was avoided.

In order to ensure the ability to operate in a daytime environment, narrow spectral band filtering was implemented. Prior experience with the sensor demonstrated that daytime operation would result in a high enough average current on PMTs to trigger the fail safe current stop, causing the high voltage power supply to switch off and halt data accumulation. For operation during an airborne campaign, this was not desired. The solution was to implement a narrow-band solid etalon and a wider band interference filter in the receiver's optical path. The etalon provided the narrow band filtering while the additional interference filter blocked additional etalon orders that would have otherwise contributed to the unwanted signal. Inevitably the inclusion of these filters increases complexity and decreases the overall optical efficiency of the receiver, an ability to operate in high noise environments. The interference filter was procured from Omega Optical

Table 5.1: Summary of POLAR spectral filter characteristics

Filter	**Clear Aperture**	**Center Wavelength**	**Bandwidth**	**Transmission**	**FSR**	**Finesse**
Wide-Band	12.5 mm	532.20 nm	300 pm	$< 55.00\%$	N/A	N/A
Solid Etalon	15 mm	532.066 nm	23.4 pm	$< 74.00\%$	236.6 pm	10.1

and has a center wavelength of 532.2 nm, a bandpass of 300 pm, 55% transmission at the center wavelength, and a clear aperture of 12.5 mm. This optic was mounted separately from the etalon to prevent bandpass shifting while the etalon was tilt-tuned. This particular filter was designed to not need any additional temperature or temperature tuning in order to further align the peak pass wavelength. A small offset from the transmitter's wavelength was accepted.

A 19 mm clear aperture solid etalon was procured from LightMachinery with the measured specifications of a transmission peak at 532.066 nm, FWHM of 23.4 pm, a free spectral range (FSR) of 236.6 pm and a total finesse of ∼10.1. These parameters were measured at 0°, 30 C°, at 532 nm by LightMachinery. The etalon itself is a 400 μm thin film stack sandwiched between two fused silica plates giving it a $> \lambda/100$ surface uniformity. A housing was designed and fabricated to allow temperature and tilt tuning of the bandpass and center wavelength. A nested design was used whereby the exposed-air exterior portions of the housing were fabricated from delrin and the interior mounting for the optic was 6061-T6 aluminum. With this housing the total clear aperture of the optic was reduced to 15 mm. The mounting configuration allowed the optic to be heated and remain in a stable temperature bath, rather than consistently loose heat to the exterior cold air. Temperature tuning and stability was controlled via an OMEGA Engineering CN32PT-33C unit combined with a KHLV-101/10-P 5 W/in^2 kapton heater, and a TH-44006-40-T thermistor with a ±0.2° C accuracy. The housing was then mounted to a ThorLabs CR1 rotation stage with $\sim$ 1.5 mrad resolution in tilt tuning. The subsystem has the ability to redshift the pass band with the temperature tuning and to blueshift the pass band with tilt tuning. The passband was able to be brought into alignment with the laser center wavelength and minimize transmission losses. The complete assembly can be seen in Fig. 5.3, without the front face in place and with a summary of the specifications in Table 5.1, and further discussions of tuning and modeling are in Appendix A.

Implementation of the etalon with the particular laser available for this project initially raised concern. The microchip series of lasers available from TEEM Photonics inherently run multi-modal at the 1 μm generation, with a second mode at about 10% of the relative amplitude, which could contribute a significant amount of signal outside the etalon pass band. However, through the second

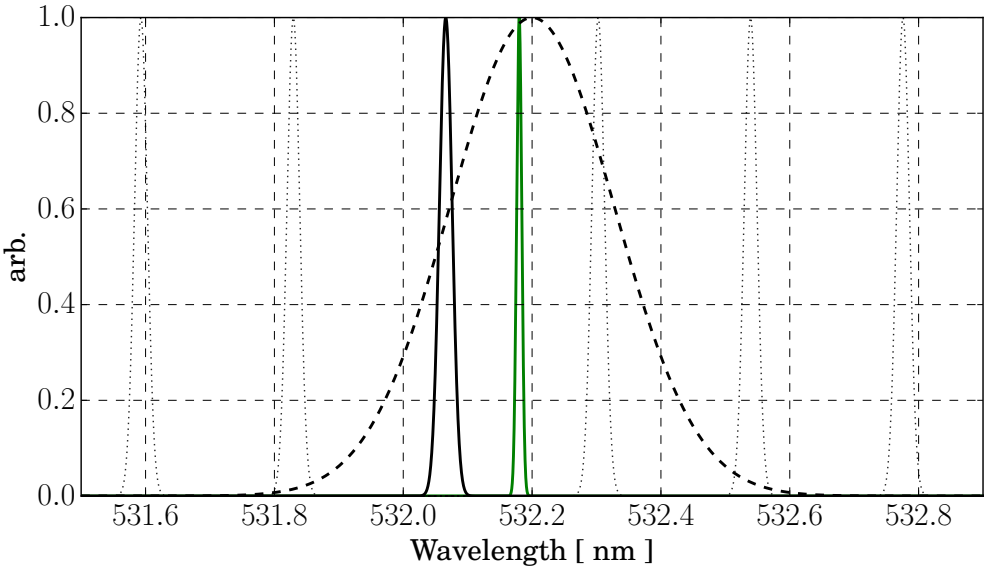

Figure 5.2: Locations and relative widths of the laser line, shown in green, the 300 pm FWHM interference filter, shown as the black dashed line, and the etalon, shown in solid black. Additional etalon orders spaced at the FSR = 236.6 pm are shown in the dotted black lines (actual out of band blocking is not zero, but ∼20 %, and is not shown between the peak and the FSR shifted locations). These locations were generated using the manufacturer's specifications and do not consider any temperature or tilt tuning. The etalon is tilt and temperature tuned to the proper location in operation.

harmonic generation, this mode is effectively suppressed and can be ignored. The manufacturer measurements estimate that the laser employed within the SPL sensor discussed within this chapter is effectively single-mode, with an estimated 532 nm linewidth of <5 pm, or ∼ 5.29 GHz, quelling concerns of lasing out of the receiver pass band.

The PMT pulses are passed through a CFD manufactured by SensL Technologies, Ltd., which removes the timing jitter from PMT gain variants. Unlike the differentiating CFD shown in Fig. 3.6 within Chapter 3, this circuit splits the signal into two parts, one of which is unchanged and a second that is inverted, fractioned, and delayed prior to being recombined with the unchanged input. This combined signal has a stable zero crossing, which then triggers an 8 ns TTL-level pulse at the final output. This 8 ns TTL pulse is fed to a SensL TDC as a STOP signal. Each detector channel has a dedicated CFD and TDC STOP to allow multiple inputs that can all be timed with 27 ps timing resolution. Each TDC has a manufacturer defined dead-time of 190 ns.

Figure 5.3: Mounted solid etalon in the aluminum inner and delrin outer housings. The front panel that completes the exterior insulating housing was removed to show etalon, sandwiched between two fused silica glass blanks, and floating in the inner housing. The ThorLabs CR1 rotation stage can be seen and the interior mounting screws (aluminum in this image, but delrin in final assembly) can be seen on the interior of the housing. The kapton heater was placed on the bottom of the interior aluminum housing with wiring exiting the right side of the delrin housing along with the thermistor wiring to the OMEGA controller.

The acquisition unit operates in what is called "resync mode," where a 250 kHz reference clock signal is fed into the START of each TDC, maintaining a stable source between all three channels that removes channel dependent time drifts and allows for high resolution cross correlations in post processing. Separate internal macrotime (time since start of experiment) and microtime (time between START and STOP signals) counters give a coarse and fine resolution to attribute the detection time to, with the microtime clock having picosecond precision. The algorithm that syncs the reference clock, macrotime counter, and microtime counter to arrive at an actual detection time-tag referenced to the start of the experiment at picosecond resolution is shown in Appendix A. It should be noted that in this configuration the laser firing signal from the pin diode is treated just as another separate detector channel and fed into its own TDC STOP, not as the START for the PMT channels. Operating in this manner puts the burden of correlation between laser firing

signals and detected photons into post processing, and has the added advantage of maintaining the timing of every laser firing so as to monitor transmitter performance. The onboard processing is limited only to the timing of each pulse. No other correlations or computations are performed.

Custom LabVIEW software was developed to communicate with the acquisition units and stream macrotimes and microtimes to file in a binary format using the SensL provided Windows DLLs. This software operates by writing out 1 second data files with a 0.1 second downtime between writes, giving a 90% duty cycle. Due to the $< 100\%$ duty cycle, some counts are missed during the acquisition process, but it was found that the duty cycle stays relatively stable in time assuming that detection rates stayed in the expected linear range.

Custom Python script was written to read in the binary data file and perform the conversion from binary to the desired values. The raw data consists of detections in the form of [CHANNEL #, MACROTIME, MICROTIME], with the channels representing the respective trigger or detector channel and the remainder being the respective FPGA clock times. Further Python script was written to perform the conversion from macrotime and microtime to time and range resolved photon time-tags. This includes resynchronizing the macrotimes and microtimes to the 250 kHz clock to generate a continuous timeline at the TDC resolution. The final output from this process is stored in a Python data frame as [CHANNEL #, DETECTION TIME, DETECTION RANGE]. This software was configured to grab data in real time to view the prior 5 seconds worth of detections during flight and analyze sensor settings.

It was anticipated that, with the acquisition unit's 190 ns dead-time, that time-tag throughput would be limited to approximately 5 MHz ($\sim 1/\tau_D$). Because of the configuration first-in-first-out (FIFO) buffer the total throughput would be shared among all three channels. Considering the 14.3 kHz PRF and an expectation that each receiver channel (signal plus noise) would be maintained to < 1 MHz, the sum across all channels was assumed to be < 4 MHz. With the implementation of narrow band filtering in the receiver chain, the throughput expectations were accurate in a majority of operational regimes. However, areas where bursts, or sustained periods of higher photon rates were present (from highly polarized solar background scatter from a water surface), this assumption

Table 5.2: Summary of the POLAR SPL specifications. All values were either directly measured, defined by the vendor, or estimated from literature.

System Parameter	**Value**
Wavelength	532.18 nm
Laser Repetition Rate	14.3 kHz
Laser Pulse-Width	<700 ps
Laser Output Energy	2.45 μJ
Transmit Divergence	2 mrad
Transmit Polarization	$[1, -0.9985, 0, 0]^T$
Telescope Diameter	90 mm
Telescope Focal Length	1250 mm
Receiver Field of View	2.5 mrad
Etalon Bandwidth	23.4 pm FWHM
Interference Filter Bandwidth	300 pm FWHM
Field Stop Diameter	2.5 mm
TDC Bin Width	27 ps
TDC Dead-Time	190 ns
CFD Dead-Time	8 ns
CFD Gain	Fixed 10X
PMT QE	40% QE
PMT SER	$\sim$ 15 mV, 3 ns FWHM
PMT Gain	10^6 at 800 mV
PMT TTS	280 ps
PMT Dark Counts	$\leq$ 300 Hz
Ideal Receiver Efficiency	14.78 %
Ideal Transmitter Efficiency	79.71 %
Data Duty-Cycle	90%

failed. Typically, when the maximum usable count-rate is reached in these systems the result, if the counter has a non-paralyzable dead-time, is a plateau of recorded photon rates at the maximum value. With the particular units used in the POLAR sensor it was found that this was not that case and instead there were issues of channel cross-talk at very high photon rates. This mixed detections between channels and resulted in an inability to correlate detections to laser shots. It was found that when this occurred a higher number of laser shots was recorded, typically in the range of $15 - 40$ kHz, which is a known quantity that should be unchanging at that magnitude. This metric was used as a flag for channel cross talk, and to avoid the use of contaminated data, a filter was put into the processing chain that examined the IPP of every laser shot. When the IPP was much greater than expected, e.g. IPP $\gg 70\mu$s, the detections from the receiver channels that

would be associated to that laser shot were ignored.

5.2.2 Assembly and Ground Testing

Collimation of the receiver optics was done in a series of three parts. First, there was a rough alignment using a pencil beam through the full receiver chain. A portion of the transmitted light was picked off and folded back into the receiver through a series of beam expanders, first a commercial 4X expander to bring the light to approximately 2 inches, then a custom 2X expander to bring the light close to 4 inches in diameter, filling the 3.5 inch telescope aperture. The light was traced through the receiver chain and the location of the collimating lens was placed after the telescope came out of focus, capturing the diverging light. This was achieved by examining the post lens interference pattern from a shear plate. However, it was recognized that this was only an approximate location, so the sensor was set zenith pointing to generate atmospheric signals. The atmosphere provides a well know signal gradient, which allowed fine tuning of the telescope's focal point during data acquisition through the primary mirror's micrometer adjustment.

It was realized after alignment and during the pre-flight testing that etendue was not conserved through the receiver due to the etalon being improperly matched to the telescope and collimating optics. This resulted in $\sim$ 4X the divergence in the receiver's optical chain than expected. Though this can sometimes be fine for optics such as the Glan-Thompson polarizer in the receiver, which has a several degree FOV, etalons require well collimated light to operate efficiently and maintain a narrow bandpass. As shown in Appendix A, the required collimation of the etalon used in this sensor is < 18.75 mrad, and with a 4X divergence the optic was operating at $\sim 20\%$ of its anticipated efficiency and the expected pass band was likely 3-4X wider, implying that there would be worse background rejection than anticipated. As shown in [75] and in Appendix A, the filter's bandwidth increases as a function of the incident cone of light's angles. When the non-collimated light goes beyond the normal-incidence acceptance angle, the effective bandwidth of the filter appears broader, namely due to a convolution of the normal-incidence bandwidth and the change in peak position due to the altered angle of incidence — e.g. $\Delta\lambda^2_{new} = \Delta\lambda^2_0 + (\Delta\lambda')^2$,

where the latter term is the added shift. The change in peak position then alters the transmission through the optic, modulated by $\Delta\lambda'$ as $T_\theta = (\Delta\lambda_0/\Delta\lambda')\arctan(\Delta\lambda'/\Delta\lambda_0)$ [75]. For practical scheduling reasons, it was decided to operate at a significantly decreased receiver efficiency but still have significant background rejection, < 100 pm bandpass.

A primary target of the POLAR sensor is discrimination of linear vertical and horizontal polarization planes of backscattered light. To ensure operation with a high degree of polarization purity in each channel, the transmitter and receiver polarization optics were optimized. This was done through a relatively simple method of fixing the transmitter's polarization to the desired plane (in this case linear vertical) and recording the Stokes components using an external analyzer as depicted in [36]. This set up utilizes a quarter wave-plate (QWP) and additional polarizer to generate estimates of linear rotation and ellipticity angles, by which the Stokes parameters can be computed, as seen in Chapter 2. The transmitter polarization was measured to be $\vec{S}_{tx} = A[1, -0.9985, 0, 0]^T$, with A being the total intensity, showing that the transmitted light had a high degree of purity.

The receiver's polarization was then set by folding the transmitted light into the receiver optics and minimizing the contribution in the cross-polarized, or linear horizontal, channel. The atmospheric gradient was used again to collect molecular Rayleigh signal, by which the co-polarized signal could be maximized. The outgoing signal from the Glan-Thompson polarizer sets the co-polarized channel as S polarized. Due to the receiver's Glan-Taylor polarizer, which reflects S-polarization while transmitting P polarization, the co-polarized signal would experience a higher rejection ratio with limited cross-talk. As seen in Fig. 5.1.

Data to compute the IRF's FWHM was generated for each receiver channel. Examples of such estimates are shown in Figs. 5.4 and 5.5, which were generated during the ARISTO-17 flight campaign discussed in the next section. Due to the introduction of roughness in the various targets used for backscattering, the IRF varied from $\sim 500 - 650$ ps with ~ 550 ps being the median value measured. The co-polarized channel shows returns that are tight around the peak with an FWHM of 541.57 ps, whereas the cross-polarized channel regularly had more dispersion about the fit with

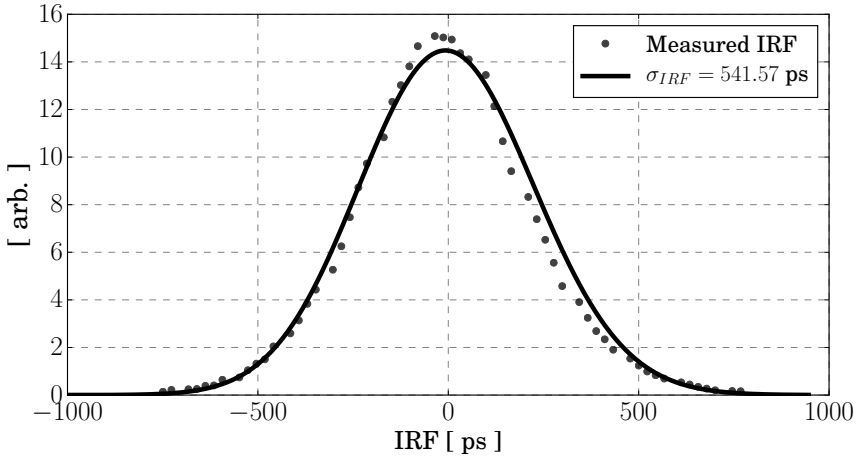

Figure 5.4: Measured IRF from the co-polarized receiver channel, shown by the black points. The fitted Gaussian profile is shown by the black line with an FWHM of 551.57 ps, or 8.118 cm.

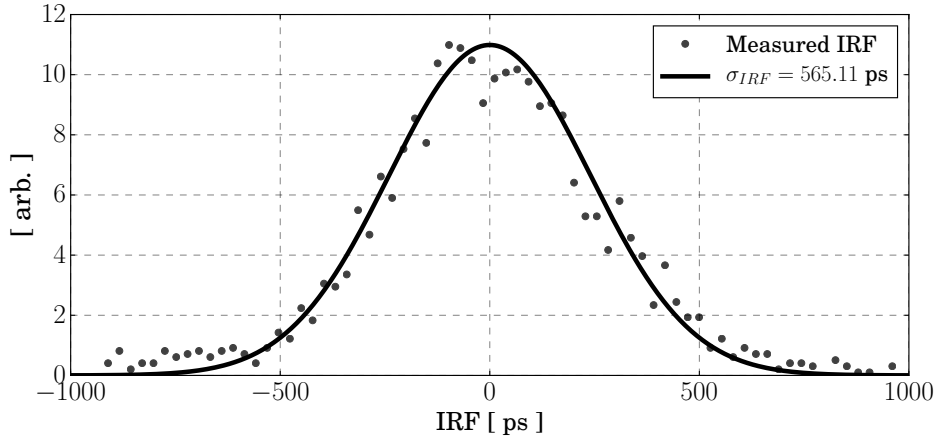

Figure 5.5: Measured IRF from the cross-polarized receiver channel, shown by the black points. The fitted Gaussian profile is shown by the black line with an FWHM of 565.11 ps, or 8.471 cm.

an FWHM of 565.11 ps. It is likely that this is due to a lack of signal over the integration period in the cross-polarized channel, and some unaccounted for timing uncertainty. Given the IRF values, some initial uncertainties can be attributed to each photon measurement per channel. For a single detection made in the co-polarized channel, the 1σ uncertainty on the measurement is 3.447 cm. For the cross-polarized channel the 1σ uncertainty of a single detection is 3.597 cm. This implies that, for any one photon detection, the estimated range will not be known to better than 3.5 cm, and while operating in photon counting mode, the distribution built up for an object will have a minimum width equal to the IRF of the channel being analyzed.

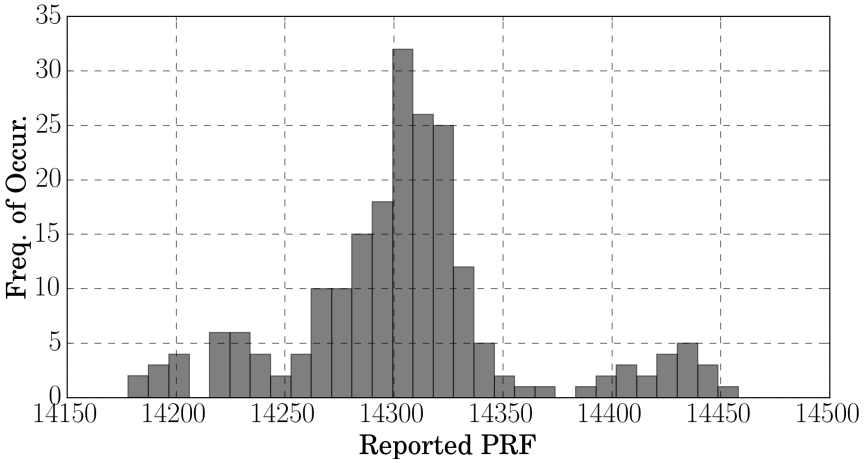

Figure 5.6: Measured distribution of laser PRFs accumulated over 250 seconds of pre-flight testing. The peak can be seen at 14.3 kHz, but a slight jitter is seen causing retrieved values at 14.18 kHz and 14.45 kHz. The jitter causes changes in the IPP, and thus unambiguous range, but is considered acceptable due to the operational range of the sensor.

The ability to log the laser's PRF was tested using the time tagging method, shown in Fig. 5.6, where 250 seconds of data was accumulated. From this data the time-tags associated with the laser were used to calculate the IPP, and the total counts per second gave the PRF. It is clear that the laser has some PRF jitter, where counts are seen ± 100 Hz on either side of the 14.3 kHz peak. This can partially be explained by the microchip laser employed which utilizes Semiconductor Saturable Absorber Mirrors (SEAM) as a passive Q-switching mechanism. The short cavity length

allows for the compact size and provides the short pulse width (< 700 ps), but is susceptible to this shot-to-shot timing jitter [54]. To monitor laser health during flight operations analysis of the PRF is performed for each data file and used as a possible erroneous data flag.

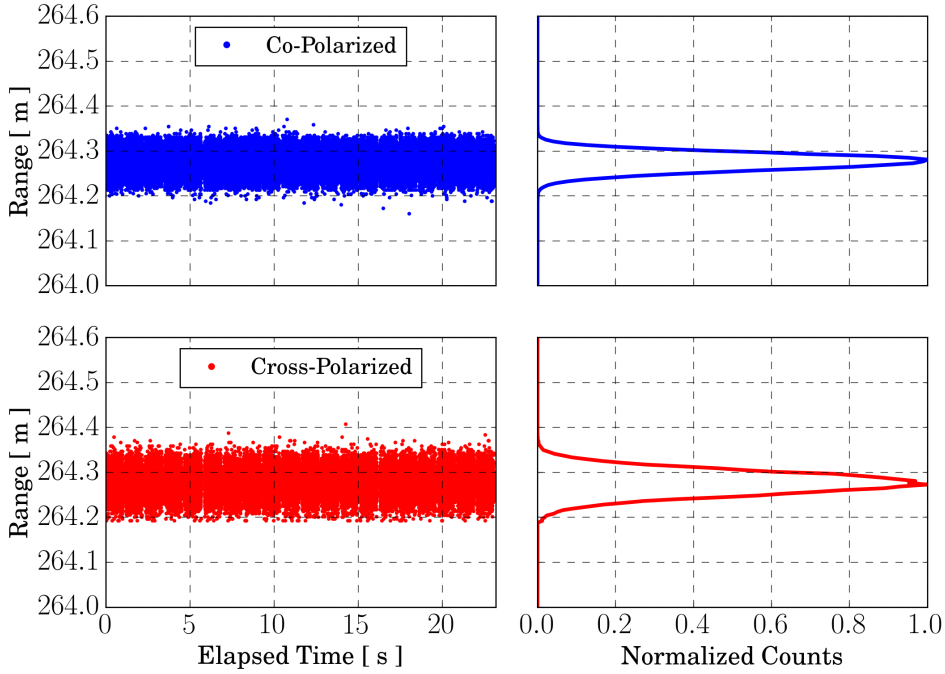

Figure 5.7: Example of the collected long range photon detections made during preflight ground testing. The top panels shows collections from the co-polarized channel, with the left showing the point cloud and the right the histogram with 4 mm bins. The lower panels show the results for the cross-polarized channel.

Ranging data was taken in a night-time environment, to minimize unwanted signal contributions and to establish long range histogram shapes for both polarization channels. The target was a rough, unpainted slate wall, which was expected to provide decent depolarization. Figure 5.7 shows panels that display >20 s of photon time-tags for each polarization plane at a stand off distance of $\sim$ 264 m. The detections were made at the 4 mm TDC resolution and accumulated into normalized histograms with equivalent bin resolution. The co-polarized channel exhibits a narrower distribution than the cross-polarized channel, resulting from sensor settings during the measurement (though it is expected that, given the nature of depolarization, the cross-polarized

channel will receive less counts and the distribution parameters will have higher uncertainty). The optical path length was used in the processing, and centimeter differences between channels was removed. Given the transmitter divergence, the illuminated spot at this range was calculated to be 52.85 cm in diameter, which was confirmed visually.

The remainder of ground testing was performed off of the atmosphere to ensure that alignment between the transmitter path, including clocking of the prisms, and the receiving path was in good agreement with geometrical models. The sensor's geometrical overlap was not directly measured, but signal strengths were compared to computed models. The sensor's geometry was computed using the biaxial formulations in Halldorsson *et al.* [41], though this simple calculation is unable to capture the additional pointing geometry due to the prisms. The model predicted that the sensor would be in full overlap $>$ 100 m for the entire unambiguous range. The acquired atmospheric data showed that, due to the prism pointing, this was an over estimate, with the true overlap point occurring closer to 50 m. Despite the uncertainty between the model and measurement of the overlap point, the sensor was overlapped out to infinity $>$100 m, ensuring that detections from the expected flight altitudes of 100 m to $>$1000 m would be easily accommodated with out any additional geometric losses.

Additional testing was performed with the etalon installed to ensure that the average PMT current did not surpass the over-current limit while operating during day time noise conditions. It was concluded that the sensor could operate in the bright daylight conditions, and after testing it was deemed that the sensor was in proper configuration for flight and ready for aircraft integration.

5.3 Relevance to Posed Thesis Questions

Development of the flight ready POLAR sensor provides a crucial step towards demonstrating many of the ideas and techniques discussed throughout the prior chapters. The initial testing and characterization created the necessary laboratory verification of sensor parameters, establishing the readiness for flight. The follow on chapters will provide demonstration and validation of this sensor and discuss relevance to the thesis questions in more detail.

Chapter 6

Flight Demonstration of the POLAR Sensor

This chapter describes efforts to experimentally demonstrate many of the topics discussed in prior chapters and to provide partial validation of the concepts presented. Emphasis was put on evaluating the photon time-tagging method in non-ideal measurement conditions utilizing the POLAR sensor and on generating data by which algorithms and further methods could be derived.

Generation of POLAR's performance metrics, expected and measured, are discussed in terms of noise rate, probability of detection, and points per linear meter (PPLM). The integration of the POLAR sensor the NCAR GV research aircraft is shown and an example of a calibration data set that demonstrates expected distribution widths and channel offsets. A high level description of necssary algorithm development is given, focusing on the two most prominent when dealing with airborne SPL data: georeferencing and surface finding. In the case of georeferencing, assimilation with aircraft data is required to perform the needed coordinate transformations and arrive in the correct ground reference frame, however it is through these transformations that POLAR vertical data accuracy degrades due to the non-ideal aircraft subsystem accuracy (i.e. GPS heights $\geq \pm 10$ cm vertical accuracy limits the absolute accuracy on the final data product). The data, and subsequent analysis, is presented in four distinct case studies: ocean surface sensing, ocean subsurface sensing, topographic mapping, and atmospheric clear air. Each are discussed for their relative pros and cons and implications of non-perfect sensor configurations that can impact data retrievals. These case studies provide data to inform robust future sensor builds for multi-campaign deployments, and provide validation for the overall measurement techniques.

6.1 NCAR ARISTO-17 - Engineering Data for Flight Evaluation

The POLAR SPL sensor was approved to fly on the NCAR Gulfstream GV, Fig. 6.1, as a part of the Airborne Research Instrumentation Testing Opportunity (ARISTO) in Spring 2017. The ARISTO program is an NSF-sponsored flight test program conducted annually on one of the NSF/NCAR aircraft in support of NSF funded (or partially funded) projects that require airborne testing or demonstration. As part of this project was funded by the NSF IIP 1500166 award, the POLAR sensor fit "Priority 2" for inclusion. There is a second aspect that makes the ARISTO program unique, which is the inclusion of students. Undergraduate and graduate students participate in the program and develop skills that are necessary to become airborne scientists, capable of contributing viable and useful science to the community. Throughout the program, engineering support was provided by the NCAR Research Aviation Facility (RAF) staff, assisting in mechanical and electrical developments as well as flight planning and research coordination.

Figure 6.1: The NSF/NCAR Gulfstream GV.

Several operational goals were laid out for the POLAR SPL sensor for the duration of the ARISTO-17 field campaign, most of which were desired in order to demonstrate the multi-functional applicability of the sensor and to show detection sensitivities in a myriad of operational regimes. It was anticipated that each of the desired measurements for multi-functional demonstration would be generated separately from each other. This was predominantly due to limited sensitivity over large

altitudes, implying that simultaneous, large altitudes of atmospheric column could not be measured while also measuring surface targets. As this experiment was an engineering demonstration, this was accepted and emphasis was put on maximizing measurements independently.

In addition, the flights also offered the ability to validate sensor models, allowing utilization of the ATLIS simulator. Representative models served to facilitate insight into conditions where POLAR could attain measurements that would fulfill the desired goals. Lastly comparison to the ATLIS simulator could assess whether performance in these conditions could properly be predicted.

6.1.1 Multi-Functional Measurement Goals

Demonstration of the POLAR SPL and its multi-functional utility requires that data collections be made simultaneously across the full column using the two receiver channels for all detections. Although it is typical to spread received signal over several detectors to achieve the desired dynamic range for each regime of signal, the POLAR SPL's emphasis was put on tuning to the strongest signals present (water surface) and accept some loss of signal from weaker scatterers. This greatly reduced the sensor complexity and allowed the implementation of only two detectors. The implemented design has measurement implications for atmosphere, water, and topography extractions, which must all be done on the same set of photon time-tags for either polarization plane. This also includes channel dependent management of the variable noise regimes that are present in each measurement environment, such as low noise rates over open ocean and high rates over the transition from land to ocean or over cloud tops.

The macroscopic goals of the flight program were to collect engineering data to advise future builds to provide

- demonstration of water surface detection;
- demonstration of water column and subsurface detection;
- demonstration of dual polarization hard target mapping; and
- demonstration of atmospheric profile generation.

In each of these demonstrations there were several performance metrics — e.g. flight altitudes, probability of detection per receiver channel, number of resolvable points— that were derived to support the operation goals of the particular sensor, shown in Table 6.1.

Table 6.1: The POLAR sensor requirements for ARISTO-17, also showing the expected and measured values.

Observation	**Channel**	**Requirement**	**Expected Value**	**Measured**
General	Both	Operational Range	100-1500 m	150-2000 m
General	Both	Operational Speed	$< 90 - 200$ m/s	$< 90 - 200$ m/s
General	Co-Polarized	Noise Rate	< 50 kHz daytime < 1 kHz nighttime	< 10 kHz < 0.5 kHz
	Cross-Polarized	Noise Rate	< 50 kHz daytime < 1 kHz nighttime	< 5 kHz < 0.5 kHz
Water Surface	Co-Polarized	P_D PPLM	$> 10\%$ for pitch $< 5°$ $\gg 1$	40 % avg. ~ 34 avg.
	Cross-Polarized	P_D PPLM	$\ll 1\%$ $\ll 1$	$< 1\%$ avg. $\ll 1$ avg.
Water Subsurface	Co-Polarized	P_D	$> 5\%$	$< 1\%$
	Cross-Polarized	P_D	$> 5\%$	$\ll 1\%$
Topography	Co-Polarized	P_D	$> 10\%$	$< 4\%$
	Cross-Polarized	P_D	$> 10\%$	$< 2\%$
	Both	PPLM	> 5	< 4 avg.
Clear Atmosphere	Both	P_D	$> 0.1\%$	$\ll 1\%$

Of the requirements, water subsurface detection proves to be the most challenging and depends on several other factors being met. For the cross-polarized channel to see depolarized water column returns, the water surface must be polarization preserving and not contribute detections that would cause the column returns to fall into a dead-time window. Expectations are that P_D and point density for water surface and topography will be met. The clear atmosphere measurements are low due to sensor design, but extraction over long integration times will be possible. Noise rates must be managed well for all requirements, with the laid out values achievable if the receiver's etalon is in place.

6.1.2 Sensor Integration and Calibration

The POLAR SPL was integrated to the forward nadir optical viewport of the GV. The polarization preserving window usually deployed with the NCAR high-spectral-resolution-lidar was used, as it had the necessary coatings for operation at 532 nm. The sensor mounting system, designed in conjunction with NCAR RAF mechanical engineers, employed a fixed tilt of 3.5° to bring the sensor's pointing as close to nadir as possible in anticipation of aircraft pitch during the planned flight lines. A solid model of the installation is shown in Fig. 6.3, displaying the sensor, mounting hardware. High frequency dampners were utilized to reduce vibrations, baffling down to the window, and subsequent light tight cover. Figure 6.2 shows the final installation inside the cabin with light tight protective cover installed. Figure 6.4 shows a view from underneath the aircraft looking at the receiver baffle, the telescope's primary and secondary mirrors, the transmit close out tube used to isolate the receiver from window reflections, and the window blank used to block the remainder of the window from contributing extra solar background to the receiver FOV.

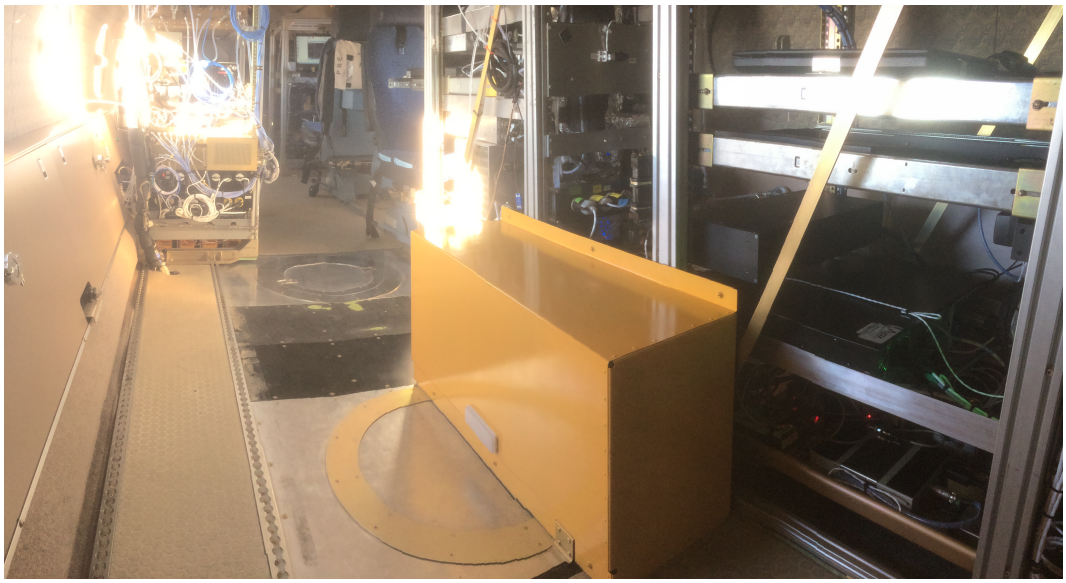

Figure 6.2: View of the mounted POLAR sensor in the GV cabin. The acquisition unit, detector controllers, and laser controller are shown on the lowest tray of the right hand side rack. The top tray has the acquisition computer to manage data collection, accessed remotely from aircraft's rear.

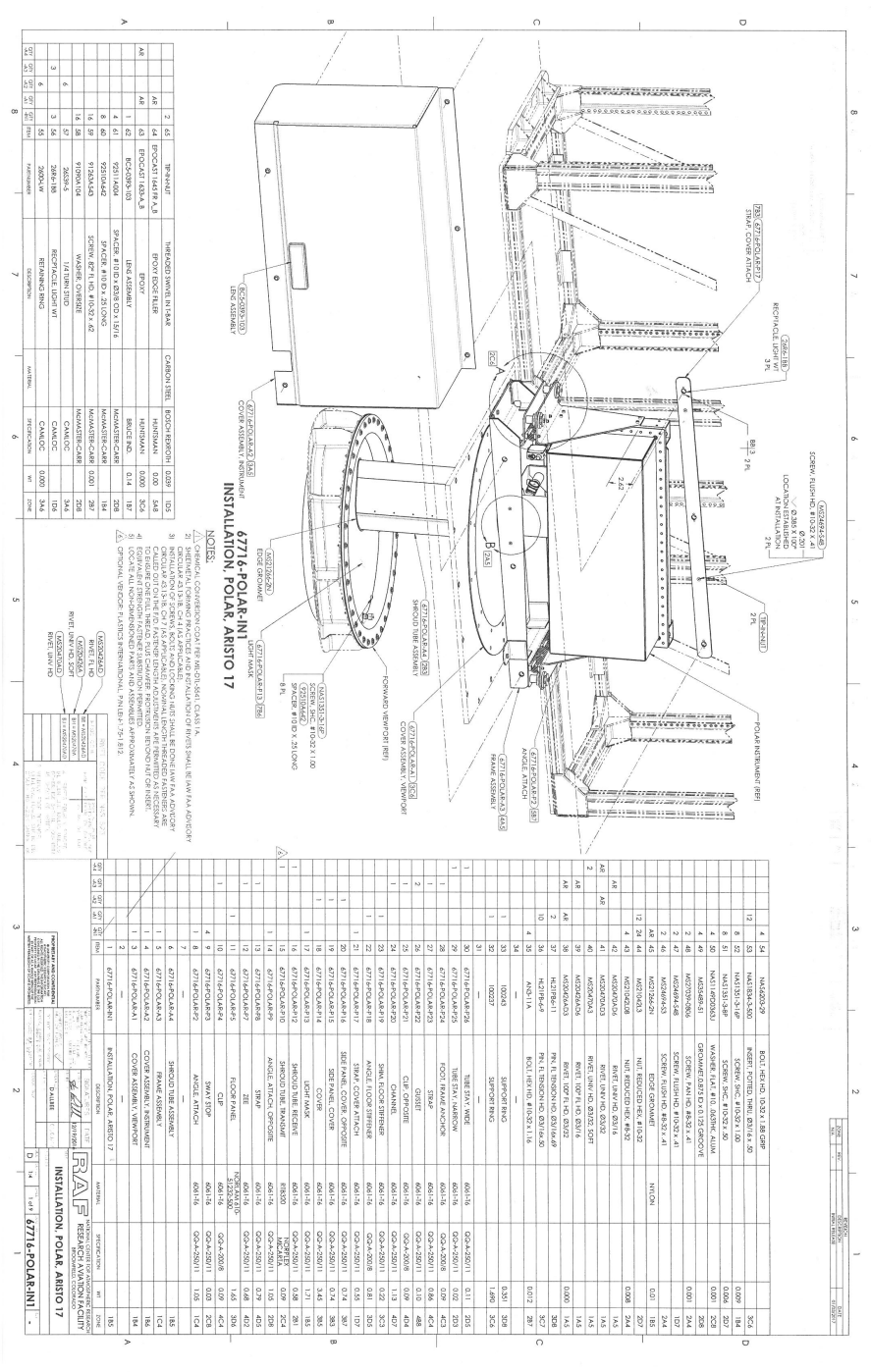

Figure 6.3: Mounting configuration for the POLAR SPL onboard the NCAR GV. The sensor has a fixed 3.5° tilt to compensate for the aircraft's attach angle during flight lines. The sensor is mounted to the seat tracts through wire rope isolators with motion restrictions that prevent large scale oscillations. A baffling system separates the transmit and receive paths of the sensor to block window reflections from entering the telescope's FOV. Un-utilized Window area was blocked by an aluminum cover to prevent excess light pollution. Further light tightening covers secured the mount to the co-located instrument racks as well.

The sensor's electronics were mounted on two trays occupied in a co-located forward rack, seen in Fig. 6.2. All acquisition electronics, including CFD/TDC and PMT controllers, were housed in the rack with the data logging computer situated at the top of the rack in a pull out tray. The data logging computer ran autonomously once acquisition started, but could be accessed remotely from the aft of the aircraft. Data logging was synced to the common aircraft time to allow correlation with other sensors onboard.

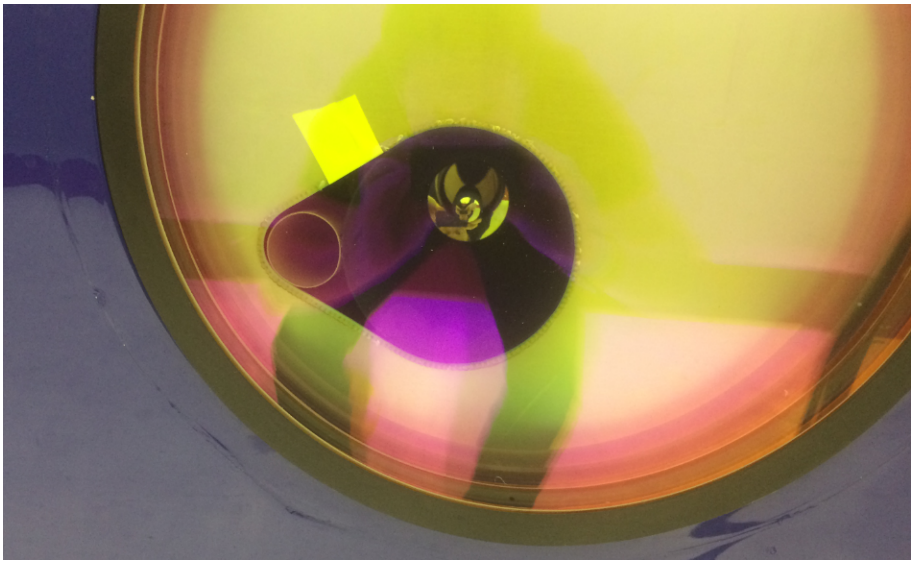

Figure 6.4: A view of the GV's underside looking upwards. Separation between the receiver baffle and transmitter tube can be seen. The unused window aperture is blocked for noise purposes.

Because POLAR is a polarization sensitive sensor all optics post transmitter must be examined for possible detrimental effects to the transmit and received polarization planes. For aircraft operations this puts emphasis on the optical window where an ill-suited coating can retard the outgoing light's polarization and decrease overall transmission. Prior experiments demonstrated that improper coatings can introduce a retardance of 10° which subsequently put energy into the S_3 Stokes parameter and causes a $> 20\%$ reduction in transmission. As shown in Chapter 3, the polarization calibrations of the POLAR sensor are within a $1 - 2^\circ$ angular offset between the transmit and receiver polarization planes. This can be viewed in two ways, either as an imperfect transmitter that has some energy put into the cross-polarized plane, or an imperfect receiver that

will not have the expected rejection ratios per S and P polarizations, both of which are exacerbated by a retarding window.

The overall effect of misaligned transmit and receive polarization planes on measurements can be consequential. The clearest example arises when the sensor is observing polarization preserving water surfaces, such as the clear ocean surface. In a sensor with perfectly matched polarization there will be no surface detections in the cross-polarized channel, unless there are signals stronger than the rejection ratio of the polarizer and leakage occurs. When the polarization planes are not matched perfectly, there is some probability of surface detections in the cross-polarized channel due to a portion of the transmitted energy being present in that plane. The long dead-time of the timing system cause erroneous water surface detection to directly reduce depolarized water column detections and negatively impact sensor performance in that regime.

Due to the 3.5° fixed tilt of the sensor relative to the airframe, analysis was performed to test for any added polarization attributes from the GV window. The transmitted Stokes vector was measured of the sensor alone earlier in this chapter, showing a DOP $> 99\%$. There were non-zero fluctuations in the S_2, but this was deemed a response to the power meter used. The GV window was put in the transmit path at $\sim 3°$ and it was found that no added retardance or rotations were present and the measured Stokes vector experienced no change. Transmission through the window was found to decrease to under 2% such that the round decrease in efficiency was on the order of 3-5%. The conclusion of pre-flight polarization testing was that measurements would not be hindered with use of the GV window. This measurement is further elaborated in Appendix A, which shows the transmitted Stokes vector estimate and experimental set up.

Range calibration of a non-scanning SPL sensor is a relatively simple endeavor and can be performed on the ground prior to flight. The primary purpose is to estimate path length differences between channels, using a known target, and the overall offset from absolute range. Both estimates are necessary for the processing of the airborne data. Figure 6.5 shows the raw photon point clouds and ranging histograms of the hangar floor as measured from the final installation location. The transmitter signal strength was decreased by an OD4.0 neutral density filter to maintain operation

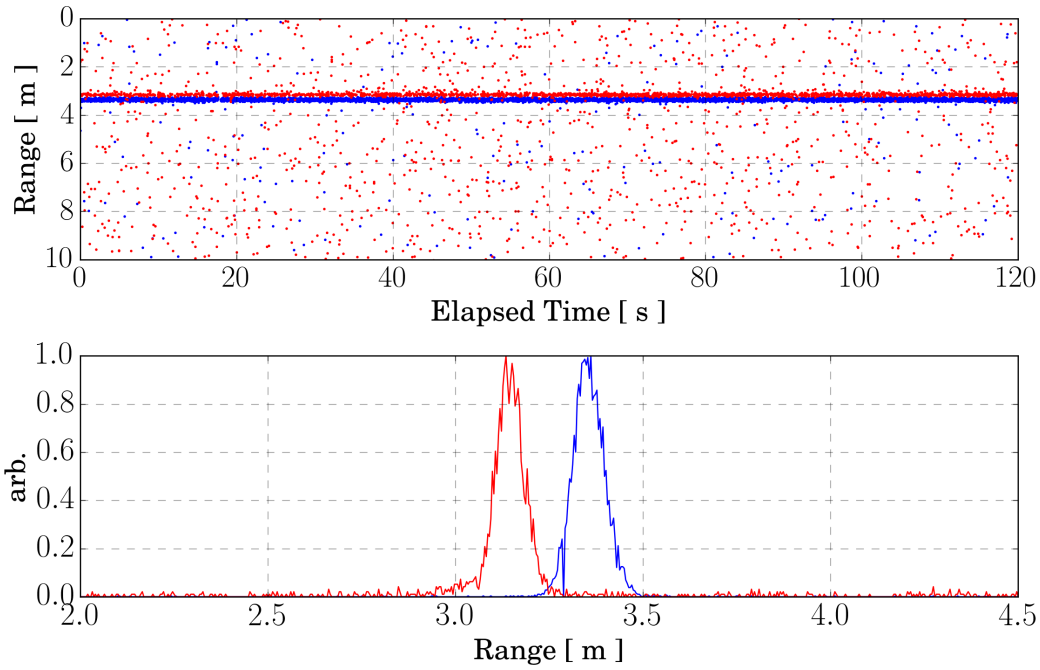

Figure 6.5: The top panel shows the raw un-calibrated point clouds, with co-polarized in blue and cross-polarized in red, ranging from the aircraft to the hangar floor. The bottom panel shows the integrated histograms over the entire time window with binning at 4 mm resolution. The offset caused by relative path length difference between channels can be seen, measured at 0.1837 m.

in photon counting mode. In this configuration channel path lengths were measured as the offset between the timing histograms, giving a difference of ~ 0.1837 m. This is primarily a result of the optical path length of the co-polarized channel. To mitigate further discrepancy between channel offsets all signal cables, including PMT to TDC and connections between the 250 kHz clock and the input TDC channel, were equivalent in length.

The calibration data in Fig. 6.5 also facilitated an understanding of relative signal diversity for the particular set of PMT and CFD settings. It was found that small deviations in the PMT high voltage or CFD settings produced no discernible effect to the retrieved data, assuming that the sensor was operating in photon counting mode. This implied that calibration parameters could be maintained for all linear counting regimes during flight.

6.1.3 Photon Time-Tag Processing

Processing the photon time-tags generated by the POLAR SPL for multi-functional observations takes two separate paths, depending on what portion of the unambiguous range is being processed, e.g. atmosphere or surface, as shown in Fig. 6.6 below.

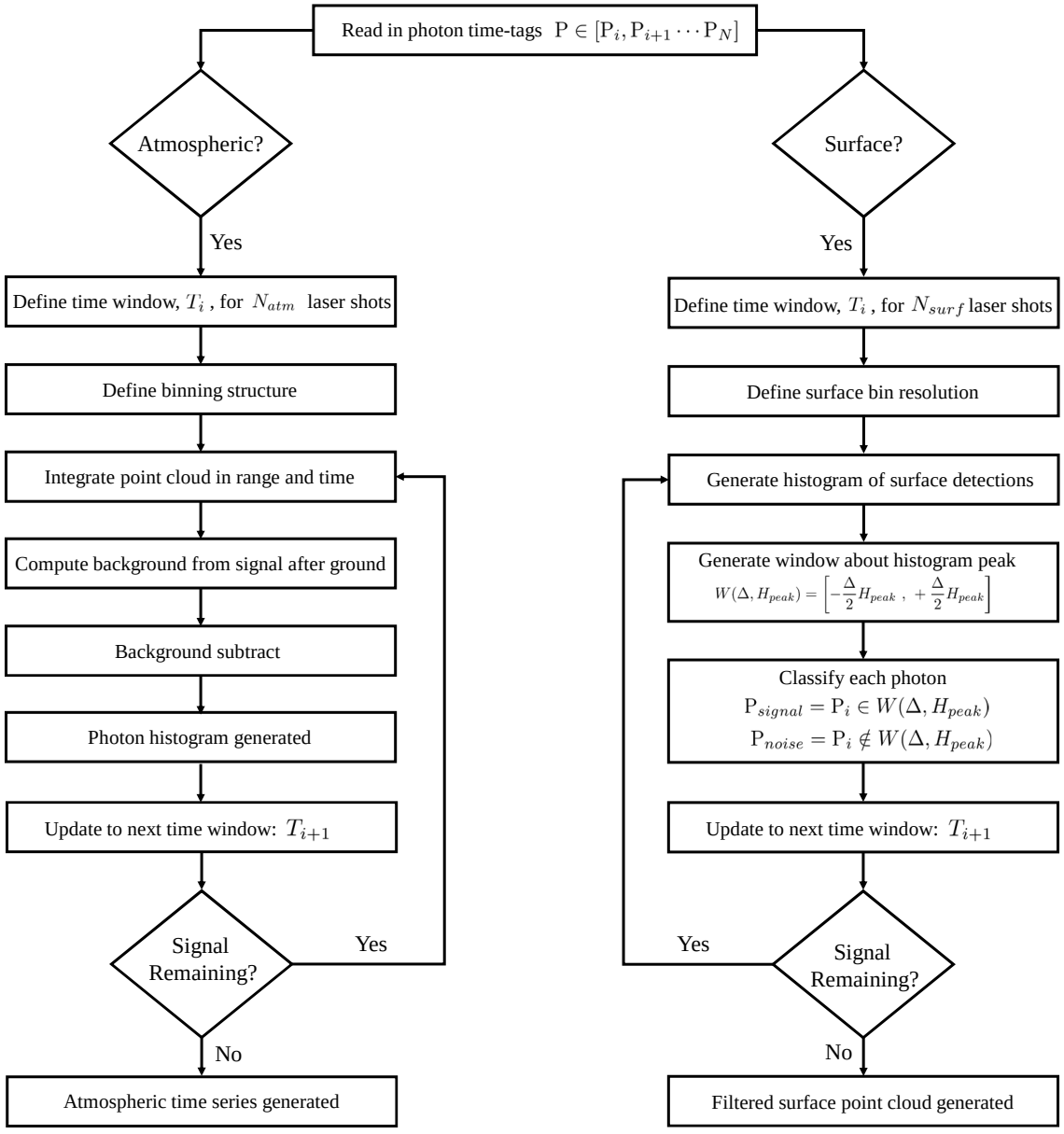

Figure 6.6: Processing flow chart for a stream of photon time-tags. The left side describes how the atmospheric signal is processed and the right side describes the flow by which surface photons are processed. This processing flow is valid for geolocated or raw photons.

The employed surface algorithm was developed for this campaign following the initial logic laid out in [52], but simplified to allow fast running for quick evaluation of data. A main objective was the ability to separate most of the unwanted signal from the target signal and remove after-pulsing if present. The processing of surface photons follows the right hand side of Fig. 6.6. First, a time window at an integer multiple of the laser's IPP, T_i, a desired range resolution, R_i, and a range window of Δ for processing is defined. Then, with an input vector of some N time-tags that have undergone time correlation with the laser sync, $[P_i, P_{i+1} \cdots P_N]$, are histogrammed over T_i with a bin resolution of R_i. The histogram bin with the maximum number of counts is retrieved, H_{peak}, and the window, $W(\Delta, H_{peak})$, is then applied to $\pm\Delta/2$ bins around H_{peak}. The resulting ranges contained within $W(\Delta, H_{peak})$ constitute the signal photons and the remainder are considered noise photons, such that classification gives: $P_{signal} = P_i \in W(\Delta, H_{peak})$ and $P_{noise} = P_i \notin W(\Delta, H_{peak})$. The time window is then slid to T_{i+1} to capture the next photons.

Performance of this technique is limited by the definitions of T_i, R_i, and Δ, which must be manually investigated for proper values prior to implementation of the algorithm. Specific values of each differ depending on the surface structure. For example, in the case of a rough surface that introduces a significant amount of geophysical timing variance to the received signal envelope and Δ must be increased to values much greater than the IRF. This is also the case for sensing in varying terrain, where slope changes introduce significant width to the surface histogram. The definitions of T_i and R_i are tuned so as to maximize the SNR of the surface signal, ensuring that the separation between correlated signal and uncorrelated noise is distinct. If T_i or R_i prove too small, the correlation analysis and windowing will fail due to lack of separation.

This specific technique works best for signals of high spatial correlation, where the simple windowing captures the histogram of surface signals and separates most noise (though it is accepted that some noise is retained in the process, and a minimized contribution is pursued). It is robust enough to enable performance analysis of the sensor, but it does not have the necessary density checks that automatically scale parameters for maximum noise classification. It should be noted that this algorithm does not operate for distributed voluminous signal, such as atmospheric or water

column, unless the spatial and temporal correlation is high. Further work should be pursued to apply this technique to cloud edges, or other atmospheric features with relatively sharp boundaries.

For atmospheric analysis an approach of generating an MCS like data set is used. Similar to surface finding, a time window over which the photon time-tags are to be integrated, T_i, is defined. However, unlike the surface finding, this is typically on the order of > 10 Hz due to the low number of atmospheric returns from the non-atmospheric optimized POLAR sensor. The range bin resolution of R_i is typically set > 10 cm, chosen from prior experience discussed in Chapter 3, and a binning structure of the full unambigous range of the sensor (~ 10.49 km) is defined such that the number of computation bins are $n_{bins} = (\sim 10.49 \text{ km})/R_i$. Each time-tag in the T_i window is distributed into the specific bin of the profile based on the time-tag's associated range. With the full profile generated, the surface bin, if present, is found and a background estimate is generated. A geometric mean is taken over the subsurface bins where it is expected that the detections are due solely to solar background and dark counts. If no ground is present, the estimate is made near the end of the unambiguous range, where it can be assumed there there is little to no signal present. The background estimate is then subtracted from the profile and the time window is slid to T_{i+1} for the next profile. The output is a time series of atmospheric returns in a form equivalent to an MCS output, where time moves along the x axis, range along y, and each bin contains the number of photon counts per that bin.

This approach was applied to the atmospheric signals shown in Chapter 3, but with changes in the integration window and where the background estimate was generated. In the case of known atmospheric signal where a cloud or other feature is present, the background estimate is taken after this feature and applied to the lower atmospheric returns with the assumption of extinguished pulse energies post cloud. If cloud tops are seen in the atmospheric column while analyzing the POLAR data collected from the flight campaign, this method can be applied.

A dedicated inertial measurement unit (IMU) and global positioning system (GPS) receiver was not flown for the ARISTO-17 campaign. Because of this, the GV's onboard IMU/GPS data stream was used to facilitate geolocation of each laser shot and received photon event. Specific

information about the subsystem hardware was not given, but a data stream and location in the aircraft fore each component was provided. Utilizing this data stream with SPL data for photon geolocation requires the data rates from each subsystem to be assimilated to a common cadence.

A method was derived to assimilate the the aircraft 50 Hz IMU, 10 Hz GPS, and asynchronous $>$ 14.3 kHz SPL data. All three data streams were time-stamped with the onboard GV timing server, providing a common timer despite the different data rates. The method employs a series of searching functions and is designed for accuracy, at the cost of computation time, and is therefore only used in post-processing. All photon detections, $[P_i(t_i), P_{i+1}(t_{i+1}) \cdots P_N(t_N)]$ are read into the script along with the aircraft data. The nearest two bounding aircraft times, before and after, for the first photon detection, P_i at time t_i, are found. A cubic spline is then fit to each desired parameter in the aircraft data, and the associated acquisition times, between these two time values and interpolated to approximately 1 MHz. A binary search is then performed on the interpolated data for the nearest time value to the detected photon. When found, the closer of the two interpolated aircraft data points is recorded. The next photon detection at t_{i+1} is then examined to see if it falls within the interpolation period, if it does then it is assigned the closest value through another binary search. This continues for all photon detections within the interpolated time window until a photon outside of the window is present. The window then slides to the next set of aircraft time values and continues the binary search process until the last P_N photon is processed. This assimilation method assumes that all data values will be linearly ordered in time and does not distinguish between signal and noise. Because of this, when there are large noise rates present the processing speed slows down significantly, implying that it is advantageous to first filter the point cloud for signal and remove noise from the time-tag vector. The output of this function is a data frame giving each laser shot, detected photon, and all associated aircraft parameters —latitude, longitude, altitude, pitch, roll, etc.

There are a number of required inputs for the georeferencing process collected from the IMU, GPS, and the SPL sensor. To reference each photon detected to the geoid height, the following is needed: GPS time, $(x, y, z)_{GPS}$, roll, pitch, yaw, and the time-tag's range from the

SPL. Measurements of offsets between the POLAR sensor, the IMU, and the GPS antenna are also required for the transform. Lever arms were measured from POLAR's laser sync detector to the IMU and GPS roof antenna to within 5-10 mm precision, using calipers and measuring tapes.

To generate geolocation information for each time-tag, the methods as described in [120, 109] were implemented. These methods require a series of rotations and transformations from the sensor frame to the aircraft frame and then to the earth-centered-earth-fixed (ECEF) WGS84 frame. In the WGS84 frame the time-tag's surface point is reported by the elevation, latitude, and longitude coordinates. The photon elevation is give by the geolocation equation [120] as

$$\vec{\rho}_{WGS84} = \vec{\rho}^{GPS}_{WGS84} + R^{-1}(\lambda, \phi - 90°, 0)R^{-1}(\beta, \alpha, \psi)\left\{R^{-1}(\Delta\beta, \Delta\alpha, \Delta\psi)\vec{r}_L + \vec{r}^{L}_{GPS}\right\}, \qquad (6.1)$$

The term $\vec{\rho}_{WGS84}$ is the final WGS84 referenced elevation, $\vec{\rho}^{GPS}_{WGS84}$ is the retrieved aircraft position from the GPS, $R^{-1}(\lambda, \phi - 90°, 0)$ are the rotation matrices to rotate into the latitude/longitude/altitude axes, $R^{-1}(\beta, \alpha, \psi)$ are the rotations from the aircraft axes to the GPS frame, $R^{-1}(\Delta\beta, \Delta\alpha, \Delta\psi)$ are the rotations into the aircraft frame that accounts for offsets of the SPL sensor relative to the IMU (here the POLAR sensor is fixed at $\Delta\alpha = -3.5°$), $\vec{r}_L$ is the measured slant range, and $\vec{r}^{L}_{GPS}$ is the lever arm between the sync detector and the GPS antenna. The notation of λ and ϕ are the longitude and latitude, respectively. The notation of β, α, and ψ give the yaw, pitch, and roll respectively. The final georeferenced point cloud contains some N number of photon detections, with each assigned WGS84 elevation, $\vec{\rho}_{WGS84}$. With the aircraft motion removed, it is this point cloud that can be analyzed for geophysical parameter estimation.

It is typical to perform specific flight lines to estimate the boresight misalignment parameters $\Delta\beta, \Delta\alpha, \Delta\psi$. As this was an engineering demonstration, these were not performed. Future iterations of this sensor build should pursue calibration flight lines in order to provide the highest resolution geolocation possible. A robust amount of literature is available for boresight calibration of airborne lidar sensors and applicability to the POLAR sensor is further discussed in detail, along with specifics of the geolocation process, in Appendix A.

6.1.4 Airborne Multi-Functional Observations

6.1.4.1 Co-Polarized Ocean Surface Sensing

A research flight was flown over the open Pacific Ocean, in a dedicated line where wings level began at < 1 km AGL and then sustained 150 m AGL for 12.5 minutes. The line's purpose was to allow in-situ sensors to acquire marine aerosols, if present, and, additionally, to allow the POLAR sensor to collect data from the ocean surface. The low altitude portion of the flight line is shown in Fig. 6.7, over plotting an image of the area with the latitude and longitude coordinates collected by the GPS receiver. Acquisition during this flight line allowed the POLAR sensor to examine the ocean surface under different flight altitudes and draw conclusions about sensor performance. This section will examine ocean data collected by the POLAR sensor and serve as a case study to compute performance metrics and compared directly to those generated by the ATLIS simulator. The overall collection of multi-functional data in a day-time ocean environment will also be evaluated.

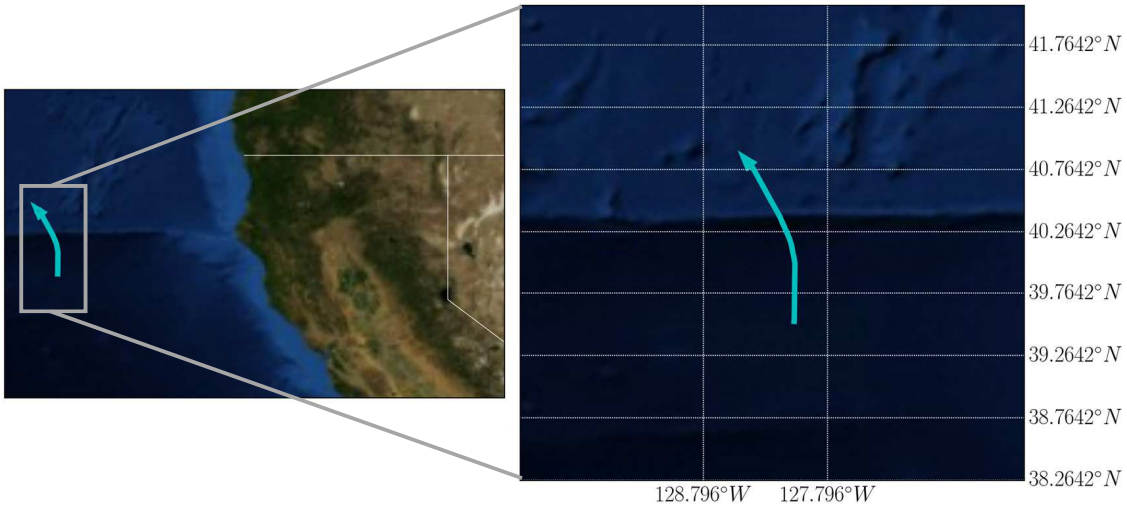

Figure 6.7: Latitude and longitude coordinates retrieved from the aircraft's GPS receiver. The left image shows the macroscopic location of the flight line, off of the northern California coast in the Pacific Ocean. The right image shows a zoom-in to the specific latitude and longitude lines that encompassed the flight line. The actual aircraft track is shown by the cyan arrow, traversing in the north north-east direction.

Figure 6.8 shows the retrieved values for the aircraft's attitude and location from the IMU and

GPS. The top panel shows the GPS altitude above mean sea level (MSL). The flight line descended from higher altitudes, maintained wings level, and then ascended back up to altitude at the end of the line. The center panel shows the reported pitch values with an average of $\sim 2.2°$. This is below the anticipated 3.5° that was worked into the POLAR mount. Due to the offset of 1.3° POLAR is not nadir point during this flight line, but remains close enough that specular returns from the wavy surface fall within the receiver's FOV. The lower panel shows the roll estimates, which remain constant except for adjustments to the line. These adjustments introduce close to a meter of non-physical surface height variation into the raw data. This is adjusted in the geolocation process, but when examining raw data must be considered.

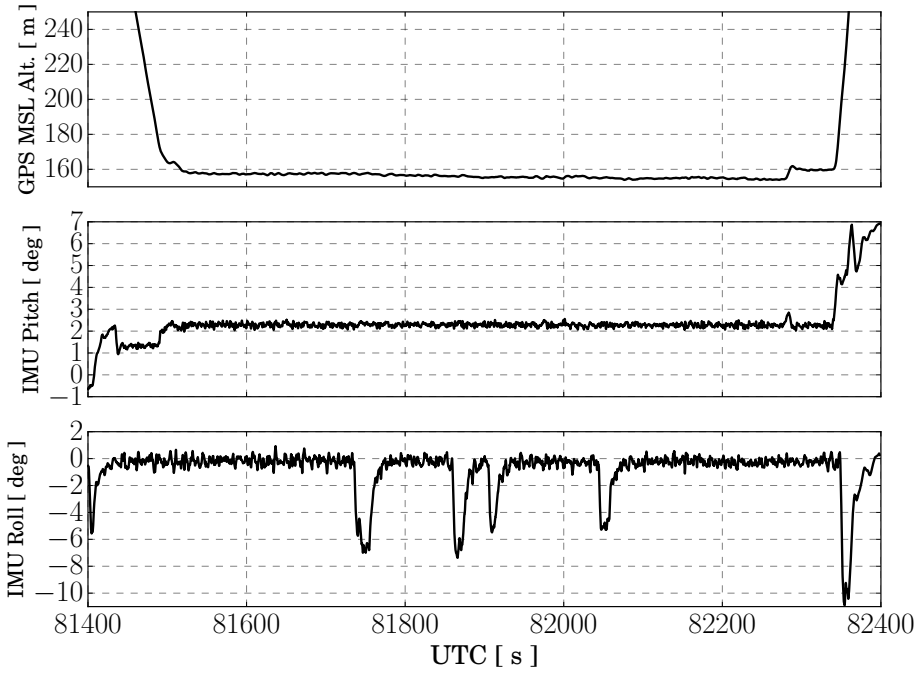

Figure 6.8: Aircraft GPS altitude and IMU pitch/roll values for the entire low altitude ocean line. The aircraft's descent and ascent can be seen in each panel, along with maneuvers performed throughout the line. The pitch stays relatively stable at $\sim 2.2°$ along with the GPS altitude above MSL at ~ 154 m.

The total point cloud of raw photon detections for the co-polarized channel is shown in Fig. 6.9, where a number of different types of scattering events can seen. Between 0-50 m atmospheric returns are evident, and, due to the aircraft's location to the ocean surface, it is likely that these

returns contain some mixture of molecular and aerosol backscatter. Although this signal is present, integration over short time scales shows that the signal is sparse and requires longer integration and larger range bins to extract signals. Throughout the point cloud a dense Poissonian noise field is evident, clearly seen in the 50-150 m ranges (returns in this range are also due to atmospheric scatter), and below the surface at > 150 m onwards.

The surface signal can clearly be seen at approximately 150 m in Fig. 6.9, with additional denser subsurface signal resulting from water column backscatter. Zooming in to examine this, Fig. 6.10 elucidates that the surface signal is actually made up of a secondary grouping of photons about 4 m, or approximately ~ 25 ns, below the first surface returns. The secondary signal is highlighted by the black points to clearly differentiate it from the real surface signal, shown in blue. The secondary surface is not geophysical, but rather an instrument artifact, indicative of afterpulsing of the co-polarized PMT. Removal of the afterpulse is necessary in order to isolate true surface signals and avoid biasing of integrations and correlations.

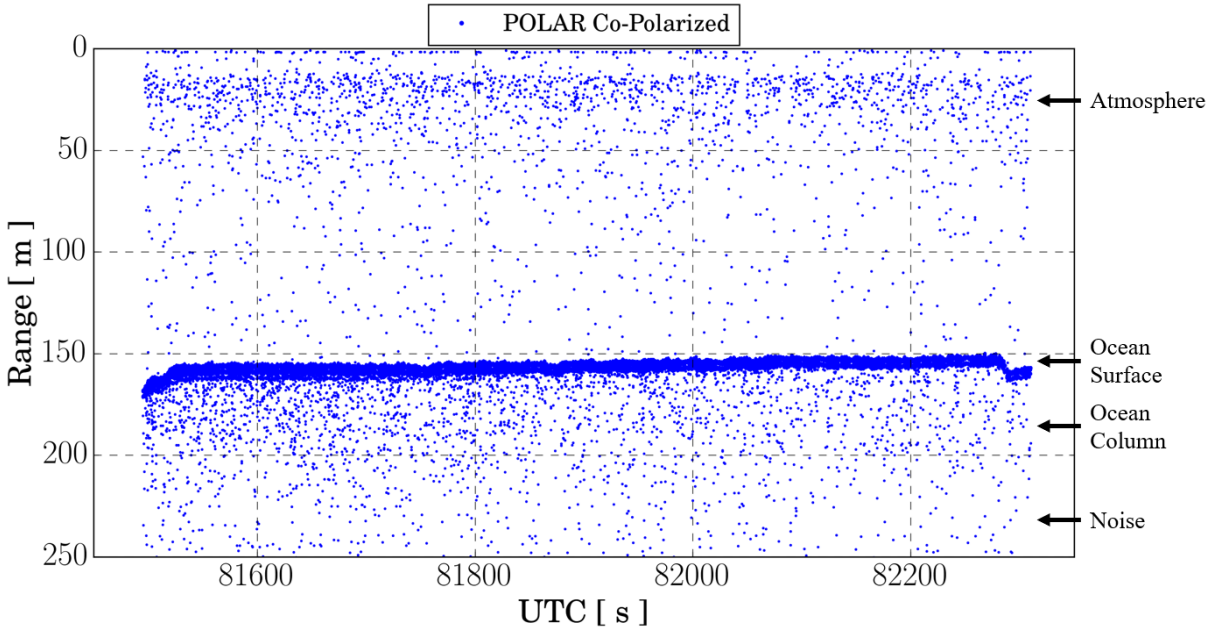

Figure 6.9: All co-polarized detections during the flight line. The initial atmospheric signal right after overlap can be seen between 0-50 m, along with the ocean surface signal at 150 m, volume returns below the ocean surface, and the background noise field.

The afterpulsing effect is typically seen in PMTs and the probability of occurrence scales with photon rates. These are spurious detections that appear after the incident photon and are always time-correlated to the detection. The effect is caused by ion feedback or luminescence of the dynode material, or glass. Secondary photoelectron generation subsequently propagates through the dynode chain and into the acquisition electronics, allowing addition to the point cloud. This effect can be a significant problem when subsequent scattering layers are expected, as the afterpulse signal appears 1-10 ns from the first detection. In the case of the water surface, the effect is only seen when the water surface signal is incident on the detector but not processed by the acquisition electronics. This happens when the surface is blanked out by dead-time due to noise or atmospheric signal, thereby allowing the afterpulsing to be processed. The point cloud shown in Fig. 6.9 displays weak atmospheric signal, and since the ocean surface maintains a high backscattered photon rate, afterpulse sampling rateand addition to the point cloud is low. This allows for isolation and removal from the water surface point cloud.

The afterpulse was partially expected due to the H4722-40 series of PMTs used. These detectors are known to exhibit significant afterpulsing when the measured photon rates are high and the associated PMT gain is also high [8]. In the case of the measurements made in this flight line, the PMT gain was set at 750 mV, which is on the upper end of this particular series of PMTs. Combined with the close stand off distance of the water surface and the specular nature of the reflection, the effect is pronounced.

Due to the specular nature of the surface signal it is expected that the probability of scattering events that remain within the FOV of the receiver is highest where the surface slope is closest to zero, or $\sim \hat{n}_{surf} \leq \Delta\alpha$, due to boresight alignment. This indicates that the majority of surface photons the sensor sees occur from the wave peaks or troughs. Because of the actual shape of the wavy surface, which are trochoidal, as opposed to the often assumed sinusoid, the peaks have greater slopes than the troughs, indicating that the wave peaks are undersampled compared to the troughs. This is the cause of the often discussed sea-state bias (SSB) and appears present in the POLAR sensor data. In [94] a sea surface elevation profile is generated and the probability of specular

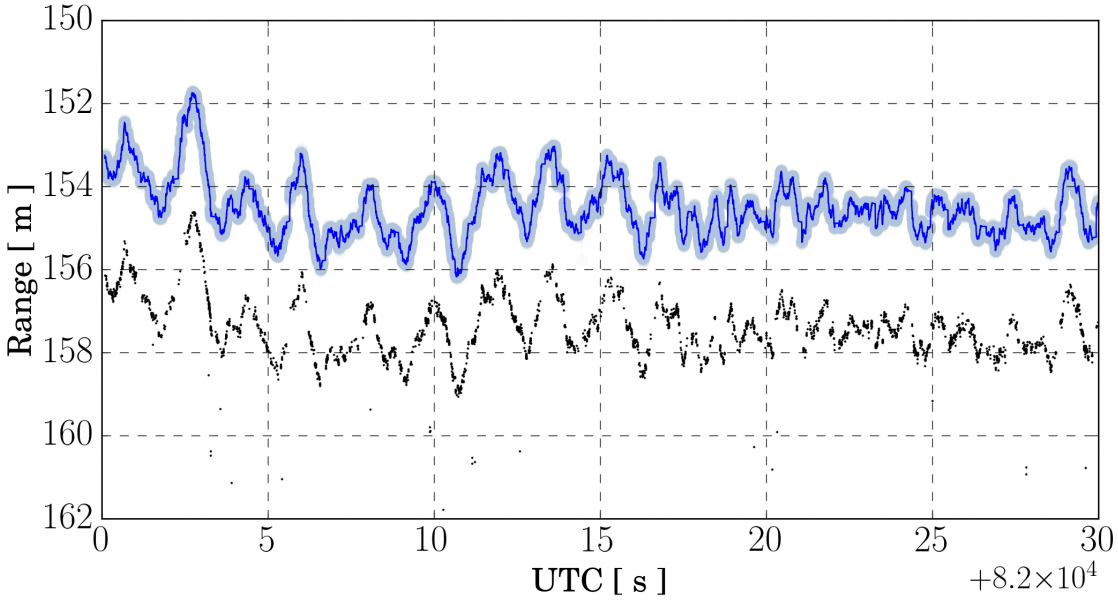

Figure 6.10: A windowed portion of Fig. 6.9 between 82000-82030 UTC seconds. In blue are the individual photon detections from the water surface with the dark line showing a the output of a smoothing window over 31 bins. In black is an instance of PMT afterpulsing, which has been isolated to allow removal from the data set.

returns is calculated. They find that the sampled mean of the retrieved photon distribution and estimated SSB are several cm below the expected surface, following the expectation of the POLAR data seen throughout the ocean line.

A minute's worth of surface returns is shown in Fig. 6.11. The top panel shows the surface returns recorded by the POLAR sensor after the water column, afterpulsing, and atmospheric returns were removed. The middle panel shows the surface photon rate per second, calculated as the total number of surface detections per second. The bottom panel shows the surface detection rate, calculated as the number of surface photons detected per PRF giving a percent detected per laser shot. As expected, the surface detection rate varies with the backscattered photon rate along the surface. The estimated mean for the entire window is $\sim 37\%$, indicated by the blue horizontal line in the lower panel. Given that the sensor was seeing $< 50\%$ detection probability per laser firing from the surface, it is assumed that the surface detections are being made while the sensor

is in linear photon counting mode. This is bolstered by the fact that the sensor has not reached the non-paralyzable steady-state count rate discussed in Chapter 3, as an increase in backscattered photon rate reflected in an increased surface detection rate and the count rate plateau is evident. This claim is further explored in Chapter 6.

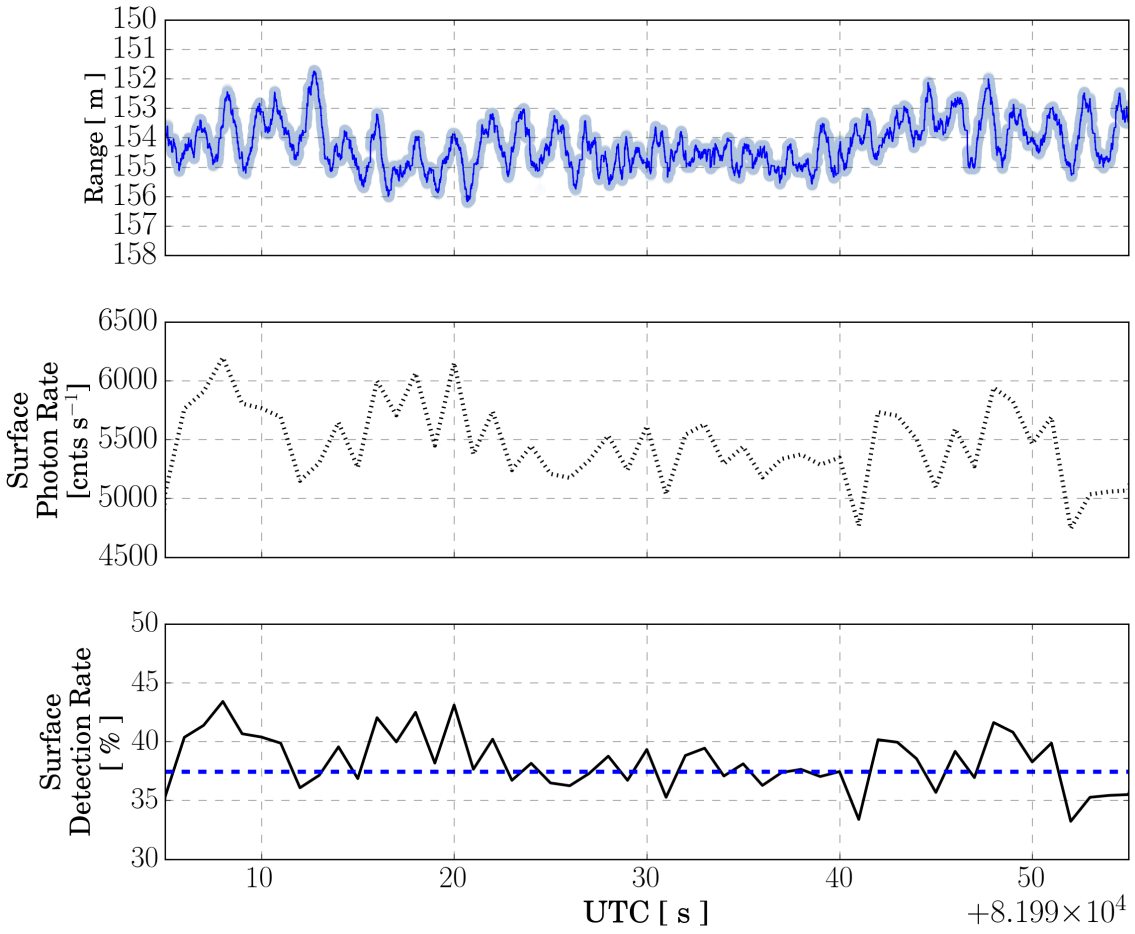

Figure 6.11: The top panel shows a portion of the filtered surface photons in the co-polarized channel. The middle panel shows the surface backscatter rate, given as counts s^{-1}. The surface detection rate is shown in the bottom panel with a mean rate of $\sim$ 37% across the time span, indicated by the horizontal blue dashed line.

With the recognition that POLAR is operating in linear photon counting mode over this portion of the flight line, the assumption of Gaussian statistics for parameter retrievals is valid and inversions can reliably be made from the surface data. Given that there is an estimate for the co-polarized channel's IRF (Fig. 5.4), the surface data can be examined for geophysical variance.

The geophysical variance is recovered using the definitions of Eq. 3.15 as

$$\sigma_{rx}^2(t_1, t_2) = \sigma_{IRF}^2(t_1, t_2) + \sigma_{SRF}^2(t_1, t_2), \tag{6.2}$$

where the integrated surface distribution's variance is assumed to be a decoupled linear combination of the IRF and SRF. The data used for this inversion requires the aircraft effects to be removed, so surface signal was denoised and geolocated to give elevations in the WGS84 coordinate system according to the flow of Fig. 6.6. The output geolocated photons accumulated from $t_1 = 81664.198031$ to $t_2 = 81707.235863$ UTC are shown in the top panel of Fig. 6.12, where the time span has been transformed to the along track distance using the interpolated aircraft speed. The accumulated photons were histogrammed with 8 cm bins and a Gaussian fit was performed to extract $\sigma_{rx}^2(t_1, t_2)$, shown in the lower panel of Fig. 6.12. The estimated IRF variance is removed from the fit's variance to generate an estimate for the geophysical contributions as

$$\sigma_{SRF}^2(t_1, t_2) = \sigma_{rx}^2(t_1, t_2) - \sigma_{IRF}^2(t_1, t_2). \tag{6.3}$$

Performing this operation with the Gaussian fit the geophysical variance is recovered as

$$\sigma_{SRF}^2(t_1, t_2) = 0.423 \text{ m}^2, \tag{6.4}$$

indicating that the total received signal width is predominantly governed by the surface wave structure contributions and dwarfing the contribution from the IRF (541.57 ps). It is useful to convert this to an FWHM and to think of it as a contribution to the total uncertainty of the measurement. The geophysical contribution equates to ~ 10.233 ns added to the total width of the signal over $t_1 \rightarrow t_2$. An example of the inversion to extract geophysical parameters from this data set is shown in [31], where the SPL derived surface variance was used to extract an estimate of surface wind speed. A model was run from this estimate to simulate the expected geophysical variance and it was found that wave field was generated by a 9.9 m/s wind speed.

This retrieval was validated through two different methods in [31]. An ocean surface wave model was fit to the lidar data to retrieve wave parameters and wind speed directly from the model. This value and the lidar derived value was then compared to satellite radar altimetry acquired in

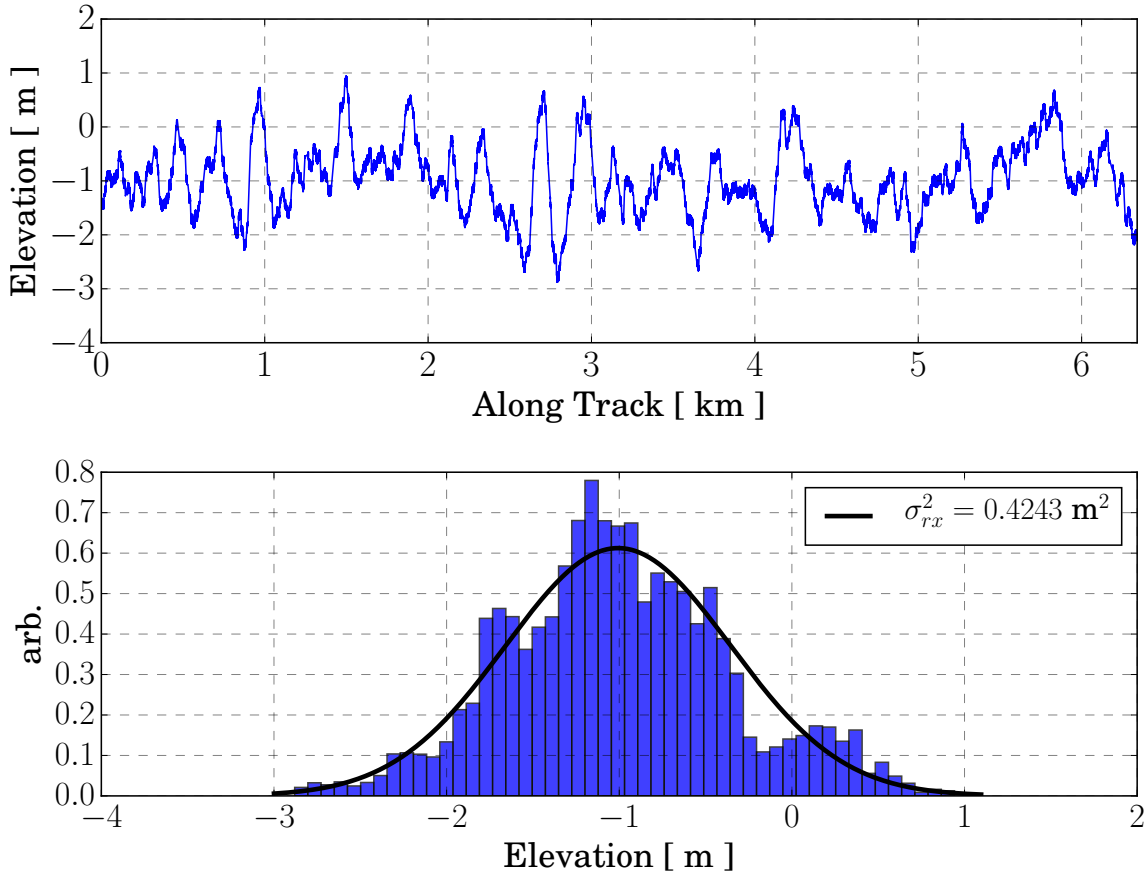

Figure 6.12: Top panel shows the denoised and geolocated surface photon time-tags plotted along track distance. The lower panel shows the total detections histogrammed in 8 cm bins and the resulting Gaussian fit with associated variance. The geophysical contribution is seen as contributing $\text{FWHM}_{SRF} = 10.233$ ns to the total signal.

the flight line area and rough time of flight, with both showing comparable and accurate results. Validated retrieval of the geophysical variance and thus wind speed directly from the POLAR SPL data provides an indication that multi-functional SPL sensors are capable of resolving ocean surface parameters. The retrievals done on satellite radar altimetry are similar in basic method and assumption, so a more robust comparison of POLAR's ocean surface retrievals would require comparison to buoy derived wave heights or some other source that directly measures the wave fields.

This analysis, recognition of afterpulsing, and the general detection rates in the co-polarized channel, raises the question of whether or not detection of the strong backscattered photon rate from the surface signal was performed in linear photon counting mode. And, if the sensor was deviated out of single photon detection, are nonlinear artifacts present? At first glance, it appears from Fig. 6.11 that the surface data is behaving linearly and in photon counting mode. This is due to the surface detection rates being below 50% per laser shot, indicating that less than one photon per transmitted pulse is expected — the hallmark of photon counting. However, the surface detection rates are higher than anticipated such that a burst of photons could shift the sensor to a nonlinear regime. Given that in the segments analyzed there was no evidence of detection rate spikes that would incur nonlinear effects, the assumption that surface backscatter is maintained in the linear regime appears valid. In general, detection in the presence of high photon rates, afterpulse effects, and high probabilities of detection do not necessarily indicate that the SPL has transitioned out of the linear photon counting regime, these effects serve as indicators of a heightened probability of multiple concurrent photons and suggest that data should be examined for anomalies.

This type of analysis confirms the Gaussian nature of the along track wave field that was assumed for the ATLIS simulator in Chapter 4, and shows that the time series of photon time-tags can be utilized to extract geophysical meaning from the scatterer. Measurement validation also confirms the methods by which operation in a linear photon counting regime is assessed for an operational SPL. With this type of fitting scheme, further estimates of the wave field can also be made. Morison *et al.* [95, 94] give indicators that estimates of the sea state bias (SSB) can be

made using solely photon returns from a lidar altimeter. This indicates that for the data shown in Fig. 6.12, there are multiple potential paths for geophysical estimation and recovery of ocean surface information.

6.1.4.2 Extracting Cross-Polarized Ocean Subsurface

The discussion of operating linearly in photon counting mode provides a good transition to analysis of the cross-polarized receiver channel and depolarized returns from the subsurface water column. In general, it is expected that the cross-polarized channel will experience lower numbers of backscattered signal photons from each regime — atmospheric, surface, column, ground — unless the scattering plane, or target, serves to introduce significant depolarization. The depolarization channel will typically exhibit linear trends and be operating in photon counting mode. This can easily be analyzed by calculating the channel detection rates, either for a scattering plane or across the entire measurement gate. For the ocean line discussed, it will be shown that the calculated detection rates for the cross-polarized channel fall below 50% and are safely assumed linear.

Figure 6.13 shows a portion of the cross-polarized signal acquired by POLAR during the ocean flight line for two different PMT high voltage settings, the left being at 725 mV and the right being at 750 mV. Windowed in range, Fig. 6.14 shows a zoom-in to the surface and column returns. Between the two settings it is seen that, increasing the PMT voltage, results in an increased sensitivity to noise additional signal from the water surface, seen as higher point density. However, the time scales shown in Figs. 6.13 and 6.14 indicate that the lower detection rates can be inferred from the lack of overall high point density. Specifically, in Fig. 6.14 it can be seen that in both gain settings the 20 seconds of data shows significantly less returns than seen from the co-polarized channel in Fig. 6.10. Because of the scattering environments (specular for the surface versus diffuse for the column) this is expected. Still there are heightened water column returns occurring between 155 and 160 m, after which the remaining returns are predominantly due to solar background.

To gain a better understanding of what regimes are contributing cross-polarized signal a slice from each portion of the point cloud is analyzed. Figures 6.15 and 6.16 show windowed

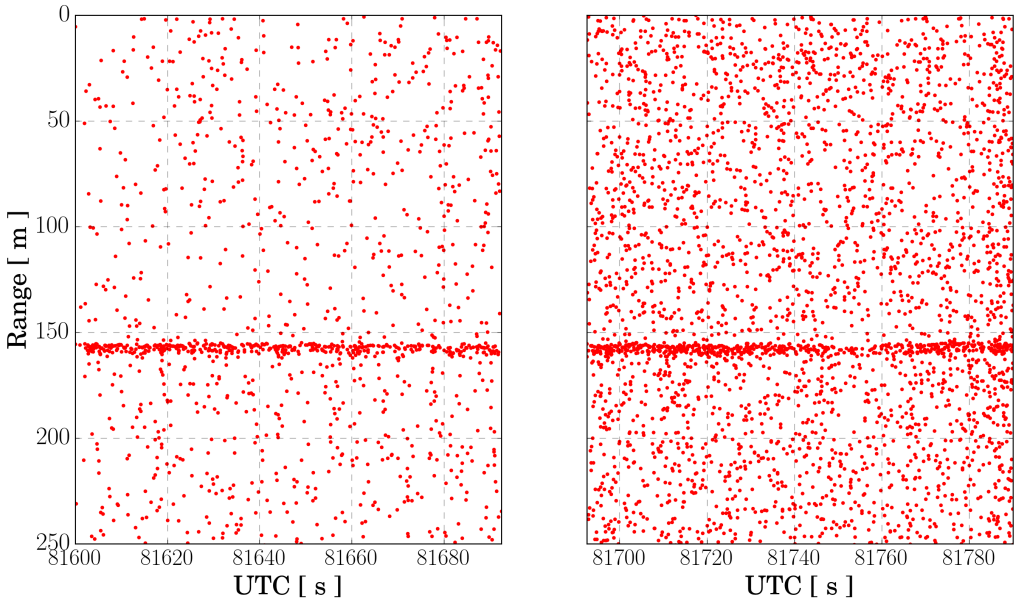

Figure 6.13: Two windows of cross-polarized signal during the flight line, with the left showing acquisition at a lower PMT gain ($\sim$ 725 mV) and the right showing acquisition at a higher PMT gain ($\sim$ 750 mV). In both panels very little atmospheric signal can be seen, contrasting the co-polarized signal, but is expected with clear air. The noise field can be seen, pervasive throughout the measurement, increased in the higher gain panel. Easily seen as well is the surface and column detections in this polarization plane, with significant detections from the column now present, also contrasting the co-polarized channel.

portions of the flight line from UTC 81600-81620 and UTC 8170-81720 respectively, where the single detections have been integrated to a larger bin resolution and the decaying subsurface signal extracted. In Fig. 6.15 the left panel shows the single photon detections and the right panel shows two different integrated profiles, where the light solid red line shows the profile at 10 cm resolution, the dark solid line shows the profile at 40 cm resolution, and the solid blue line is the estimate mean surface location over the time period. For both resolutions the profiles show signs of decaying column returns, although they are most pronounced in the larger bin resolution due to the higher counts per bin. This is also true for the higher gain settings in Fig. 6.16, where the single photon detections and the integrated profiles are shown again. For the higher gain settings there is an accompanying increase in signal photons in addition to noise. In this figure, a band of heightened

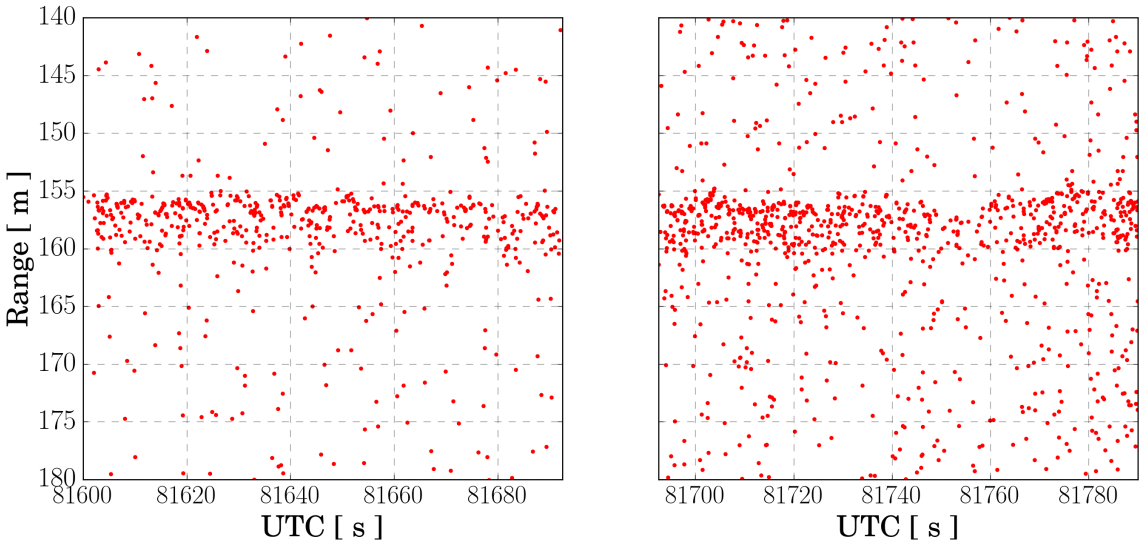

Figure 6.14: Zoomed in portion of the point cloud shown in Fig. 6.13 for each gain setting. The surface signal, noise, and column returns can clearly be seen. The denser band of returns between 155-160 m indicate column returns before the signal extinguishes.

signal is seen from a subsurface layer with higher scattering efficiency. Contrasting the co-polarized surface detections, the detection rates seen at five meters into the water column are less than one percent at 0.119%. This can be interpreted as confirmation that the cross-polarized channel is acquiring in photon counting mode and the detections can be considered linear.

In both Figs. 6.15 and 6.16 it is clear that the cross-polarized channel is seeing a substantial amount of backscatter from the water surface. In the absence of ocean surface clutter, such as foam or floating particles, the backscattered photon rate will preserve the incident polarization such that an ideal SPL would see the water surface signal only in the co-polarized receiver channel. The POLAR sensor, however, does not operate with an ideal transmit polarization. As described in Chapter 3, alignment of the transmitter and receiver polarization planes was calibrated with an offset of $\sim 1.5°$, implying that specularly reflected transmit light could be detected in the cross-polarized plane if signal strengths are high enough. Even though the portion of transmit light that is in the cross-polarized plane is only a few percent, the strong water surface signals make it such

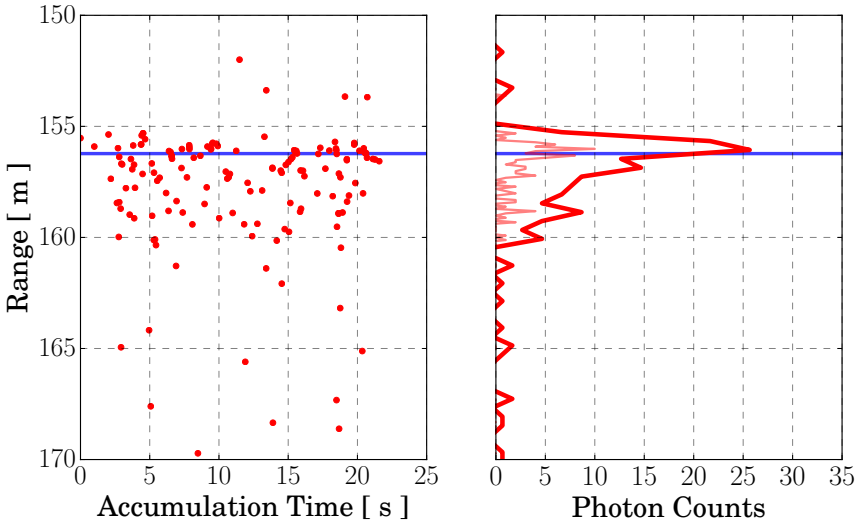

Figure 6.15: The left panel shows the cross-polarized returns over 20 seconds, starting at UTC 81600, from the surface and column bins. The right panel shows profiles generated over the time window from integration with a 10 cm bin resolution, light solid line, 40 cm bin resolution, dark solid line, and the mean surface signal is shown as the blue dashed line. Column returns can be seen over several meters for both profiles, but the larger bin resolution clearly shows the column returns with significant signal for 5 m. Noise can be seen before 155 m and below 165 m.

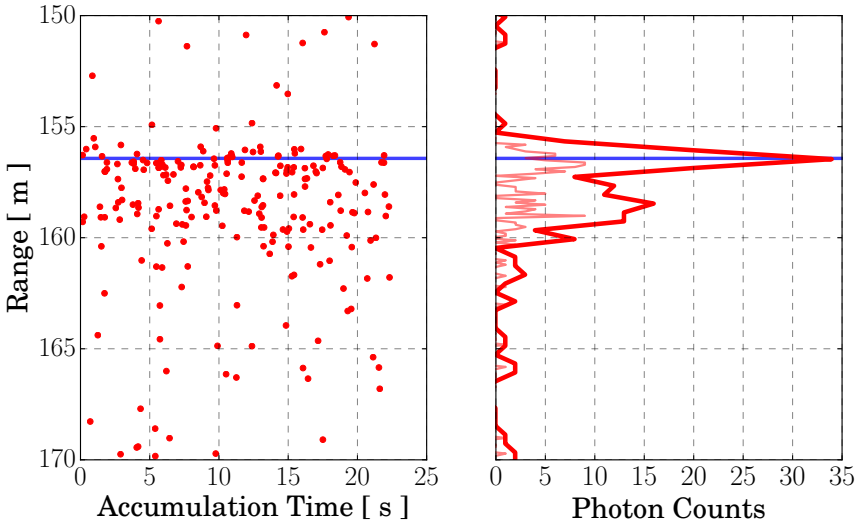

Figure 6.16: The left panel shows another set of cross-polarized returns over 20 seconds, starting at UTC 81700, from the surface and column bins. The right panel again shows profiles generated over the time window integrated with a 10 cm bins, light solid line, 40 cm bins, dark solid line, and the mean surface signal is shown as the blue line. Showing a subsurface concentration of points and column scattering again.

that significant contributions are still detected by the orthogonal polarization plane.

The ATLIS simulator was used to better understand the effect of transmitter/receiver polarization misalignment. Simulated data was generated for the cross-polarized plane with an input of the flight characteristics and the use of the relative misalignment values in the model. The ATLIS model calculates the ideal scattering scenario where no surface clutter is present and only polarization misalignment will contribute to surface signal, providing direct understanding of this effect. Figure 6.17 shows the model's output point cloud and integrated profiles, where resolutions were chosen to match those of the POLAR data and the surface was placed at the 155 m range bin.

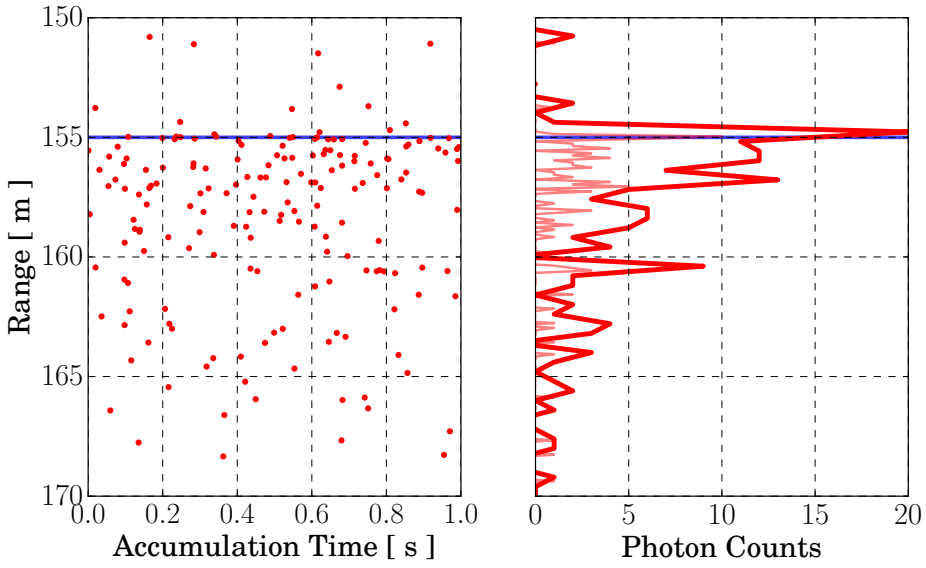

Figure 6.17: Simulated cross-polarized returns from the ocean surface and column for 1 second worth of laser firings, in the left panel. The right panel shows profiles generated over the time window integrated with a 10 cm bins, light solid line, and 40 cm bins, dark solid line. The simulated ocean surface is the blue line.

The integrated profiles in the right panel of Fig. 6.17 immediately show that the introduction of polarization misalignment results in surface signal being present in the cross-polarized channel. The relative magnitude of the surface signal to column signal match well with the POLAR data in Figs. 6.15 and 6.16. Despite the strong surface signal, and dead-time impact, column detections are still seen. Slightly higher column scatter shows down to ~ 7 m as opposed to 5 m in the measured

data. Efficiency scales are not matched exactly to the POLAR sensor, since the photon rates are increased in the simulation and data is shown at a shorter time scale. As this is linear and scalable, more importance should be placed on the accurate prediction of depth penetration, profile shape, and relative ratio of surface to column returns.

The measured cross-polarized ocean response shown in Figs. 6.15 and 6.16 and the ATLIS modeled response in Fig. 6.17 emphasize proper tuning of an SPL's polarization optics in an effort to decouple the sensor effects from the anticipated measurement. In addition to introducing further difficulties to isolating the water column scatter, surface detections in the cross-polarized channel serve to reduce the total number of column detections made and decrease the overall efficiency of collection for this regime. This is a direct implication of the SPL dead-time, where due to the surface detection in the subsequent bin, photons are received during a dead-time window and not detected. This bolsters the rational for reducing the total dead-time of the sensor such that recovery occurs rapidly and the sensor can process photons into detections. An implication of the reduced counts is that longer integration times and larger bin widths are need for profile generation and the ability to resolve fine features is significantly diminished.

The lower detection rate in the cross-polarized channel emphasizes the difficulties of operating a depolarization channel at 532 nm in daylight conditions. The diffuse signal rate is low in magnitude and comparable to the noise rates, or lower, implying that detection is difficult and relies on good management of the background noise. The windowed portion of the cross-polarized signal showed in Fig. 6.13 demonstrates the density of the noise field, where much higher density is seen in the cross-polarized channel compared to the co-polarized channel for the same time window.

6.1.4.3 Ocean Flight Line Data Rates

One of the novelties of the TCSPC approach to SPL can be further seen by examining the total size accumulated data over the duration of the ocean flight line. The total point clouds for the co-polarized and cross-polarized channels (all detections made including afterpulsing over the full 10.49 km of the IPP are stored) and the logged laser firings reached a size of 200.97 MBytes over

the 850 s of accumulation. Figure 6.18 shows the total data rate per second as a function of the entire line, where, for a majority of the line the rate stays stable at < 250 kBytes/s with an average rate of ~ 236.44 kBytes/s. This is significantly lower than most day-time operated lidar sensors, where data is typically down sampled before being saved. As the POLAR sensor has such low data overhead, real-time analysis of the full point cloud is enabled, where atmospheric and hard target returns can be examined simultaneously at the full fidelity of the TDC resolution.

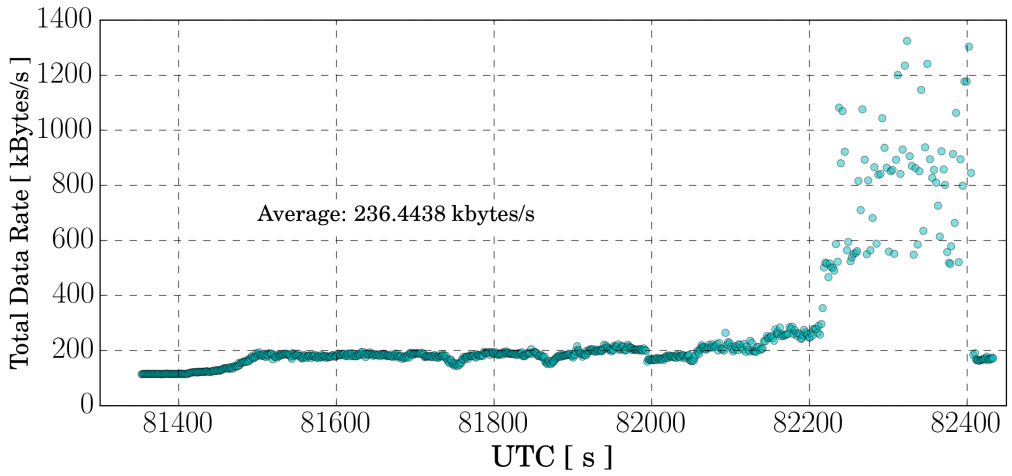

Figure 6.18: Total data rates, for both receiver channels and laser sync, of the POLAR sensor for the complete ocean flight line.

6.1.4.4 Topographic Mapping

Portions of the ARISTO-17 campaign involved flights over varying topography near the NCAR RAF. This allowed for testing of the sensor's ability to retrieve dual-polarization topographic returns, including sampling and detection statistics between channels and responses to varying surface topography with differing slopes. This section will display results for two flight lines and various retrievals that were made from the collected data.

Figure 6.19 shows the first example of a flight line from which topographic photons detected by the POLAR sensor will be analyzed. The data was taken over farm land, in Northern Colorado,

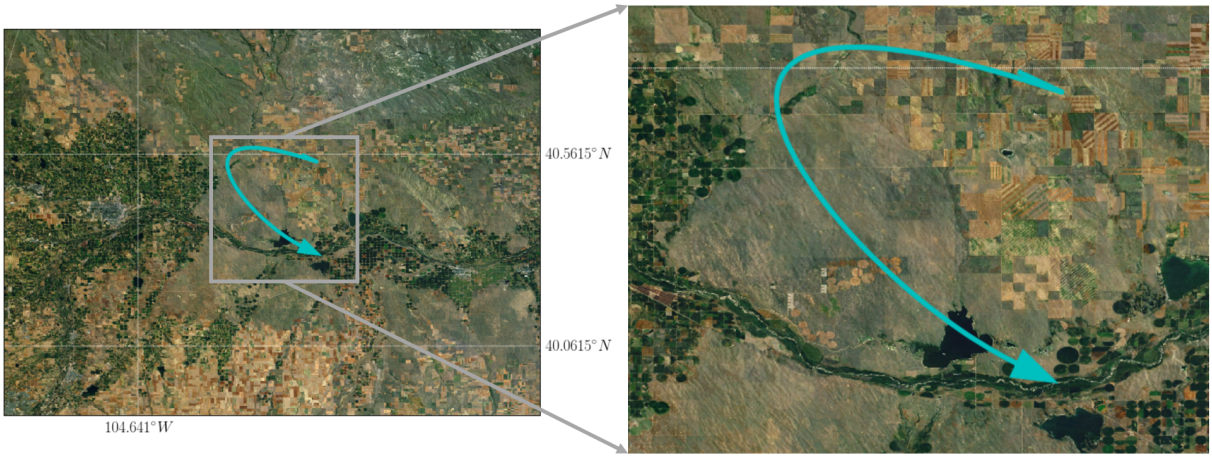

Figure 6.19: Latitude and longitude coordinates retrieved from the aircraft GPS receiver. The left image shows the macroscopic location of the flight line in Northern Colorado, and the right shows a zoom-in to the flight line. The actual aircraft track is shown by the cyan arrow.

with low amounts of elevation gain. Towards the end of the line a small reservoir is passed over in an effort to capture lake bathymetry and water surface features. There was a significant banking maneuver performed during the line, so this particular analysis window will also provide information on algorithm performance for removing aircraft motion. Throughout the pass, noise rates were high, due to mid-day operation and a high solar angle, as were surface detection rates, providing easy identification of correlated surface signal within the uncorrelated noise.

Figure 6.20 shows data collected from the non-complex farming terrain over several hundred seconds of transit, with the top panel showing the raw co-polarized point cloud and the bottom panel showing the raw cross-polarized point cloud. The left side of each figure shows the ground signal coming into view as the aircraft descends to the nominal wings level altitude for the line. The right side of the figure shows the small water body. The topographic to bathymetric transition is evident through an abruptly stark contrast in noise between the high albedo local topography and the low albedo water surface. For both polarization planes the solar background rate over the water body is significantly lower than the surrounding terrain. Surface signals can be seen, but not consistently across the entire water body.

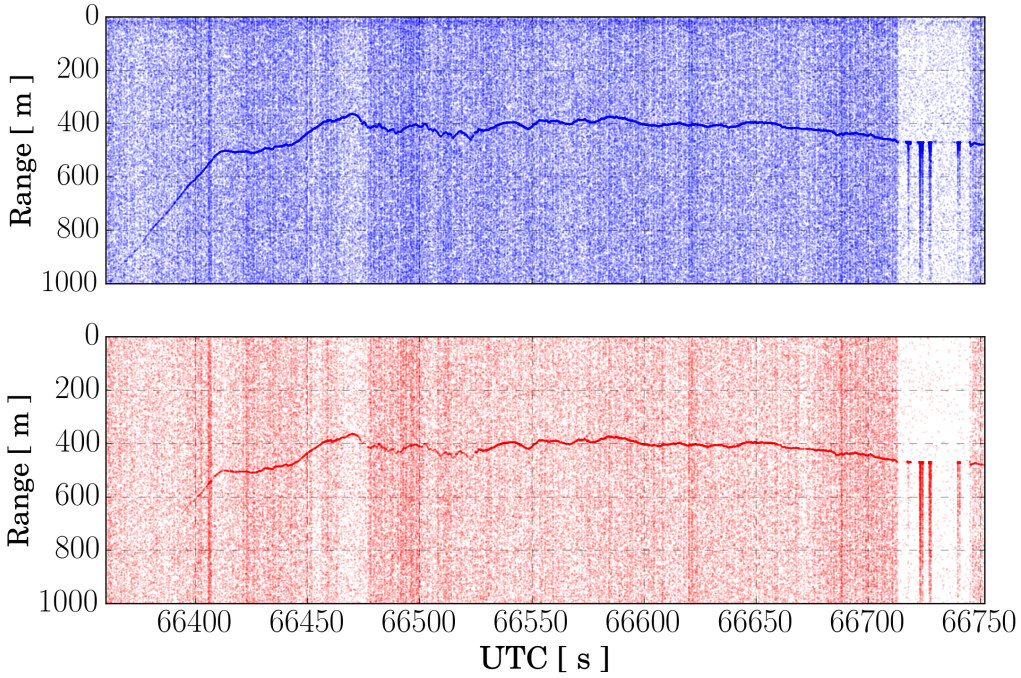

Figure 6.20: Raw topographic data for the co-polarized, top panel, and cross-polarized, bottom panel. The uncorrelated noise field is seen in both polarization planes, along with densely correlated topographic and bathymetric signal.

To further examine signals, Fig. 6.20 was processed to remove the solar background and isolate the topographic and bathymetric detections. The derived surface photons were then geolocated to provide elevation estimates in the WGS84 coordinate system. The aircraft speed was used to convert the time of each detection to an along track distance with respect to the flight line, shown in kilometers. The final data is shown in Fig. 6.21 as along track distance versus surface elevation. Due to varying surface slopes, the filtering finding algorithm was set to have a wider range window about the peak surface bin, $\Delta/2 = \pm 5$ m, to allow capturing of larger surface slopes. An increased window size resulted in retention of some solar background close to the surface, giving the spread of surface points a larger magnitude than what would be seen with only the correlated surface photons being retained. However, these points fall away when considering histograms of the surface due to the non-correlation with signal. Examining the feature extent, elevation versus

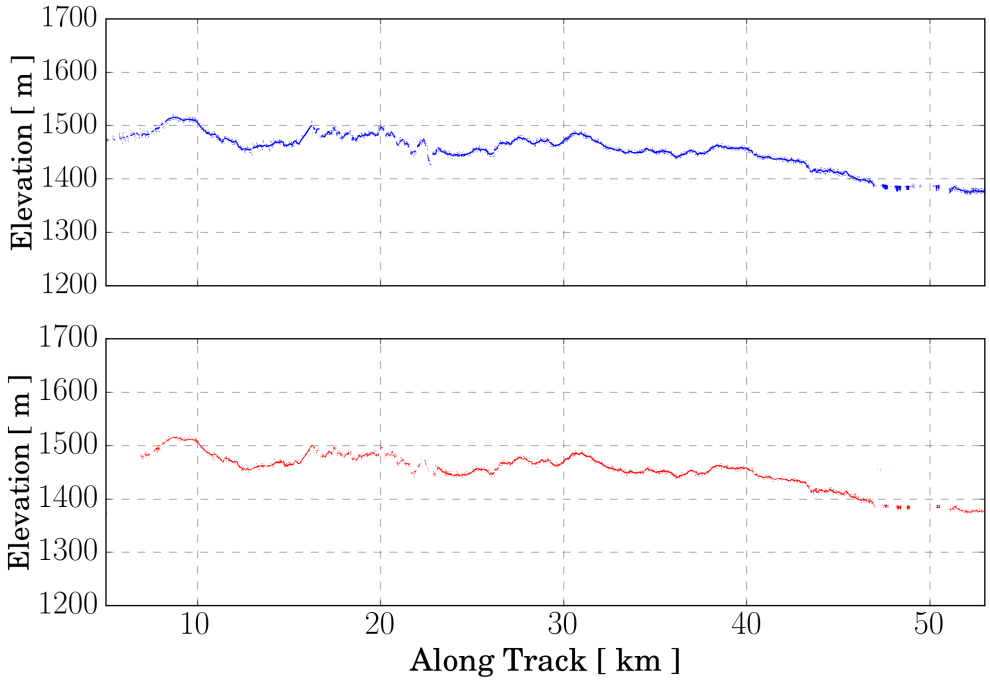

Figure 6.21: Processed point clouds from Fig. 6.20, shown referenced to along track distance using the mean aircraft speed of 127.62 m/s. The data in each channel was passed through the surface finding algorithm to filter noise and then was geolocated to the WGS84 coordinate system.

along track distance, many of the features are likely the result of low rolling hills and gullies, likely for irrigation, and without simultaneously acquired visual images it remains difficult to determine and classify exact surface feature content within the point cloud.

Selecting a window of returns from each channel at UTC 66584, or 30.48 km along track, the single photon elevations in each channel were integrated at 4 mm histogram bin resolution over 0.5 s, as shown in Fig. 6.22. The left panel shows the elevation point clouds and the right panel shows the histogram of counts over the duration of the window, for both channels. From the point cloud it is clear that there is a small feature present within the time window, approximately 10-20 cm in height, giving a slight bias in the histogram. Though present, the feature proves difficult to resolve more specifically. Given the hard target scatterer and the implemented channel calibration routine to eliminate path length differences, it can be assumed that any residual offset between histograms will be the result of the scattering plane. Both polarization channels align well, with the cross-polarized signal less in extent than the co-polarized signal and with a lower photon rate.

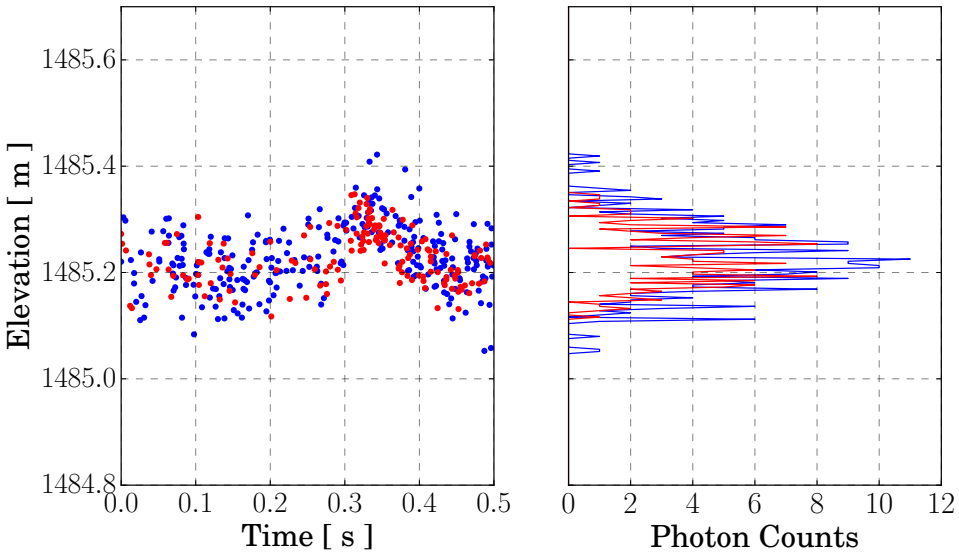

Figure 6.22: Selection of ground returns from Fig. 6.21 at UTC 66584, with the co-polarized is shown in blue and cross-polarized shown in red. The left panel shows the elevation point clouds and the right panel shows the surface histogram integrated with 4 mm bin resolution.

The histograms in the right panel of Fig. 6.22 were Gaussian fitted to allow extraction of the received waveform's FWHM, shown in Fig. 6.23. By using the fit's variance, the co-polarized waveform was estimated with an $\text{FWHM}_{rx}^{\parallel} = 1095.722$ ps, and the cross-polarized waveform was estimated with an $\text{FWHM}_{rx}^{\perp} = 995.045$ ps. Considering the IRF for each channel there appears to be ≥ 500 ps of timing uncertainty (several centimeters) introduced to the received waveform from the surface scatterer. This is expected due to the roughness of the terrain being observed. In both Figs. 6.22 and 6.23, the cross-polarized histogram is derived from a lower photon rate and the distribution does not fill out a comparable width of the co-polarized channel, specifically with the lower elevation side showing the main difference. From the point cloud in Fig. 6.22 it is evident that this occurs in the earlier part of the time window but not the later, suggesting a difference in scattering response in the different polarization planes.

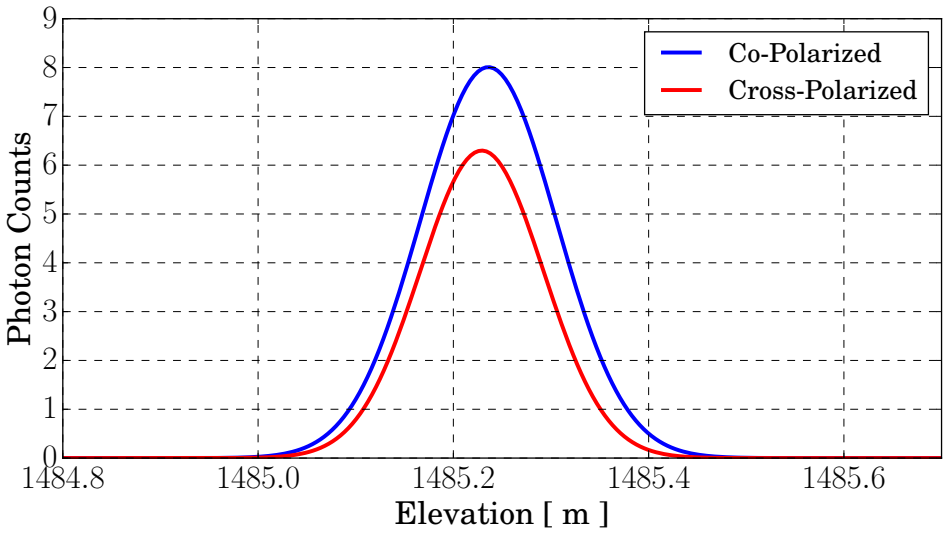

Figure 6.23: Fitted Gaussians to the histograms shown in Fig. 6.22, where the co-polarized FWHM was calculated at 1095.722 ps and the cross-polarized at 995.045 ps.

An explanation for the cross-polarized histogram weight towards higher elevations can be given by considering the transformation to WGS84 coordinates from the sensor frame. In the sensor frame, the histogram is weighted towards the sensor, which shows a shorter range. When

transformed to elevation this is still true, but the measurement is now from the center of the Earth in the ECEF frame, not the sensor frame, implying that the vector has opposite directional. The coordinate system in Fig. A.11 of Appendix A provides a clear image of this.

Another example of topographic returns, with evidence of atmospheric Rayleigh signal in the co-polarized receiver channel, is shown in Fig. 6.24. Both channels are plotted over each other to further demonstrate agreement between polarizations. These point clouds are essentially void of noise due to late afternoon operation and waning sunlight. Subsequent analysis of each channel's topographic returns is performed to demonstrate how the raw photon time-tags can be processed to give above ground level height estimates of features.

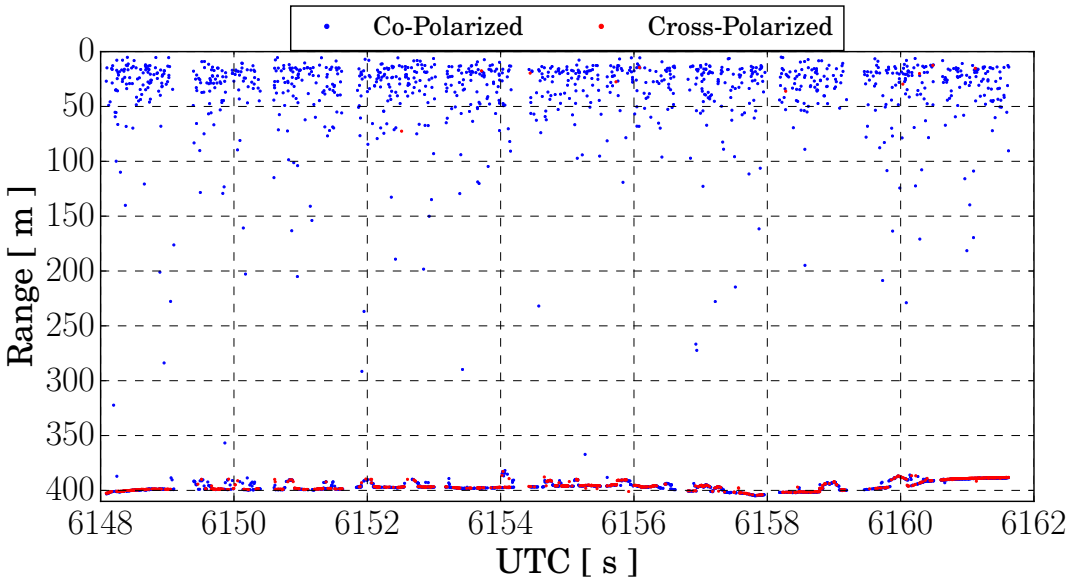

Figure 6.24: Raw photon time-tags accumulated for the co-polarized and cross-polarized channels at 400 m altitude. Molecular atmospheric returns can be seen in the co-polarized channel from 10-30 m after the Tx/Rx window. Ground returns are consistently seen in both polarization channels, providing topographic mapping abilities and the possibility of ground depolarization estimates.

Figure 6.24 gives the completely un-processed photon time-tags collected from 400 m flight altitude and accumulated over 18 seconds in both receiver channels. Despite the complete raw nature of the data, several topographic depressions and structural features are clearly evident on the ground, indicating that, even without assimilation with the GPS/IMU, raw data from the

POLAR sensor is still useful for a number of analyses. The molecular atmospheric returns are seen in the raw co-polarized detections, along with a few returns in the cross-polarized channel, as expected for a clear atmosphere exhibiting $< 1\%$ depolarizing Rayleigh scatter.

Processing the point cloud in Fig. 6.24 produces Fig. 6.25, where aircraft IMU and GPS estimates (pitch, roll, and height AGL) were used to extract ground features as a relative height above local level. The reference frame shown here is the local ground coordinates in along track meters. In Fig. 6.25 several topographic signatures are present, including a structural feature at 10 meters in height, the presumed top of vegetation next to the structure, and the local ground slope changes. Each feature provided a strong depolarizing signal, implying that the surfaces were fairly rough in the scattering characteristics, and that the scattering matrix had a non-unity element in the $F22$ term. The estimated 10 m structure height matches the expected height of apartment complexes in the observation area (Broomfield CO) indicating that the ranging subsequent aircraft data assimilation capabilities are providing reasonable estimates.

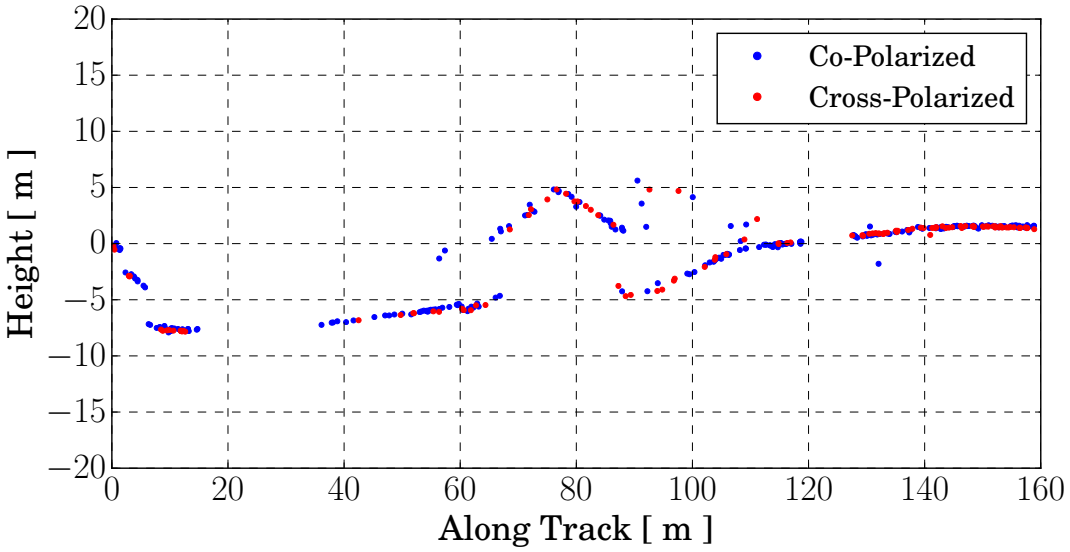

Figure 6.25: A zoom in to the UTC 6160 s mark in Fig. 6.24, adjusted for aircraft INS estimates of pitch and roll and converted to along track distance using the aircraft speed. The building is clearly seen in the data where the roof peaks at 10 m height above ground and returns from vegetation are shown after the building leading to a sloping upward rise in the ground returns. The aforementioned data gaps due to a $< 100\%$ duty cycle are seen here.

Performing an analysis of the structural feature's roof in Fig. 6.25 allowed a direct estimate of channel dependent surface distributions and the measured uncertainty. The top panel of Fig. 6.26 shows the right side of the roof zoomed and adjusted in range such that the pitch can be estimated. A linear fit was performed to each of the polarization channel's detections such that the slope could be estimated and subsequently removed to estimate the residual spread of points about the scattering plane. The lower panel shows the resulting distibution of residuals for the collection of points after the linear trend was removed. The co-polarized channel has a total of 18 returns from this portion of the roof, providing a narrower distribution between the two channels and giving 1.5 points per linear meter along this feature. The cross-polarized channel has a total of 7 returns with a greater spread of the points, and gives a total of 0.58 points per linear meter on this feature. A further confirmation that the processing is operating as expect is the retrieved roof pitch in both polarization channels. From the top panel in Fig. 6.26 the roof pitch can be estimated at a 4 to 12 ratio of height to run to create a $\sim 18.5°$ angle.

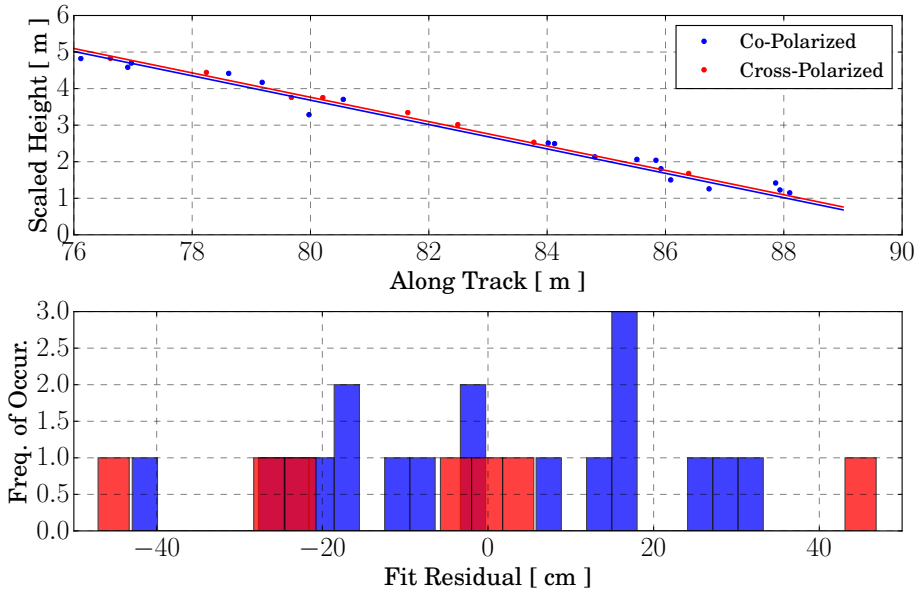

Figure 6.26: Analysis done to the right hand roof slope in Fig. 6.25, where a linear fit was performed to the returns in each channel to facilitate a de-trended estimate. The estimated roof slope fits the common 4/12 pitch used in construction. The residuals are then shown in the lower panel, estimating the distribution of points about the slope estimate. The small number of photon returns increases the variance about the roof trend.

6.1.4.5 Extracting Atmospheric Returns

Several measurements of atmospheric state were made by the POLAR sensor during the ARISTO-17 flight campaign. The configuration, as flown, was not tuned specifically for atmospheric returns, which would require specific PMT high voltage and CFD settings, but instead for topographic and bathymetric sensing. In addition, the optical layout was not originally designed for airborne atmospheric monitoring. This proved to decrease the detectability of signal and reduce the overall functionally for atmospheric measurements. However, POLAR still generated profiles of clear air regularly throughout flights and facilitated an understanding of the SPL response to simultaneous atmospheric and topographic/bathymetric data collection.

Figure 6.27 shows 120 s of integrated atmospheric returns in the co-polarized channel. These profiles were generated from above the ocean surface shown in Fig. 6.9, where the Rayleigh clear air backscatter is sparse in comparison to ocean signal but still present in the total point cloud. The time-tags were binned to three different resolutions to emphasis the dynamic binning available when higher SNR is needed. For each profile resolution the introduction of signal after geometric overlap is evident.

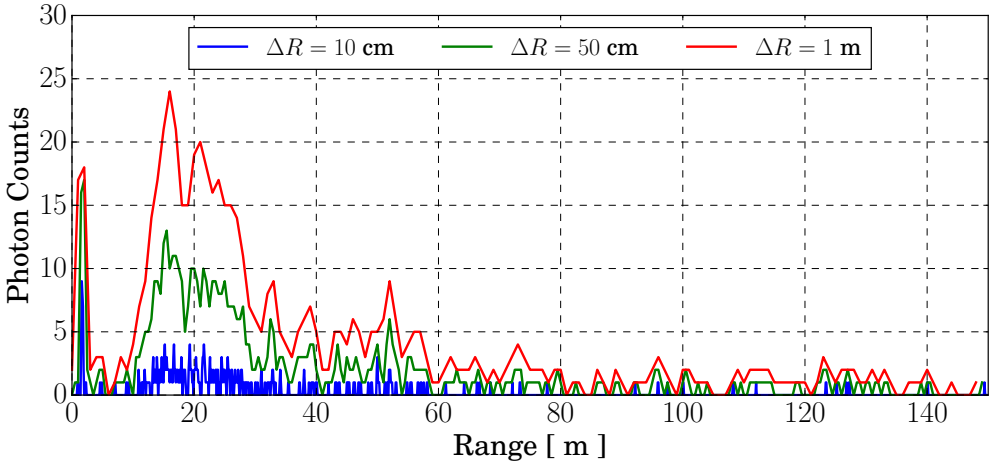

Figure 6.27: Integrated profile of atmospheric returns from Fig. 6.9. The three profiles are binned to 10 cm, 50 cm, and 1 m over a total of 120 s of accumulation. Longer integration times were necessary due to the low backscatter rate during this flight line.

A profile with higher SNR, generated from the returns in Fig. 6.24 is shown in Fig. 6.28. This profile is binned to 1 m bins, but, due to higher backscatter rates, integration is performed over only 10 s. Despite a higher SNR, the profile still shows a significant amount of variation, indicative of shot noise. However, the clear atmospheric signal can still readily be seen, where the exponential decay, combined with the overlap and $1/R^2$ effects, occurs over 60 m after the transmit window.

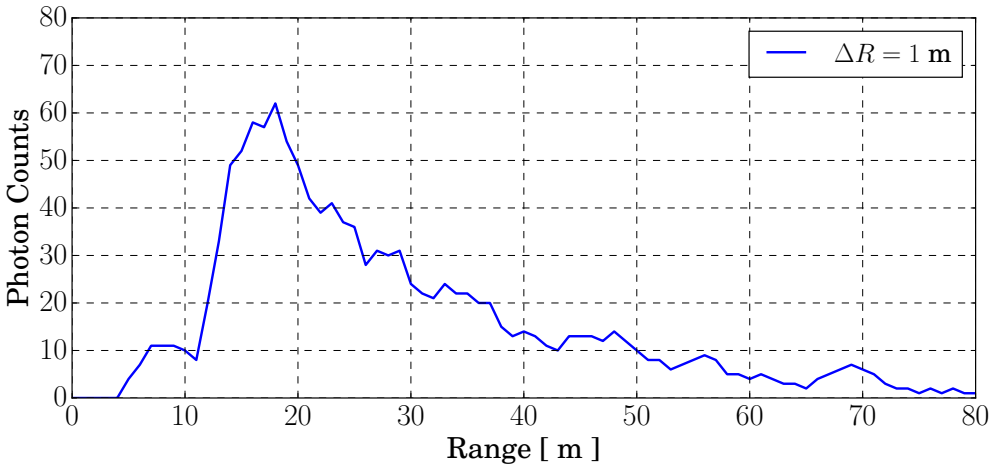

Figure 6.28: Integrated profile of atmospheric returns from Fig. 6.24 over 10 s at 1 m vertical resolution. The combined exponential decay, overlap, and $1/R^2$ effects come in at $\sim$ 18 m and reach shot noise at 80 m.

Using the ATLIS simulator, a modeled atmospheric point cloud was generated and binned over 10 s at 1 m bin resolution to match the data. A comparison is shown in Fig. 6.29, with the left panel displaying the ATLIS modeled and POLAR measured profiles. The peak photon counts, geometric overlap point, and decimation of signal over the first 70 m agree. Modeled data under-estimates the measured from 20-60 m, likely due to non-exact modeling of the noise and atmospheric conditions. The right panel shows the photon counts per each bin plotted with respect to each other over the first 70 m and the one-to-one line. The scatter of points predominantly lay on the measured side of the one-to-one line indicating the under estimation of the ATLIS modeled values, likely due to an inability to capture the exact atmospheric state in the model parameters. The correlation was calculated through a linear regression routine giving a value of $r^2 = 0.8947$,

indicating an overall good fit between the ATLIS and POLAR atmospheric point clouds.

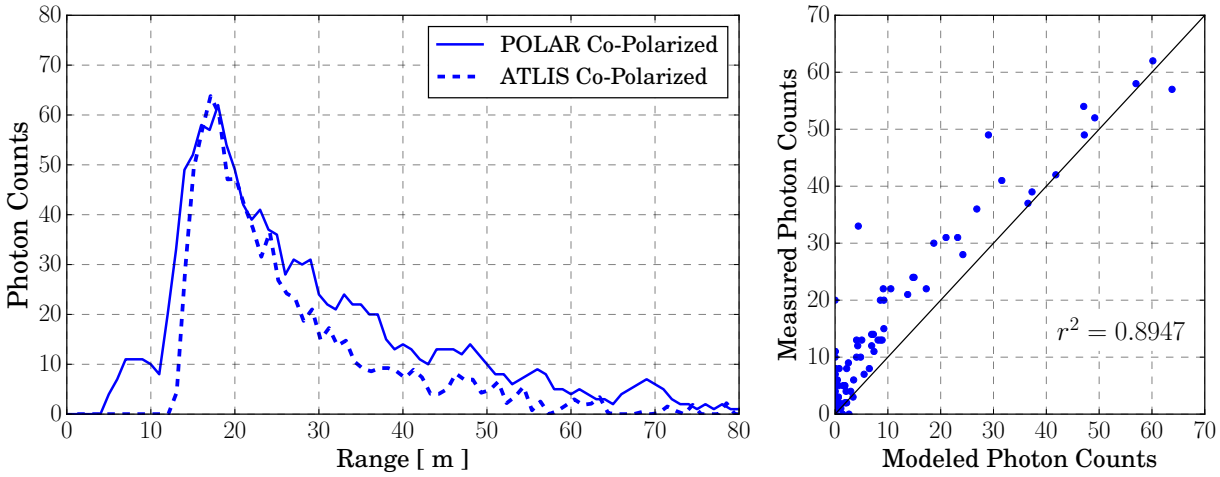

Figure 6.29: Comparison of the POLAR measured atmospheric profile in Fig. 6.28 and modeled atmospheric returns from the ATLIS simulator. The left panel shows both profiles were binned over 10 s worth of accumulation at 1 m bin widths. The right panel shows the counts plotted against each other and correlation value.

The atmospheric data shown here was collected with the sensor operating in a linear photon counting mode. This is illustrated by the number of detected counts, and by a detection rate that is $< 1\%$ per laser shot. With knowledge that the sensor is operating linearly in this regime, the ATLIS model can be used to estimate sensor efficiency and other related parameters. These can then be used to facilitate the analysis of detections from higher photon rates at different portions of the column, serving as a calibration for the surface.

The ability to generate accurate clear air atmospheric measurements with the POLAR sensor proves that an SPL sensor is capable of atmospheric sensing from an airborne platform. It also indicates that the sensor can make these measurements in the same receiver channel that is simultaneously generating high resolution topographic or bathymetric data. With the correct noise management and acquisition characteristics measurements of clouds and aerosols, similar to those in [85, 129], should be possible, but with the higher resolution afforded by TCSPC.

6.1.5 Influence of Unwanted Signal on Multi-Functional Sensing

Data quality and overall sensor performance is driven by the rejection of unwanted signals. The ability to generate detections from any of the regimes shown in the prior section relies on the sensor being out of a dead-time window and able to process photons. As unwanted signal rate increases, there is a two fold effect on SNR. The first is that the associated noise is increased so that there is a decrease in SNR. The second is that wanted signal detections decrease as well, further exacerbating the decrease in SNR. The addition of higher unwanted signal rates creates an asynchronous dead-time window, which propagates randomly in range throughout the measurement profile. There is some probability for this window to blank out signal returns from a target, therefore decreasing the overall detection rates for wanted signal. This effect then further exacerbates the decrease in SNR such that when the unwanted signal rates increase, sensor performance decreases, showing an anti-correlation.

Since the POLAR SPL is a polarimetric sensor, the response to solar background signal differs between channels due to a preferential polarization from surface or atmospheric scattering. Predicting which channel will be subjected to higher noise rates can be done through comprehensive modeling of the surface, atmospheric, and solar states, but this proves difficult due to the assumptions required in capturing directional surface and isotropic atmospheric scattered solar background [133]. However, without rigorous modeling and comparison, an understanding of the detected solar background and the resulting impact on performance metrics can still be derived directly from the data, where estimates of "noise" or unwanted signal can be made per flight line.

Understanding that the total unwanted signal as seen by the acquisition system will be a combination of solar background (several Hz to >kHz depending on the polarization plane) and detector dark counts (< 300 Hz), the total number of observed counts can be calculated per receiver channel per second using the raw data. From the analysis of the ocean flight line in the prior sections it is known that the water surface and atmospheric signal is in the $0 \rightarrow 200$ m ranges and that the remainder of the unambiguous range is assumed to not contain any photons from backscattered

signal. It is assumed that the laser energy is fully extinguished beyond this depth. The total number of noise photons in a 1000 m bin is generated, N_{rx} in the ΔR between 1-2 km bin, as the sum of discrete detections per channel.

Conversion to a metric that can be compared between sensors is done by considering N_{rx} and normalizing by the number of laser shots for the duration of the integration window and the time for light to travel one bin. This gives an estimate of the unwanted signal rate as

$$\xi = \frac{N_{rx}}{n_s(2\Delta R/c)}, \tag{6.5}$$

where the range bin is converted into time elapsed to the bin in interest, and n_s is again the number of shots considered. This output metric is in units of counts/shot/bin, not total contributions per second.

Figure 6.30 shows the data derived noise rates for each polarization channel for the entire ocean flight line path. The blue left axis shows the co-polarized channel where the average value is below 300 Hz over the entire period, implying that there is minimal noise throughout the acquisition. This confirms the signal analysis shown in Fig. 6.11, where the ocean signal dominates over the background signal and detection rates are high. The red right axis shows the cross polarized channel, where ∼100 kHz values are reached at the end of the line. Until UTC 81400, rates are similar between channels, but as the receiver gain was raised during the line in an effort to boost signal detections, the noise rate also increased. With the increased gain, the described transmitter/receiver misalignment provided more surface detections which hindered additional column detections, indicating that the trade off between increased gain, noise rate, and signal detection is ideal for the POLAR sensor when noise rates are minimized. After UTC 82200, the cross-polarized signals reflect values indicates that data from this time period became corrupted. This is elaborated on further in Appendix A.

The mean arrival rate of noise photons was calculated using the data in Fig. 6.30. The left panel of Fig. 6.31 shows both co-polarized and cross-polarized signals, where at the beginning of the line both receiver channels maintain comparable values on the order of microseconds, indicating

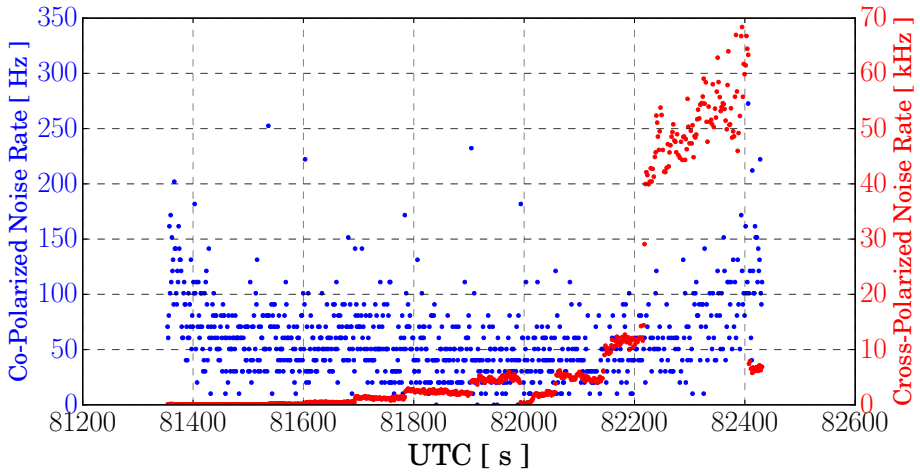

Figure 6.30: Observed noise rates for the co-polarized and cross-polarized channel during the ocean flight line. The twin axes shows the difference between rate magnitude when comparing the two channels.

that both are seeing < 1 noise photon/shot/bin. Therefore, the likelihood of a noise induced dead-time window preventing surface detections is small. Considering that the noise photons occur over the sensor's full unambiguous range, and the signal photons are limited to a window of < 1 m, this operating regime seems ripe for high signal detection. This rate is maintained through the first portion off the line until the cross-polarized noise is increased. The increased cross-polarized noise is seen as discrete steps in Fig. 6.31 until UTC 81800s, indicative of gain adjustments.

The right panel of Fig. 6.31 shows a zoom in to the UTC 81800-82200 time window where only the cross-polarized channel is shown. The increased noise rate can be seen to result in arrival times that become comparable with the IPP, implying that there would be at least one noise photon per shot per bin. Though the cross-pol noise rates in Fig. 6.30 remain in the kHz range, the estimated values on the peak end are unlikely to be a product of the physical environment. Figure A.15 in Appendix A shows this to be true by demonstrating a correlation between an incorrectly reported laser PRF and the cross-polarization noise rate. This is the result of an issue in the acquisition unit's buffer and channel sorter where noise detections were assigned the incorrect channel code for the laser instead of the cross-polarized TDC.

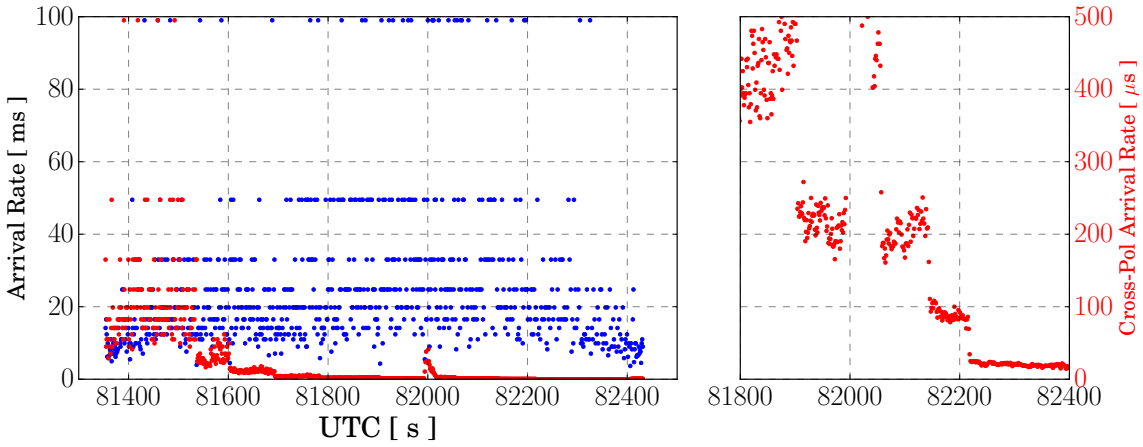

Figure 6.31: Estimated arrival rate of background signal per polarization plane. The right panel shows a zoom-in to cross-polarized signal, where rates are increased towards the line's end.

An explanation for the cross-polarized channel's heightened susceptibility to unwanted signal can be gleaned by analyzing the measurement geometry with respect to the Sun. Solar background signal reflected off the ocean surface will be preferentially S polarized in the ocean surface's plane. The relative coordinates of the wavy ocean surface's normal and the solar zenith angle is dependent on the ocean surface's mean slope at any given point. The rough orientation of these two axes are known and they do not align with the sensor's S and P polarization axes on the aircraft. By considering a projection of the polarizer's transmission and rejection axes onto the ocean surface, it becomes clear that both of the sensor's principle axes fall into the ocean's S plane. This implies that the surface scatter will be polarized in a direction that could contribute to the co-polarized and cross-polarized receiver channels and that the solar azimuth angle will modulate the rotation angle of the surface polarization with respect to the polarizer's transmission axis. Noise variability is then introduced through the relative motion of the aircraft and the sun, differing per polarization channel, and changing throughout the line due to the maneuvers performed.

Both Figs. 6.30 and 6.31 provide an indication of what points throughout the flight line is likely to fall within the correct SNR regime and allow parameter estimates. They also provide assistance in estimating where target signals have decreased, giving a metric by which efficiency of

collection can be judged. This analysis shows the realistic difficulty of employing an SPL for ocean detections, where noise rates are highly variable and thus signal detection rates are also variable.

When the rate estimate can be considered solely due to actual background, and not sensor effects, it can be used as a proxy for understanding relative surface albedo changes, since it is expected that transitions from water to land or snow to land, for example, result in background rate changes. This is seen in Fig. 6.32, where the noise and arrival rates were calculated for Fig. 6.20. This flight line proves interesting as it provides a direct contrast between the high albedo surface terrain and the lower albedo water surface.

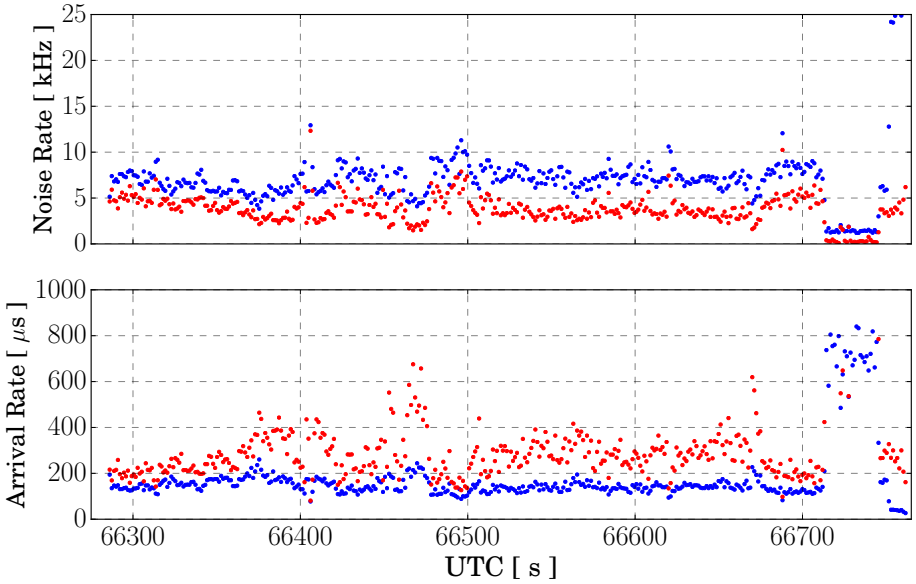

Figure 6.32: The top panel shows the observed noise rates for the co-polarized, blue, and cross-polarized channels, red, while the bottom panel shows the single noise photon arrival rate for the data shown in Fig. 6.20. The noise remains fairly constant for the varying topographic terrain and drops significantly when crossing a small lake just after UTC 66700.

The top panel of Fig. 6.32 shows that for portions of the line that are over varying surface topography, the noise rates have little variation, consistently staying between 5-10 kHz per shot. These values prove manageable and do not drastically impact surface detection rates, as high density can be seen in Fig. 6.21. When the aircraft crosses over the small lake feature, noise rates

can be seen to drop significantly due to the darker surface of the water (0.5-1.5 kHz depending on the channel). This increases the possible detection rates per surface targets. After the water body, the return of bright topography leads to the heightened noise rate.

The lower panel of Fig. 6.32 shows the temporal spacing between arriving noise photons. The spacing stays in the microseconds for most of the line, and then increases to milliseconds over water. Compared to the ocean line, this data shows no clear anomalies that could lead to data corruption, and arrival rate stay larger than the laser's IPP for the entire line. This indicates that the sensor behaved linearly with detection rates not hindered by excessive, unwanted signal detections.

6.2 Sensor Development and Flight Campaign Conclusions

Many of the goals laid out for the ARISTO flight campaign and the airborne demonstration of the POLAR sensor were achieved. Foremost was the overall integration and airborne demonstration of TSCPC in an SPL sensor. This included acquisition of a number of different geophysical quantities, including returns from topographic, bathymetric, and atmospheric measurement regimes. Reliable water surface detection were made with the co-polarized channel, and a long dead-time, with geophysical quantities deduced. Water column detection was shown with the cross-polarized channel, albeit with decreased detection rates. Neither the co-polarized, nor cross-polarized channels were able to detect subsurface hard targets or provided bathymetric mapping capabilities. Both co-polarized and cross-polarized channels exhibited great ability to provide hard target topographic mapping capability, with multiple examples bolstering the technique's validity. As the POLAR sensor was not tuned for atmospheric profile generation, there were limited areas where full profiles could be extracted from the noise. There were certain instances shown where the co-polarized channel exhibited the required SNR, over long integration times, to generate an atmospheric profile, but the cross-polarized signal was limited and not achievable.

The flight campaign demonstrated that the counting system employed showed significant issues when the total counts through the buffer come close to 1 MHz. This drastically limited sensor operation and required electronically blocking noise at the loss of target signal. Realization

of the ARISTO-17 depended on the performance of the SensL counting system, and when non-linearities were present, or high background, the system could not achieve the measurement goals. It was concluded that the SensL CFD/TDC combination is not suited to aircraft operations and an acquisition board that could maintain > 15 MHz reliably should be sought.

Individual flight lines were not repeated during the campaign, so collection was performed on a single pass with knowledge of the expected altitude AGL prior to the pass. This required planning that included a best guess at sensor parameters to be made prior to the line — e.g. PMT high voltages, CFD settings— and then adjusted at the beginning to optimize detection efficiencies. However, occasional adjustments would need to be made mid-line to increase, or decrease detection rates, and maintain photon counting operation. This resulted in portions of the line having different sensor settings than others. Due to the nature of the flight campaign, this was acceptable and can be worked around to prove out measurement principles. In an operational sensor, where science data is collected, there are typically repeat ground tracks for the same line, such that the final optimized settings from the first can be used for all subsequent flights.

6.3 Relevance to Posed Thesis Questions

The summation of efforts contained in the prior and current chapters show the progression of the POLAR sensor from the entry TRL-4 to the exit TRL-5. This work showed a prototype sensor with demonstration in a relevant and operational environment. The overall conclusion of the ARISTO-17 flight campaign was that the POLAR sensor provided a novel measurement that leveraged TCSPC and that the techniques employed can provide high resolution geoscience data with accompanying low data rates. The measurement capabilities provide the foundation for future sensor development, where different geophysical quantities can be targeted by specialized receiver channels and transmitter tuning. This would be a drastic step beyond the POLAR sensor, creating a capability for multiple field deployments with targeted scientific objectives.

The POLAR sensor's deployment directly addresses the third thesis question posed. In addition, analysis of the resulting data facilitates a better understanding of the first two posed

thesis questions. A summary of how the work in this chapter addresses these questions is below.

(1) What are the implications of utilizing the time-correlated single photon counting approach for geophysical parameter estimation from "soft" volume scattering environments?

- The POLAR sensor showed that measurements of voluminous scattering media, ocean column and atmospheric, can be made with a single SPL sensor employing the TCSPC acquisition technique. Although limited airborne atmospheric measurements were demonstrated, there were several instances of water column detections, indicating a sensitivity to diffuse scattering layers.

(2) How are estimates of backscattered photon rate and target range affected by the implementation of the photon time-tagging approach?

- Implementation of TCSPC acquisition introduces biases caused by strong signals, but the acquired data can be analyzed through detection rate estimation to understand where these are evident. In practice, photon rates can be estimated over some temporal integration period. Data acquired by the POLAR sensor from the ARISTO-17 shows that photon rates can be estimated relative to laser firings and can be subsequently used to understand sensor linearity and provide confidence in bias mitigation.

(3) Can polarimetric lidar incorporate time-correlated single photon counting, and what are the implications to high resolution multi-functional measurements of atmosphere, ocean, and hard targets?

- Integration and operation of the POLAR sensor from the NCAR GV research aircraft provided a demonstration of a polarimetric lidar operating with TCSPC, confirming the theory presented in Chapters 3 and 4. The experimental data generated by the POLAR sensor demonstrates the viability of these techniques for multi-functional operation by generating measurements of different geophysical quantities, namely from topography and open ocean.

Chapter 7

Evaluating POLAR's Single Photon Counting Signals with ATLIS

In practice a fielded SPL is evaluated for single photon counting validity through probability analysis of the photon time-tags, where an assumed probability of detection in the teens is "likely" to generate time-tags that are the result of single photons incident at the detector face. This technique was employed throughout the ARISTO-17 field campaign by the POLAR sensor, where the simple method of evaluating the number of acquired target photons (filtered to avoid the inclusion of asynchronous unwanted signal) in comparison to the number of laser firings over the accumulation window was regularly used. This method generates a target detection rate, with units of photon detections per laser firing, and when this value is $< 50\%$ it is likely that the sensor is detecting single photons and the pile up of concurrent photons is being avoided. Becker *et al.* [8] provides a value of $< 1\%$ to ensure single photon counting, but the sensing this is applied to involves predictable and consistent count rates that are observed from static platforms that facilitates large collection windows. This is significantly different from the count rate bursts and resulting collection strategies in SPL sensing. Though, in practice, these methods provide information for on-the-fly adjustments, but lack the means to provide robust and clear determination of single photon counting.

Further analysis to provide insight into the claim of single photon counting can be had by including unwanted signal into the calculations and generating an estimate for the total throughput of the FIFO buffer. This then can be compared to the maximum usable count-rate, as dictated by the TDC dead-time ($\sim 1/\tau_D$). This does not directly imply that the target signal is linear or non-linear, the calculated throughput can indicate that the temporal separation of arriving photons

is near the dead-time value. When this condition is true, the target signal is regularly missed by the counting, due to falling within a dead-time window or concurrent photons arriving and only a single detection is registered. When the total throughput is near maximum value, it is likely that the counting system is behaving in a non-linear fashion, and adjustments to the detection statistics should be made. This again gives only a high level non-concrete method of single photon counting determination.

The combination of both methods proved reliable in predicting target count rates in a linear regime over the course of the ARISTO-17 flight campaign. The analyzed data provided bounds for sensor linearity and fostered an understanding of the resulting relationship between counting linearity and the PMT and CFD settings. Despite the usefulness of rule of thumb techniques, more robust methods are necessary to ensure sensor linearity and a deeper understanding of when a sensor is operating in a regime that is experiencing significant dead-time effects.

This chapter will present a novel approach for determining whether a SPL sensor employing TCSPC is operating in linear photon counting mode. The photon time-tagging approach employed provides no direct measurement of detector pulse heights, which results in counting ambiguities when attempting to determine whether a binary detection in the data stream is the result of a single or multiple concurrent photons. To address this problem the ATLIS model is utilized in a "forward" configuration, where the model output can be aligned to the measured POLAR data, after which the model outputs can be used as a pseudo-truth to facilitate further calculations that would otherwise be unachievable with the time-tagging data, such as working with the simulated signal waveform prior to the TDC sampling.

7.1 Utilizing ATLIS to Compare Measured and Modeled Point Clouds

Forward modeling of lidar signals has been utilized in the past to understand ICESat lidar returns in comparison the European Centre for Medium-Range Weather Forecasts (ECMWF) atmospheric model [123], to analyze the detection of winds and recovery of backscatter coefficients by an incoherent doppler lidar [87], to simulate satellite, airborne, and terrestrial lidar with a discrete

anisotropic radiative transfer model [127], and countless other instances. These forward models are derived from the physics that describes the laser light interaction with the environment, hardware effects embedded within the retrieved data, and the necessary geophysical parameters necessary to describe the measurement. A key distinction is that a forward model provides a cause and effect relationship between the modeled environment and sensor. This is necessary to state as it is not a specialized form of an inversion to be performed on the data, i.e. measuring the effect and inferring the cause [107].

Earlier in this thesis ATLIS was discussed as a comprehensive method by which environmental and instrument parameters can be combined to provide a full scale simulation of a nadir pointing SPL that employs TCSPC. A key function of ATLIS is that it generates the inherent signal waveform, akin to what would be seen in an analog detection regime, and then applies a sampling routine to generate the discrete photon time-tags. Linking the point cloud to the incident signal waveform requires collapsing the point cloud into a single profile, but due to the sparse detections of a SPL, longer integration times are needed to generate a histogram with enough structure that will allow the probability mathematics derived in Chapter 3 to be applied. In an airborne sensor this is not advantageous, as rapidly moving terrain will smear features and give an incorrect estimate of photon counts originating from a semi-uniform terrain. A method is then needed to link the measured point cloud to the modeled signal waveform without loosing the spatial and temporal advantages present in the point cloud format, and facilitate production of an answer to the validity of the single photon counting assumption.

7.1.1 Aligning ATLIS Signal Strengths to POLAR

Alignment of the ATLIS simulator and the POLAR measured data is performed by matching the point clouds. Once this is performed it is assumed that signal waveforms generated by the ATLIS simulator are representative of the signals incident on the detector face of the POLAR sensor. The ATLIS output then contains the modeled point clouds, waveforms, and associated statistics for each.

Some educated assumptions must be made to allow tuning of the ATLIS simulator, most of which are applied to the scattering environment. These include fixed depolarization values, solar background levels, backscattering cross-sections, and spatial variation of all environmental parameters. These are relatively straight forward values to estimate due to an abundance of information in the literature that can be explored knowing the POLAR measurement environment is (i.e. ocean vs. fresh water, high vs. low solar background etc...). By leaving these environmental values fixed, the instrument parameters are then used as the primary tuning method for signal strength modulation. Specifically, since the true efficiency of the POLAR sensor was not measured, the input parameters for the transmitter and receiver optical and electrical efficiencies are adjusted until the correct received count rate is achieved.

This is summarized in Fig. 7.1, where the flow for matching the ATLIS output to the POLAR measured data is shown. Input parameters are varied until the modeled and measured detection rates are within close proximity. Iterations are then continued until the difference of the detection rates is minimized, which, in the case of photon counting, can be considered as valid when the shot noise limit is reached. Time spent minimizing beyond the inherent shot noise is unnecessary as the shot noise sets the lowest bound for uncertainty in a SPL sensor, when several counts are considered. It is necessary to select a window of range bins in which this can be evaluated, ideally containing a target or feature that provides counts well above the shot noise limit, such that the difference can be considered statistically significant and not noise. In the case of the POLAR measurements being considered for evaluation, the ocean surface provides such a source of photons that can be tracked in the measured and modeled data.

Figure Fig. 7.2 shows an example of a total output point cloud from the ATLIS simulator. In this case the total convolved ocean surface signal was taken as the evaluation range window. The simulator was run for 10 seconds worth of data, creating a time series representative of the signal densities seen during the ocean line in Chapter 5. The peak of the ocean surface signal was placed at 155 m, which is representative of the mean ocean signal during the flight line example shown in Fig. 6.9, with the ocean scattering characteristics set up to mimic those of open ocean

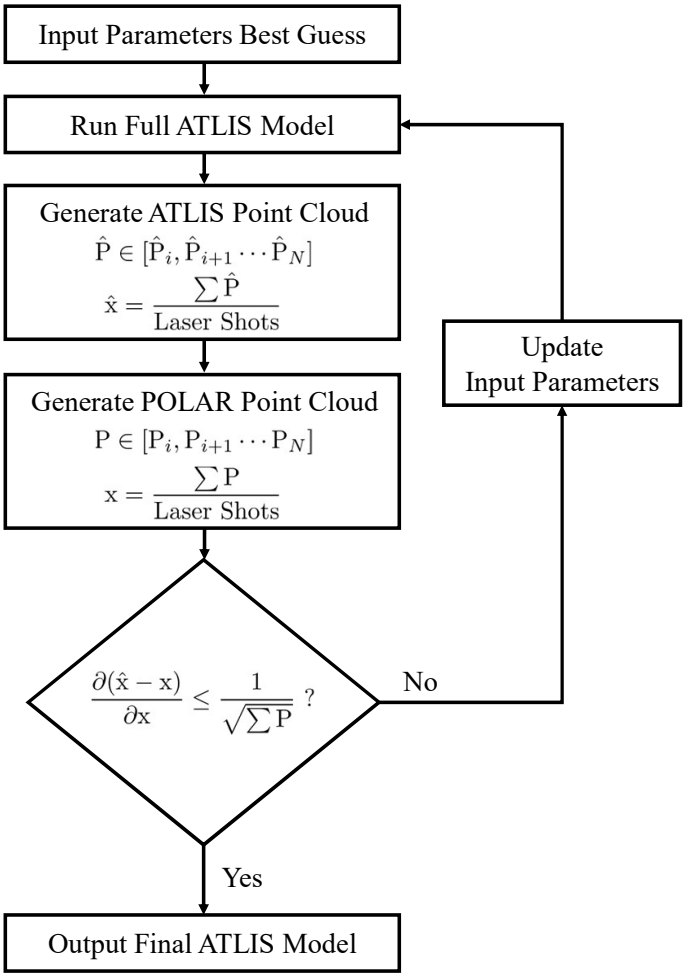

Figure 7.1: Flow diagram of the steps taken to match the ATLIS model outputs with the measured POLAR data. The decision step is based on a minimization of the surface detection rate difference between measured and modeled data, and considered achieved when the shot noise limit is reached.

water. The output modeled data captures the geometric overlap and atmospheric signal, the water surface and water column signal, and the solar background, indicating that the physics of the raw SPL measurement can accurately be captured and fine tuned in the ATLIS simulator.

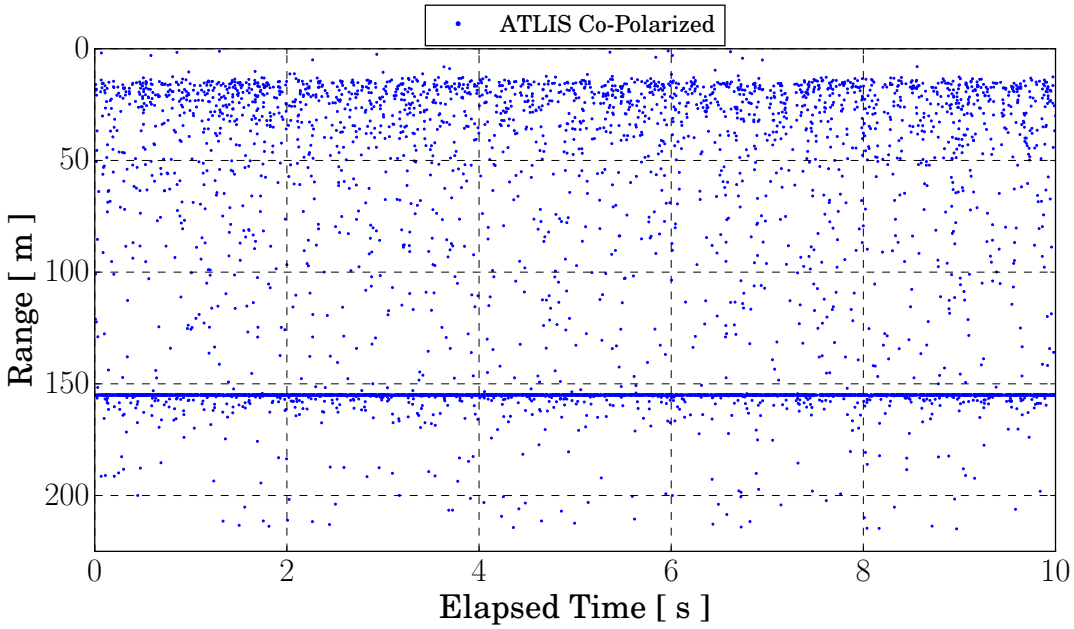

Figure 7.2: Ten seconds of modeled co-polarized detections over an open ocean environment with a moderate noise level. The ocean surface is located at 155 m from the sensor. The macroscopic characteristics of the measured point cloud in Fig. 6.9 are all captured, including the atmospheric returns, ocean surface, moderate column returns, and noise.

In Fig. 7.2 the heightened photon counts from the ocean surface can clearly be seen at approximately 155 m, with additional denser subsurface signal resulting from sporadic water column backscatter. Not seen in the ATLIS simulator output is the effects of afterpulsing or other detector induced effects. The simulator does not account for these effects as they are not needed for the comparison once the measured data has been filtered properly.

The distribution of ocean surface photon counts is calculated from an averaged surface representation generated for many wave cycles (as discussed in Chapter 4). Over short time windows the measured data will trace out the surface variation of the wave, but the modeled data will show a detection from the time averaged representation and does not exhibit the clustering expected.

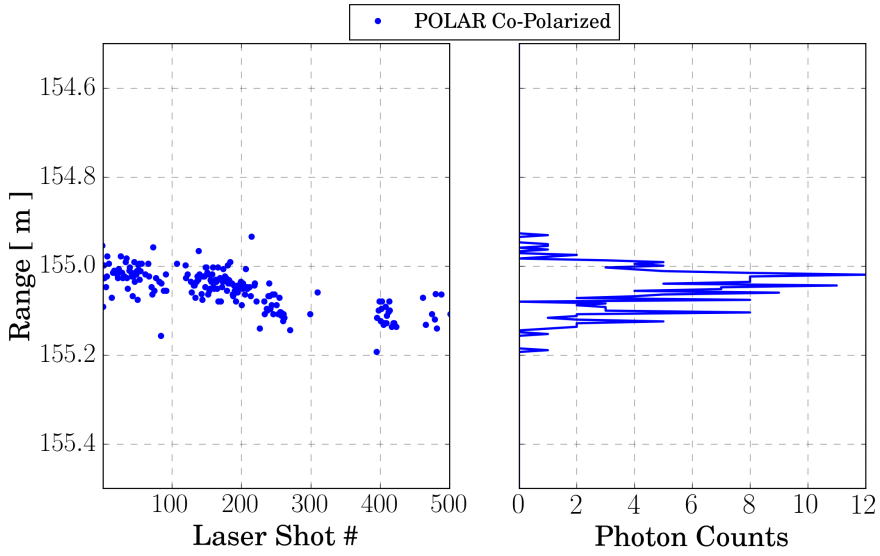

Figure 7.3: Measured returns from an open ocean surface in the co-polarized receiver channel over 500 laser shots. The right panel shows the distribution of the point cloud in range and the left panel shows the integrated profile, at 4 mm bin resolution, over all 500 shots.

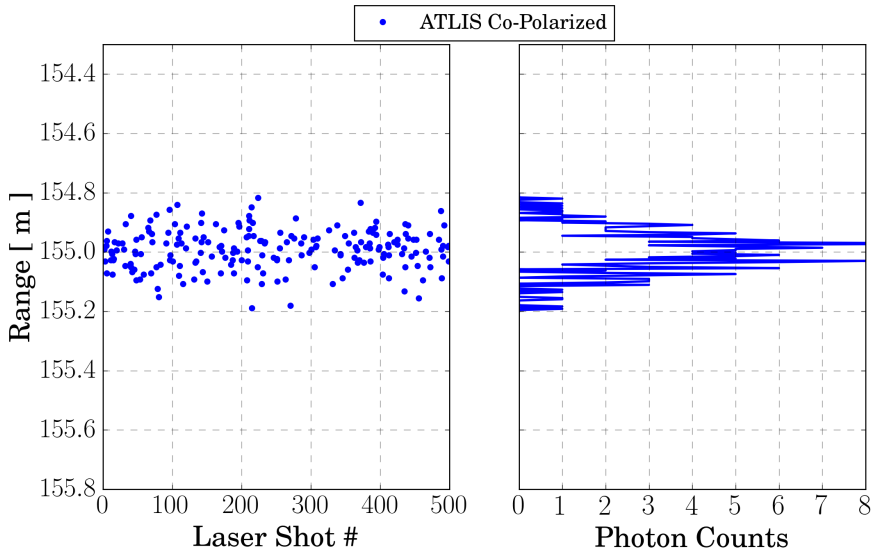

Figure 7.4: Simulated returns from an open ocean surface in the co-polarized receiver channel over 500 laser shots. The right panel shows the distribution of the point cloud in range and the left panel shows the integrated profile, at 4 mm bin resolution, over all 500 shots.

Despite this difference, the ATLIS surface representation is still considered computationally valid and can describe the surface wave structure accurately, as shown in Fig. 6.12 where the fitting function used in the ATLIS model was used to predict Gaussian surface features in the POLAR measured data. A direct comparison of surface detection rates and distribution variances should be expected as close, but not exact, as shown. A more complete representation of the wave structure requires discrete ray tracing and robust surface structure models, such as those described in [31], and requires an MC approach that randomly samples the wave structure over the course of the measurement.

Figures 7.3 and 7.4 show the photon returns and integrated histogram with 4 mm bins over 500 shots of accumulation for the POLAR measured data and ATLIS modeled data, respectively. Some wave structure can be seen in the POLAR point cloud and histogram as the detections skew to larger range estimates. Additionally, the clustered nature of the surface returns is an indication of the physics driving which backscattered photons are detected. Calculating the surface detection rates over the 500 shot period, it can be seen that both the measured and modeled rates are similar in magnitude. During this time window POLAR measured rates at $x = 0.386$ photons per laser shot and ATLIS estimated the modeled rate as $\hat{x} = 0.408$ photons per laser shot. This gives a $\sim 5.5\%$ percent different between the retrieved values, indicating that the ATLIS simulator is providing realistic comparisons to the measured surface signal. The surface detection rate metric used here provides an easily calculated and comparable value, whose ratio gives a pseudo detection probability that directly reflects sensor performance over that window. Due to the specular nature of the returns, it would be expected that the measured surface data will exhibit varying detection rates across the surface, and it can be seen in other portions of the surface profile that the surface detection rate varies between $0.20 \leq x \leq 0.50$ photons per shot, but the averaged value over larger time windows reduces the uncertainty in estimates.

Given the small percent difference between the measured and modeled surface detection rates, the computation scheme shown in Fig. 7.1, $\hat{x}$ and x, can be used to test the alignment of the ATLIS

simulator. If the hypothesis of

$$\frac{\partial(|\hat{x} - x|)}{\partial x} \leq \frac{1}{\sqrt{\sum \mathrm{P}}}, \tag{7.1}$$

is found to be true, then it is assumed that the ATLIS modeled data set is representative of the measured data. After several ATLIS model runs a vector of surface detection rates was generated, with a window of the final output model shown in Fig. 7.4 and used for the prior evaluations. The minimized difference between the photon detection rates is

$$\frac{\partial(|\hat{x} - x|)}{\partial x} = 0.022, \tag{7.2}$$

and the computed shot noise on the POLAR measured data for $\sum \mathrm{P} = (\mathrm{x}) * (500 \text{ shots})$ gives

$$\frac{1}{\sqrt{\sum \mathrm{P}}} = 0.07198. \tag{7.3}$$

It is shown that this hypothesis is true for the given ATLIS modeled data set as the minimized difference between the surface detection rate is ~ 3 times smaller than the calculated shot noise for the measured POLAR data over this timing window. It should be noted that if a different window of data is considered, smaller or larger, the hypothesis should be tested again for validity. Due to the burst nature of photons from surfaces there could be a tendency of the null hypothesis for too small of a window.

7.2 Interpreting POLAR Photon Time-Tags with ATLIS Signal Waveforms

The series of time-tags collected by the POLAR contain no inherent information content beyond the detection time and range. Integrated over some time window these give a pseudo waveform that can then be interpreted in terms of the number of counts that fall into a bin over some number of fired shots. With the ATLIS modeled data now matched to the POLAR measured data, the full functionality of a full waveform simulator can be accessed providing the full altitude range of information per single shot. This represents a large step in information content and allows the use of the single shot waveforms as an interpretation of the photon time-tags. From the single shot signal waveforms a number of closed form calculations can be performed on the forward

modeled data, namely direct calculation of the probability of detection as shown in Chapter 3, that give an indication as to at what point in the measurement profile the sensor may have been operating out of single photon counting.

It is necessary to ask whether or not it is appropriate to consider the single shot waveform as a proxy for the singular time-tag. It can be assumed that the once the point clouds have been matched the modeled time tag is a single sampling instance of the modeled signal waveform, such that the intensity described by the waveform is indicative of where detection rates will be high or low. In addition, the ATLIS waveforms are generated at the TDC resolution of the POLAR sensor, implying that single photon time-tags can be understood in terms of their finite probability of detection at every range over the full column measurement though these continuous waveform estimates.

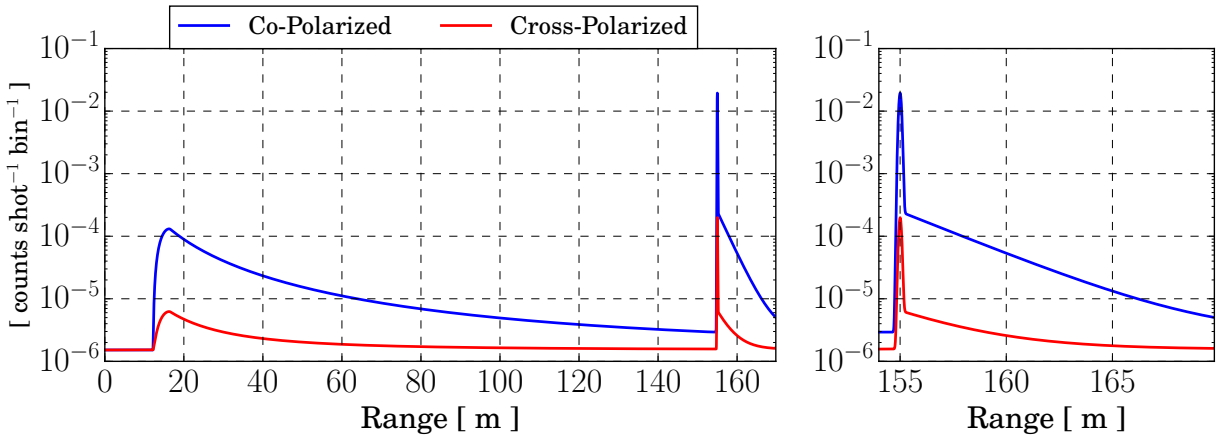

Figure 7.5: Modeled single shot signal waveforms for the co-polarized and cross-polarized receiver channels, generated from the POLAR signal strength aligned ATLIS simulator. The left panel shows the complete range from aircraft window to ocean surface and column, and the right panel shows the heightened surface signal and column decay.

Figure 7.5 shows the modeled co-polarized and cross-polarized single shot received signal waveforms prior to sampling by the TDC, giving units of counts per shot per bin, and void of dead-time effects. The co-polarized waveform shown here is the single shot realization used to generate the point cloud shown in Fig. 7.2. The resolution is set to be equivalent to the TDC

at 4 mm per bin. These waveforms are indicative of what the continuous stream of backscattered photons would look like at the faces of the POLAR PMTs as seen by a digitizer with no introduced effects. The co-polarized signal, shown in blue, can be seen to exhibit a stronger signature than the cross-polarized signal due to the polarization-preserving scattering environments of the clear atmosphere and water surface.

As previously stated, the statistics needed to compute whole profile estimates of detection probabilities are not compatible with the sparsely sampled data inherent to a time-tagging SPL. However, with access to the backscattered signal waveforms for the POLAR sensor the probability of detecting a photon event per bin, given the TDC resolution and dead-time, can be computed using the statistics from Chapter 3. Figure 7.6 shows the results from computed the probability of detecting one or more photons from the co-polarized channel through the entire measurement profile using the ATLIS waveforms as an intensity input to the equations. The top panels showing the probability of detection with, $W_j P(k \geq 1; j)$, and without, $P(k \geq 1; j)$, dead-time effects applied. The lower panels show the dead-time weighting function's, W_j, response to the signal environment as a function of range.

When including the dead-time weighting function to the probability of detection estimate, the deviations from a dead-time free estimate are evident, but not overwhelming, resulting in decreases of less than an order of magnitude in all cases. The response to geometric overlap can be seen at 40 m range with a reduction of $\sim 30\%$. Though this seems large, given that $P(k \geq 1; j) \ll 1$ already, a further reduction of less than 50% does not drastically change the detection statistics and recovery occurs within $\sim 5\%$ prior to the ocean surface backscatter, as indicated by W_j in the lower left panel. This is different than the atmospheric response seen in Chapter 3, where hundreds of meters were necessary to achieve approximate recovery at $\sim 1\%$. The difference in detection responses between the two atmospheric signals can be attributed to the lower signal strength in the POLAR system while in airborne configuration, due to decreased efficiency and detuned system parameters to ensure single photon counting.

A complete appreciation for the dead-time impacts is seen in the lower panels of Fig. 7.6,

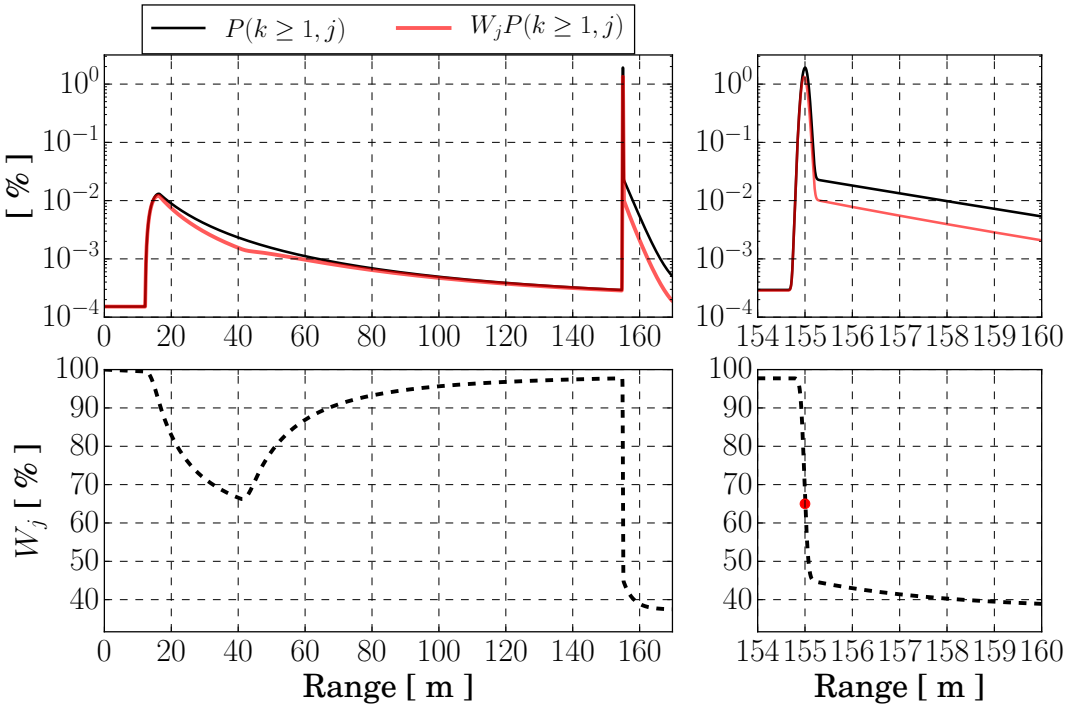

Figure 7.6: Computed probability profiles for the single shot signal waveforms shown in Fig. 7.5. The top panels show the percent probability of detection without dead-time, black, and including the 190 ns dead-time of the POLAR SPL, red. The bottom panels show the dead-time weighting factor, in percent where 100% equates to no dead-time effects, for the entire profile. The red dot in the lower right panel indicated the point at which the peak probability of detection occurs.

where the totality of the decimation factor can be seen. Of specific note is that the location of peak detection from the water surface occurs at a W_j point that is midway between the max and min, indicated by the red dot at $\sim 65\%$. This is the case as the system becomes impacted by dead-time from the leading edge of the return signal and the peak of this signal is now being impacted by an integration along the entire leading edge.

The inclusion of a 190 ns dead-time induces two significant effects that can be seen in the ocean surface response, shown in the left panel of Fig. 7.7. The first is a decrease of $\sim 24\%$ in peak probability of detection. The second is a forward bias in the location of the bin that contains the peak probability, approximately 1.5 cm. If this peak bin is compared to the peak bin without dead-time considered, it is seen that the decrease probability of detection alters by a percent or two, such

that comparison, in this case, can be done between the same bin in each profile without introducing unmanageable error. The overall bias of a 1-2 cm is significantly lower than the overall uncertainty of the IRF, but should still be noted as present. In comparison to the biases shown in Chapter 3, these will not manifest as altered distributions when several photon events are accumulated. The trailing edge of the ocean signal maintains the decreased probability of detection as it is providing an estimate that integrates across the peak of the ocean surface signal in the weighting function.

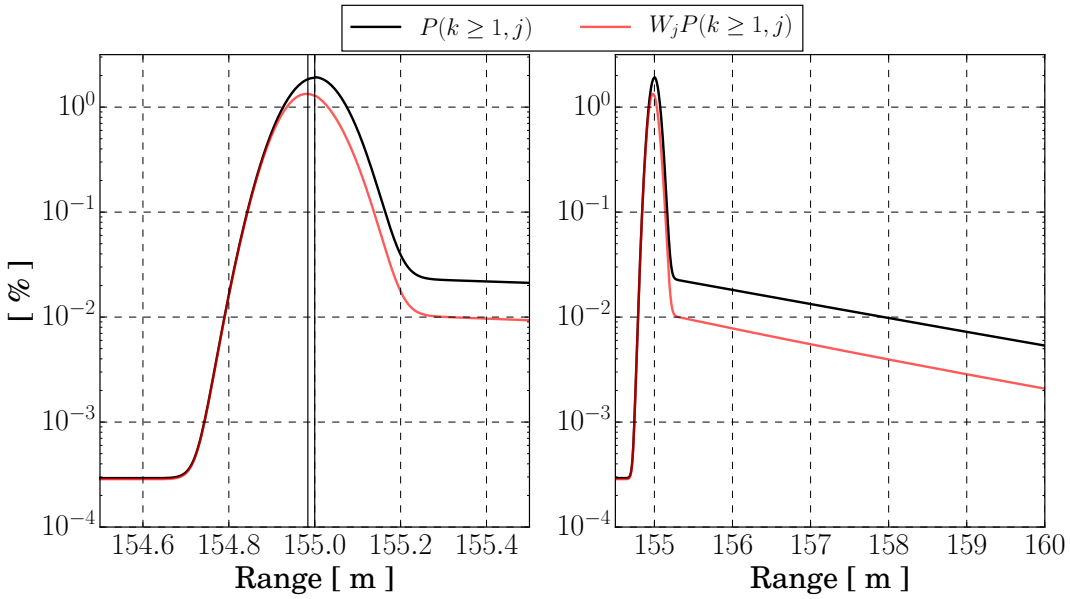

Figure 7.7: This figure shows a zoom in range to the top right panel of Fig. 7.6. The left panel shows the dead-time induced difference in peak probability of detection, shifted forward towards the sensor by centimeters and decreased in amplitude. The right panel shows the reduction in column detection probability when dead-time is considered.

The right panel of Fig. 7.7 shows the probability of detection for the first 5 m of ocean column. Here the dead-time inclusion can be seen to reduce the overall probability of detection throughout the entire column by a constant value of $\sim 76\%$. Given that the surface signal provided $\ll 100\%$ probability, the immediate surface transient response into the column signal is reduced (contrary to what was seen in the atmospheric signal), and the column probability recovers in the immediate bins to the expected value. The probability of detection is low near the surface at $\sim 0.001\%$, but still large enough that there is an expectation for several thousands of shots to

yield column detections in the data stream. This is also, in part, due to the less than 100% surface detection probability per shot. In the case that the surface was registered every shot the dead-time would blank out subsequent column detections in that respective channel. This then explains why the column signal is sporadic, but present, in the measured POLAR data shown in Fig. 6.9 and modeled ATLIS data in Fig. 7.2.

Interpretation of the continuous probability curves for an SPL sensor provides a novel way by which a multi-functional sensor can be evaluated in totality for its performance across regimes. By including the system dead-time and the full range of signal strengths, detectability can be fully examined. This method now allows the hypothesis of single photon detection to be tested explicitly.

7.2.1 Probability of Detecting k $\geq$ 2 Photons

A direct approach to estimate the likelihood of receiving multiple target photons from a single laser pulse can be derived through Poisson statistics and applied to the ATLIS signal waveforms. Prior derivations in this thesis work have examined the probability of $k \geq 1$ photons, which inherently includes contributions from higher order terms due to $k = 2, 3, 4...$ photons, with the assumption that if the probability of detecting a single photon is low then it will be the case that the probability of more than one is much lower. Though this is a valid argument it is increased rigor, and moving away from rule-of-thumb approaches, demands requisite analysis to support this claim. To understand the non-unity photon contributions to the overall distribution it is necessary to derive and estimate the $k \geq 2$ detection probability and compare to the $k \geq 1$ estimate. Through this comparison SPL signals can be examined for where $P(k \geq 2; t_1, t_2) \gg 0$, which would indicate higher likelihood of deviation out of single photon counting.

To estimate the $k \geq 2$ detection probability the conventions from Chapter 3 are utilized, such that the impinging rate function is equivalent between formulae. The probability of detecting two or more photons in the j_{th} timing bin, assuming a specified system dead-time and time bin width, can be given generally as

$$P(k \geq 2; t_1, t_2) = W_j[1 - P(k = 0; t_1, t_2) - P(k = 1; t_1, t_2)]. \tag{7.4}$$

This equation can then be expanded by implementing a Poissonian detection scheme in a discretized bin space. It is assumed that the rate function is a linear combination of the backscattered photon rate and a constant noise contribution. This then allows the single photon detection probability to be derived as $P(k=1;j) = (S_j + \xi)\exp(-S_j - \xi)$ and the null detection probability as $P(k=0;j) = \exp(-S_j - \xi)$. These can be substituted into Eq. 7.4, which then becomes

$$\begin{aligned} P(k \geq 2; j) &= W_j[1 - \exp(-S_j - \xi) - (S_j + \xi)\exp(-S_j - \xi)] \\ &= W_j[1 - (1 + S_j + \xi)\exp(-S_j - \xi)]. \end{aligned} \tag{7.5}$$

This equation differs from Eq. 3.26 in Chapter 3 by an added factor of $\exp(-S_j - \xi)$, which serves to drastically reduce the probability of detecting more than one photon. However, these equations are similar in the sense that the dead-time weighting function is unchanged from the single photon to multi-photon detection probabilities. The presence of the dead-time weighting function serves to counteract the intuition that as the backscattered photon rate increases so will the $k \geq 2$ detection probability. Though this is generally true, when rates are high the dead-time serves to decrease the overall probability of detection for all values of k, including the higher order terms. This serves as important, as when W_j is furthest away from unity the already low probability for $k \geq 2$ will be further reduced, which implies a higher likelihood of operating in the single photon counting regime.

7.2.2 The Single Photon Counting Metric

A single photon counting metric can now be defined and utilized to further understand, and test, when a SPL sensor could be operating in a linear single photon counting mode. Given that the prior computations have been performed through the range dependent signal waveforms, the results of the metric will also be range dependent. This acknowledgment indicates that differing scattering regimes throughout the column can be discretely evaluated for their adherence to the SPL criterion, and different regimes can be independently classified by linearity.

The single photon counting metric can be defined by the ratio of the single photon and

multi-photon detection probabilities as

$$\begin{aligned}\Omega_j(S_j,\xi) &= \frac{P(k\geq 2;j)}{P(k\geq 1;j)} \\ &= \frac{1-(1+S_j+\xi)\exp(-S_j-\xi)}{1-\exp(-S_j-\xi)},\end{aligned} \tag{7.6}$$

where the ratio of the detection probabilities $P(k \geq 1; j)$ for $k = 1, 2, 3...$ photons and $P(k \geq 2; j)$ for $k = 2, 3, 4...$ photons are utilized. By definition the dead-time effects are removed within this metric and the way at which Ω_j changes throughout the measurement column can be attributed solely to the backscattered photon rate and noise. This provides the clearest connection to single photon detection as the non-linear instrument effects have been removed.

Equation 7.6 provides a convenient analysis of of single photon counting, as when the sensor is operating in a low count rate regime, Ω_j will be minimized and single photon detection will occur. As count rates increase $\Omega_j(S_j, \xi)$ does as well, indicating an increased likelihood of deviation out of single photon counting. Given that $\Omega_j(S_j, \xi)$ is a per bin estimate, when examining the range dependent signals of an airborne multi-functional SPL Eq. 7.6 can be computed for the entire estimated signal waveform. This is an important ability due to the differing signal rates that are seen in a full column measurement, where atmospheric signal is expected to be much lower than ocean surface signal. These different regimes can then be evaluated for adherence to single photon detection and where deviations could be expected. This metric can be thought of as an indicator for the direct separation between the two probability estimates.

To test the applicability and usefulness of the single photon counting metric the ATLIS estimated co-polarized signal waveform is used as an input to each of the probability of detection estimates. The values of $P(k \geq 1; j)$, in the presence of a 190 ns dead-time, are computed from Eq. 3.26 and shown in the top panels of Fig. 7.8. The separation between atmospheric and ocean surface peak probabilities are separated by two orders of magnitude, where the ocean surface signal demonstrates 1.9%. This presence of the significantly lower atmospheric probability provides an indication as to the structure of the expected point cloud, as seen in Fig. 7.2. In all regimes across the profile, the likelihood of a single photon is low, lending credence to the claim that the POLAR

sensor operated in the photon counting regime over the entire measurement column.

The middle panels of Fig. 7.8 show the computed values of $P(k \geq 2; j)$ for the whole measurement column, as calculated according to Eq. 7.5 and maintaining the 190 ns dead-time. The atmospheric and ocean surface peak signals now show a separation of over four orders, creating a clear deviation from the single photon detection curve. The ocean surface signal now peaks significantly lower than 1% at 0.02% per shot. Given that this value is the estimate for all multi-photon detections combined, this is an indication that the likelihood of detecting $k = 2, 3, 4...$ per shot is very low can be assumed to not be present in the retrieved data set. This is also the case for the atmospheric signal, which has already been acknowledged as sparse in the POLAR and ATLIS point clouds, where the probability of detection for multi-photon detections in this regime is $\ll 1$, and each registered detection in the point cloud can be considered the result of a single photon.

Using the $P(k \geq 1; j)$ and $P(k \geq 2; j)$ data from the top and middle panels of Fig. 7.8, respectively, Eq. 7.6 was used to conduct the single photon counting test, shown in the bottom panels. Some care is necessary when interpreting plots of Ω_j. Due to the ratio, Ω_j is only equal to or greater than unity when $P(k \geq 2; j) > P(k \geq 1; j)$, which indicates a high likelihood of multi-photon detection. In the case when $P(k \geq 2; j) < P(k \geq 1; j)$ then the ratio will always be less than unity. Examining the atmospheric signal, it can be seen that its peak value occurs four orders of magnitude below unity at 6.5×10^{-5}. This large separation from unity solidifies the previous assumption that the atmospheric signal is photon counting.

The Ω_j response to the ocean surface signal can be seen in the bottom right panel of Fig. 7.8. The combined low atmospheric signal and noise floor prior to surface response is six orders down from unity implies that there are no dead-time effects prior to surface. The peak surface signal shows two orders of magnitude below unity at 9.5×10^{-3}. This gives the immediate indication that the photon rate from the surface is low and that the returns are occurring within a single photon counting regime. This conclusion is aided by examining $P(k \geq 2; j)$, where the peak ocean surface return is 10^{-2}% for multiple incident photons. Interpreting Fig. 7.3 with these conclusions, the POLAR sensor's point cloud of ocean surface detections has a strong likelihood to be operating

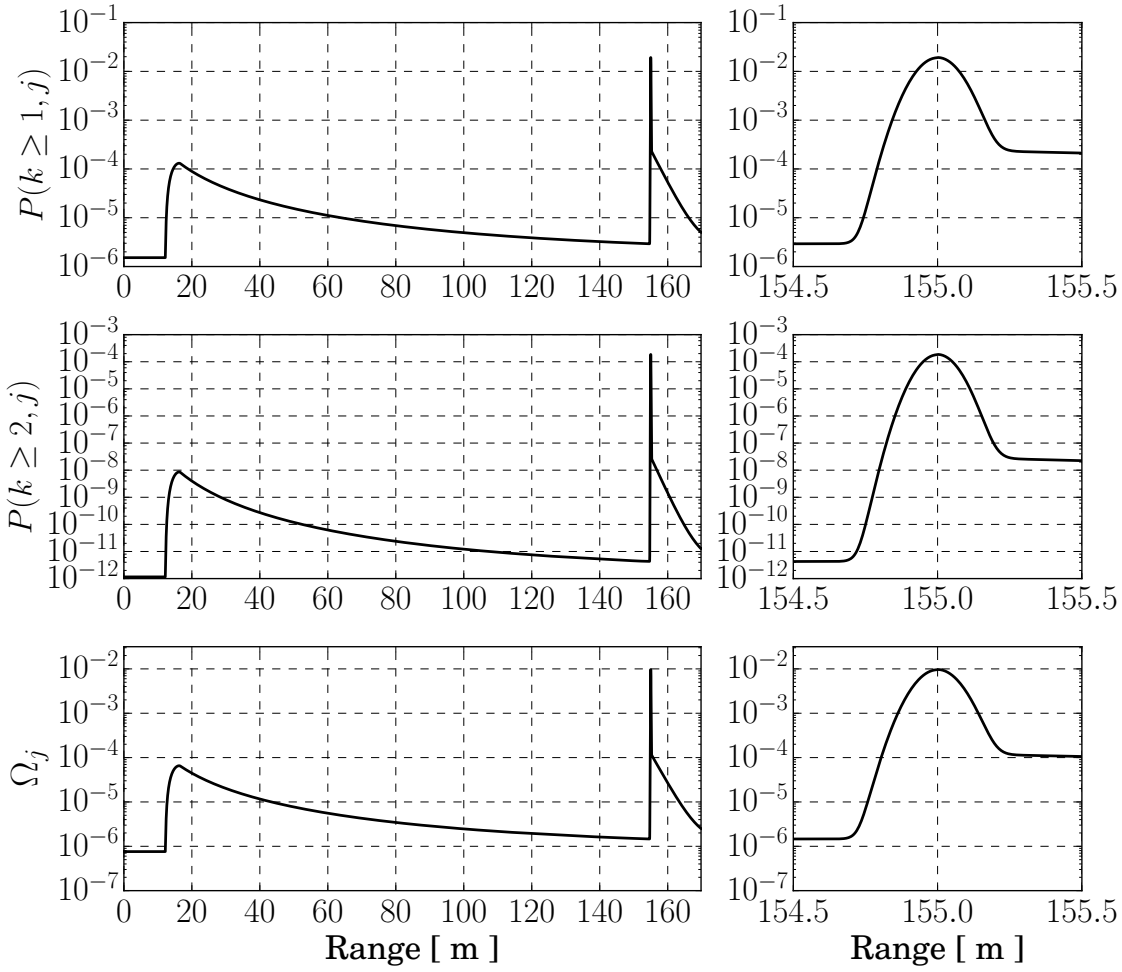

Figure 7.8: The top panels show the computed probability of detection profiles for one or more photons per bin, $P(k \geq 1; j)$, the middle panels show the probability of detecting two or more photons per bin, $P(k \geq 2; j)$, and the single photon counting metric Ω_j is shown in the bottom panels. Each curve was computed using the estimated co-polarized signal waveform shown as the blue curve in Fig. 7.5.

in the single photon counting regime with minimal to no dead-time effects present. The resulting integrated histogram then can be interpreted as an integrated power without more adjustments.

The question should be asked as to what magnitude away from unity is necessary for to establish that the received signal is single photon counting? The answer to this is subjective due to the variable nature of Ω_j. If Ω_j shows two orders of separation between $P(k \geq 2; j)$ and $P(k \geq 1; j)$, this can generally be taken to be good. However, examination of two simple case studies indicates that doesn't necessarily remove the possibility for multi-photon counting. In the case that $P(k \geq 1; j) = 1\%$, then two orders down gives $P(k \geq 2; j) = 0.01\%$, which is acceptable. But if $P(k \geq 1; j) = 100\%$, or near to it, then two orders down gives $P(k \geq 2; j) = 1\%$, which is not acceptable. In the latter example there is a high probability for multiple photons to return per every one hundred shots, but in this example a SPL operating with a 100% single photon detection probability is unlikely for a number of reasons. It is then the case that values of Ω_j and $P(k \geq 1, j)$ must examined together to say something consequential about operational modes.

7.3 Single Photon Counting Performance Test Conclusion

The single photon counting metric, along with the individual probabilities of detecting $k \geq 1$ and $k \geq 2$ photons, provides a novel method for evaluating SPL sensors for operation in the single photon counting regime. The use of this metric is made possible by utilizing ATLIS as a sensor forward model. By aligning the measured data with the modeled data, ATLIS can be tapped for additional information content which is not typically associated with a SPL utilizing a standard photon counting or TCSPC approach. Namely, with the access to the originating continuous signal waveforms a number of calculations can be performed.

The analysis performed in this chapter was able to concretely show that the POLAR sensor was operating in a linear photon counting regime during the ARISTO-17 flight campaign. In specific, the ocean sensing portion of the campaign was analyzed and it was found that the ocean surface detections were unlikely to contain significant dead-time artifacts that are documented earlier on in this thesis. The probability for multi-photon detection from the ocean surface was

shown to be very low and unlikely to contribute to the detections shown in Fig. 7.3. This conclusion then lends credence to the SWH and other retrievals performed from this data set, indicating that the POLAR sensor is capable of utilizing a single polarization plane to extract high resolution geoscience. Given that the co-polarized receiver channel detected higher count rates than the cross-polarized channel, the conclusion of single photon counting can then be extended to both receiver channels, providing a whole sensor verification of linearity for this particular evaluation.

The additional atmospheric signal collected by a multi-functional SPL is an added benefit, even if adequate signal levels are achieved through significant temporal and spatial averaging. In fact, it is the case that when the clear air atmospheric signals are low enough to be $\ll 1\%$ the signal can be considered to be in the single photon counting regime. These signals can then be considered as a possible region to perform calibrations, where high count rate locations can be compared for against for linearity tests. In addition to a calibration regime these atmospheric signals have significant scientific viability.

It can be concluded that the forward modeling example in this chapter provides validation of a route forward for SPL sensors, but each sensor must be evaluated on a case-by-case basis. The metric present is not absolute and some additional conclusions must be drawn once the magnitude of Ω_j is known. This indicates that though this metric is useful, if a sensor is altering its detection scheme (detector gain, threshold, etc...) the forward model must be recomputed and the metric estimated for each instance. Though this represents a large computational expenditure, if each measurement regime is forward modeled, singular instances can bolster conclusions and if sensor configurations are un-altered the same conclusions can be carried over to additional measurements.

7.4 Relevance to Posed Thesis Questions

A major crux of the SPL measurement is understanding where and when the sensor is operating linearly and in photon counting mode solely from the acquired photon time-tags. In an effort to further develop solutions to these problems data measured by the POLAR sensor was combined with simulated ATLIS data to create a forward model that could provide greater information con-

tent and be analyzed further. The results showed that this method is possible and allows for these questions to be directly addressed and the acquired photon time-tags could be estimated as linear or not. Given that a SPL measures only a binary detection, this represents a leap forward in data analysis and opens possibilities for further uses of SPL forward modeling.

The work contained within this chapter produced a comprehensive answer to both of these prominent issues for the POLAR sensor and directly contributed to answering two of the three thesis questions:

(1) How are estimates of backscattered photon rate and target range affected by the implementation of the photon time-tagging approach?

- Through the aligned forward model the continuous signal waveforms can be analyzed and interpreted using the mathematics developed in Chapter 3 and additional metrics developed in this chapter. Utilizing this additional information content the POLAR sensor, and other SPLs, can be analyzed for any dead-time effects present in the data set. A key aspect of this is that statistics which include dead-time and those that do not can be directly compared to determine what impact to photon rate and range bias can be expected. This is all done through the forward model, and can be utilized to inform sensor operation.

(2) Can polarimetric lidar incorporate time-correlated single photon counting, and what are the implications to high resolution multi-functional measurements of atmosphere, ocean, and hard targets?

- This chapter provided concrete methods by which the TCSPC technique could be evaluated in a field deployed polarimetric lidar. Data collected by the POLAR sensor during ARISTO-17 was used as a case study for evaluating these techniques. The results shows that POLAR operated in a photon counting regime, and indicated that multi-functional measurements are possible.

Chapter 8

Concluding Remarks

8.1 Advancing Single Photon Counting Lidar

This thesis investigated the use of time-correlated single photon counting in lidar sensors to provide high resolution measurements of geophysical quantities. The work contained within this thesis enhances the lidar community's understanding of SPL modeling and measurements, furthering the contribution of knowledge to lidar sensors that time-tag individual photon detections. New methods, emphasizing the measurement's fundamental statistical nature, were developed in order to investigate and understand the use of SPL for atmospheric and hard target sensing. Utilization of these methods and tools led to several journal publications, [5] and [6], and over ten conferences presentations or invited talks throughout this thesis. The research has a tangible impact on the part of lidar community that is pursuing technology development of geoscience applications, with a journal reviewer quoted as saying that "The dissemination of this analysis will be beneficial for the part of the scientific community involved in the analysis of data provided by the mission ICESat-2" and "...on the use of time tagged single-photon counting data acquisition for atmospheric lidar I think the impact could be significant", lending credence to the application impacts and novelty of the work presented.

The overarching hypothesis examined throughout this thesis was that: **photon counting lidar sensors utilizing time-correlated single photon counting techniques can provide multi-functional capabilities and facilitate high resolution geophysical parameter estimation**. To address this research hypothesis, three specific questions were posed:

(1) What are the implications of utilizing the time-correlated single photon counting approach for geophysical parameter estimation from volume scattering environments?

(2) How are estimates of backscattered photon rate and target range affected by the implementation of the photon time-tagging approach?

(3) Can polarimetric lidar incorporate time-correlated single photon counting, and what are the implications to high resolution multi-functional measurements of atmosphere, ocean, and hard targets?

The related answers and conclusions to each question, including relevant publications, are discussed specifically here. Each portion of the research to answer these questions raised additional questions that could form the basis of future research.

8.1.1 Observing Volume Scattering and Geophysical Parameter Estimation

The ability to make measurements of voluminous scattering medium is vital for lidar sensors expecting to perform geophysical parameter estimation. Atmospheric and ocean sensing with lidar relies solely on this scattering scenario. Using SPL sensors that employ TCSPC and photon time-tagging to perform atmospheric or ocean monitoring is novel to this thesis. Atmospheric measurements made by the laboratory demonstration sensor show the technique's viability, achievable resolutions, and the resulting low data rates. These reasons, and more, provide a solid foundation for delineating the advantages of SPL sensors. The results published in Barton-Grimley *et al.* (2018) [5] give robust analysis and justification for the argument of SPL application to atmospheric monitoring, while also presenting the measurement novelty and necessary frame of thinking required for successful operation. The data presented in Chapter 6 provides examples of open ocean profiles generated from the POLAR SPL sensor, demonstrating that integrated single photon returns from the SPL sensor can form the basis of intensity based understanding of the measurement environment.

8.1.2 Verifying SPL Operation in Photon Counting Mode

Operation of SPL sensors with TCSPC acquisition electronics requires extreme care when considering signal count rates and the implications of operating with a non detector dead-time. These effects result solely from the use of time-tagging electronics. When the SPL measurement requires only a range estimate, the effects are all but ignored completely in previous studies. For an estimate of backscattered photon rate, or intensity, the effects are considered, but focus on detector dead-time and acquisition dead-time is often neglected. The thinking is based on the assumption that data from a sensor operating outside of the linear regime can be corrected in post-processing so that the resulting data are linear once again. There are many methods by which this has been achieved, but emphasis has not been put on the transition from linear to non-linear and how estimates of where and when this happens. This thesis showed that with the fine resolutions offered by utilizing TCSPC, any ignorance of these effects cannot be afforded. The results published in Barton-Grimley *et al.* (2019) [6] show biases and distortions can be expected when a SPL is operated out of photon counting mode, and where they start to occur in terms of mean signal count rate. The publication also provides a basis by which data can be judged for biases by analyzing the accumulated distribution shapes. Using these techniques, while also considering calculations of signal detection rates, allows a rule of thumb judgment as to whether or not a sensor is operating in single photon counting mode. Prior to this work, published knowledge of these effects was sparse and not applicable to geoscience retrievals, but with the publications generated throughout this thesis it is expected that a wide spread understanding of nuances incurred by implementing TCSPC approach will occur.

Additional methods were developed within this thesis to analyze SPL data for adherence to the photon counting assumption. A forward model for the sensor and measurement environment can be generated and aligned to the measured data. This forward model provides additional information content beyond the binary TCSPC measurement and allows in depth analysis of the continuous signal waveforms, in both intensity and statistics spaces. These methods represent a novel analysis

route for SPL sensors and it is anticipated they will be utilized to bolster the ARISTO-17 flight data in an upcoming publication.

8.1.3 POLAR Airborne Measurement Demonstration

Deployment of the POLAR sensor during the ARISTO-17 field campaign represented a step forward in SPL sensing. Prior to this demonstration, most airborne sensors utilizing photon counting techniques did not employ TCSPC. In addition these sensors were of the million-dollar-plus grade of research instruments. The POLAR sensor provides proof that high resolution geoscience can be done with small sensors and in lieu of tremendous hardware investment. This was achieved by relying on a deep understanding of the SPL measurement's physics, by which exploitation of the naturally occurring statistics, polarization, and scattering can lead to high quality data. The deployment was aided by the development of the ATLIS simulator. ATLIS provided a method to understand the airborne TCSPC measurement prior to flight, and then allowed validation and understanding of signals post-flight. Within a single photon time-tag stream, measurements of the atmosphere and ocean, or atmosphere and hard targets were made. In the case of ocean sensing, the dual polarization approach allowed surface signals to be partially isolated from column measurements. For topographic sensing, the dual polarization approach provided information about the surface scatterer through the relative intensity per channel. It was found that unwanted signal is the largest hindrance to SPL operation during day-time. This included a decrease in signal acquisition, in addition to the overwhelming solar background counts. However, with modest sensor tuning single photon detections were made in a plethora of measurement regimes utilizing a 532 nm laser and highly sensitive PMTs during the bright day-time sun light. It was also found that although $1 - 2^{\circ}$ of polarization misalignment may seem manageable, it actually introduces enough coupling between receiver channels that measurements become highly contaminated with unexpected signal.

The sensor development, model development, and results for the POLAR sensor are currently being prepared for publication: Barton-Grimley, Rory A., et al. "Dual polarization single photon

counting lidar development for multi-functional geoscience sensing" (2019) - In Preparation. It is expected that this publication will pave the way for future research grade SPL development and enable geoscience a high resolution.

8.2 Outlook: Meeting Science Requirements with the Next Generation of SPL Sensors

Throughout this thesis work, three macroscopic areas were identified and advances were made that facilitate further research. They are discussed below in separate sections.

8.2.1 Decreased Data Rates

Implementation of the photon time-tagging technique was shown to provide an efficient method to acquire photon events, with the advantages of generating detections per laser firing at picosecond timing resolution throughout the measurement column. This capability can prove favorable for measurement scenarios with limited time on target due to relative platform motion, such as aircraft and spacecraft observations. In a spaceborne environment high bandwidth telemetry is not possible, so introduction of techniques that decrease the overall data load are favorable. Furthermore, nadir viewing airborne and spaceborne lidar systems often capture both atmosphere as well as land and ocean backscattered returns. Flexibility in the TCSPC approach would allow for such diverse scattering scenarios to be fully captured and post-processed for multi-functional retrievals requiring dynamic resolutions. The results shown from the deployment of the POLAR sensor provide an indication of these possibilities.

8.3 Increased Linearity and Collection Efficiency

The measurements shown throughout this thesis reduced complexity in optics and detectors while demonstrating advanced capabilities, and were capable of generating several novel geoscience measurements. However, it was shown that susceptibility to non-linear effects is high through the implemented approaches. The use of arrayed detectors was identified in Chapter 4 as a method by

which collection efficiencies can be increased, while simultaneously decreasing the non-linear effects that result from deviation out of linear photon counting. Implementation of some n_e detector elements to spatially sub-sample each received wavefront would provide a drastic increase to science output from a single sensor, bringing the overall SPL approach into a different category of sensing. Arrayed detectors also have the ability to provide relaxed system design — though at the cost of increased data routing and management. A single large format array could be used for multiple different receiver channels, all of which are providing different scientific measurements. This could be done by parsing different portions of the array to dedicated channels, or more elaborate schemes where different measurements are pursued with different cadences but utilize the same array elements. It is the conclusion of this thesis work that the future SPL sensor builds should utilize these detector types.

8.4 High Resolution Earth Science

The anticipated ICESat-2 data releases will provide the first glimpse of photon counting techniques in space, specifically for science. Though the ATLAS sensor will provide some minimum set of measurements, it is limited in its applicability to atmospheric and ocean subsurface retrievals. Further spaceborne lidar sensors have been identified by the ESDS, where the candidate measurements are applicable to multi-functional operation. These include: differential absorption lidar for water vapor and methane studies, and high-spectral-resolution lidar for clouds, aerosols, and ocean based science. It is likely that one of these sensors will utilize photon counting due to the inherently weak signals present. It would be advantageous to advocate the use of TCSPC, or some TCPSC-like style of acquisition, to meet the resolution and data bandwidth demands of these measurements.

It was shown that the TCSPC technique significantly reduces a sensor's IRF. However, backscattered signals recorded with picosecond timing cannot be considered independent until integration to the IRF width (several centimeters) has been reached. Even so, centimeter range resolutions in a number of geoscience applications is a new capability and can begin to contribute to

understanding fine-scale processes. For atmospheric sensing these techniques could be applied to investigate cloud formation, turbulence, laminae, and other phenomena. Furthermore, this technique can be applied to the wide variety of lidars often applied to atmospheric studies, such as differential absorption lidar, Raman lidar, and resonance-fluorescence lidars, whose scattering properties may be conducive to small-scale observation or dynamic integration. For topographic and bathymetric sensing the possible applications are also broad. The transition between land and water into the shallow regime is one that is not probed well by current lidar sensors. This includes rivers, glacial melt runoff, and coastal environments, all of which could benefit from the advancement of a dedicated small scale sensor.

Bibliography

[1] J. M. Alvarez, Mark A. Vaughan, C. A. Hostetler, W. H. Hunt, and D. M. Winker. Calibration technique for polarization-sensitive lidars. Journal of Atmospheric and Oceanic Technology, 23(5):683–699, 2006.

[2] Hans-Albert Bachor and Timothy C. Ralph. A guide to experiments in quantum optics. Wiley, 2004.

[3] Rory A. Barton-Grimley. Atmospheric Polarimetric Lidar Applied to Glacial Melt Water Measurements, AMS Fall Meeting - Polar Lidar Observations, Seattle, WA, January 2017.

[4] Rory A. Barton-Grimley. High resolution atmospheric lidar using time-correlated single photon counting principles, AGU Fall Meeting - Atmospheric Measurement Techniques, New Orleans, LA, December 2017.

[5] Rory A. Barton-Grimley, Robert A. Stillwell, and Jeffrey P. Thayer. High resolution photon time-tagging lidar for atmospheric point cloud generation. Optics Express, 26(20):26030–26044, 2018.

[6] Rory A. Barton-Grimley, Jeffrey P. Thayer, and Matthew Hayman. Nonlinear target count rate estimation in single-photon lidar due to first photon bias. Optics Letters, 44(5):1249–1252, 2019.

[7] Matthew J. Beals, Jacob P. Fugal, Raymond A. Shaw, Jiang Lu, Scott M. Spuler, and Jeffrey L. Stith. Holographic measurements of inhomogeneous cloud mixing at the centimeter scale. Science, 350(6256):87–90, 2015.

[8] Wolfgang Becker. Advanced time-correlated single photon counting techniques, volume 81. Springer Science & Business Media, 2005.

[9] Max Born, Emil Wolf, Avadh Behari Bhatia, et al. Principles of optics: electromagnetic theory of propagation, interference and diffraction of light, volume 7. Cambridge university press Cambridge, 1999.

[10] Kelly M. Brunt, Robert L. Hawley, Eric R. Lutz, Michael Studinger, John G. Sonntag, Michelle A. Hofton, Lauren C. Andrews, and Thomas A. Neumann. Assessment of NASA airborne laser altimetry data using ground-based GPS data near Summit Station, Greenland. Cryosphere, 11(2):681–692, 2017.

[11] Kelly M. Brunt, Thomas A. Neumann, Jason M. Amundson, Jeffrey L. Kavanaugh, Mahsa Sadat Moussavi, Kaitlin M. Walsh, William B. Cook, and Thorsten Markus. Mabel photon-counting laser altimetry data in alaska for icesat-2 simulations and development. The Cryosphere, 10(4), 2016.

[12] Kelly M. Brunt, Thomas A. Neumann, Kaitlin M. Walsh, and Thorsten Markus. Determination of local slope on the Greenland ice sheet using a multibeam photon-counting lidar in preparation for the ICESat-2 mission. IEEE Geoscience and Remote Sensing Letters, 11(5):935–939, 2014.

[13] Anthony Bucholtz. Rayleigh-scattering calculations for the terrestrial atmosphere. Applied Optics, 34(15):2765–2773, 1995.

[14] Gerald S. Buller, Ross D. Harkins, Aongus McCarthy, Philip A. Hiskett, Gordon R. MacKinnon, George R. Smith, Raymond Sung, Andrew M. Wallace, Robert A. Lamb, Kevin D. Ridley, and John G. Rarity. Multiple wavelength time-of-flight sensor based on time-correlated single-photon counting. Review of Scientific Instruments, 76(8):1–7, 2005.

[15] Gerald S. Buller and Andrew M. Wallace. Ranging and three-dimensional imaging using time-correlated single-photon counting and point-by-point acquisition. IEEE Journal of selected topics in quantum electronics, 13(4):1006–1015, 2007.

[16] James R. Campbell, Dennis L. Hlavka, Ellsworth J. Welton, Connor J. Flynn, David D. Turner, James D. Spinhirne, V. Stanley Scott III, and I.H. Hwang. Full-time, eye-safe cloud and aerosol lidar observation at atmospheric radiation measurement program sites: Instruments and data processing. Journal of Atmospheric and Oceanic Technology, 19(4):431–442, 2002.

[17] Domenic Carr and Grady H. Tuell. Estimating field-of-view loss in bathymetric lidar: application to large-scale simulations. Applied Optics, 53(21):4716–4721, 2014.

[18] James H. Churnside, Johnathan W. Hair, Chris A. Hostetler, and Amy Scarino. Ocean backscatter profiling using high-spectral-resolution lidar and a perturbation retrieval. Remote Sensing, 10(12):2003, 2018.

[19] James H. Churnside, James M. Sullivan, and Michael S. Twardowski. Lidar extinction-to-backscatter ratio of the ocean. Optics Express, 22(15):18698–18706, 2014.

[20] P.B. Coates. Analytical corrections for dead time effects in the measurement of time-interval distributions. Review of scientific instruments, 63(3):2084–2088, 1992.

[21] Van De Hulst and Hendrik Christoffel. Light scattering by small particles. Wiley, 1957.

[22] Brian J. DeBoo, Jose M. Sasian, and Russell A. Chipman. Depolarization of diffusely reflecting man-made objects. Applied Optics, 44:5434–5445, 2005.

[23] John J. Degnan. Photon-counting multikilohertz microlaser altimeters for airborne and spaceborne topographic measurements. Journal of Geodynamics, 34(3-4):503–549, 2002.

[24] John J. Degnan. Scanning, multibeam, single photon lidars for rapid, large scale, high resolution, topographic and bathymetric mapping. Remote Sensing, 8(11), 2016.

[25] D.P. Donovan, J.A. Whiteway, and Allan I. Carswell. Correction for nonlinear photon-counting effects in lidar systems. Applied optics, 32(33):6742–6753, 1993.

[26] Matthew D. Eisaman, Jingyun Fan, Alan Migdall, and Sergey V. Polyakov. Invited review article: Single-photon sources and detectors. Review of scientific instruments, 82(7):071101, 2011.

[27] Ellyn Enderlin, Ian Howat, Seongsu Jeong, Myoung-Jong Noh, Jan van Angelen, and Michiel van den Broeke. An improved mass budget for the Greenland ice sheet. Geophysical Research Letters, 41:1–6, 2014.

[28] Connor J. Flynn, Albert Mendoza, Yunhui Zheng, and Savyasachee Mathur. Novel polarization-sensitive micropulse lidar measurement technique. Optics Express, 15(6):2785, 2007.

[29] Volker Freudenthaler. About the effects of polarising optics on lidar signals and the delta 90 calibration. Atmospheric Measurement Techniques, (9):4181–4255, 2016.

[30] Takashi Fujii and Tetsuo Fukuchi. Laser remote sensing. CRC press, 2005.

[31] Bryce Garby. The effect of ocean waves on airborne lidar bathymetry. 2019.

[32] C.S. Gardner. Target signatures for laser altimeters: an analysis. Applied Optics, 21(3):448–453, 1982.

[33] Philip Gatt, Steven Johnson, and Terry Nichols. Geiger-mode avalanche photodiode ladar receiver performance characteristics and detection statistics. Applied Optics, 48(17):3261–3276, 2009.

[34] Gary G. Gimmestad. Reexamination of depolarization in lidar measurements. Applied Optics, 47(21):3795–3802, 2008.

[35] Andrew Washington Gisler. Monte carlo simulations of polarized light propagating through optically dense media with applications for lidar systems. 2015.

[36] Dennis H. Goldstein. Polarized light. CRC press, 2017.

[37] Joseph W. Goodman. Some effects of target-induced scintillation on optical radar performance. Proceedings of the IEEE, 53(11):1688–1700, 1965.

[38] Joseph W. Goodman. Statistical Optics. John Wiley & Sons, 2015.

[39] Gary C. Guenther. Airborne laser hydrography: System design and performance factors. Technical report, NATIONAL OCEANIC AND ATMOSPHERIC ADMINISTRATION ROCKVILLE MD, 1985.

[40] Johnathan W. Hair, Chris A. Hostetler, Anthony L. Cook, David B. Harper, Richard A. Ferrare, Terry L. Mack, Wayne Welch, Luis Ramos Izquierdo, and Floyd E. Hovis. Airborne high spectral resolution lidar for profiling aerosol optical properties. Applied Optics, 47(36):6734–6752, 2008.

[41] T. Halldorsson and J. Langerholc. Geometrical form factors for the lidar function. Applied Optics, 17(2):240–244, 1978.

[42] David Harding, James Abshire, Philip Dabney, Antonios Seas, Christopher Shuman, Xiaoli Sun, Susan Valett, Aleksey Vasilyev, Tony Yu, Tim Huss, et al. The swath imaging multipolarization photon-counting lidar (simpl): A spaceflight prototype. In Proceedings of the 2008 IEEE International Geoscience & Remote Sensing Symposium, pages 06–11, 2008.

[43] David Harding, Philip Dabney, Susan Valett, Anthony Yu, Aleksey Vasilyev, and April Kelly. Airborne polarimetric, two-color laser altimeter measurements of lake ice cover: A pathfinder for NASA's ICESat-2 spaceflight mission. International Geoscience and Remote Sensing Symposium (IGARSS), pages 3598–3601, 2011.

[44] Zachary T. Harmany, Roummel F. Marcia, and Rebecca M. Willett. This is spiral-tap: Sparse poisson intensity reconstruction algorithms - theory and practice. IEEE Transactions on Image Processing, 21(3):1084–1096, 2012.

[45] Matthew Hayman. Optical theory for the advancement of polarization lidar. 2011.

[46] Matthew Hayman and Scott Spuler. Demonstration of a diode-laser-based high spectral resolution lidar (HSRL) for quantitative profiling of clouds and aerosols. Opt Express, 25(24):1096–1110, 2017.

[47] Matthew Hayman, Scott Spuler, Bruce Morley, and Joseph VanAndel. Polarization lidar operation for measuring backscatter phase matrices of oriented scatterers. Optics Express, 20(28):29553–29567, 2012.

[48] Matthew Hayman and Jeffrey P. Thayer. Explicit description of polarization coupling in lidar applications. Optics Letters, 34(5):611–613, 2009.

[49] Matthew Hayman and Jeffrey P. Thayer. General description of polarization in lidar using Stokes vectors and polar decomposition of Mueller matrices. Journal of the Optical Society of America. A, Optics, image science, and vision, 29(4):400–9, 2012.

[50] Markus Henriksson. Detection probabilities for photon-counting avalanche photodiodes applied to a laser radar system. Applied Optics, 44(24):5140–7, 2005.

[51] Markus Henriksson, Hakan Larsson, Christina Gronwall, and Gustav Tolt. Continuously scanning time-correlated single-photon-counting single-pixel 3-D lidar. Optical Engineering, 56(3):031204, 2016.

[52] Ute Christina Herzfeld, Brian W. McDonald, Bruce F. Wallin, Thomas A. Neumann, Thorsten Markus, Anita Brenner, and Christopher Field. Algorithm for detection of ground and canopy cover in micropulse photon-counting lidar altimeter data in preparation for the icesat-2 mission. IEEE Transactions on Geoscience and Remote Sensing, 52(4):2109–2125, 2014.

[53] Philip A. Hiskett, Colin S. Parry, Aongus McCarthy, and Gerald S. Buller. A photon-counting time-of-flight ranging technique developed for the avoidance of range ambiguity at gigahertz clock rates. Optics Express, 16(18):13685–13698, 2008.

[54] Simon Hooker and Colin Webb. Laser Physics. Oxford University Press, 2010.

[55] Chris A. Hostetler, Michael J. Behrenfeld, Yongxiang Hu, Johnathan W. Hair, and Jennifer A. Schulien. Spaceborne lidar in the study of marine systems. Annual review of marine science, 10:121–147, 2018.

[56] Sebastian Isbaner, Narain Karedla, Daja Ruhlandt, Simon Christoph Stein, Anna Chizhik, Ingo Gregor, and Jörg Enderlein. Dead-time correction of fluorescence lifetime measurements and fluorescence lifetime imaging. Optics Express, 24(9):9429–9445, 2016.

[57] Michael F. Jasinski, Jeremy D. Stoll, William B. Cook, Michael Ondrusek, Eric Stengel, and Kelly M. Brunt. Inland and near-shore water profiles derived from the high-altitude multiple altimeter beam experimental lidar (mabel). Journal of Coastal Research, 76(sp1):44–55, 2016.

[58] David C. Jenn. Radar and laser cross section engineering. Washington, DC: American Institute of Aeronautics and Astronautics, Inc, 1995., 1995.

[59] Steven Johnson, Philip Gatt, and Terry Nichols. Analysis of geiger-mode apd laser radars. In Laser Radar Technology and Applications VIII, volume 5086, pages 359–368. International Society for Optics and Photonics, 2003.

[60] Miroslaw Jonasz and Georges Fournier. Light scattering by particles in water: theoretical and experimental foundations. Elsevier, 2011.

[61] Damien Josset, Peng-Wang Zhai, Yongxiang Hu, Jacques Pelon, and Patricia L. Lucker. Lidar equation for ocean surface and subsurface. Optics Express, 18(20):20862–20875, 2010.

[62] Peter Kapusta, Michael Wahl, and Rainer Erdmann. Advanced photon counting. Springer Series on Fluorescence, 15, 2015.

[63] George W. Kattawar. Genesis and evolution of polarization of light in the ocean [invited]. Applied Optics, 52:940–8, 2013.

[64] George W. Kattawar and Charles N. Adams. Stokes vector calculations of the submarine light field in an atmosphere-ocean with scattering according to a Rayleigh phase matrix: Effect of interface refractive index on radiance and polarization. Limnology and Oceanography, 34(8):1453–1472, 1989.

[65] Michael J. Kavaya. Polarization effects on hard target calibration of lidar systems. Applied Optics, 26(5):796–804, 1987.

[66] James D. Klett. Stable analytical inversion solution for processing lidar returns. Applied Optics, 20(2):211, 1981.

[67] Yuri I. Kopilevich, Viktor I. Feygels, Grady H. Tuell, and Alexey Surkov. Measurement of ocean water optical properties and seafloor reflectance with scanning hydrographic operational airborne lidar survey (shoals): I. theoretical background, 2005.

[68] Nils J. Krichel, Aongus McCarthy, and Gerald S. Buller. Resolving range ambiguity in a photon counting depth imager operating at kilometer distances. Optics Express, 18(9):9192–9206, 2010.

[69] R. Kwok, G.F. Cunningham, J. Hoffmann, and T. Markus. Testing the ice-water discrimination and freeboard retrieval algorithms for the icesat-2 mission. Remote sensing of environment, 183:13–25, 2016.

[70] Zhijian Li, Jiancheng Lai, Chunyong Wang, Wei Yan, and Zhenhua Li. Influence of dead-time on detection efficiency and range performance of photon-counting laser radar that uses a geiger-mode avalanche photodiode. Applied Optics, 56(23):6680–6687, 2017.

[71] Shih-Yau Lu and Russell A. Chipman. Interpretation of Mueller matrices based on polar decomposition. Journal of the Optical Society of America A, 13(5):1106, 1996.

[72] Jing Luo, Dong Liu, Binyu Wang, Lei Bi, Kejun Zhang, Yuling Liu, Chunao Wen, Lingying Jiang, Liming Yang, and Lin Su. Effects of a nonideal half-wave plate on the gain ratio calibration measurements in polarization lidars. Applied Optics, 56(29):8100–8108, 2017.

[73] Yue Ma, Song Li, Wenhao Zhang, Zhiyu Zhang, Rui Liu, and Xiao Hua Wang. Theoretical ranging performance model and range walk error correction for photon-counting lidars with multiple detectors. Optics Express, 26(12):15924–15934, 2018.

[74] Aurora Maccarone, Aongus McCarthy, Ximing Ren, Ryan E. Warburton, Andy M. Wallace, James Moffat, Yvan Petillot, and Gerald S. Buller. Underwater depth imaging using time-correlated single-photon counting. Optics Express, 23(26):33911, 2015.

[75] H. Angus Macleod. Thin-film optical filters. CRC press, 2010.

[76] Lori A Magruder and Kelly M. Brunt. Performance Analysis of Airborne Photon- Counting Lidar Data in Preparation for the ICESat-2 Mission. IEEE Transactions on Geoscience and Remote Sensing, pages 1–8, 2018.

[77] Leonard Mandel and Emil Wolf. Optical coherence and quantum optics. Cambridge university press, 1995.

[78] Willem J. Marais, Robert E. Holz, Yu Hen Hu, Ralph E. Kuehn, Edwin E. Eloranta, and Rebecca M. Willett. Approach to simultaneously denoise and invert backscatter and extinction from photon-limited atmospheric lidar observations. Appl. Opt., 55(29):8316–8334, Oct 2016.

[79] Thorsten Markus, Tom Neumann, Anthony Martino, Waleed Abdalati, Kelly Brunt, Beata Csatho, Sinead Farrell, Helen Fricker, Alex Gardner, David Harding, Michael Jasinski, Ron Kwok, Lori Magruder, Dan Lubin, Scott Luthcke, James Morison, Ross Nelson, Amy Neuenschwander, Stephen Palm, Sorin Popescu, C. K. Shum, Bob E. Schutz, Benjamin Smith, Yuekui Yang, and Jay Zwally. The Ice, Cloud, and land Elevation Satellite-2 (ICESat-2): Science requirements, concept, and implementation. Remote Sensing of Environment, 190:260–273, 2017.

[80] John S. Massa, Gerald S. Buller, Andrew C. Walker, Sergio Cova, Manikam Umasuthan, and Andrew M. Wallace. Time-of-flight optical ranging system based on time-correlated single-photon counting. Applied optics, 37(31):7298–7304, 1998.

[81] John S. Massa, Gerald S. Buller, Andrew C. Walker, George Smith, Sergio Cova, Manickam Umasuthan, and Andrew Wallace. Optical design and evaluation of a three-dimensional imaging and ranging system based on time-correlated single-photon counting. Applied Optics, 41(6):1063–1070, 2002.

[82] John S. Massa, Andrew M. Wallace, Gerard S. Buller, S.J. Fancey, and Andrew C. Walker. Laser depth measurement based on time-correlated single-photon counting. Optics letters, 22(8):543–545, 1997.

[83] Aongus McCarthy, Robert J. Collins, Nils J. Krichel, Verónica Fernández, Andrew M. Wallace, and Gerald S. Buller. Long-range time-of-flight scanning sensor based on high-speed time-correlated single-photon counting. Applied Optics, 48(32):6241–6251, 2009.

[84] Aongus McCarthy, Nils J. Krichel, Nathan R. Gemmell, Ximing Ren, Michael G. Tanner, Sander N. Dorenbos, Val Zwiller, Robert H. Hadfield, and Gerald S. Buller. Kilometer-range, high resolution depth imaging via 1560 nm wavelength single-photon detection. Optics Express, 21(7):8904–8915, 2013.

[85] Matthew McGill, Dennis Hlavka, William Hart, V. Stanley Scott, James Spinhirne, and Beat Schmid. Cloud physics lidar: Instrument description and initial measurement results. Applied Optics, 41(18):3725–3734, 2002.

[86] Matthew McGill, Thorsten Markus, Stanley S. Scott, and Thomas Neumann. The multiple altimeter beam experimental lidar (MABEL): An airborne simulator for the ICESat-2 mission. Journal of Atmospheric and Oceanic Technology, 30(2):345–352, 2013.

[87] Matthew McGill, Wilbert R. Skinner, and Todd D. Irgang. Analysis techniques for the recovery of winds and backscatter coefficients from a multiple-channel incoherent doppler lidar. Applied Optics, 36(6):1253–1268, 1997.

[88] Raymond Measures. Laser remote sensing: fundamentals and applications. Krieger Publishing Company, 1984.

[89] M.I. Mishchenko and J.W. Hovenier. Depolarization of light backscattered by randomly oriented nonspherical particles. Optics Letters, 20(12):1356–1358, 1995.

[90] Steven E. Mitchell. Remote measurement of shallow media depth using polarization lidar. 2013.

[91] Steven E. Mitchell and Jeffrey P. Thayer. Ranging through shallow semitransparent media with polarization lidar. Journal of Atmospheric and Oceanic Technology, 31(3):681–697, 2014.

[92] Steven E. Mitchell, Jeffrey P. Thayer, and Matthew Hayman. Polarization lidar for shallow water depth measurement. Applied Optics, 49(36):6995–7000, 2010.

[93] Curtis D. Mobley. Light and water: radiative transfer in natural waters. Academic press, 1994.

[94] J. Morison. Icesat-2 atbd atl12 ocean surface elevation. 2018.

[95] J. Morison, R. Kwok, S. Dickinson, D. Morison, C. Peralta-Ferriz, and R. Andersen. Sea state bias of icesat in the subarctic seas. IEEE Geoscience and Remote Sensing Letters, 15(8):1144–1148, 2018.

[96] Amin R. Nehrir, Christoph Kiemle, Mathew D. Lebsock, Gottfried Kirchengast, Stefan A. Buehler, Ulrich Löhnert, Cong-Liang Liu, Peter C. Hargrave, Maria Barrera-Verdejo, and David M. Winker. Emerging technologies and synergies for airborne and space-based measurements of water vapor profiles. Surveys in Geophysics, 38(6):1445–1482, 2017.

[97] Amin R. Nehrir, Kevin S. Repasky, and John L. Carlsten. Eye-safe diode-laser-based micropulse differential absorption lidar (dial) for water vapor profiling in the lower troposphere. Journal of Atmospheric and Oceanic Technology, 28(2):131–147, 2011.

[98] Desmond O'Connor. Time-correlated single photon counting. Academic Press, 2012.

[99] Ali H. Omar, David M. Winker, Mark A. Vaughan, Yongxiang Hu, Charles R. Trepte, Richard A. Ferrare, Kam-Pui Lee, Chris A. Hostetler, Chieko Kittaka, Raymond R. Rogers, et al. The calipso automated aerosol classification and lidar ratio selection algorithm. Journal of Atmospheric and Oceanic Technology, 26(10):1994–2014, 2009.

[100] Gregory R. Osche. Optical detection theory for laser applications. Wiley-VCH, page 424, 2002.

[101] Athanasios Papoulis. Probability & statistics, volume 2. Prentice-Hall Englewood Cliffs, 1990.

[102] Matthias Patting, Michael Wahl, Peter Kapusta, and Rainer Erdmann. Dead-time effects in TCSPC data analysis. Proc. SPIE, 6583:658307–658310, 2007.

[103] Agata M. Pawlikowska, Abderrahim Halimi, Robert A. Lamb, and Gerald S. Buller. Single-photon three-dimensional imaging at up to 10 kilometers range. Optics Express, 25(10):11919–11931, 2017.

[104] Sara Pellegrini, Gerald S. Buller, Jason M. Smith, Andrew M. Wallace, and Sergio Cova. Laser-based distance measurement using picosecond resolution time-correlated single-photon counting. Measurement Science and Technology, 11(6):712, 2000.

[105] J.M. Picone, A.E. Hedin, D.P. Drob, and A.C. Aikin. Nrlmsise-00 empirical model of the atmosphere: Statistical comparisons and scientific issues. Journal of Geophysical Research: Space Physics, 107(A12):SIA–15, 2002.

[106] Michael R. Roddewig, James H. Churnside, and Joseph A. Shaw. Mapping the lidar attenuation coefficient in yellowstone lake, yellowstone national park, usa. In Propagation Through and Characterization of Atmospheric and Oceanic Phenomena, pages PTu3F–2. Optical Society of America, 2018.

[107] Clive D. Rodgers. Inverse methods for atmospheric sounding: theory and practice, volume 2. World scientific, 2000.

[108] Jun J. Sakurai and Eugene D. Commins. Modern quantum mechanics, revised edition. AAPT, 1995.

[109] Jie Shan and Charles K. Toth. Topographic laser ranging and scanning: principles and processing. CRC press, 2018.

[110] Kristofer Y. Shrestha, K. Clint Slatton, William E. Carter, and Tristan K. Cossio. Performance Metrics for Single - Photon Laser Ranging. IEEE Geoscience and Remote Sensing Letters, 7(2), 2010.

[111] Benjamin E. Smith, Alex Gardner, Adam Schneider, and Mark Flanner. Modeling biases in laser-altimetry measurements caused by scattering of green light in snow. Remote sensing of environment, 215:398–410, 2018.

[112] William A. Sneed and Gordon S. Hamilton. Validation of a method for determining the depth of glacial melt ponds using satellite imagery. Annals of Glaciology, 52(59):15–22, 2011.

[113] James D. Spinhirne. Micro pulse lidar. IEEE Transactions on Geoscience and Remote Sensing, 31(1):48–55, 1993.

[114] Scott M. Spuler, Kevin S. Repasky, Bruce Morley, D. Moen, Matthew Hayman, and Amin R. Nehrir. Field-deployable diode-laser-based differential absorption lidar (DIAL) for profiling water vapor. Atmospheric Measurement Techniques, 8(3):1073–1087, 2015.

[115] Ove Steinvall. Effects of target shape and reflection on laser radar cross sections. Applied Optics, 39(24):4381–4391, 2000.

[116] Robert A. Stillwell, Ryan R. Neely III, Jeffrey P. Thayer, Matthew D. Shupe, and David D. Turner. Improved cloud-phase determination of low-level liquid and mixed-phase clouds by enhanced polarimetric lidar. Atmospheric Measurement Techniques, 11(2):835, 2018.

[117] Jeffrey P. Thayer, Norman B. Nielsen, Russell E. Warren, Craig Heinselman, and Jens Sohn. Rayleigh lidar system for middle atmosphere research in the arctic. Optical engineering, 36(7):2045–2062, 1997.

[118] Bin-Ming Tsai and C.S. Gardner. Remote sensing of sea state using laser altimeters. Applied Optics, 21(21):3932–3940, 1982.

[119] M. Vaughan. The Fabry-Perot interferometer: history, theory, practice and applications. CRC press, 1989.

[120] CR Vaughn, JL Button, WB Krabill, and D Rabine. Georeferencing of airborne laser altimeter measurements. International Journal of Remote Sensing, 17(11):2185–2200, 1996.

[121] Michael Wahl, Tino Röhlicke, Hans-jürgen Rahn, Rainer Erdmann, Gerald Kell, Andreas Ahlrichs, Martin Kernbach, Andreas W. Schell, and Oliver Benson. Integrated multichannel photon timing instrument with very short dead time and high throughput Integrated multichannel photon timing instrument with very short dead time and high throughput. Review of Scientific Instruments, 043102(2013), 2013.

[122] Claus Weitkamp. Lidar: range-resolved optical remote sensing of the atmosphere, volume 102. Springer Science & Business, 2006.

[123] Jonathan M. Wilkinson, Robin J. Hogan, Anthony J. Illingworth, and Angela Benedetti. Use of a lidar forward model for global comparisons of cloud fraction between the icesat lidar and the ecmwf model. Monthly weather review, 136(10):3742–3759, 2008.

[124] Rebecca M. Willett and Robert D. Nowak. Multiscale poisson intensity and density estimation. IEEE Transactions on Information Theory, 53(9):3171–3187, 2007.

[125] David M. Winker, Mark A. Vaughan, Ali Omar, Yongxiang Hu, Kathleen A. Powell, Zhaoyan Liu, William H. Hunt, and Stuart A. Young. Overview of the calipso mission and caliop data processing algorithms. Journal of Atmospheric and Oceanic Technology, 26(11):2310–2323, 2009.

[126] Yuekui Yang, Alexander Marshak, Stephen P. Palm, Tamás Várnai, and Warren J. Wiscombe. Cloud impact on surface altimetry from a spaceborne 532-nm micropulse photon-counting lidar: System modeling for cloudy and clear atmospheres. IEEE Transactions on Geoscience and Remote Sensing, 49(12):4910–4919, 2011.

[127] Tiangang Yin, Nicolas Lauret, and Jean-Philippe Gastellu-Etchegorry. Simulation of satellite, airborne and terrestrial lidar with dart (ii): Als and tls multi-pulse acquisitions, photon counting, and solar noise. Remote Sensing of Environment, 184:454–468, 2016.

[128] J.E. Yorks, M.J. McGill, S.P. Palm, D.L. Hlavka, P.A. Selmer, E.P. Nowottnick, M.A. Vaughan, S.D. Rodier, and W.D. Hart. An overview of the cats level 1 processing algorithms and data products. Geophysical Research Letters, 43(9):4632–4639, 2016.

[129] John E. Yorks, Matthew McGill, V. Stanley Scott, Shane W. Wake, Andrew Kupchock, Dennis L. Hlavka, William D. Hart, and Patrick A. Selmer. The airborne cloud–aerosol transport system: Overview and description of the instrument and retrieval algorithms. Journal of Atmospheric and Oceanic Technology, 31(11):2482–2497, 2014.

[130] Anthony W. Yu, David J. Harding, and Philip W. Dabney. Laser transmitter design and performance for the slope imaging multi-polarization photon-counting lidar (simpl) instrument. In Solid State Lasers XXV: Technology and Devices, volume 9726, page 97260J. International Society for Optics and Photonics, 2016.

[131] Neal H. Zaun, Carl Weimer, Yakov Sidorin, and David Lunt. Solid-etalon for the calipso lidar receiver. In Earth Observing Systems IX, volume 5542, pages 141–146. International Society for Optics and Photonics, 2004.

[132] Peng-Wang Zhai, George W. Kattawar, and Yongxiang Hu. Comment on the transmission matrix for a dielectric interface. Journal of Quantitative Spectroscopy and Radiative Transfer, 113(16):1981–1984, 2012.

[133] Guanhua Zhou, Wujian Xu, Chunyue Niu, and Huijie Zhao. The polarization patterns of skylight reflected off wave water surface. Optics Express, 21(26):32549–32565, 2013.

Appendix A

Supporting Information

A.1 Etalon Modeling and Housing Design

To facilitate daytime operation, a solid etalon was purchased from LightMachinery and installed to the POLAR sensor's receiver. The as-purchased specifications are given in Fig. A.1. Due to some uncertainty of the exact wavelength of the Teem Photonics laser used in the transmitter (the manufacturer specified at 532.18 nm, but would not provide precision on their measurements), the etalon was specified with as close to 532 nm as possible. The delivered optic had a peak wavelength of 532.066 nm, indicating that tilt and temperature tuning would be necessary. As these etalons are multi-mode, with additional pass-bands under 1 nm away from the central it was necessary to use an additional interference filter to block these addition modes. An 300 pm bandpass filter from Omega Optical was purchased and installed in front of the etalon mounting assembly on a separate non-tiling mount.

	Measurement	Specification	Comment
Etalon Thickness	400.7 micron	400 +/- micron	Measured at 1550 nm at 24 deg C
Thickness uniformity RMS	0.6 nm	< 1.5nm	Measured at 1550 nm at 24 deg C
Coating Reflectivity	74.2-74.4%	74.5% +/- 0.5% at 532nm	
AR Coating	<0.1%	<0.2% at 532nm	
Transmission Peak Position	532.066 nm		Measured at 532 nm at 30 deg C
Transmission peak FWHM	23.4 pm	22-25 pm	Measured at 532 nm at 30 deg C
Trapsnmission peak FSR	236.6 pm	238 +/- 2 pm	Measured at 532 nm at 30 deg C
Finesse	10.1	9.5-10.7	Calculated from transmission paramters at 532nm at 30 deg C

Figure A.1: LightMachinery Fused Silica solid etalon as-delivered specifications. The optic was spec'd for 532 nm operation, a <30 pm bandwidth, and a >10 finesse. The delivered optic was a leftover from a run that matched out specifications and was provided heavily discounted.

To understand the theoretical necessities for correctly integrating the etalon with the rest of the receiver optics, the etendue of the system and the etalon response to temperature and angular variations were considered.

The equations to properly match the etendue of the telescope and the etalon are given from [119] as

$$A_T\Omega_T = (\pi r_T^2)(\pi\theta_T^2) \tag{A.1}$$

$$A_E\Omega_E = (\pi r_E^2)(2\pi\Delta\lambda/\lambda) \tag{A.2}$$

where θ_T and θ_E are the FOV half angles for the telescope and etalon respectively, r_T is the radius of the telescope, r_E is the radius of the rays entering the etalon, $\Delta\lambda$ is the etalon bandwidth, and λ is the wavelength of peak transmission. With these equations, the optical system leading up to the etalon can be analyzed to ensure that proper collimation is passed through the system while also filling the necessary clear aperture of the optic.

A simple shows how angular tuning the etalon can vary filter bandwidth, peak transmittance, and peak wavelength. It is the case that "collimated" light in the receiver is actually still partially diverging or converging. Under the assumption that the "collimated" rays make up a cone of semi-angle Θ and defining the angle of incidence of the cone of rays as Φ, the range of angles that are incident on the face of the etalon will be $\Phi \pm \Theta$. In the case of the optic discussed here, angular tuning shifts the pass-band blue-ward towards smaller wavelengths. According to [75], the angular response of the peak wavelength in a dielectric thin-film filter can be given as

$$\lambda_{peak} = \lambda_0 \left(1 - \frac{\Phi^2 + \Theta^2}{2n^2}\right) \tag{A.3}$$

Also according to [75], the angular response of the filter's FWHM bandwidth and peak transmittance is given as

$$\Delta\lambda_{new} = \sqrt{\Delta\lambda^2 + \left(\frac{2\Theta\Phi\lambda_0}{n^2}\right)^2} \tag{A.4}$$

$$\tau_{peak} = \left(\frac{\Delta\lambda_{new}}{\frac{2\Theta\Phi\lambda_0}{n^2}}\right) \arctan\left[\frac{\frac{2\Theta\Phi\lambda_0}{n^2}}{\Delta\lambda_{new}}\right] \tag{A.5}$$

where $\Delta\lambda_{new}$ is the adjusted bandwidth, λ_0 is the initial peak wavelength at normal incidence, and n is the index of refraction, which is equal to 1.4607 for fused silica. With a new estimate of the FWHM bandwidth the interferometer's solid angle and full collection angle, FOV, can be calculated

$$\Omega_E = \pi\theta_E^2 = \frac{2\pi\Delta\lambda_{new}}{\lambda_0} \tag{A.6}$$

which then gives

$$\theta_E = 2\sqrt{2\Delta\lambda_{new}/\lambda_0} \tag{A.7}$$

showing that as the bandwidth increases, so does the FOV of the etalon.

Unfortunately to an oversight on my part, the etendue of the receiver system was not optimized for the etalon correctly, resulting in a mismatch of focal lengths and a beam radius of 2.5-3 mm on the etalon face, instead of the expected 12 mm. The result of the mismatched etendue gave the collimated receiver light at best 70-90 mrad of divergence. The effects of this mismatched are characterized and show in Fig. A.2. The tolerance to miss alignments in tilt become very small, as 5 mrad off normal incidence and the transmission drops over 20 % with the equations reaching a essentially flat steady state value until much larger tilt angles are used. Some of these calculations were done after the fact to understand the transmission of the etalon and why the receiver throughput was significantly less than expected. Adjustments to the optical system were not able to be done again before flight, so optimization of this configuration was necessary for the GV deployment.

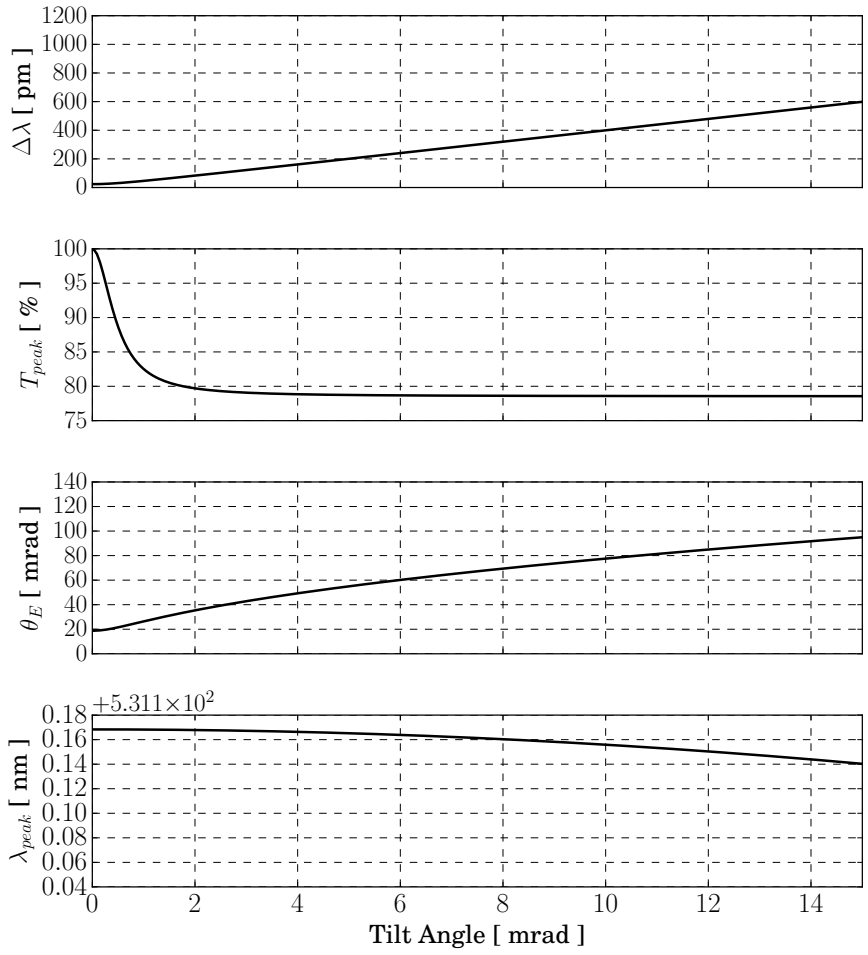

Figure A.2: Bandwidth, transmission, and etalon acceptance FOV as a function of the tilt tuning angle θ for the poor 120 mrad divergence configuration. As can be seen, the transmission of the system reaches 50 % by the 10 mrad tilt angle, and the bandwidth has increased to over 50 pm. By the full tilt angle of 40 mrad, the etalon bandwidth has approached the interference filter width of 300 pm and the transmission has dropped below 20%.

The etalon was installed to the sensor and testing was done to maximize the tilt and temperature of the optic by taking atmospheric profiles. The idea being that a baseline for the instrument already existed for the range of signals seen over an atmospheric profile, so knowing those numbers the instrument could be walked back to a closely optimized location. To compensate for transmission losses and maximize throughput amplifiers in the CFD were utilized, recognizing that this solution only partially solves the bar to increased detection rates.This was done over the course of

two evenings of trials and after this was done the sensor was immediately installed to the NCAR GV for flight campaigns.

With these calculations in mind simulations were run to understand what beam diameter and collimation is necessary to facilitate a high throughput in future receiver re-designs. Figures A.4 and A.5 show contours for the pass bandwidth and peak transmission as a function on tilt angle and beam divergence. It as assumed that the beam divergence will not go beyond 10 mrad and limited tilt tuning to 40 mrad is allowed. The specifications shown in A.1 were used to generate the contours.

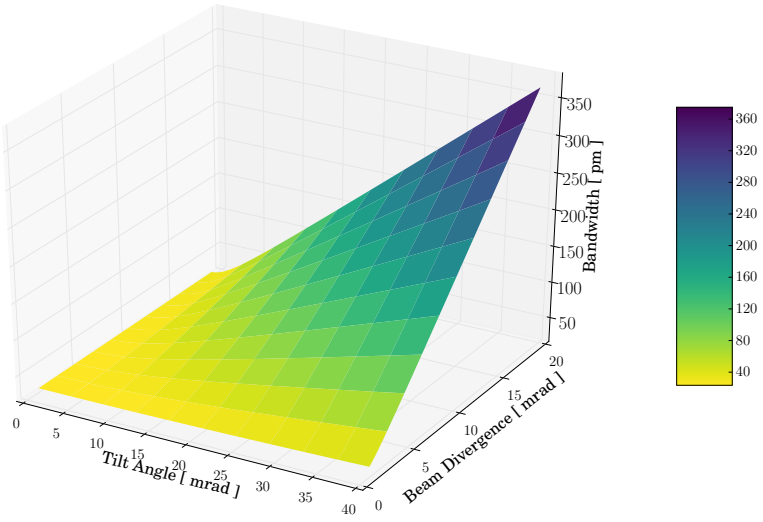

Figure A.3: A comparison between the tilt tuning range and divergence of the rays passing through the etalon and their impact on the bandwidth of the optic. The bandwidth starts at the normal incidence value of 23.4 pm and reaches 350 pm when the tilt of the optic has reached 40 mrad and at peak divergence. For lower divergences, under 4 mrad, the bandwidth is less prone to change under tilt tuning.

The bandwidth is shown to have the largest dependence on beam divergence, and that non-normal incidence does play a roll but the effects are more drastic when the collimation of the rays is poor. The transmission can be seen to drop of quickly for both tilt angle and beam divergence. These figures imply that specific attention needs to be paid to matching the etendue of the etalon to the rest of the receiver, and the telescope FOV may not be the limiting FOV if etendue is not matched properly. Using these figures and calculating the etendue of possible telescope and

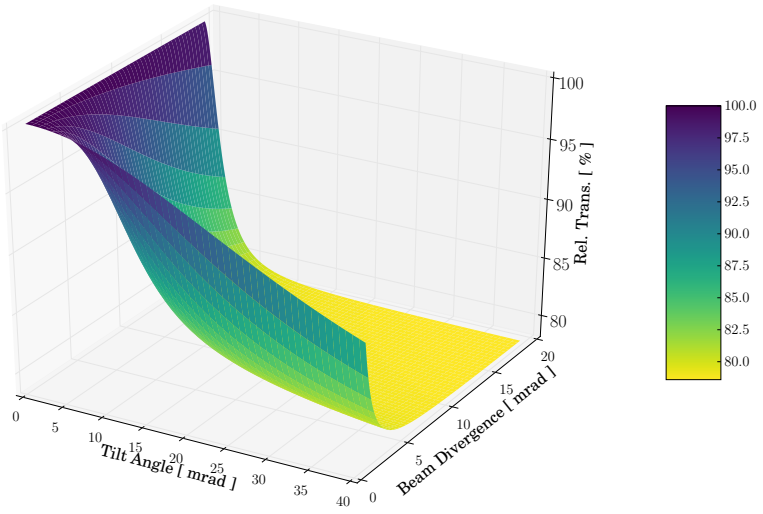

Figure A.4: A comparison between the tilt tuning range and divergence of the rays passing through the etalon on their impact on the transmission coefficient of the optic. As the divergence reaches the maximum allowable value and the optic is tilted to 40 mrad, the transmission drops to 20%. From this figure, it can be seen that for a beam divergence of under 4 mrad, the tilt tuning can reach 10 mrad before dropping below 80% transmission.

collimating lens combinations, an optimum divergence can be found and then maximized through proper tilt tuning.

The etalon housing was designed to compensate for the thermal expansion of the optic and the surrounding aluminum, ensuring that the probability of damage to the glass "sandwich" blanks was low. The inner housing was then put into a delrin machined housing to act as an insulator and the housing was tapped on each side for Thorlabs SM1 threads to accept windows. An early diagram of the housing is shown in Figs. A.5 and A.6. The clear aperture of the etalon was specified at 15 mm, and the housing encroached by 1.5 mm in radius, reducing the clear aperture to 12 mm. The housing was then mounted to a Thorlabs CR1 manual rotation stage with a 5 arcmin read out, or 1.45 mrad, and low backlash for tilt tuning, seen in Fig. A.7. The etalon was temperature controlled as discussed in Chapter 5, allowing redshifting of the pass-band.

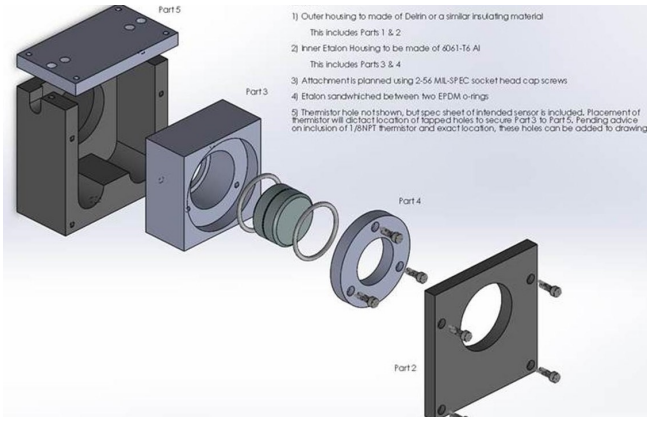

Figure A.5: Partial representation of the final design for the etalon thermal housing.

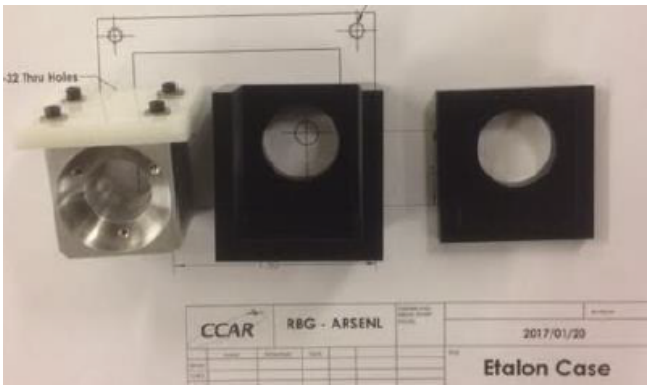

Figure A.6: Machined parts for the etalon housing.

Figure A.7: Final assembly of the housing without the front delrin cover.

A.2 ARISTO-17 Data Specifics

A.2.1 Lidar and Aircraft Data Assimilation

This section will document the efforts to develop a callable Python function that can be given a photon time-tag and retrieved the associated GV values through a search and interpolation routine. The purpose of this development is so that each detected photon can be geolocated relative to the WGS84 ellipsoid and have the aircraft motion removed from the ranging information.

As the SPL data is asynchronous in time, with detection rates from Hz to MHz depending on the measurement environment, and the GV's IMU and GPS values have a defined sampling frequency, there is a necessity to find relatively fast and efficient method to assimilate these values together. The aircraft data has the following data rates: IRS yaw/pitch/roll 50 Hz, GPS altitude/latitude/longitude 10 Hz, and time is kept at 1 Hz (not reported at higher frequency, but it is assumed that the >1 Hz rates are initialized on the second, so the times can be extrapolated for each device). An example of GPS altitude and the delta values are shown in Fig. A.8

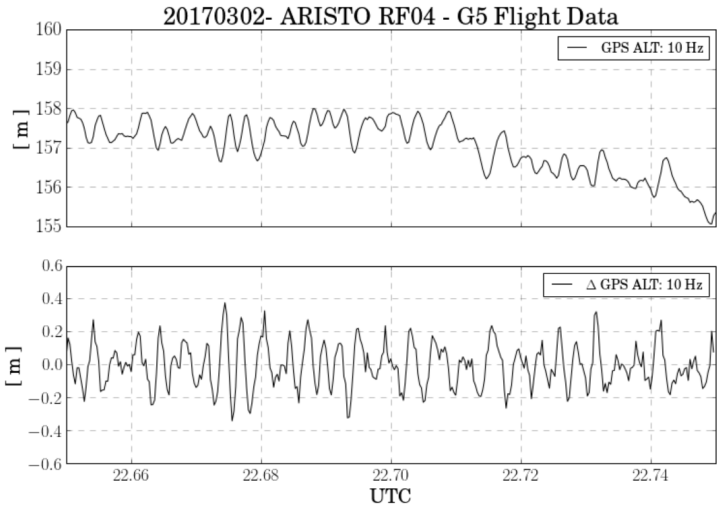

Figure A.8: Captured GPS altitude data from ARISTO-17 research flight 4, with the top panel showing the raw data and the bottom panel showing the delta between points.

High frequency changes in the data must be captured accurately. It was found that a cubic

spline captures both high and low frequency changes in the data with highest accuracy. Using the delta of the IMU altitude, to give another example of a aircraft parameter, it is easy to see both frequencies present in the data and the accuracy of the fit, shown in Fig. A.9.

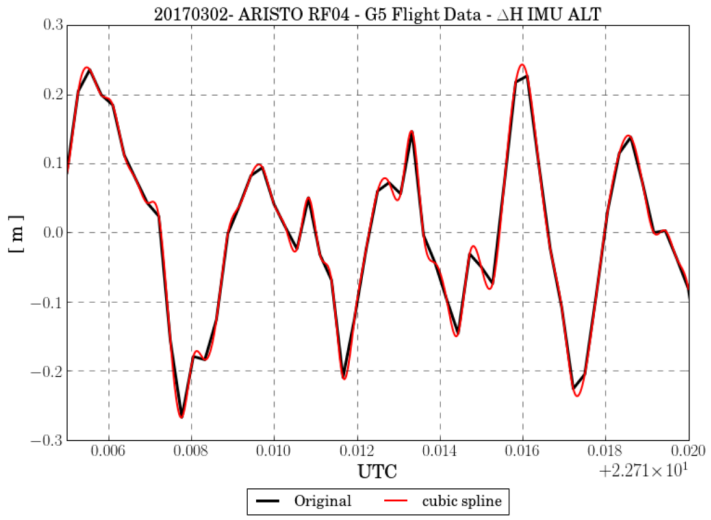

Figure A.9: Example of a cubic spline fit to the reported aircraft IMU altitude. The delta between IMU points was created and used as the sample set.

To actually retrieve the parameters a low point density cubic spline is fitted to each aircraft data parameter needed and then a binary search mechanism reliably finds two points in the aircraft data that bound the photon detection. A point density of the interpolation is then increased between the two points to achieve the closest match in time to the photon detection. The output from this routine is a data frame where each column gives the photon detection time and then the associated aircraft values from the search/interpolation algorithm.

A series of test points were generated and pushed through the routine to test functionality. A picosecond precise time-tag was input into the routine, using the detection time only, and the subsequent aircraft values were then found. The output from the assimilation is shown in Fig. A.10. For each test point the recovered IMU pitch and roll at the detection is shown in the top two panels and the GPS altitude, longitude, and latitude are shown in the bottom three panels. It can be seen that the detection times, black line, agree well with values on the lower sampling frequency

aircraft data, shown in cyan. Though this is a fairly brute force method to generating the SPL and aircraft assimilation, resulting in execution times that would not facilitate real-time products when in operation, the method was shown to work well and was implemented in all post-processing analysis of the ARISTO-17 field campaign data.

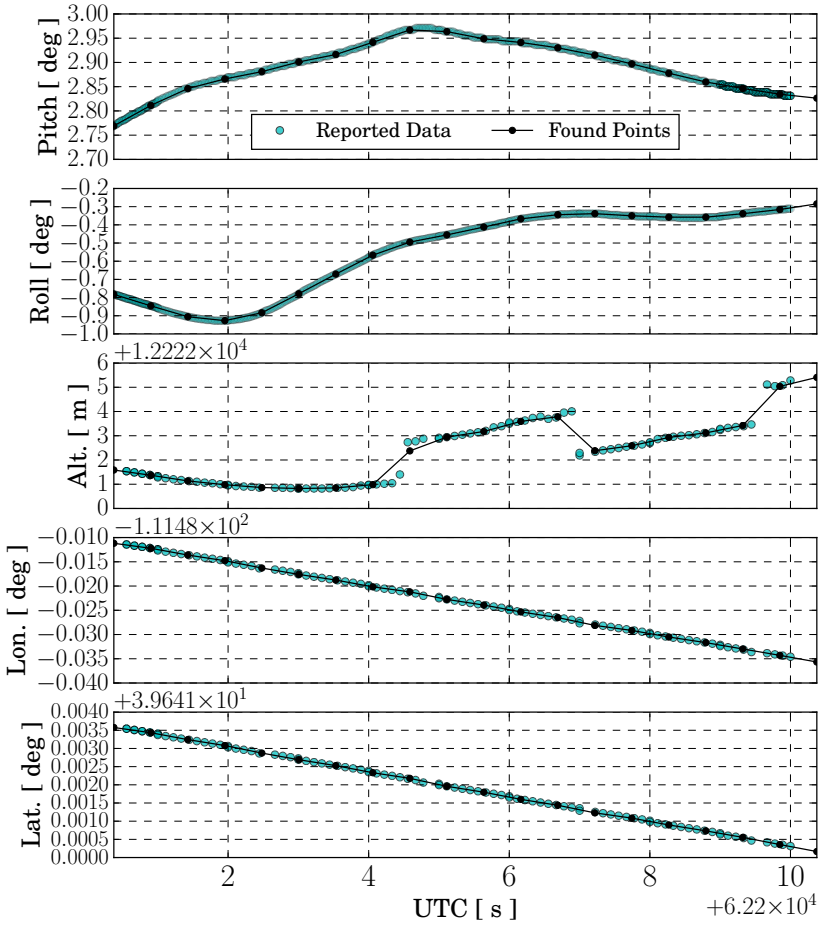

Figure A.10: Outputs from the search function for test photon detections, shown in black, for the IMU's roll and pitch and the GPS's latitude, longitude, and altitude. The input aircraft data from the GV is shown as cyan points.

A.2.2 Georeferencing Photon Detections

The georeferencing equation was introduced in Chapter 5 as

$$\vec{\rho}_{WGS84} = \vec{\rho}^{GPS}_{WGS84} + R^{-1}(\lambda, \phi - 90°, 0)R^{-1}(\beta, \alpha, \psi)\left\{R^{-1}(\Delta\beta, \Delta\alpha, \Delta\psi)\vec{r}_L + \vec{r}^{L}_{GPS}\right\} \tag{A.8}$$

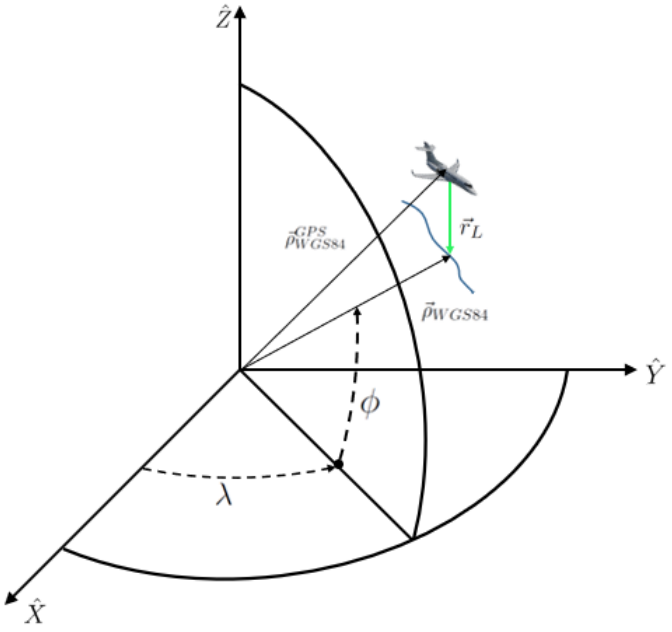

Figure A.11: Geometry of the georeferencing equation.

in an effort to provide the final data as elevations on the WGS84 ellipsoid. Like the notation in [120], $R(\beta, \alpha, \psi)$ is shortened from $R_1(\beta)R_2(\alpha)R_3(\psi)$. The same notation is also used for $R^{-1}(\beta, \alpha, \psi)$. The general form for the rotation matrices are:

$$R_1(\theta) = \begin{bmatrix} 1 & 0 & 0 \\ 0 & \cos(\theta) & \sin(\theta) \\ 0 & -\sin(\theta) & \cos(\theta) \end{bmatrix} \tag{A.9}$$

$$R_2(\theta) = \begin{bmatrix} \cos(\theta) & 0 & -\sin(\theta) \\ 0 & 1 & \sin(\theta) \\ \sin(\theta) & 0 & \cos(\theta) \end{bmatrix} \tag{A.10}$$

$$R_3(\theta) = \begin{bmatrix} \cos(\theta) & \sin(\theta) & 0 \\ -\sin(\theta) & \cos(\theta) & 0 \\ 0 & 0 & 1 \end{bmatrix} \tag{A.11}$$

from which the inverses can then be calculated for the georeferencing algorithm. The term $\vec{r}^{L}_{GPS}$ is the lever arm from the GPS to the lidar of form $[X^L_{GPS}, Y^L_{GPS}, Z^L_{GPS}]^T$ measured manually prior to flight. The term $\vec{r}_L$ is the measured range by the lidar of form $[0, 0, Z_L]^T$. The term $\vec{\rho}^{GPS}_{WGS84}$ is the measured position as reported by the GPS.

Since no boresight calibration flights were flown the term $R^{-1}(\Delta\beta, \Delta\alpha, \Delta\psi)$, which account for offsets in mounting from the aircraft's frame, the only value known was $\Delta\alpha = -3.5^\circ$ due to the fixed pitch compensation built into the sensor mount. The remainder of the terms were set to zero when input into the rotation matrices.

A.3 SensL CFD and TDC Specifics

The purpose of this section is show some necessary information for the counting system that was not appropriate for the thesis text. This includes diagrams of operation, pseudo-code for re-synchronizing the time-tags and an explanation of the FIFO buffer failure.

Figure A.14 shows the physical wiring for the TDC module as flown. The 250 kHz internal clock to the TDC module was routed through a splitter into the start channels for each receiver channel. The stop is the routed from each detector in each receiver channel. The synchronization of the clocks required to use this implementation is discussed briefly in the next section.

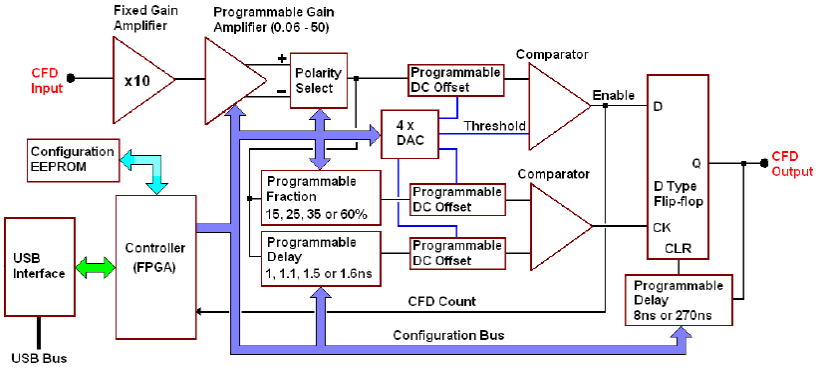

Figure A.12: A diagram of the SensL CFD module's signal handling. Important is the fixed 10X amplifier gain and the delay, fraction, and inversion portions. The output is a volt level TTL-pulse and the internal electronics have a 8 ns dead-time. The programmable amplifier was typically run at ∼1-1.5X gain. The CFD output goes to the TDC input in Fig. A.13.

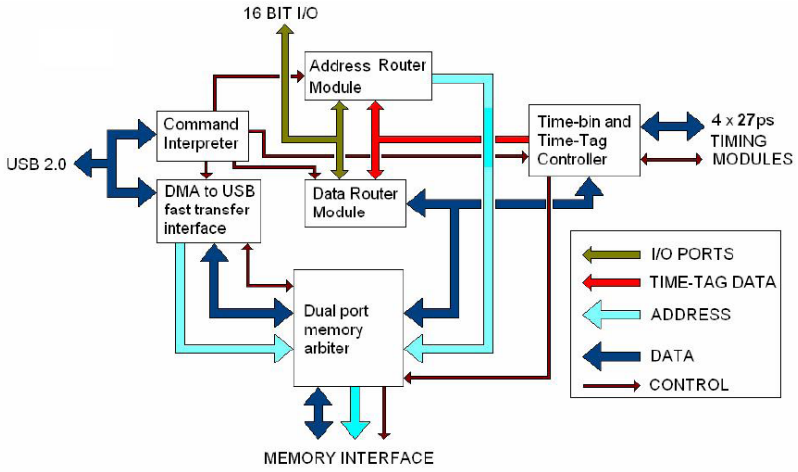

Figure A.13: SensL TDC module routing diagram. The time-tag controller, USB interface and routers can be seen. The separate TDC modules shown in the diagram receive inputs from the CFD module.

A.3.1 Synchronizing Macrotime and Microtime TDC Clocks

The TDC module was operated in "resync" mode, where photon events are written out as macrotime and microtime values and must be processed to arrive at the actual detection's time-tag. Each time-tag consists of a 32-bit unsigned value, with the first reporting the MICROtime

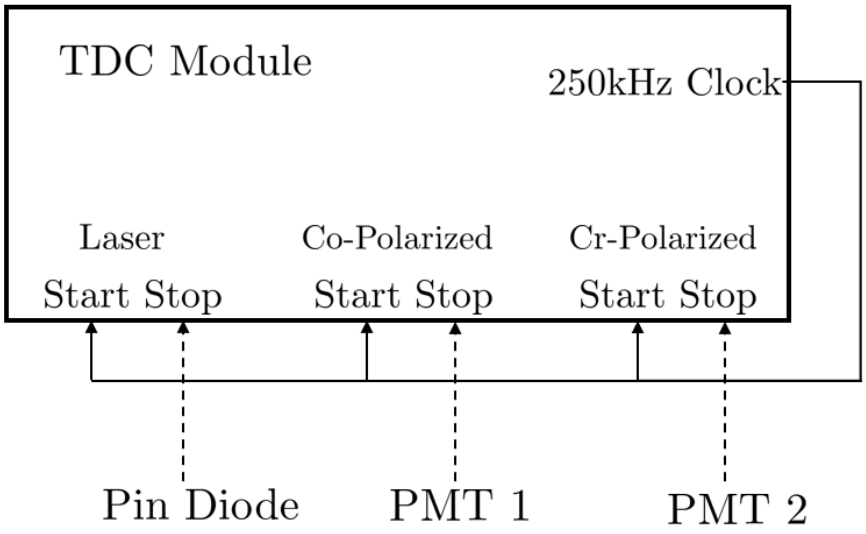

Figure A.14: SensL TDC module signal routing diagram. RG316 SMA cables route from the internal clock to the Start for each channel. The pin diode, PMT1, and PMT2 refer to the inputs from the associated CFD channels.

and channel number and the second reporting the MACROtime value. The MICROtime counting as a value of 26.9851 ps, setting the TDC resolution. The first word reports the MICRO time and channel number. The second word reports the MACROtime with a least significant bit of 25 ns, reading out the 250 kHz START clock. This counter is reset to 0 on every cycle of the 250KHz clock.

Each photon time-tag value, to picosecond precision, is calculated as follows:

- Calculate offset between MACRO and MICRO timers
  - The first time-tag is used to calculate the MACRO offset MACoffset as follows: MACROoffset = FirstMACRO-((FirstMICRO*26.9851)/25000) $\cdots$ (25000ps = 25ns) Gives the count of the MACRO when the first 4μs frame is started.
- Calculate the current 4μs frame
  - FrameNo = (MACRO-MACROoffset)/160 $\cdots$ (160*25ns = 4μs or 250KHz)

- Calculate the remainder of MACRO counts
    - Remainder = REM of (MACRO-MACROoffset)/160
- Adjust the FrameNo based on possible boundary conditions
    - If (Remainder<60 & MICRO>100000) then FrameNo=FrameNo-1

      i.e. If MACRO is just past boundary and MICRO is large then Rollover hasnt occurred
    - If (Remainder>110 & MICRO<40000) then FrameNo=FrameNo+1

      i.e. If MACRO is near end of boundary and MACRO is small the ROLLOVER has already occurred

A.3.2 Implications of FIFO Buffer Failure

During the ARISTO-17 campaign it was found that in certain high noise environments the TDC model would fail and report bad data. The failure seems to result in a mixing of channel designations such that it is impossible to designation whether a detection is real or from a different channel. As seen here in Fig. A.15, the expected 14.3 kHz laser sync signal becomes corrupted and returns non-real values, upwards of 30 kHz in some areas.

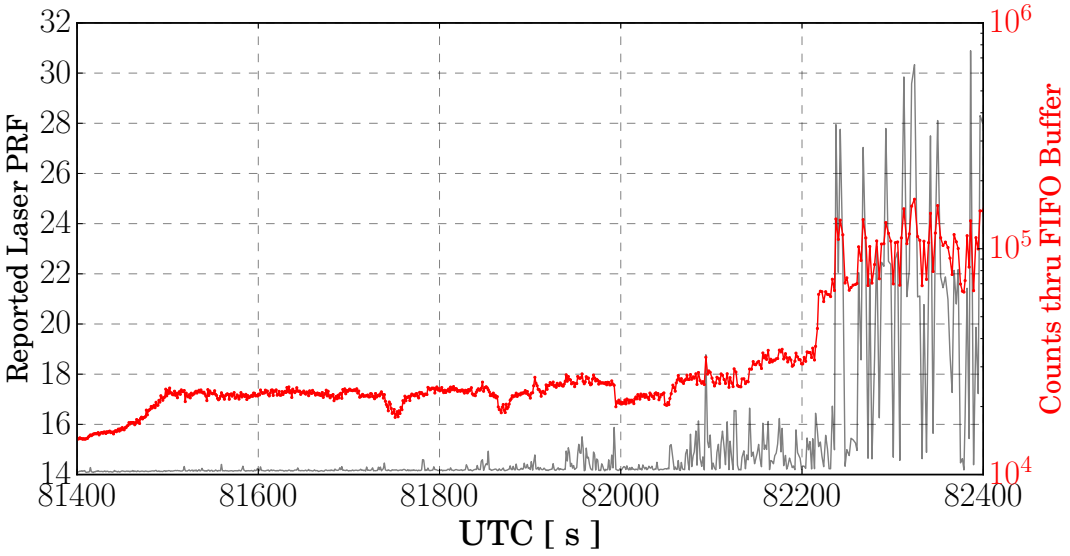

Figure A.15: This figure shows the implications of when the SensL TDC module reaches high throughput and fails, providing higher than expected laser sync signals. The left axis shows the reported laser PRF, in black, and the right axis shows the total number of counts pushed through the FIFO buffer in the TDC module, in red.

To mitigate using bad data for signal processing, a filter was implemented in the processing chain to flag data where the laser sync had increased in PRF. This was done on a per shot basis by computing the IPP between shots and comparing against the expected value of $\sim 70\mu$s. This issue occurred in several flight environments, but seemed to always be linked to the noise rates and thus the total counts through the buffer. The total allowable is quoted at 5 MHz by SensL, but failure was found at $\sim 10^5$ total counts.

A.4 GV Window Polarization Tests

The transmitted Stokes vector for POLAR sensor was measured before and after the aircraft window using a quarter wave plate, polarizer, and integrating sphere, shown in Fig. A.16. A neutral density filter of ND6 was also included to decrease transmit energies. The sensor was tilted at ∼3.5 degrees to simulate the correct orientation.

The measured value post window was:

$$\vec{S} = A \begin{bmatrix} 1 \\ -0.9985 \\ 0 \\ 0 \end{bmatrix} \tag{A.12}$$

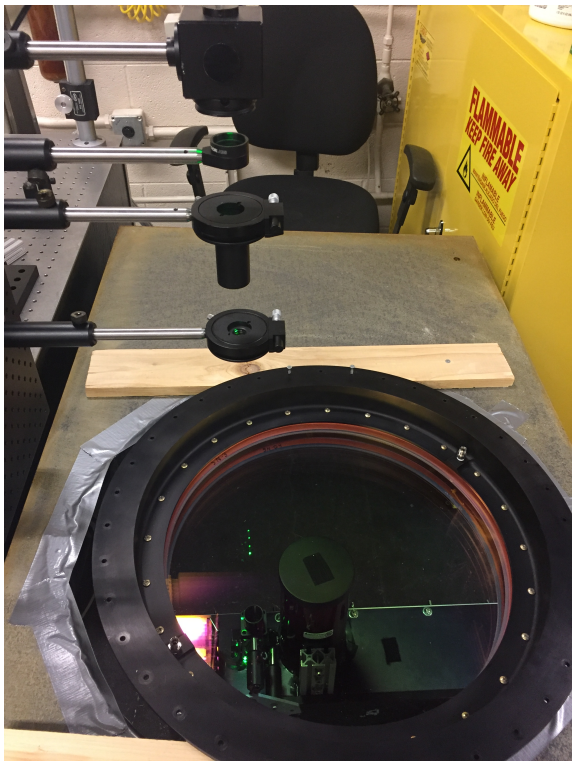

Figure A.16: Set up for measuring the transmitted stokes vector prior to aircraft installation. The aircraft window as placed horizontal with the POLAR sensor transmitting vertically through the glass.